

Bichromatic Slowing of Metastable Helium

Michael Andrew Chieda, Ph.D.

University of Connecticut, 2012

This dissertation describes experiments to develop and realize an atomic decelerator (or “slower”) for metastable helium using the optical bichromatic force (BCF). The research comprises two subtopics—using the bichromatic force at very large detunings, and developing a chirped BCF slower. There is experimental evidence that as bichromatic detunings approach 300 times the natural linewidth, the BCF breaks down. The likely cause is that large Doppler frequency shifts from the rapid deceleration result in cumulative dephasing of the Rabi cycling of the atom. To circumvent this and other problems, we have developed an alternate slower design in which the center frequency of a narrow BCF force profile is swept to stay resonant with the atoms as they are slowed. Results from a first-generation experiment show atomic slowing larger than has previously been possible with a large fixed detuning. Additional refinements will allow the design to be scaled up enough to slow metastable helium atoms to magneto-optical trapping velocities, with a brightness comparable to modern Zeeman slowers, but in a much smaller and considerably simplified configuration. I close with a discussion of prospects for direct laser slowing of molecules using the BCF. An estimate for CaF shows that a buffer-gas cooled beam can be slowed to rest, and proof-of-principle experiments in atomic helium yield very promising results.

Bichromatic Slowing of Metastable Helium

Michael Andrew Chieda

B.A., Northwestern University, Evanston, IL 1993

M.S., University of Connecticut, Storrs, CT 2011

A Dissertation

Submitted in Partial Fulfilment of the

Requirements for the Degree of

Doctor of Philosophy

at the

University of Connecticut

2012

Copyright by

Michael Andrew Chieda

2012

APPROVAL PAGE

Doctor of Philosophy Dissertation

Bichromatic Slowing of Metastable Helium

Presented by

Michael Andrew Chieda, B.A., M.S.

Major Advisor

Edward E. Eyler

Associate Advisor

George N. Gibson

Associate Advisor

Juha Javanainen

University of Connecticut

2012

For my wife, Jenny

ACKNOWLEDGEMENTS

Despite the many long days spent alone in lab, this work did not happen in a vacuum—many people contributed in many ways to my success. In particular, I’d like to thank:

My advisor, Ed Eyler, for his guidance, support and encouragement throughout these experiments, through funding losses and equipment failures. Ed has been an exceptional mentor, role model, and friend, and it is an honor to now consider him a colleague.

George Gibson and Juha Javaneinen, my associate advisors, for their insights, thoughtful contributions to, and thorough editing of this work.

Hal Metcalf at Stony Brook University for his optimism, enthusiasm, availability to answer questions and offer guidance, and for providing the original Fortran OBE numerical solution code. I also need to thank his graduate students for their encouragement and willingness to share their technical expertise, especially Claire Allred (Sheehan), Jason Reeves, Matthew Cashen, Matthew Partlow, Chris Corder, Daniel Stack, and John Elgin.

John Leakavich at IntraAction for his unwavering customer service and technical support with the high frequency AOMs. John repeatedly went above and beyond what was asked of him to keep my experiments running.

Brian Lincoln at Nufern for his diligence facilitating the repair, return, and loan of the fiber laser amplifiers.

Jennifer Carini for her generosity and flexibility in loaning the 2 GHz oscilloscope to me for the chirp calibrations.

Michael Bellos, Brian Conway, and Nicholas Destefano for their contributions to these experiments.

Alan Chase for his friendship and help maintaining perspective whenever I had research tunnel vision.

The gentlemen of P210—Nolan Samboy and J.C. Sanders, for their friendship and comraderie during long homework sets, failed experiments, and weekend celebrations. And the rest of my classmates for their company, discussions, diversions, and collaborations that have immeasurably enriched this experience.

Derek Burkins and his family for their invaluable friendship, comic relief, and much needed vacations in Vermont.

My sister-in-law Katy and mother-in-law Barbara, and the whole Damato family for their love and friendship, many words of encouragement, and prayers of support. I could not have married into a finer family.

My parents and two brothers who, without ever having imagined this day, have always believed in me.

Lastly, and most importantly, I need to thank my wife, Jenny, whose unconditional love and encouragement through the sacrifices, long weeks apart, and uncertainty has been my guiding light, making all of this possible.

TABLE OF CONTENTS

1. Introduction	1
1.1 Radiative Force	3
1.1.1 Zeeman Slowers	6
1.1.2 Optical Molasses	7
1.2 Sub-Doppler Cooling of Multi-Level Atoms	8
1.3 Dipole Force	9
1.4 Rectified Optical Dipole Forces	11
2. The Bichromatic Force	15
2.1 π -Pulse Model	16
2.2 Doubly-Dressed Atom Model	21
2.3 Numerical Calculation	29
2.4 Shifting the Center of the Force	31
2.5 BCF Characteristics	33
2.5.1 Optimum Rabi Frequency	34
2.5.2 Bichromatic Beam Irradiance Requirement	34
2.5.3 Velocity Range	35
2.5.4 Bichromatic Slowing Time	35
2.5.5 Cooling	36
3. Large Detuning Limitations and Slower Design Considerations	37
3.1 Decelerative Dephasing	39
3.2 ac Stark Shift	44
3.3 Non-Adiabatic Following of Landau-Zener Transitions	49

3.4	Collisional Dephasing	51
3.5	Engineering Limitations	54
3.5.1	Intensity	55
3.5.2	Phase	55
4.	Large-Detuning BCF: Experiment	60
4.1	Large Detuning BCF Overview	60
4.2	Metastable Helium Source	61
4.2.1	Design and Construction	64
4.2.2	Operation and Characterization	70
4.3	Time of Flight Velocity Profiling	71
4.4	Metastable Helium Detection	74
4.4.1	Detector and Ceratron Electron Multiplier	74
4.4.2	Transimpedance Amplifier	74
4.5	Diode Laser and Frequency Stabilization	78
4.5.1	Diode Laser	78
4.5.2	Saturated Absorption Spectroscopy	78
4.6	Bichromatic Frequency Production	80
4.7	Optical Amplification	83
4.8	Doppler Shifting The Bichromatic Force	85
4.9	RF Phase Adjustment	86
4.10	Interaction Region	87
4.10.1	Beam Waists	87
4.10.2	Polarization Control	88
4.10.3	Optimal Irradiance	89
4.11	Data Acquisition	89

4.11.1	Data Averaging and Analysis	91
5.	Large Detuning BCF: Analysis	92
5.1	Experimental Slowing Results and Analysis	92
5.2	Evidence of a Possible Upper Limit	96
5.3	Discussion of Single-Beam Forces	99
6.	Chirped BCF: Experiment	102
6.1	Chirped BCF Experiment Overview	102
6.2	Biased Photodiodes	106
6.3	Lasers and Shifting the Force	107
6.3.1	Lasers	107
6.3.2	Laser Frequency Modulation Interface	107
6.3.3	Frequency Stabilization	111
6.4	Bichromatic Frequency Generation	114
6.5	RF Phase	114
6.6	Frequency Chirping	117
6.7	Interaction Region	122
7.	Chirped BCF: Analysis	123
7.1	Experimental Results	123
7.2	Analysis	127
7.3	First Generation Chirped BCF Hardware Shortcomings	130
7.3.1	Bichromatic Beat Note Phase Lock	130
7.3.2	Bichromatic Beam Pointing	132
7.3.3	Repeatability of the Chirp Peak Magnitude	133
7.4	Extension to a Useful He* Slower	133

8. BCF in Multilevel Systems	136
8.1 BCF in He* with π -Polarized Light	137
8.1.1 Theoretical Considerations	137
8.1.2 Experiment and Results	140
8.2 Direct Laser Slowing of Molecules	143
9. Next Generation BCF Decelerator for He*	150
9.1 Bichromatic Detuning Increase	150
9.2 Improved Beat Note Phase Stability	154
9.3 Improved Optical Access to Interaction Region	155
9.4 Prescale the Heterodyne Frequency	157
9.5 Liquid Crystal Variable Retarders	158
9.6 Reconfiguration of the He* Source and Beam Machine	158
A. Numerical OBE Solver Programs	160
A.1 Numerical OBE Solver in Fortran	161
A.2 Numerical OBE Solver in Mathematica	165
B. Data Acquisition Programs	169
C. Toptica DL-MOD FET Current Modulation Circuit	181
D. Microcontroller-based Frequency Synthesizer	183
E. FFT-Based Heterodyne Chirp Analysis Program	185
F. Chirped BCF Monte Carlo Simulation	189
References	199

LIST OF FIGURES

2.1	A Bloch vector $\rho(t) = (u(t), v(t), w(t))$ elevated by the polar angle $\theta(t)$ as defined in Eq. (2.1.1). Its projection onto the w -axis gives the population difference between levels $ a\rangle$ and $ b\rangle$. The points A and B correspond to the stationary states $ a\rangle$ and $ b\rangle$.	17
2.2	A pair of bichromatic beams, showing beat notes in the irradiance as seen by an atom at rest. Choosing the detuning δ such that the π -pulse repetition rate is large compared to the decay rate $\gamma \equiv 1/\tau$, several bichromatic cycles will occur for each spontaneous emission.	18
2.3	Two manifolds of uncoupled energy levels of the combined atom-field states (indicated at left). The short red upwards arrow represents excitation via absorption of a photon from the red-detuned field $ n\rangle$, and the short blue downwards arrow excitation via absorption from the blue-detuned field $ m\rangle$. The equal spacing of levels $\hbar\delta$ is due to the symmetric detuning of the bichromatic fields.	23
2.4	Bichromatic dressed energy levels as a function of spatial position for $\delta = 154\gamma$ and $\chi = \pi/4$. Plot A shows the result for the π -pulse condition $\Omega_r = (\pi/4)\delta$ while plot B shows the result for $\Omega_r =$ $\sqrt{3/2}\delta$. The highlighted (red) trace shows a potential pathway accessed by the bichromatic force. The corresponding standing wave amplitudes from Eq. (2.2.1) are shown in plot C. Note the similarity to independently calculated plots in Refs. [35, 36] for much smaller detunings.	25

2.5 Spatial variation of dressed state levels from the lower manifold in Fig. 2.3 for $\delta = 154\gamma$, $\Omega_r = \sqrt{3/2}\delta$, and $\chi = \pi/4$. The bare atom is in its ground state on levels marked in blue (bold lines). An atom on path A spends approximately 75% of the time in the excited state and is therefore more likely to undergo spontaneous emission than an atom on path B. Note the similarity to independently calculated plots in Refs. [35, 36] for much smaller detunings.	27
2.6 Calculated bichromatic force vs. velocity for $\delta = 154\gamma$ and phase $\chi = \pi/4$ with different values of Ω_r . The optimum Rabi frequency, defined as the value yielding the largest central force, occurs at $\Omega_r = \sqrt{3/2}\delta$, in agreement with the DDA treatment in Section 2.2, and not at $(\pi/4)\delta$ as the π -pulse analogy predicts. Note that the force magnitude is scaled by twice the radiative force, $F_{\text{rad}} = \hbar k\gamma/2$.	32
2.7 Bichromatic force in the laboratory frame with center frequencies Doppler shifted by $\pm \vec{k} \cdot \vec{v}_c$, resonant with the atom moving at velocity \vec{v}_c .	33
3.1 Compilation of numerical computation results as described in Section 2.3 for high detunings with $\Omega_r = \sqrt{3/2}\delta$ and $\phi = \pi/2$. The linear increase of both the BCF magnitude and velocity range indicates the lack of an upper bound. Successful BCF slowing experimental results for He* to date are limited to $\delta \leq 184\gamma$	38

3.2 Representations of the Bloch sphere (see Fig. 2.1) depicting one Rabi cycle of the atom from ground state $ g\rangle$ to upper state $ n\rangle$ and back. For the cases of no shift and a static shift (at left and center), the atom makes one complete Rabi cycle. However, if the shift is time dependent (at right), the Rabi cycle may not be complete due to the frequency difference between the cycle beginning and end. This produces in small dephasings $\Delta\varphi$, which accumulate over one upper-state lifetime t' . If the accumulated dephasing $\approx \pi$, the force reduces direction and the time-averaged BCF is reduced.	40
3.3 Bichromatic dressed energy levels as a function of spatial position for $\delta = 370\gamma$ and $\chi = \pi/4$ for increasing Doppler shifts top to bottom. Notice the energy gaps at avoided crossings are proportionate to the difference in photon energy between the red and blue detuned Doppler shifted fields.	43
3.4 He* levels of interest in these experiments in both unperturbed and ac Stark shifted configurations. In the case of large detunings the upper bichromatic component $\omega_{12} + \delta$ is close enough to the 2^3P_1 level to induce significant coupling with the 2^3S_1 level, with the relevant detuning shown by the short red arrow. The unwanted coupling shifts the 2^3S_1 level down and the 2^3P_1 level up by ΔE , resulting in an asymmetry in the bichromatic detunings relative to the 2^3P_2 level.	45

3.5 BCF degradation due to the indicated detuning asymmetries for $\delta = 184\gamma$ and $\phi = \pi/2$ from numerical solutions to the OBEs. Note the force magnitude is reduced by more than 50% for an asymmetry of 0.2δ .	48
3.6 Mean BCF magnitude with and without the detuning asymmetry due to ac Stark shifts. BCF results were numerically calculated from solutions to the OBEs for $\Omega_r = \sqrt{3/2}\delta$, $\phi = \pi/2$, and assuming 10% of the total irradiance in the π -polarized fields relevant for the ac Stark effect.	48
3.7 Energy levels for $\Omega_r = 1.1\delta$ and $\chi = \pi/4$ for detunings $\delta = 185\gamma$ in (a) and $\delta = 370\gamma$ in (b) for comparison. Note that the Rabi frequency is below the optimal value and the avoided crossings shown to touch in Fig. 2.4 now have an increased separation for clarity. Dashed lines represent the energy level gradients ∇E . An example of a desired crossing is circled in green, and an undesired (force reversing) crossing is circled in red. Note the uniform scaling of both energy levels and avoided crossings with δ .	50
3.8 Dependence of the BCF magnitude on phase difference (in $E(z, t)$) from the optimum $\chi = \pi/4$ for detunings of 185γ , 370γ , and 570γ for $\Omega_r = \sqrt{3/2}\delta$. Results are based on numerical solutions to the OBEs as described in Section 2.3. Note the increased sensitivity to phase with increasing detuning.	56

3.9 Calculated average BCF magnitude (normalized to optimum conditions) as a function of total phase change over one BCF slowing time, as described in Section 2.5.4. Using information from Table 3.1, the average force experienced by the atoms drops sharply with increasing phase change, and the relative change in force magnitude increases for larger detunings.	57
3.10 Average force applied to an atom during one BCF slowing time taking into account the phase change, assuming an initial atom velocity of 1000 m/s, compared to the force for fixed $\chi = \pi/4$. Note the leveling off of the force magnitude at high detunings, which sets a limit on the maximum slowing.	58
4.1 Somewhat simplified experimental layout for the large-detuning BCF decelerator.	62
4.2 Energy level diagram for helium showing the transitions of interest to these experiments. Note that the level spacings are not drawn to scale.	63
4.3 Metastable helium source. Source operation is described in the text .	65
4.4 Metastable helium source detail showing nozzle end of Pyrex tube with cathode needle installed. The nominal spacing is 15 mm from the needle tip to the front end of the Pyrex tube. The teflon needle centering spacer is also shown surrounding the polished aluminum needle holder. Notice the Pyrex insulator tube beginning at the rear of the centering spacer that runs the rest of the electrode length to suppress unwanted glow discharges in the rear of the source. . . .	65

4.5	Metastable helium source discharge. Source nozzle at left, skimmer at right. Along with metastable helium atoms and visible light, the source produces a significant amount of ultraviolet light.	66
4.6	Beam Machine layout top (upper) and side (lower) views showing source location and related connections.	67
4.7	UConn first-generation metastable helium source installed in the vacuum chamber showing source nozzle and skimmer (at right), helium inlet (lower left), liquid nitrogen fill and drain lines (braided stainless steel), and source exhaust bellows. Louvers for the water-cooled oil trap above the diffusion pump are visible below the source. . .	69
4.8	Critical distances in the bichromatic slower time of flight. The $\pm kv$ mirror positions represent the final turning mirrors before the slower beams cross the metastable helium beam, nominally at the center of the mirror separation. The relatively large mirror separation facilitates a small crossing angle between the slowing lasers and the atom beam, providing the longest overlap possible.	72
4.9	Time of flight spectra for metastable helium. The sharp peak at $t \approx 0.0$ ms is the uv light peak and the broader peak is from the metastable helium atoms. Note that the zero of the timebase has been shifted to coincide with the center of the uv peak.	73
4.10	Metastable helium detector with modified Faraday cup.	75
4.11	Transimpedance amplifier circuit for the metastable helium TOF signal.	76
4.12	Gain and phase delay measurements for the transimpedance amplifier. All measurements were made using a 22 nA peak-to-peak sine wave input and recorded with a Tektronix TDS 3036 oscilloscope. . . .	77

4.16 Diagram of data acquisition and processing. For an N sample average, the acquisition is broken into subunits of size n , where n is usually 200. This helps to reduce the effects of slow drifts in the source brightness over long acquisitions, reducing offset errors when comparing the slowed velocity distribution (BCF) to the unslowed (Bkgnd) distribution. Circles represent repetition and averaging by the number indicated inside the circle.	90
5.1 Experimentally observed velocity profiles for BCF slowing, increasing in detuning from top to bottom. The dotted black trace is the unslowed (background) distribution, red is the slowed distribution, and blue is the difference. Notice the anomalous result at $\delta = 278\gamma$, which seems to support the observation of an upper limit for the BCF detuning.	93
5.2 Comparison of experimental results with $\delta = 278\gamma$ and a Monte Carlo random walk model with a BCF profile $61 \gamma/k$ wide with simulated random strong dephasing ($\Delta\phi = \pi$). Doppler shifts for the model and experiment are the same.	98
5.3 Comparison of the observed “single beam” force (green) to a simulated velocity profile using a monochromatic laser field and the radiative force (blue), with an unperturbed atomic velocity distribution with the dashed black line.	100
6.1 Chirped BCF slower experiment block diagram showing key optical and electronic components.	103

6.2 Chirped BCF slower experimental layout showing frequency stabilization and bichromatic frequency generation optics. The He [*] source and the optics in the beam machine are the same as shown in Fig. 4.11	104
6.3 Chirped BCF slower electronic components and connections showing frequency stabilization and chirped signal generation.	105
6.4 Photodiode bias circuit. The reverse bias voltage, which reduces diode capacitance, can be anywhere from 9 V to 15 V. We typically used one type A23 12 V battery to eliminate the problems associated with external power supplies—power supply voltage fluctuations, noise pickup in power cables, and ground loops.	106
6.5 FET current modulation interface circuit for the TuiOptics DL100. The modulation input voltage on the FET gate causes a small amount of current to bypass the laser diode, changing the lasing frequency. The 2N4148 diodes limit the modulation voltage, protecting the laser diode. In addition to this circuit, the laser diode voltage sense (U-LD) had to be re-routed from its original measurement point at the rear of the laser head to sense the voltage drop directly at the diode as shown.	109
6.6 DL100 FET current modulation board installations showing the factory installed PCB and the custom built circuit. In all photos, the laser head connector plane is to the right, and the laser diode mount is the brass block on the left. The lasers are facing to the left.	110
6.7 Calibration of the UConn FET current modulation circuit and comparison to the commercial Toptica DL-MOD FET current modulation board. Data for DL-MOD response curve was taken from [82]. . .	111

6.8 Schematic of the rf phase shifting method used to electronically control the relative rf phase in two AOMs. Reference oscillator frequency f_{ref} is supplied by the master PLL circuit. Additional information can be found in Ref. [78].	115
6.9 Phase detection circuit used for rf phase lock feedback in the chirped BCF experiment.	117
6.10 Example of properly calibrated frequency chirps showing good overlap between the laser B ($+kv$, red) and laser A ($-kv$, blue) chirps, done for 300 MHz chirp over approximately 40 μs . Note that despite the chirp ramps having the same return back to zero, the two diode laser responses are distinctly different. There is no need to correct for this as it does not play a role in slowing the atoms.	120
6.11 Chirp pulse waveforms for 100 MHz and 300 MHz chirps showing the increasing nonlinearity in the laser A ($-kv$) voltage ramp necessary to compensate for differences in the FET current modulation and laser diode responses.	121
7.1 Experimentally observed velocity profiles for $\delta = 74\gamma$, $\Omega_r = \sqrt{3/2}\delta$, and $\phi = \pi/2$ bichromatic force chirped by 0 MHz, 100 MHz in 30 μs , 200 MHz in 40 μs , and 300 MHz in 50 μs	124

8.1 (a) Relevant energy levels in metastable helium, showing the two BCF frequency components and an off-resonant coupling to the 2^3P_1 state, discussed in the text. The distant $J' = 0$ fine-structure level plays no significant role and is not shown. (b) Zeeman sublevels, with vertical solid arrows indicating allowed transitions for π -polarized light, labeled with their relative transition strengths [60]. The vertical dashed lines indicate transitions giving rise to off-resonant excitation and ac Stark shifts, and the angled dashed line indicates the transition excited by σ^+ polarization in the conventional BCF configuration for He^*	138
8.2 Comparison of bichromatic slowing of metastable helium using σ^+ polarization (top) and π polarization at twice the laser irradiance (bottom). The atom velocity profile without the BCF present is shown in dashed black line, with the BCF in red, and the difference in blue. Effects of the BCF are observed between about 400 and $600 \gamma/k$, but are confined to about 20% of the atoms within the BCF velocity range, because of limited transverse overlap with the tightly focused lasers. The additional shifts in the velocity profile at $600 - 750 \gamma/k$ are not bichromatic in nature—they arise from the strongly saturated force from one of the four component beams acting alone, as discussed in Section 5.3.	141

8.3 Rotationally closed transition from the $N''=1$ level of the $X^2\Sigma^+$, $v''=0$ ground state of CaF to $J'=1/2$ in the $A^2\Pi_{1/2}$, $v'=0$ state. The corresponding transition in SrF was used for laser cooling in Ref. [96]. The ground-state fine structure and hyperfine structure give rise to a total of 12 m'_F and m''_F levels, not shown. In traditional notation [97] this is a combination of the near-degenerate $Q_{12}(0.5)$ and $P_{11}(1.5)$ branches. Figure is reproduced from Ref. [91].	145
8.4 Arrows show the four quasi-cycling transitions between the m''_F and m'_F sublevels of the $Q_{11}(0.5)$ branch in CaF, when illuminated with π -polarized light. All four line strengths are the same. Energies are not drawn to scale. Radiative decay to $N'' = 2$ is allowed, so a rotational repumping laser tuned 62 GHz to the red is required. Figure is reproduced from Ref. [91].	146
9.1 Proposed second generation chirped BCF slower. Major changes include increasing the bichromatic detuning to $\delta = 123\gamma$, inclusion of tapered amplifiers, and the reconfiguration of the bichromatic frequency AOM.	151
9.2 Diagram of the improved interaction tube described in Section 9.3 showing the single TA configuration with both bichromatic beams copropagating through the interaction region. The arrows indicate red or blue detuning, and the leading arrow of the pair indicates the beam detuned to interact with the atomic beam.	153

9.3 Proposed interaction tube showing basic structure and essential elements. The He* atomic beam passes through the center of the tube. Internal mirrors, mounted at fixed 45° angles to the central axis at either end, are angle ground to minimize the distance to the atomic beam. External optics steer the bichromatic beams to cross the atomic beam at $\approx 1^\circ$. Electrically adjustable quarter-wave retarders rotate the linearly polarized bichromatic beams to either σ^+ and σ^+ or σ^- and σ^- .	156
9.4 Proposed reconfiguration of the He* source and beam machine to replace the detector side of the beam machine with an interaction tube for improved optical access and reduced <i>in vacuo</i> optics. The direction of the He* source is reversed and the interaction tube is coupled to the TOF tube using an intermediate chamber acting as a coupler and attachment point for the turbomolecular pump.	159
B.1 Data acquisition and experiment control program written in National Instruments LabView®. Main program sections are outlined and described in more detail in following pages. Sections are: (A) data acquisition, (B) TOF data to velocity distribution and analysis, (C) data file formatting and saving, and (D) TOF instrument function deconvolution (not fully implemented).	170
B.2 (A) LabView code section for the data acquisition subroutine showing expanded acquisition loop.	171
B.3 (A) LabView data monitor control, in use when not actively acquiring a data run. Continuously displays the TOF data (only) with user selectable averaging.	172

B.4 (B) LabView code section to convert TOF data to a velocity distribution using the VI shown in Fig. B.7. Analysis of the change in velocity distribution due to the presence of the BCF is calculated using the VI shown in Fig. B.8.	173
B.5 (C) LabView code section to save the data to a text file. There are three primary functions—compile the header text, assemble the data into a structure that the LabView Save Datafile can use, and write the data to disk. Note some wires unrelated to the tasks described have been removed for clarity.	174
B.6 (D) Instrument function routine. Partially functioning, not implemented. For reference only.	175
B.7 LabView SubVI to calculate the velocity distribution from the raw time of flight data.	176
B.8 LabView SubVI to perform quantitative analysis on the slowed atom peak and hole to assess optimization of BCF parameters. The VI calculates the location, normalized height and area, and FWHM of the peak and “hole” in the velocity distribution, as well as an estimate of the amount of velocity slowing and the change in the total atom number.	177
B.9 User interface showing main experiment control tab.	178
B.10 User interface showing data file save options tab, including automatic and manual file header information.	179

B.11 User interface showing data acquisition parameter setup tab. The other tabs not specifically discussed are for the display of information for debugging purposes and the TOF instrument function, which is not implemented.	180
C.1 Toptica DL-MOD FET current modulation circuit. A positive voltage on the FET gate causes a portion of the laser diode current to be shorted to ground around the laser diode. Two unidentifiable components were the Zener diodes and the small inductor. Note that there appear to be additional changes to the main current and temperature interface PCB in the laser head with the DL-MOD.	182
F.1 3D BCF surface calculated for $-100\gamma/k < v < +100\gamma/k$ and $\Omega_r \leq \sqrt{3/2}\delta$, for $\delta/2\pi = 100$ MHz.	190

LIST OF TABLES

2.1	Fundamental properties of the bichromatic force for detuning δ , where $\omega_r = \hbar k^2 / 2m$ is the recoil frequency.	34
3.1	Calculated phase shifts during BCF slowing at high detunings. Slowing has been observed at $\delta = 185\gamma$, BCF slowing was attempted and failed at $\delta = 370\gamma$, and $\delta = 570\gamma$ is necessary if a single stage slower is to achieve velocities in the MOT loading range. Note that the BCF magnitude is reduced by 50% for a phase change of $\pm 5^\circ$ from optimum.	57
4.1	Values for various properties of the $2^3S_1 \rightarrow 2^3P_2$ transition in helium used in these experiments, taken from [9].	63
4.2	Calculated optimal irradiances and optical powers for bichromatic detunings used in these experiments. The frequencies missing from this sequence (350 MHz and 400 MHz) could not be investigated due to the unexpected failure of the laser amplifier.	89
5.1	Summary of BCF slowing results on metastable helium. Slowing measurements are made from the maximum of the peak to the minimum of the corresponding hole in the velocity distribution. The velocity range is measured using the Metcalf group convention of the FWHM of the combined peak and corresponding hole in the velocity distribution.	95

7.1	Summary of experimental BCF Chirp results for $\delta = 74\gamma$. All experiments used the optimal BCF parameters $\Omega_r = \sqrt{3/2}\delta$ and $\phi = \pi/2$	127
8.1	Calculated BCF magnitude and measured BCF depletion percentages, as a function of the frequency shift of ω_0 from exact atomic resonance. Shifts are measured as a fraction of the bichromatic detuning δ . Because the interaction length for this measurement was 3 – 4 times the BCF slowing distance, little effect is expected until the force is reduced by a corresponding factor. The calculated BCF magnitude for a shift of 0.4δ could not be quantified due to the presence of resonance peaks and noise.	142
8.2	Representative BCF parameters for CaF, assuming no vibrational repumping, $P_e = 2/19$, $\eta = 0.78$, and a degeneracy factor of 6/19 in Eq. (8.2.5). With vibrational repumping, T_{loss} would increase to $\approx 350 \mu\text{s}$ and Δv_{loss} would exceed Δv_b , although the forces F_b and F_{rad} would be reduced by nearly a factor of two due to the additional degeneracy of 17 dark states with $v''=1$.	148

Chapter 1

Introduction

The field of laser slowing and cooling goes back nearly thirty years to the ground breaking work done by Wineland and Hänsch [1–3] in the 1970s. Their proposals to use the photon scattering force to slow and cool atoms paved the way for what is now a major subfield in AMO physics. The growth has been rapid—both in the fundamental research of photon-atom interactions as well as their practical applications. By the mid-1980s several labs were pursuing applications of these ideas [4–7] leading ultimately to the first realization of a magneto-optical trap [8]. In fact, laser slowing and cooling of atoms is a critical tool in much of contemporary AMO research, from Bose-Einstein condensates (BECs) to atom lithography [9–11].

As is common in physics research, the evolution of laser slowing and cooling has been one punctuated by developing a technique, realizing its limitations, and developing a new technique attempting to overcome those limitations. Attempts to impart forces on atoms larger than the radiative force lead to the development of the dipole force, rectified dipole force, and bichromatic force (BCF).

Despite these later developments, most laser slowing methods still use the radiative force in a monochromatic field. The momentum transfer arising from photon absorption allows atoms to be accelerated or decelerated, and their velocity

distribution to be narrowed (cooled). Slowing of atomic beams is typically accomplished by directing a laser against the atomic beam to radiatively decelerate the atoms. However, the radiative force is limited in its magnitude by the spontaneous emission rate and often requires long distances to slow atoms, especially lighter species such as helium. With long slowing times, the small transverse velocities in the atomic beam significantly reduces the source brightness, negatively impacting MOT loading times.

Unlike the radiative force, the dipole force arises from intensity gradients in a monochromatic standing wave and is not limited in magnitude. However, it alternates sign on the scale of an optical standing wave. The average force is zero, limiting its usefulness in a slower. One way around this, demonstrated by Kazantsev and Krasnov [12], is to rectify the dipole force. Adding a second frequency to the standing wave results in a modulated light shift, which can be adjusted to keep the sign of the dipole force positive. This technique eventually resulted in the deflection of sodium atoms by a few m/s by Grimm and coworkers [13].

Continued refinement of slowing techniques in bichromatic fields by Grimm and coworkers over several years lead to the observation of a large rectified dipole force with a velocity range of 225 m/s in cesium by Söding [14]. This was the birth of the optical bichromatic force (BCF), which relies on a pair of bichromatic beams that, when the intensity and standing wavelength are carefully selected, will coherently drive the atom through a cycle of photon absorption and stimulated emission much more rapidly than the radiative decay rate.

These developments led to more extensive research into the nature and origins of the bichromatic force, which to date has been demonstrated in Cs [14], Na [15], Na₂ [16], Rb [17, 18], and He [19, 20]. Despite this progress and the ad-

vantages of such a strong optical force, a useful atomic slower based on the BCF has never been realized.

It is the goal of this research to further the application of the BCF as a fully functional atomic slower. This work comprises two distinct projects. The first is an attempt at designing a slower using the BCF with large detunings, including theoretical and experimental exploration of the BCF at very large bichromatic detunings, where there is some evidence of an upper limit. The second project is the partial development of a novel chirped BCF slower which uses the bichromatic force with a relatively narrow velocity range, but dynamically adjusts the Doppler shifts to track the atoms as they are slowed, significantly increasing the amount of slowing. This technique appears to be the most probable route to a fully realized BCF slower for metastable helium.

1.1 Radiative Force

The simplest model of an optical force is that of a two-level atom in a resonant monochromatic light field, interacting through the absorption and spontaneous emission of single photons, as shown in Fig 1.1. The two-level atom is idealized in that it has only two internal energy levels: ground $|g\rangle$ and excited $|e\rangle$. No atoms actually have this configuration, but it is a good approximation for many cases in which two internal electronic states are strongly coupled to a monochromatic light field. The energy separation of the two levels in the atom is $\hbar\omega_a$ where ω_a is the atomic transition frequency, and the upper state lifetime is τ . The light field has the single frequency ω_ℓ and wavelength $\lambda = 2\pi/|\vec{k}|$, where $\vec{k} = \omega_\ell/c \hat{z}$ and \hat{z} is the direction of propagation.

When the atom absorbs a photon from the laser field it receives a momentum

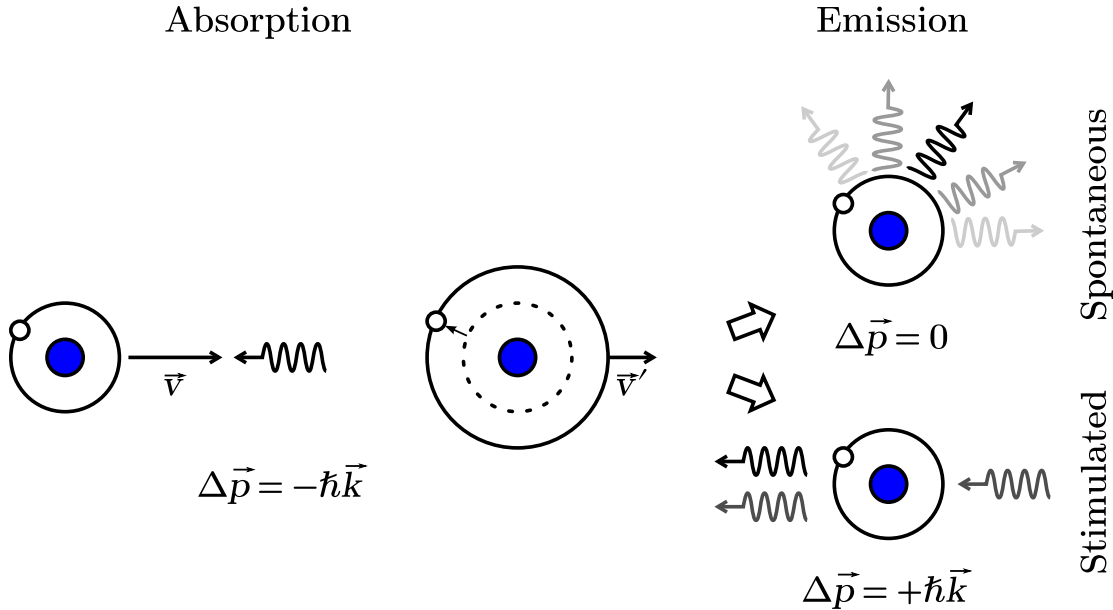


Fig. 1.1: Illustration of photon absorption and emission processes in a two-level atom. At left, the atom is internally excited by absorption of a photon and receives a momentum kick of $\Delta \vec{p} = -\hbar \vec{k}$. De-excitation can occur via one of two photon emission processes: spontaneous decay through a randomly directed photon (top), or stimulated emission resulting in $\Delta \vec{p} = +\hbar \vec{k}$ that negates the momentum kick from the photon absorption. Averaging over several cycles, the average momentum change for a cycle ending with spontaneous emission is $\Delta \vec{p} = -\hbar \vec{k}$ whereas for a cycle ending with stimulated emission it is $\Delta \vec{p} = 0$.

kick of $\hbar \vec{k}$ in the direction of the photon. If the laser intensity is sufficiently low that stimulated emission can be ignored, the atom will emit a photon via spontaneous decay and receive a second momentum kick of $\hbar \vec{k}'$. The direction of the photon emitted during a spontaneous decay, however, is random so the average contribution from this process over several cycles is zero. The time-averaged radiative force depends only on the momentum kicks from the photon absorption. The absorption / spontaneous decay cycle shown in Fig. 1.1 repeats at a rate somewhat less than the spontaneous decay rate $\gamma = 1/\tau$. This scattering

rate γ_{sc} is given for an atom moving with velocity \vec{v} by

$$\gamma_{\text{sc}} = \frac{s\gamma/2}{1 + s + (2(\delta - \vec{k} \cdot \vec{v}))/\gamma^2}. \quad (1.1.1)$$

Here, $\delta = \omega_\ell - \omega_a$ is the detuning of the laser from resonance and $-\vec{k} \cdot \vec{v}$ is the Doppler shift. The quantity s is known as the on-resonance saturation parameter:

$$s = \frac{I}{I_{\text{sat}}}, \text{ where } I_{\text{sat}} \equiv \frac{\pi hc}{3\lambda^3\tau}. \quad (1.1.2)$$

Over many such cycles at the rate γ_{sc} , the net force acting on the atom in the direction of the laser beam is

$$F_{\text{rad}} = \hbar k \gamma_{\text{sc}}. \quad (1.1.3)$$

For the transition of interest in metastable helium, the saturation intensity is relatively small at 0.17 mW/cm², with $\lambda = 1083$ nm and $\tau = 98$ ns ($\gamma = 1/\tau = 2\pi \times 1.6$ MHz).

Increasing the laser intensity only increases the scattering rate to a certain point, known as saturation. For $s \gg (\delta/\gamma)^2$ the scattering rate levels off at $\gamma/2$. Consequently the radiative force saturates to a maximum of

$$F_{\text{rad}}^{\text{max}} = \frac{\hbar k \gamma}{2} \quad (1.1.4)$$

as shown in Fig. 1.2. This expression remains valid for high intensity ($s \gg 1$), even though the dominant decay mechanism is then stimulated emission rather than spontaneous decay. When an atom undergoes stimulated emission, the momentum kick is in the same direction as the stimulating photon (opposite the momentum kick received with absorption), so there is no net force as shown in Fig. 1.1. The

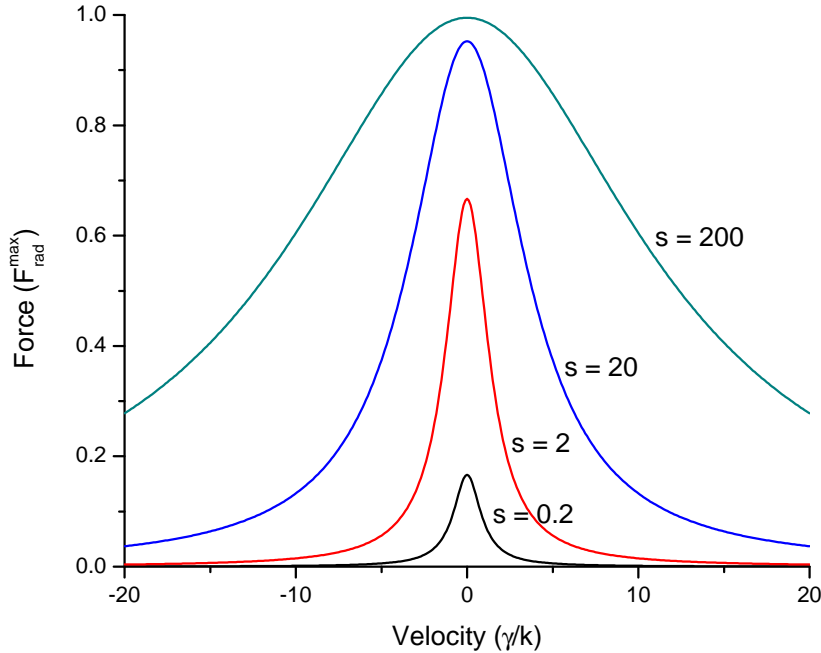


Fig. 1.2: Plot of the radiative force for $\delta = 0$ as a function of velocity v , showing effects of saturation as s increases from 0.2 to 2000. The plot is scaled in units of the maximum radiative force, $F_{\text{rad}}^{\text{max}} = \hbar k \gamma / 2$

velocity range of the radiative force is approximately $\pm\gamma/k$, becoming somewhat broader at very high irradiances, as can be seen in Fig. 1.2. Typically γ/k is on the order of several m/s.

1.1.1 Zeeman Slowers

To create a useful atomic slower using the radiative force, the central velocity of the force profile must be shifted away from zero to compensate for the Doppler shift of the moving atoms. However, because of the narrow velocity range of the radiative force, for large changes in velocity the Doppler shift must change as the atoms are slowed. This is typically accomplished one of three ways:

1. Add a frequency detuning $\delta = -\vec{k} \cdot \vec{v}$ to the laser [21, 22].

2. Apply a magnetic field to the atoms to manipulate the atomic transition frequency ω_a via the Zeeman shift [6].
3. Apply an electric field to the moving atoms to manipulate the atomic transition frequency ω_a through a Stark shift [23].

The most widely employed scheme for helium slowers is the Zeeman shift. A Zeeman slower uses a tapered solenoid magnet to apply a decreasing magnetic field to the atoms. The magnetic field is configured such that the Zeeman shift experienced by the moving (and continually slowing) atoms compensates for the Doppler shift. The Zeeman slower is very successful in slowing atoms from thermal velocities down to a few m/s, but in the case of light atoms the slowers must be 2 – 3 m long [24–27]. For metastable helium, the atom of interest for these experiments, the most common Zeeman scheme cycles the $2^3S \rightarrow 2^3P$ transition at $\lambda = 1083$ nm, with an upper-state lifetime of $\tau = 100$ ns. The maximum radiative force provides a deceleration of 5×10^7 m/s, resulting in a minimum distance of 2.25 m to slow He* atoms from 1500 m/s to rest. Further, a peak magnetic field of several hundred gauss is required. This requires many turns of wire and high currents with water cooled coils, making for a very complicated and cumbersome system. Compounding the problems, due to the length of the slower, source brightness becomes a significant factor.

1.1.2 Optical Molasses

A critical development in atom cooling and trapping came from utilizing a counterpropagating pair of red-detuned lasers. If a laser is red-detuned from resonance (i.e., $\omega_\ell - \omega_a = \delta < 0$) an atom moving in the field, due to the Doppler shift, will experience a larger force when its motion is opposite the direction of

\vec{k} than when it is collinear with \vec{k} . If a second red-detuned laser is introduced counterpropagating to the first, it produces a larger force on atoms moving in the opposite direction. The total force of the two fields can be added together in the low intensity limit [9] to yield

$$\vec{F}_{\text{OM}} = \hbar \vec{k} \frac{\gamma s/2}{1 + s + (2(\delta - \vec{k} \cdot \vec{v})/\gamma)^2} - \hbar \vec{k} \frac{\gamma s/2}{1 + s + (2(\delta + \vec{k} \cdot \vec{v})/\gamma)^2}. \quad (1.1.5)$$

Note the change of sign of \vec{k} between the two terms. The net force \vec{F}_{OM} is proportional to, and always opposed to, the velocity of the atom. For slow-moving atoms this is an analog of viscous damping, and is commonly referred to as “optical molasses”. When the optical molasses is combined with a magnetic field gradient, it forms a Magneto-Optical Trap [9].

1.2 Sub-Doppler Cooling of Multi-Level Atoms

In 1988 the groups of Phillips and Metcalf observed temperatures of sodium atoms released from an optical molasses to be much lower than the expected Doppler temperature limit $T_D = \hbar\gamma/2k_B$ [9]. Several theories were soon developed [28, 29] to explain this surprising result. These new theories included atomic sublevels, such as Zeeman sublevels or hyperfine levels, extending the original two-level treatment. The sub-Doppler cooling was produced by a spatially dependent optical pumping process, variations of which are now widely used, achieved through polarization gradients or a dc magnetic field. In either case atoms must climb a potential “hill” until, somewhere near the peak, conditions are met for the atom to be optically pumped to a different magnetic sublevel of lower energy. The difference in energy is dissipated to the radiation field. The cycle repeats, and each

time the atoms loses a small amount of energy equal to the difference between the sublevels, until it can no longer climb the potential hill. This is generally known as the “Sisyphus effect” and is described in great detail in Refs. [9, 30].

While this discovery has been a crucial development in ultra-cold AMO physics, the forces in the sub-Doppler regime have at most the same magnitude and velocity range as optical molasses. Therefore, they are of limited use in atomic slowing applications where larger forces over larger velocity ranges are required.

1.3 Dipole Force

The dipole force for an atom in a standing wave arises from intensity gradients that create energy shifts ΔE_g in the atomic levels,

$$F_g = -\frac{\partial}{\partial z} \Delta E_g. \quad (1.3.1)$$

When the laser is detuned far from resonance, light shift of the ground state can be written as [9]

$$\Delta E_g = \frac{\hbar \Omega_r^2}{4\delta}, \quad (1.3.2)$$

where δ is the laser detuning and Ω_r is the Rabi frequency given by

$$\Omega_r = -\vec{d} \cdot \vec{E}/\hbar. \quad (1.3.3)$$

Now we reintroduce the saturation parameter s (Eq. (1.1.2) expressed in an alternate form [9]),

$$s \equiv 2|\Omega_r|^2/\gamma^2 = I/I_{\text{sat}}. \quad (1.3.4)$$

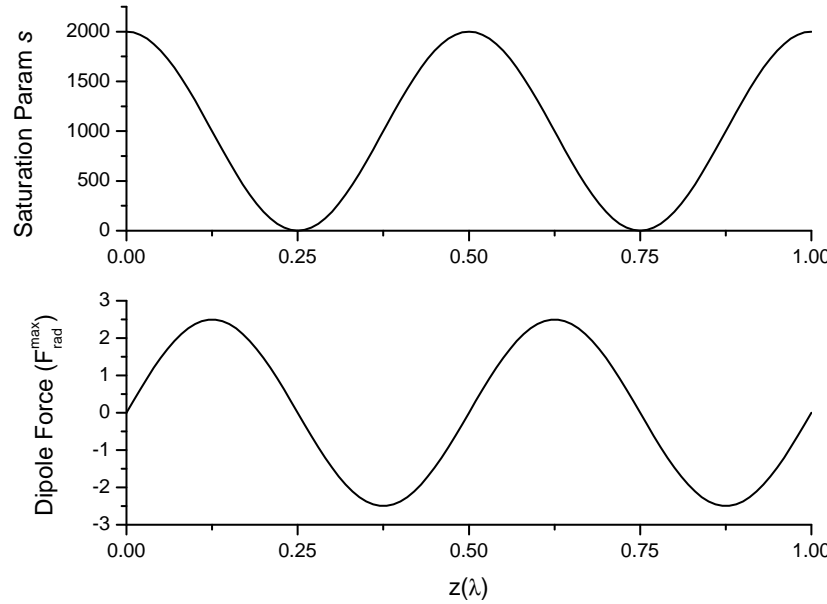


Fig. 1.3: Standing wave saturation parameter (top) and calculated dipole force (bottom) on an atom in the ground state for $\delta = 200\gamma$ and $s = 2000$, showing the oscillating sign of the force. The peak magnitude $|\vec{F}_{\text{dip}}^{\max}| = 2.5|\vec{F}_{\text{rad}}^{\max}|$.

Here, the laser field intensity I is periodic, $I(z) = I_0 \cos^2(kz)$. Combining Eqs. (1.3.1), (1.3.2), and (1.3.4) yields an expression for the dipole force:

$$F_{\text{dip}}(z) = -\frac{\partial}{\partial z} \left(\frac{\hbar\gamma^2}{8\delta} \frac{I(z)}{I_{\text{sat}}} \right) = \frac{\hbar k \gamma^2 I_0}{8\delta I_{\text{sat}}} \sin(2kz). \quad (1.3.5)$$

There are two key elements to this expression for F_{dip} , as shown in Fig. 1.3:

1. The dipole force has no saturation or upper limit like the radiative force—the magnitude of the force increases linearly with laser intensity as long as the large detuning condition $|\delta| \gg |\Omega_r|$ remains valid [9].
2. The force is proportional to a sine function, and therefore changes sign (direction) over the period of the standing wave. The spatial average of the force over one standing wave period is zero.

Although the non-saturating magnitude is a step in the right direction, the spatial average of zero prevents the dipole force from being directly useful to slow atoms.

1.4 Rectified Optical Dipole Forces

The dipole force could be useful as a slower if it were possible to eliminate the sign change by “rectifying” the force on the wavelength scale. Several of the methods that have been developed, such as the Sisyphus effect [31] and multi-photon “Doppleron” resonances [32], suffer both from limited magnitude ($\approx 3F_{\text{rad}}^{\text{max}}$) and velocity range ($\approx \gamma/k$), rendering them unsuitable as general-purpose atom slowing forces.

However, another method to rectify the dipole force on the wavelength scale, demonstrated by Kazantsev and Krasnov [12] and described by Javanainen [33], comes closer. They devised a way to rectify the dipole force using a bichromatic standing light wave (BSLW) by overlapping two standing waves of different detunings and intensities, as shown in Fig. 1.4. The first standing wave $s_1(z)$ with detuning δ_1 exerts a strong dipole force on the atom as described in Section 1.3. The second standing wave $s_2(z)$, with intensity $|s_2|^2 > |s_1|^2$ and detuning δ_2 , provides a light shift to spatially modulate the sign of the detuning of the first wave. The result is a rectified dipole force with the same sign over an optical wavelength, as shown in Fig. 1.4(d).

The standing waves $s_1(z)$ and $s_2(z)$ can be defined as $s_1(z) = \bar{s}_1(1 - \cos(2k_1 z))$ and $s_2(z) = \bar{s}_2(1 - \cos(2k_2 z))$ where $\bar{s}_{1,2}$ denotes half of the saturation parameter at peak intensity. Rewriting the wave vectors in terms of the detuning Δk ($\Delta k \ll k_1, k_2$), with $k_1 = k$ and $k_2 = k + \Delta k$, the standing waves

can be written as

$$\begin{aligned}s_1(z) &= \bar{s}_1(1 - \cos(2kz)) \\ s_2(z) &= \bar{s}_2(1 - \cos(2kz + \phi))\end{aligned}\tag{1.4.1}$$

with a periodic phase shift $\phi = 2z\Delta k = 2z|\delta_1 - \delta_2|/c$. The phase shift is periodic on a scale of $\pi c/|\delta_1 - \delta_2| \gg \lambda$, and can be considered constant over many optical wavelengths.

To calculate the dipole force, Eq. (1.3.5) can be rewritten for detuning δ_1 and Rabi frequency Ω_1 as [34]:

$$F_{\text{dip}}(z) = -\frac{1}{2} \hbar \gamma \frac{\delta_1/\gamma}{(\delta_1/\gamma)^2 + 1 + s_1(z)} \nabla s_1(z).\tag{1.4.2}$$

The detuning of the atom due to the light shift induced by the second standing wave is

$$\Delta_{\text{eff}} = \delta_1 + \frac{\gamma^2 s_2(z)}{4\delta_2},\tag{1.4.3}$$

and alternates sign with the same period as the dipole force. For the correct choice of detunings, the second wave reverses the sign of the dipole force profile from the first wave whenever the force is negative, resulting in the rectified dipole force profile shown in Fig. 1.4.

The rectified dipole force has been experimentally verified by the authors of Ref. [13] by deflecting a thermal sodium beam. Estimates of the magnitude of the force based on a measured transverse velocity change of 1.8 m/s = 0.3 γ/k and a transit time of the atoms through the standing waves of 500 ns give a force of $4F_{\text{rad}}^{\max}$. Other experiments [37, 38] have made similar measurements of the rectified dipole force magnitude of several times the radiative force. While enough to be somewhat useful, the improvement is not particularly impressive.

A second limitation is that, due to the sensitivity of the rectified dipole force on the detunings of the two lasers from resonance, the mechanism can only tolerate small Doppler shifts. While they may be useful for such tasks as increasing the brightness of an atomic source, they are not well suited for atomic beam slowing.

Fortunately, other choices for the intensities and detunings of the bichromatic beams lead to very different forces with significantly larger magnitudes and velocity ranges, as will be discussed in Chapter 2.

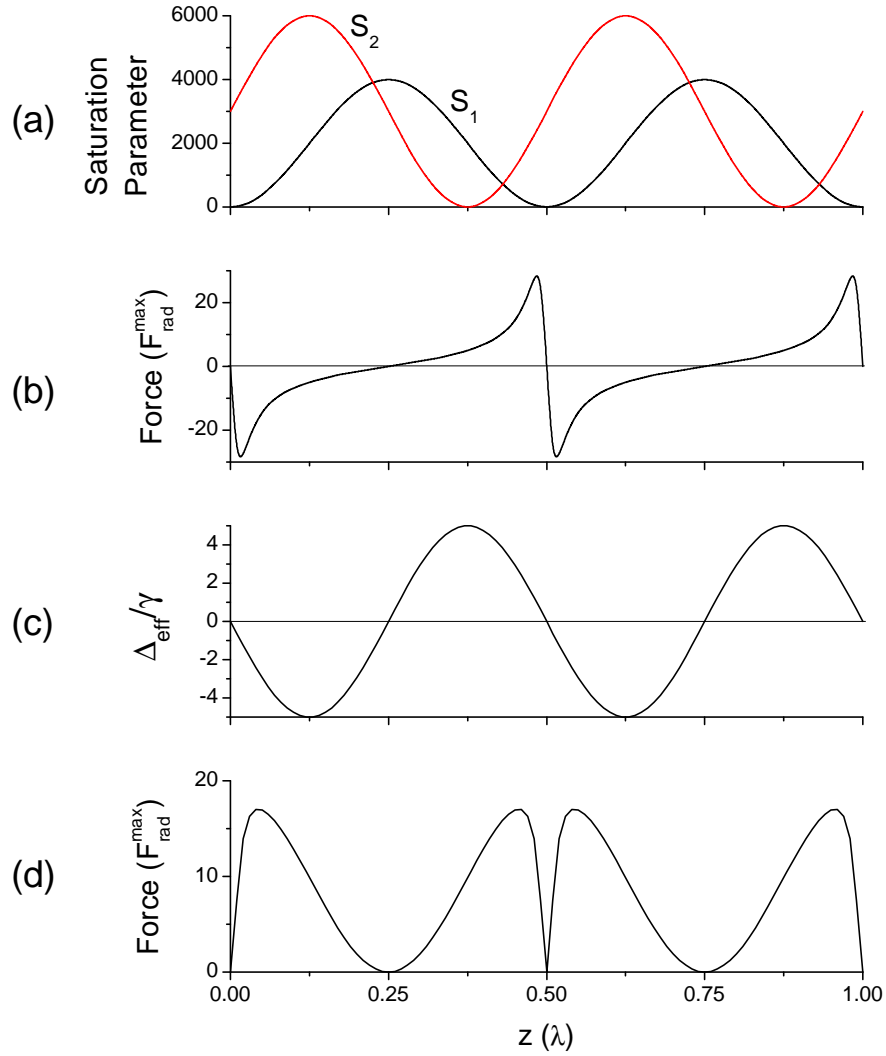


Fig. 1.4: Rectified dipole force components for laser parameters: $\delta_1 = 3\gamma$, $\bar{s}_1 = 2000$, $\delta_2 = -150\gamma$, $\bar{s}_2 = 3000$, $\phi = \pi/2$, replicating results from Refs. [35, 36]. (a) Intensity profiles of the two standing waves $s_1(z)$ and $s_2(z)$ are shown at top. (b) Dipole force on the atom from $s_1(z)$. (c) Effective detuning Δ_{eff} caused by the presence of $s_2(z)$. (d) The resulting rectified dipole force.

Chapter 2

The Bichromatic Force

Although the counterpropagating beam optical bichromatic force (BCF) was originally developed as a special case of the rectified dipole force (see Section 1.4), there are some distinct characteristics that need to be addressed in providing a more thorough description. In particular, specific choices for the detunings and intensities are essential for achieving the hallmark the optical bichromatic force, a very large deceleration accompanied by a very large velocity range.

The BCF fundamentally involves the coherent control of momentum between the atom and the laser field. The overlapping laser fields can be modeled as a series of beat notes or a periodic standing wave. The net effect of either is that the atom is coherently driven through cycles of momentum exchange with the laser field at a rate much greater than the radiative decay rate, giving rise to a much larger force.

There are three mostly independent treatments that have evolved to model and describe the optical bichromatic force. I will discuss each in turn in the following sections, working from the most intuitive but limited, the π -pulse model, to the most accurate, numerical solutions of the optical Bloch equations.

In the following discussions, there are two phases related to bichromatic fields. I will define them now for the sake of clarity: χ is the phase related to the

electric field E , and ϕ is the phase of E^2 .

2.1 π -Pulse Model

The most intuitive description of the bichromatic force is the π -pulse model, developed by Voitsekhovich *et al.* [15, 16]. The name “ π -pulse” originates from a description of a pure two-level system as a radial vector on a sphere, originally devised by Felix Bloch for problems in nuclear magnetic resonance [39]. On the Bloch sphere shown in Fig. 2.1, the ground state is located at the “South Pole” (B), and the excited state is at the “North Pole” (A). If the system, a metastable helium atom, is initially its ground state, a rotation of the Bloch vector polar angle θ by π puts the atom in its excited state.

The π -pulse originates mathematically from solving the Bloch vector equations of motion for a two-level system in the rotating frame [40]. For a resonant electric field in the rotating frame with amplitude $E(t)$ we can define the polar angle as [41]

$$\theta(t) = \int_{-\infty}^t \frac{d}{\hbar} E(t) dt, \quad (2.1.1)$$

where d is the magnitude of the dipole matrix element, $d \equiv |\langle b | \vec{r} | a \rangle|$.

In the case of the optical bichromatic force, a pair of monochromatic beams are symmetrically detuned by δ above and below the atomic resonance ω_a , $\omega = \omega_a \pm \delta$. Assuming that the two frequency components are of equal amplitude, the electric field amplitude can be expressed as

$$E(z, t) = E_0 \cos[(k + \Delta k)z - (\omega_a + \delta)t] + \cos[(k - \Delta k)z - (\omega_a - \delta)t], \quad (2.1.2)$$

where $k = 2\pi/\lambda = \omega_a/c$ and $\Delta k = \delta/c$. Grouping terms, we can rewrite Eq. (2.1.2)

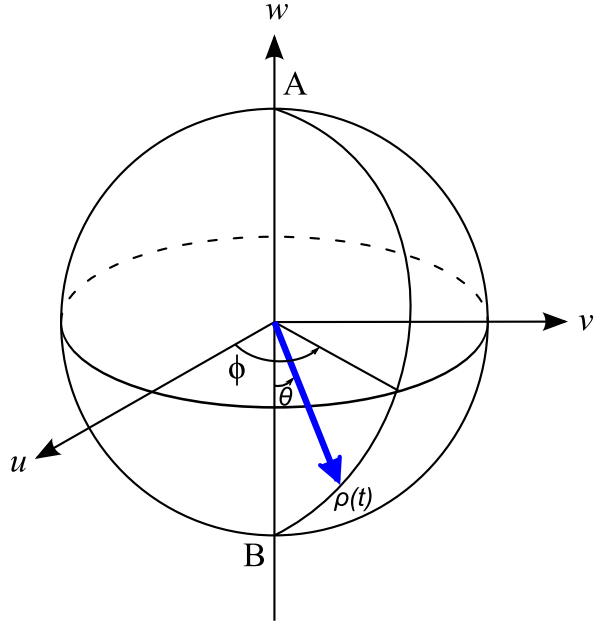


Fig. 2.1: A Bloch vector $\rho(t) = (u(t), v(t), w(t))$ elevated by the polar angle $\theta(t)$ as defined in Eq. (2.1.1). Its projection onto the w -axis gives the population difference between levels $|a\rangle$ and $|b\rangle$. The points A and B correspond to the stationary states $|a\rangle$ and $|b\rangle$.

as

$$E(z, t) = 2E_0 \cos(kz - \omega_a t) \cos(\delta t - \Delta kz), \quad (2.1.3)$$

which has the form of a traveling amplitude-modulated wave of amplitude $2E_0$, with a modulation (beat) frequency δ , and a carrier frequency ω_a . When examining the irradiance, which is proportional to E^2 , each beat (or pulse) has a period π/δ as shown in Fig. 2.2.

For a bichromatic beat note that satisfies the π -pulse condition, Eq. (2.1.1) can be rewritten in terms of the Rabi frequency as

$$\theta(t) = \int_{-\pi/2\delta}^{+\pi/2\delta} 2\Omega_r \cos(\delta t) dt = \pi. \quad (2.1.4)$$

The Rabi frequency for each component field $\vec{E}(z, t)$, Ω_r , defined in Eq (1.3.3),

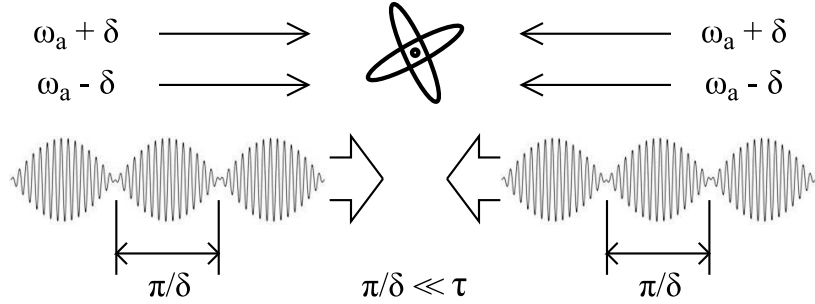


Fig. 2.2: A pair of bichromatic beams, showing beat notes in the irradiance as seen by an atom at rest. Choosing the detuning δ such that the π -pulse repetition rate is large compared to the decay rate $\gamma \equiv 1/\tau$, several bichromatic cycles will occur for each spontaneous emission.

can be rewritten as

$$\Omega_r(z, t) = -\vec{d} \cdot \vec{E}(z, t)/\hbar, \quad (2.1.5)$$

The Rabi frequency describes the frequency of Bloch vector oscillation for a given atomic transition in the light field $E(z, t)$. The coupling between the atomic transition and the light field is described by the electric dipole moment \vec{d} .

Integrating Eq. (2.1.4) and solving for the Rabi frequency in terms of δ gives the BCF π -pulse condition

$$\Omega_r = \frac{\pi}{4}\delta. \quad (2.1.6)$$

When this condition is met, each bichromatic beam acts like a train of π -pulses as shown in Fig. 2.2.

If one train of π -pulses were used, the atom would simply be cycled between the ground and excited state with no net momentum transfer from the laser field. However, if a second counterpropagating train of π -pulses is added, it is possible by carefully arranging the phase (relative arrival time) of the incoming trains of π -pulses to create a large net momentum transfer. The π -pulses are phased in such a way that the pulse from the right arrives first, exciting the atom and providing

a momentum kick of $\hbar k$ in the same direction. Then, a pulse from the left causes stimulated emission, returning the atom to the ground state with a momentum kick of $\hbar k$ opposite the pulse direction (i.e., in the same direction as the first kick). The atom receives a total transfer of $2\hbar k$ from the light fields in this cycle. The process is repeated as the next π -pulse arrives from the right, with a repetition rate of δ/π . In the following discussion, it is assumed that the preferred sequence is one in which pulses from the right excite the atom, and pulses from the left de-excite it. The total bichromatic force F_{BCF} on the atom would then be

$$F_{\text{BCF}} = \frac{\Delta p}{\Delta t} = \frac{2\hbar k}{\pi/\delta} = \frac{2\hbar k\delta}{\pi} \gg F_{\text{rad}}^{\max} = \frac{\hbar k\gamma}{2}. \quad (2.1.7)$$

An important feature of the BCF is that the force is independent of the decay rate of the atom, depending only on the rate of momentum exchange set by δ .

The effect of spontaneous emission cannot be ignored, as it will reset the atom to the ground state with a random phase relative to the π -pulses. The atom may then experience the next excitation by a π -pulse from the left, starting it in the opposite sequence, experiencing a force in the opposite direction (i.e., an acceleration instead of a deceleration). If the arrival of the counterpropagating beats is evenly spaced in time (phase of $E^2 \phi = \pi$) they are spatially symmetric and lack a preferred direction. After several spontaneous emission cycles the average force will be zero.

However, by adjusting the relative phase of the beats a preferred direction can be established using the asymmetry of the pulse timing. Decreasing ϕ so that the counterpropagating pulse arrives shortly after the pulse from the right has two effects:

1. It reduces the probability of an unwanted spontaneous emission by reducing

the time between the pulses (the time the atom spends in its excited state).

2. In the case where the atom finds itself in the “wrong” sequence, the chance that another spontaneous emission returns the atom to the preferred sequence is improved by increasing the time between the end of one sequence and the start of the next.

This simplified reasoning and detailed numerical calculations both show (see Section 2.3) that the optimum phase difference is $\phi = \pi/2$. If $\phi < \pi/2$, the beat overlap is too large and the π -pulse picture breaks down. In the extreme case where $\phi = 0$ the atom no longer sees distinct π -pulses at all, but a standing wave, and the force vanishes. On the other hand, if $\phi > \pi/2$ we approach the limit $\phi = \pi$ where again there is no preferred direction and the force vanishes. With the phase set to $\pi/2$ the atom is in the “wrong” sequence 1/4 of the time, and in the “right” sequence the other 3/4. This results in an average force half that of Eq. (2.1.7),

$$F_{\text{BCF}} = \frac{\hbar k \delta}{\pi}. \quad (2.1.8)$$

This is still much greater than the radiative force for $\delta \gg \gamma$, and can be made arbitrarily large by increasing δ . Note also that the direction of the force reverses if the phase is changed to $\phi = 3\pi/2$.

This intuitive description of the bichromatic force is considerably oversimplified and as such has several shortcomings. The first, as we will see in Sections 2.2 and 2.3, is that the predicted optimum Rabi frequency (Eq. (2.1.6)) is underestimated and differs from that predicted by the more accurate treatments. This prediction has been experimentally verified [14, 35, 36, 42, and this work]. Second, the model assumes that the beats are perfect π -pulses exactly on resonance. In

real systems where δ can be 150γ or more and the interaction length is on the order of $3 - 4$ cm, deviations caused by Gaussian beam profiles, differences in phase between the start and end of the interaction region, the actual shape of the beat pulse envelope, and the continuum of Doppler shifts, insure that an atom rarely, if ever, sees a true π -pulse.

2.2 Doubly-Dressed Atom Model

The second, and more accurate description of the BCF is the doubly-dressed atom (DDA) picture [34, 43, 44]. In the DDA, the atom, laser field, and atom-laser interaction are treated as one system with coupled energy levels called “dressed states”. The dressed atom theory is well developed for an atom in a monochromatic laser field [45], providing useful insights into such atom-light interactions as Sisyphus cooling [31]. In Section 2.1, I showed that in the π -pulse model the momentum transfer originates from sequenced counterpropagating beat notes. The origin of the force in the DDA picture, however, is the spatial gradient of the field-dressed energy levels. Instead of pairing the bichromatic frequencies in each laser beam to create beats as in the π -pulse model, the counterpropagating beams of each frequency are grouped to form standing waves:

$$E = 2E_0[\cos(kz + \chi/2) \cos[(\omega_a + \delta)t] + \cos(kz - \chi/2) \cos[(\omega_a - \delta)t]]. \quad (2.2.1)$$

The spatial phase of the standing waves is given by $\chi = 2\Delta kz = 2\delta z/c$. Note that χ is the phase of E , and is equal to $\phi/2$, the phase of the intensity (E^2).

The dressed state construction begins with ground and excited bare atom states $|g\rangle$ and $|e\rangle$, with energies $\epsilon_g = 0$ and $\epsilon_e = \hbar\omega_a$ respectively. The laser

field has two modes: one blue detuned ($\hbar\omega_a + \delta$) with m photons, and one red detuned ($\hbar\omega_a - \delta$) with n photons. Combining the laser field number states $|m\rangle$ and $|n\rangle$ with the bare atom states allows us to construct a basis of uncoupled states, $|g, m, n\rangle$ and $|e, m, n\rangle$, with energies [34]

$$\begin{aligned} E_{g,m,n} &= (m+n)\hbar\omega_a + (m-n)\hbar\delta, \\ E_{e,m,n} &= (m+n+1)\hbar\omega_a + (m-n)\hbar\delta. \end{aligned} \quad (2.2.2)$$

The uncoupled states form a series of infinite manifolds as shown in Fig. 2.3. The manifold separation of $\hbar\omega_a$ corresponds to the loss of a photon from the combined atom-field states (e.g. spontaneous emission). Movement between adjacent states represents absorption of a photon from one field (either blue or red detuned) and stimulated emission of a photon back into either field.

To “dress” the states, the atom-field coupling potential term $V_{\pm} = \Omega_r \cos(kz \mp \phi/2)$ is added to the Hamiltonian \mathcal{H} . Relative to an arbitrary initial photon index (m_0, n_0) , the infinite Hamiltonian matrix can be written in tridiagonal form (truncated here to 7×7) as

$$\mathcal{H}/\hbar - (m+n)\omega_a = \begin{bmatrix} 3\delta & V_- & 0 & 0 & 0 & 0 & 0 \\ V_- & 2\delta & V_+ & 0 & 0 & 0 & 0 \\ 0 & V_+ & \delta & V_- & 0 & 0 & 0 \\ 0 & 0 & V_- & 0 & V_+ & 0 & 0 \\ 0 & 0 & 0 & V_+ & -\delta & V_- & 0 \\ 0 & 0 & 0 & 0 & V_- & -2\delta & V_+ \\ 0 & 0 & 0 & 0 & 0 & V_+ & -3\delta \end{bmatrix}. \quad (2.2.3)$$

In the following calculations, the approximate eigenvalues, shown in Fig. 2.4,

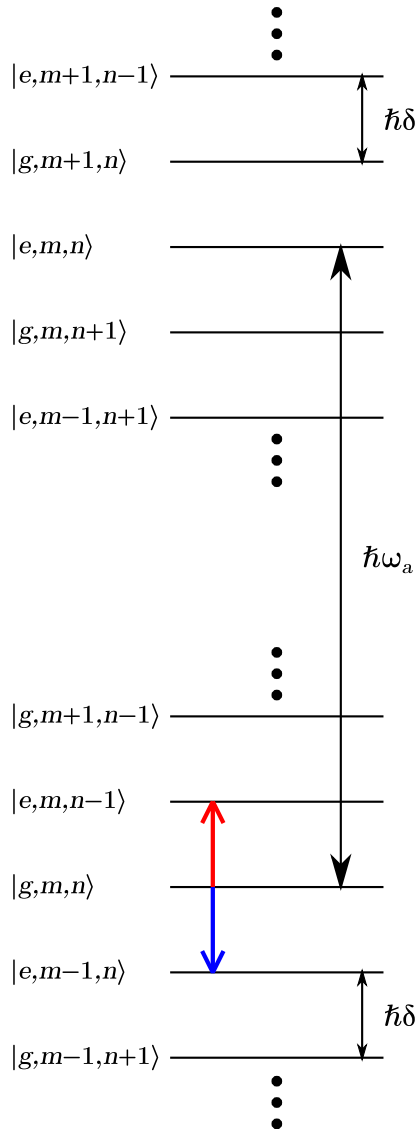


Fig. 2.3: Two manifolds of uncoupled energy levels of the combined atom-field states (indicated at left). The short red upwards arrow represents excitation via absorption of a photon from the red-detuned field $|n\rangle$, and the short blue downwards arrow excitation via absorption from the blue-detuned field $|m\rangle$. The equal spacing of levels $\hbar\delta$ is due to the symmetric detuning of the bichromatic fields.

are found by truncating the infinite Hamiltonian matrix to a manageable size (15×15) and numerically computing the eigenvalues using Mathematica. The spatial variation of the standing wave Rabi frequency causes a spatially dependent variation in the energy levels, with avoided crossings appearing at the nodes of each of the standing waves shown in Fig. 2.4 (C).

Fig. 2.4 (A) shows the energy levels when $\Omega_r = (\pi/4)\delta$, which exhibit avoided crossings with considerable energy gaps. However, if the Rabi frequency is increased to $\Omega_r = \sqrt{3/2}\delta$ the avoided crossings touch as shown in Fig. 2.4 (B). An atom has a finite probability of moving diabatically through an avoided crossing, given for an isolated crossing by the Landau-Zener (LZ) formula [46]. The probability of an atom making such a diabatic transition is [47, 48]

$$P_{\text{LZ}} = \exp\left(-\frac{\pi U^2}{\hbar v \nabla E}\right) \quad (2.2.4)$$

where $2U$ is the energy splitting at the avoided crossing, v is the atom velocity, and ∇E is the energy level gradient on either side of the crossing. As the energy splitting at the avoided crossing becomes small, $P_{\text{LZ}} \rightarrow 1$. This applies when $\Omega_r \simeq \sqrt{3/2}\delta$ and $\chi \simeq \pi/4$ as shown in Fig. 2.4 (B). In this scenario the atom will make a diabatic transition at each avoided crossing, following a path similar to the one highlighted in red. As the atom transitions from one dressed energy level to the next, the atom/field system gains energy, which must come from the kinetic energy of the atom through the conversion of photons from one standing wave field to the other. The process is reversible and can proceed in the opposite direction as well—the atom can follow a path of multiple crossings decreasing in energy, resulting in an increase in the atom's kinetic energy.

Over many standing wave cycles, if the atom is always on the correct path,

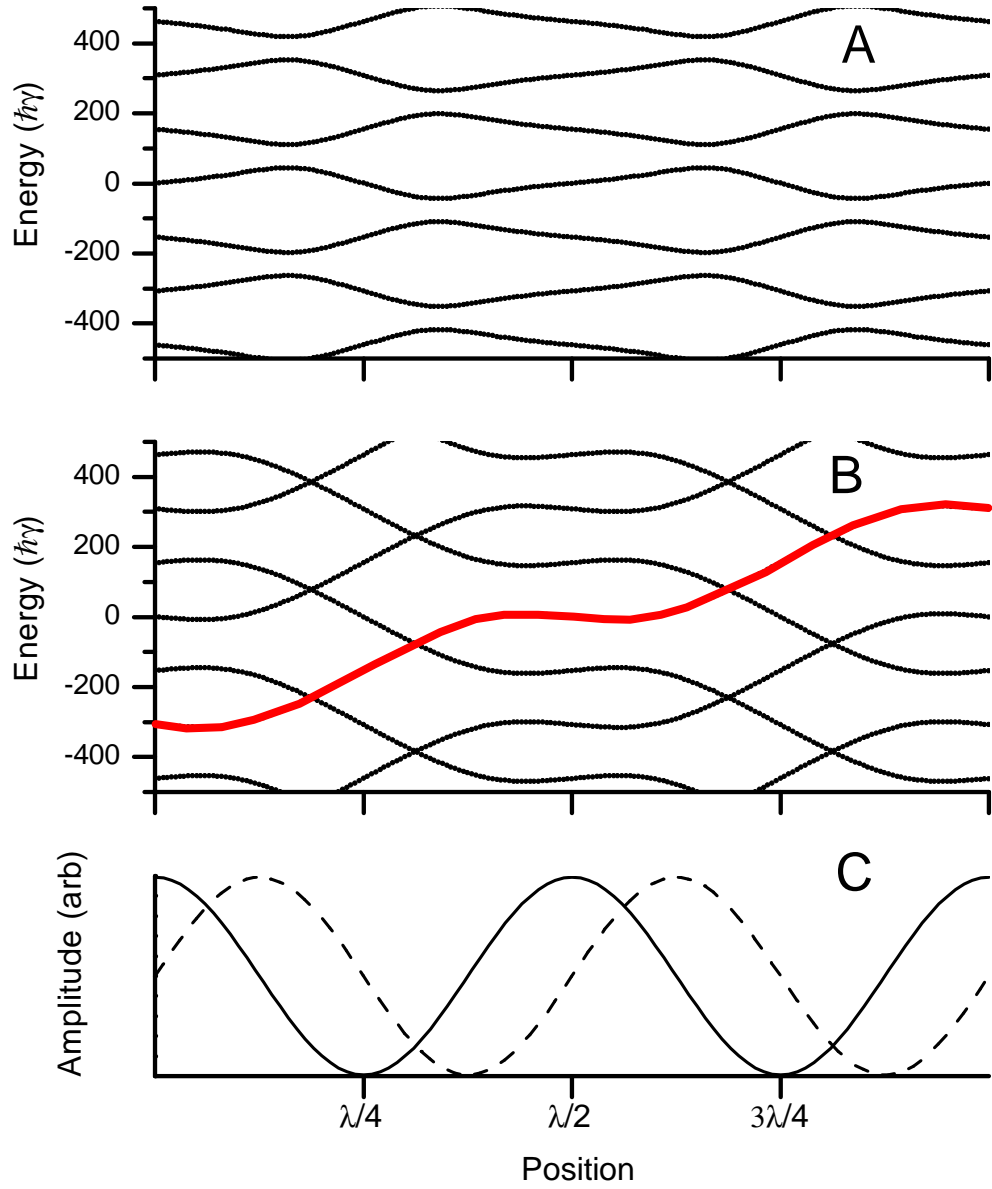


Fig. 2.4: Bichromatic dressed energy levels as a function of spatial position for $\delta = 154\gamma$ and $\chi = \pi/4$. Plot A shows the result for the π -pulse condition $\Omega_r = (\pi/4)\delta$ while plot B shows the result for $\Omega_r = \sqrt{3/2}\delta$. The highlighted (red) trace shows a potential pathway accessed by the bichromatic force. The corresponding standing wave amplitudes from Eq. (2.2.1) are shown in plot C. Note the similarity to independently calculated plots in Refs. [35, 36] for much smaller detunings.

it will experience a spatially averaged force proportional to the average slope of the path. The force, estimated from the slope of the energy level over half a wavelength agrees perfectly with Eq. (2.1.7):

$$|F| = \left| \frac{\Delta E}{\Delta z} \right| = \frac{2\hbar\delta}{\lambda/2} = \frac{2\hbar k \delta}{\pi}. \quad (2.2.5)$$

However, this estimate for the force assumes that the atom stays on the prescribed path. Dephasing events, most notably spontaneous emission, will cause the atom to occasionally drop to a lower manifold with the wrong phase, changing the sign of the path slope. Fig. 2.5 shows the spatially dependent dressed state eigenvalues for the lower manifold from Fig. 2.3. The blue [bold] lines indicate levels corresponding mostly to the bare atom in its ground state ($|g, m, n\rangle$). When on these paths it is therefore less likely to undergo spontaneous emission than when on one of the paths depicted with a thin line. For example, path A has a greater admixture of the bare atomic excited state than does path B. If an atom is on path A, it spends more time in its excited state and is more likely to return to a path parallel to B (but in another manifold), so on average, the atom is more likely to follow paths like B.

Therefore, with $\chi = \pi/4$, the atom will, averaged over many spatial periods, spend 1/4 of its time on path A (effectively counteracting the preferred force) and 3/4 of its time on path B. This reduces the force to 1/2 of Eq. (2.2.5),

$$F_{\text{BCF}} = \frac{\hbar k \delta}{\pi}. \quad (2.2.6)$$

which again agrees with the π -pulse model result, Eq. (2.1.7).

The DDA model also provides some insight into the origin of the velocity

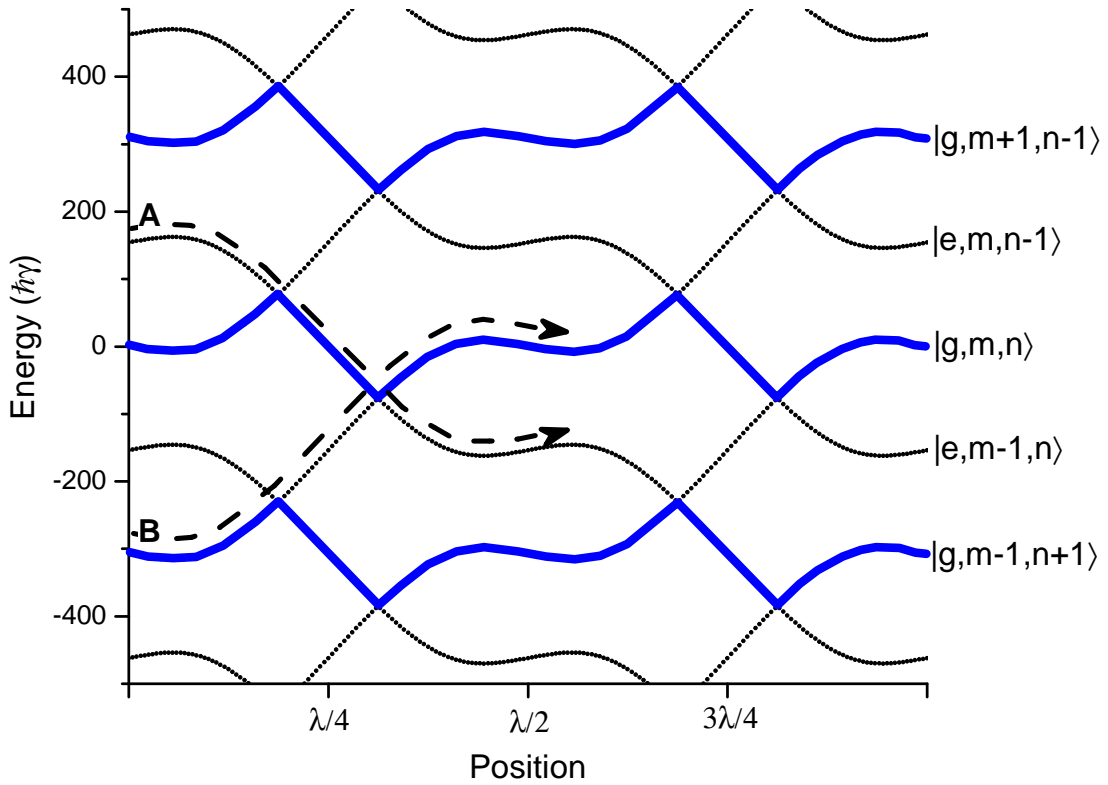


Fig. 2.5: Spatial variation of dressed state levels from the lower manifold in Fig. 2.3 for $\delta = 154\gamma$, $\Omega_r = \sqrt{3/2}\delta$, and $\chi = \pi/4$. The bare atom is in its ground state on levels marked in blue (bold lines). An atom on path A spends approximately 75% of the time in the excited state and is therefore more likely to undergo spontaneous emission than an atom on path B. Note the similarity to independently calculated plots in Refs. [35, 36] for much smaller detunings.

range of the bichromatic force. In order for an atom to accurately follow path B in Fig.2.5, it must move diabatically through the crossings while adiabatically following the energy levels in between. However, if the velocity is very large, the probability of the atom undergoing diabatic transitions in between the avoided crossings increases, putting the atom on paths that counteract the force. This model is most accurate for atoms with small Doppler shifts. Faster moving atoms will see a Doppler-shifted BCF resulting in asymmetric energy spacings in the manifold, which is discussed in more detail in Section 3.3. Eventually the fastest atoms reach the limiting velocity case where they are close to resonance with one of the bichromatic frequency components. In this case neither the π -pulse nor DDA models are appropriate.

More recently an alternative approach to the bichromatic dressed atom picture was developed using a Floquet Hamiltonian [49–51] by Metcalf and Yatsenko [44]. The Floquet Hamiltonian is constructed in such a way that the time variation is the difference in frequency between the two laser fields, 2δ . This provides a time-independent Hamiltonian allowing for analytic solutions for the optimal Rabi frequency and phase, confirming the previous DDA results. Also, using a Landau-Zener estimate and second-order perturbation theory, the method provides insight into the velocity range of the bichromatic force. Both methods calculate the velocity range to be $\pm\delta/4k$. This number agrees with the numerically calculated range for a Rabi frequency of exactly $\sqrt{3/2}\delta$, but is less than the actual total range of the bichromatic force when the atom sees a shifted Rabi frequency or a varying Rabi frequency, as shown in Fig. 2.6. The authors of [44] believe that the underestimate of the velocity range stems from ignoring Doppler shifts due to the atom velocity, and are proposing a second Floquet treatment in

the moving frame of the atom to correct the omission.

2.3 Numerical Calculation

The methods discussed in Sections 2.1 and 2.2 are primarily qualitative, providing estimates of basic BCF properties such as direction and magnitude, and predicted optimal values for key parameters such as Ω_r and ϕ . A detailed calculation of the atom state evolution inside the bichromatic laser field taking into account the populations of the upper and lower states, excitation and stimulated emission, and spontaneous decay is needed to obtain a complete picture of the BCF. The Bloch vector introduced in Section 2.1 describes the internal state of a pure two-level atom in a classical optical field [40]. The equations of motion for the Bloch vector are known as the optical Bloch equations (OBEs) and describe the time evolution of the atomic state.

Complete derivations of the OBES can be found in [40, 41, 52, 53] so I will simply summarize the results here. The optical Bloch equations in the rotating frame (rotating at optical frequency ω_a) can be written as

$$\begin{aligned}\dot{u}(z, t) &= -(\gamma/2)u(t) - \Delta v(t) - \text{Im}(\Omega_r)w(t), \\ \dot{v}(z, t) &= \Delta u(t) - (\gamma/2)v(t) - \text{Re}(\Omega_r)w(t), \\ \dot{w}(z, t) &= \text{Im}(\Omega_r)u(t) + \text{Re}(\Omega_r)v(t) - \gamma(w(t) + 1).\end{aligned}\tag{2.3.1}$$

The Bloch vector components, $(u(t), v(t), w(t))$ can be rewritten in terms of the

excited and ground state populations as [9]

$$\begin{aligned} u(t) &= c_g c_e^* + c_g^* c_e \\ v(t) &= i(c_g c_e^* - c_g^* c_e) \\ w(t) &= |c_g|^2 - |c_e|^2. \end{aligned} \tag{2.3.2}$$

Here (*) denotes the complex conjugate and $|a|^2 \equiv aa^*$, and the quantities $|c_g|^2$ and $|c_e|^2$ represent the populations of the ground and excited states. The interaction of the atom with the bichromatic standing wave is included through the Rabi frequency Ω_r defined in Eq. (2.1.5). The detuning Δ in Eq. (2.3.1) comes from the choice of a rotating frame. For an atom in a monochromatic laser field, selection of the laser frequency as the rotating frame frequency is natural and Δ is the laser detuning from resonance, $\omega_\ell = \omega_a + \Delta$. However, when the atom is in a bichromatic field, the choice is not as clear since any rotating frame will leave some time dependence in Ω_r . In these calculations the rotating frame is selected to be the center of the bichromatic frequencies. Therefore, Δ is the detuning of the center of the bichromatic spectrum from resonance. This makes sense in that the center of the bichromatic frequencies corresponds to the center of the bichromatic force, but there is some time dependence left in Ω_r .

The force on the atom can then be calculated using Ehrenfest's theorem [54],

$$F(z, t) = \hbar[u(t)\nabla \text{Re}(\Omega_r(z, t)) - v(t)\nabla \text{Im}(\Omega_r(z, t))]. \tag{2.3.3}$$

To numerically solve the OBEs in Eq. (2.3.1) and calculate the force on the atoms, Harold Metcalf provided the Fortran source code used for their work at Stony Brook [19, 20, 35, 36, 42, 55], based on earlier code written by the authors

of [14]. I modified the code to use a freely available ordinary differential equation solver subprogram instead of the commercial package used previously. Details of the changes and of the ODE solver can be found in Appendix A. The code computes the bichromatic force for atoms resonant with the center frequency of the bichromatic field as a function of velocity. The velocity is not explicit in Eq. (2.3.3), but is inferred using a constant velocity approximation assuming that the atom position is given by $z = vt + z_0$. Taking $z_0 = 0$, Eqs. (2.3.1) are numerically solved over small time steps. Eq. (2.3.3) is evaluated after each solution. The calculation is repeated for discrete velocities over the desired range, yielding a profile of the force as a function of velocity. I wrote a second version of the program in Mathematica, primarily to verify the output from the Fortran program. The force profiles from the two programs are identical, validating the use of the new ODE solver. Both programs are discussed in more detail in Appendix A.

Example output from the numerical solution of the OBEs is shown in Fig. 2.6 for $\delta = 154\gamma = 2\pi \times 250$ MHz. Force profiles generated by the Fortran code have previously been experimentally verified for a range of parameters by the authors of Refs. [17, 18]. They show the peak bichromatic force occurs for the condition $\Omega_r = \sqrt{3/2}\delta$, in agreement with the DDA results, but again different from the π -pulse estimate.

2.4 Shifting the Center of the Force

Examination of the bichromatic force profiles in Fig. 2.6 reveals three important features of the BCF:

1. The bichromatic force has the same sign (direction) for all velocity groups—the BCF can only push in one direction for a given choice of the beat note

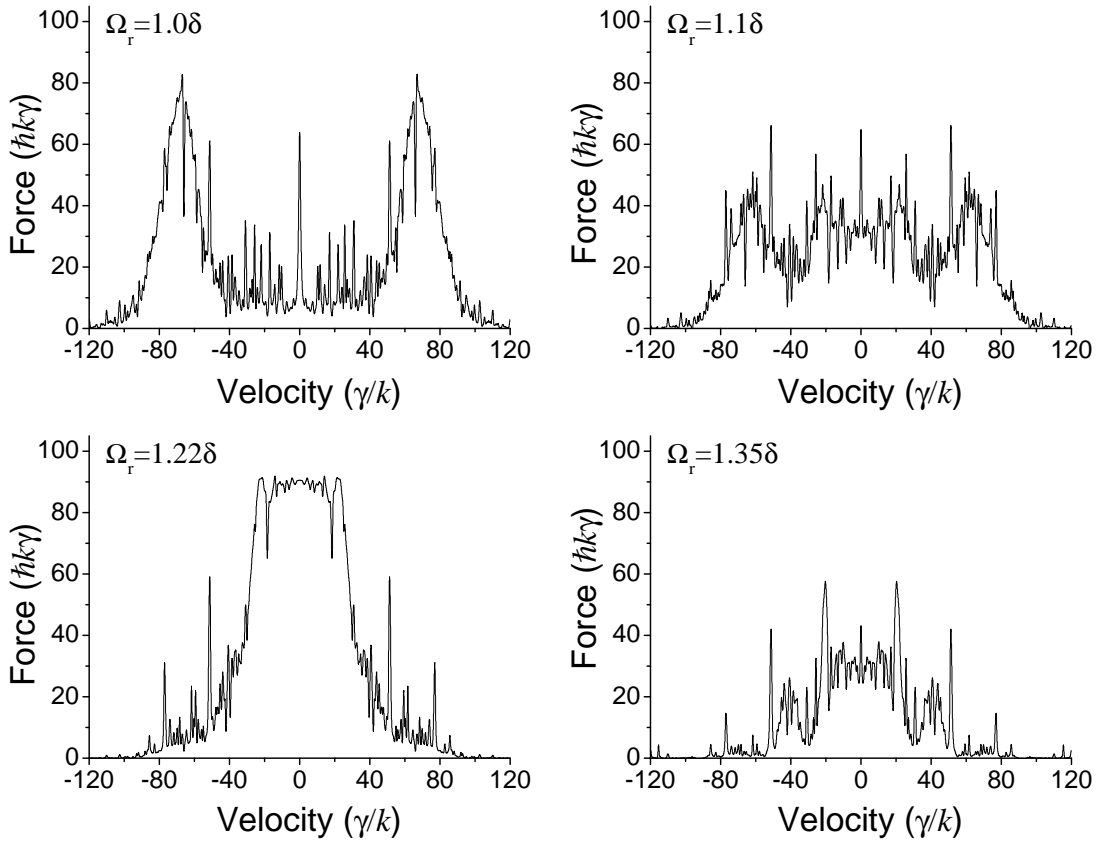


Fig. 2.6: Calculated bichromatic force vs. velocity for $\delta = 154\gamma$ and phase $\chi = \pi/4$ with different values of Ω_r . The optimum Rabi frequency, defined as the value yielding the largest central force, occurs at $\Omega_r = \sqrt{3/2}\delta$, in agreement with the DDA treatment in Section 2.2, and not at $(\pi/4)\delta$ as the π -pulse analogy predicts. Note that the force magnitude is scaled by twice the radiative force, $F_{\text{rad}} = \hbar k\gamma/2$.

phase χ .

2. The range of the force is centered around the zero velocity group, where the center frequency of the bichromatic components is resonant.
3. The edges of the BCF drop off steeply at either extreme of the velocity range, regardless of the choice of δ .

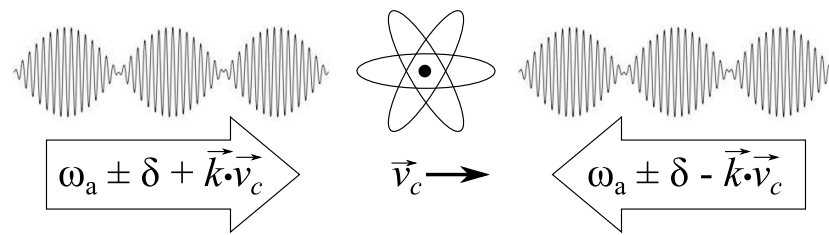


Fig. 2.7: Bichromatic force in the laboratory frame with center frequencies Doppler shifted by $\pm \vec{k} \cdot \vec{v}_c$, resonant with the atom moving at velocity \vec{v}_c .

To slow a non-zero velocity group of atoms in the laboratory frame if the Doppler shift exceeds the BCF velocity range $\Delta v \simeq \pm \delta / 4k$, the center of the bichromatic force must be Doppler-shifted on to resonance as shown in Fig. 2.7. This can be done in a number of ways, keeping in mind that for a metastable helium beam the Doppler shifts range from 700 MHz to 1 GHz. In our experiments, the Doppler shifts are achieved using frequency up- and down-shifts from acousto-optic modulators and offset frequency locks as discussed in Sections 4.8 and 6.3.

2.5 BCF Characteristics

Table 2.1 shows a summary of the characteristics of the bichromatic force. Each entry is described in more detail in the following sections.

Table 2.1: Fundamental properties of the bichromatic force for detuning δ , where $\omega_r = \hbar k^2/2m$ is the recoil frequency.

Quantity	Value
Optimum Ω_r	$\sqrt{3/2} \delta$
Velocity Range	$< \delta/k$
Slowing Time	$\pi/(2\omega_r)$
Cooling	Depends on details of force profile

2.5.1 Optimum Rabi Frequency

The first important result of the preceding calculations and models is that the optimal Rabi frequency is

$$\Omega_r = \sqrt{\frac{3}{2}} \delta. \quad (2.5.1)$$

The results from both the DDA and numerical OBE solutions are in agreement, and differ from the prediction of the π -pulse estimate of $(\pi/4)\delta$.

2.5.2 Bichromatic Beam Irradiance Requirement

The optimum irradiance scales quadratically with the detuning or Rabi frequency, which can be expressed as [9]

$$\Omega_r = \gamma \sqrt{\frac{I}{2I_s}} \quad (2.5.2)$$

where I is the irradiance of a single bichromatic beam component and I_s is the saturation irradiance of the transition. For the transition used in these experiments with metastable helium, $I_s = 0.17 \text{ mW/cm}^2$. Solving for I and substituting Eq. (2.5.1) yields an expression for the optimum irradiance as a function of detuning

$$I = 2I_s \left(\frac{\Omega_r}{\gamma} \right)^2 = 3I_s \left(\frac{\delta}{\gamma} \right)^2. \quad (2.5.3)$$

Note that this is per bichromatic component, so the required irradiance of each bichromatic beam is twice as large.

2.5.3 Velocity Range

The bichromatic force profile has dramatically different shapes and ranges depending on the Rabi frequency, as shown in Fig. 2.6. If the criterion for optimization is to obtain the largest force at the center of the profile, then Ω_r should be $\sqrt{3/2}\delta$ and the velocity range is approximately $\delta/2k$ (if defined by its full width at half maximum). However, as is shown in Fig. 2.6, for Rabi frequencies around $\Omega_r = \delta$ the range of the force can be as great as δ/k . If the bichromatic slowing lasers had rectangular “top hat” profiles, then the velocity range would be sharply defined as shown in these profiles. In practice, however, the gaussian beam profiles mean the atom will experience a range of Rabi frequencies so the effective velocity range will fall somewhere between $\delta/2k$ and δ/k . Averaging of the profiles in Fig. 2.6 probably provides a more realistic representation of the bichromatic force.

2.5.4 Bichromatic Slowing Time

The time required for acceleration of an atom across the velocity range δ/k can be estimated assuming a constant average force of $\hbar k\delta/\pi$:

$$\Delta t = \frac{m\Delta v}{F} = \frac{m(\delta/k)}{\hbar k\delta/\pi} = \frac{\pi/2}{\omega_r}, \quad (2.5.4)$$

where $\omega_r \equiv \hbar k^2/2m$ is the recoil frequency. Notice that this time is independent of δ , depending solely on the atom properties. A minimum interaction length for a bichromatic force slower of any atom or molecule can be calculated from $L = \bar{v}\Delta t$.

For helium ($m = 4$ amu) $\Delta t = 5.9 \mu\text{s}$. To slow a fast beam of metastable helium atoms ($\bar{v} \sim 1000 \text{ m/s}$), the interaction length can in principle be less than 1 cm.

2.5.5 Cooling

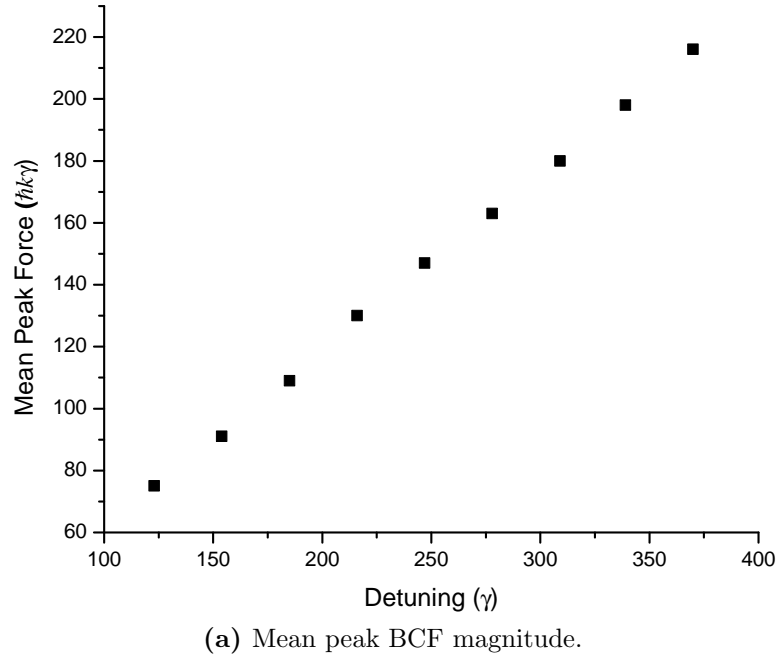
The bichromatic force drops off sharply at either end of its range, as can be seen in Fig. 2.6. If the force is applied for a time greater than the bichromatic slowing time (Eq. (2.5.4)), atoms within the velocity range of the force will pile up at the low-velocity limit. This can yield significant cooling in addition to deceleration, as can be seen in Fig. 5.1 and Refs. [14, 35, 36]. Recently Harold Metcalf has argued in a somewhat controversial paper that the cooling is due to radiation exchange between the bichromatic fields, with no inherent limitations tied to the rate of spontaneous emission [56].

Chapter 3

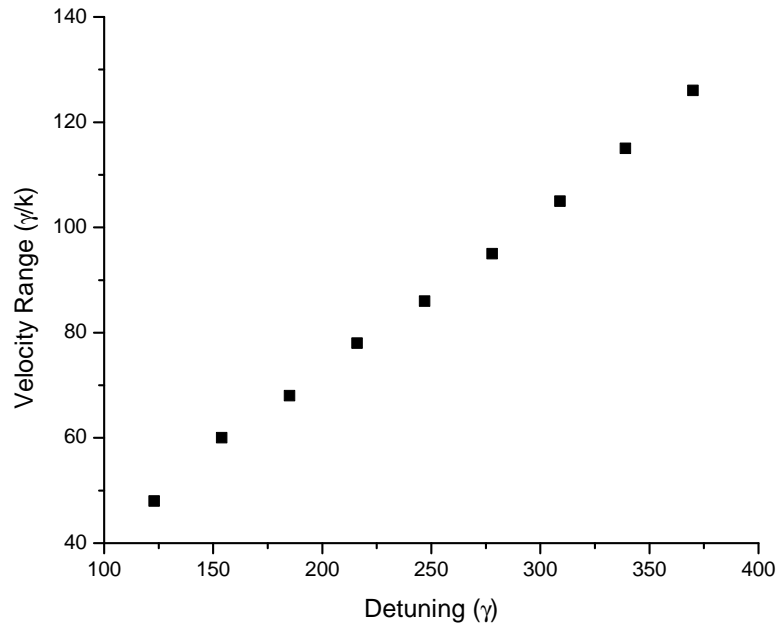
Large Detuning Limitations and Slower Design Considerations

None of the models or numerical calculations of the BCF described in Chapter 2 show any signs of an inherent upper limit to either the magnitude or the velocity range of the force. In theory, given sufficient laser power to maintain the criterion $\Omega_r = \sqrt{3/2} \delta$ it is possible to slow an atom from any arbitrary velocity to zero using the BCF with a sufficiently large δ . The numerically solved optical Bloch equations described in Section 2.3 were used to generate force profiles at large detunings ($\delta > 150\gamma$). The profiles show linear increases in both magnitude and velocity range indicating the lack of an upper bound to the force for δ up to 370γ , as summarized in Fig. 3.1.

Cashen and Partlow [35, 36] observed the predicted bichromatic slowing results in He* at $\delta = 184\gamma$, with a measured velocity width of $\Delta v = 325$ m/s $\approx \delta/k$. However, when the detuning was doubled to $\delta = 368\gamma$ no indication of slowing was observed [36]. In our own work, evidence for a failure of the force rectification is seen at $\delta = 278\gamma$, as will be discussed in Chapter 5. The presence of an upper limit to the BCF is not only in conflict with the models described in Chapter 2, but is of critical importance to the design and implementation of an atomic slower.



(a) Mean peak BCF magnitude.



(b) Velocity range as FWHM of force profile.

Fig. 3.1: Compilation of numerical computation results as described in Section 2.3 for high detunings with $\Omega_r = \sqrt{3/2} \delta$ and $\phi = \pi/2$. The linear increase of both the BCF magnitude and velocity range indicates the lack of an upper bound. Successful BCF slowing experimental results for He* to date are limited to $\delta \leq 184\gamma$

To further explore the source and nature of a potential upper limit to the BCF, I considered various potentially detrimental effects that have the property of increasing in magnitude along with an increasing BCF detuning. The potential mechanisms we have considered are:

1. Dephasing of the Rabi oscillations due to rapid Doppler shifts. This is a concern at large detunings where significant decelerations create substantial changes in the Doppler shifts within the atom's radiative lifetime.
2. Laser-induced mixing with distant states and the contamination of a closed 2-level cycling transition by unwanted m_J levels, resulting in ac Stark shifts.
3. Dephasing from collisions, beam nonuniformity, etc.
4. Breakdown of the adiabatic approximation within the dressed-atom picture due to rapid level shifts.

Estimates of the Rabi depahsing due to rapid Doppler shifts predicts an onset of problems at a value of δ that matches experimental observations, and is the most likely cause for an upper limit identified at the time of this thesis. However, because of the failure of our fiber laser amplifier, I was not able to acquire sufficient experimental data above $\delta = 185\gamma$ to provide definitive answers systematically investigating the behavior of the BCF in this range.

3.1 Decelerative Dephasing

The most likely cause for an upper limit of the BCF is the result of multiple dephasing events during each radiative lifetime. Because the cycling of an atom is “reset” to the correct phase only by radiative decay, multiple small dephasings

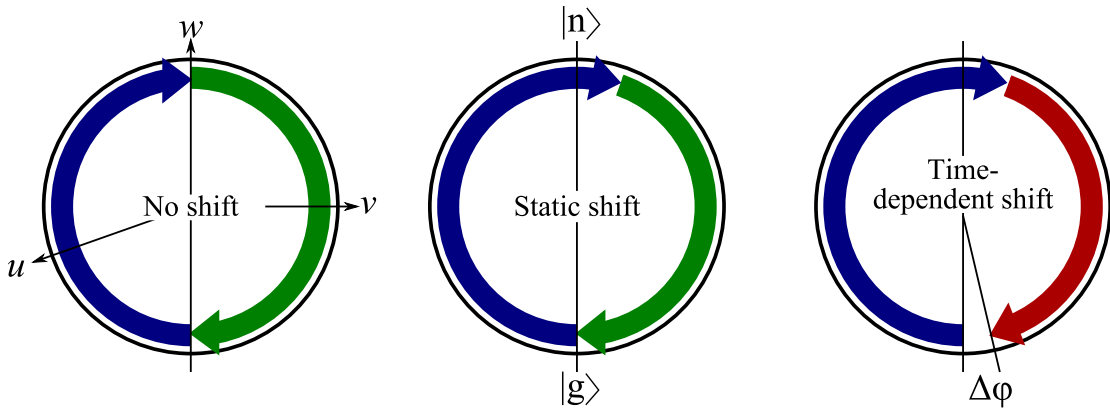


Fig. 3.2: Representations of the Bloch sphere (see Fig. 2.1) depicting one Rabi cycle of the atom from ground state $|g\rangle$ to upper state $|n\rangle$ and back. For the cases of no shift and a static shift (at left and center), the atom makes one complete Rabi cycle. However, if the shift is time dependent (at right), the Rabi cycle may not be complete due to the frequency difference between the cycle beginning and end. This produces in small dephasings $\Delta\varphi$, which accumulate over one upper-state lifetime t' . If the accumulated dephasing $\approx \pi$, the force reduces direction and the time-averaged BCF is reduced.

can accumulate between radiative decays, and may reach levels that affect the BCF. Dephasing events include the motion of the atom through the laser profile, causing the atomic states to cycle far from the optimal Rabi frequency, and the deceleration of the atom causing time-varying frequency shifts, “decelerative dephasing”, which alters the effective Rabi frequency for each frequency component to

$$\Omega'_r = \sqrt{\Omega_r^2 - \Delta\omega(t)^2}, \quad (3.1.1)$$

where $\Omega_r = \sqrt{3/2}\delta$ is the on-resonance Rabi frequency and $\Delta\omega(t)$ is the time-varying detuning from resonance. When there is no shift present, each of the bichromatic frequencies contributes exactly half of a complete Rabi cycle due to the symmetric bichromatic detunings, as shown in Fig. 3.2. If the frequencies are shifted but static, the ratio of each frequency’s contribution changes, but the atom

still completes one Rabi oscillation. However, if the shift is time-dependent, the change in shift between the beginning and end of the Rabi oscillation will cause the cycle to be incomplete, as shown in Fig. 3.2. The next Rabi cycle will then start where the previous one ended, resulting in a small dephasing $\Delta\varphi$. These dephasings in each Rabi cycle accumulate until the atom's phase is reset by a radiative decay. If the atom's phase changes by a factor of π within a radiative lifetime, the direction of the force reverses, which would be expected to greatly reduce the time-averaged BCF. We can express this constraint on the change in Rabi frequency as

$$\Delta\Omega_r t' \leq \pi/2. \quad (3.1.2)$$

It is straightforward to make a rough estimate of the detuning at which this problem should become severe. To estimate the change in Rabi frequency due to the atomic deceleration, we can expand Eq. (3.1.1) and use the second order term:

$$\Delta\Omega_r \simeq \frac{1}{2} \frac{\Delta\omega^2}{\Omega_r}. \quad (3.1.3)$$

We can write the detuning in terms of the velocity change as

$$\Delta\omega = \vec{k} \cdot \Delta\vec{v}, \quad (3.1.4)$$

where the velocity change can be written in terms of the bichromatic force using Eq. (2.1.8) as

$$\Delta v \simeq \frac{F_{\text{BCF}}}{m} t' = \frac{\hbar k \delta}{m \pi} t', \quad (3.1.5)$$

where m is the atomic mass and t' is the average time between radiative decays. Assuming an upper state population of 0.25 due to the rapid BCF cycling, we

estimate that $t' \simeq 4\tau$ where $\tau = 98$ ns is the 2^3P_2 lifetime.

Substituting for $\Delta\Omega_r$ from Eq. (3.1.3) in Eq. (3.1.2) and rearranging, the constraint can be written as

$$\frac{\Delta\omega^2}{\Omega_r} \leq \frac{\pi}{t'}. \quad (3.1.6)$$

Using Eqs. (3.1.4) and (3.1.5), Eq. (3.1.6) can be written as

$$\frac{\hbar^2 k^4 \delta^2}{m^2 \pi^2} t'^2 \leq \frac{\pi \sqrt{3/2} \delta}{t'}. \quad (3.1.7)$$

Finally, solving Eq. (3.1.7) for the detuning δ provides an estimate of the onset of accumulated dephasing problems

$$\delta \leq \frac{m^2 \pi^3 \sqrt{3/2}}{\hbar^2 k^4 t'^3} = \sqrt{\frac{3}{32}} \frac{\pi^3}{\omega_r^2 t'^3}, \quad (3.1.8)$$

where $\omega_r = 2.67 \times 10^5$ s⁻¹ is the atomic recoil frequency. Assuming $t' = 4\tau = 392$ ns, the onset of decelerative dephasing problems occurs at $\delta = 2\pi \times 352$ MHz = 217γ . This correlates surprisingly well with the experimental observations of efficient slowing at 185γ but not at 278γ , as discussed in Section 5.2.

Decelerative dephasing is not taken into account in either the DDA model (Section 2.2), which calculates the time-independent spatial atomic energy levels over one rf wavelength, nor the numerical calculations of the OBEs described in Section 2.3, which uses the rotating wave approximation. The OBE program was originally written for small detunings of approximately 40γ , where the change in atomic velocity over one radiative lifetime is small compared to the Rabi frequency. An approximation in the solver assumes a constant atomic velocity over several radiative lifetimes, which is appropriate at small detunings. There is evidence that the calculated force profiles correlate well to the observed velocity profiles

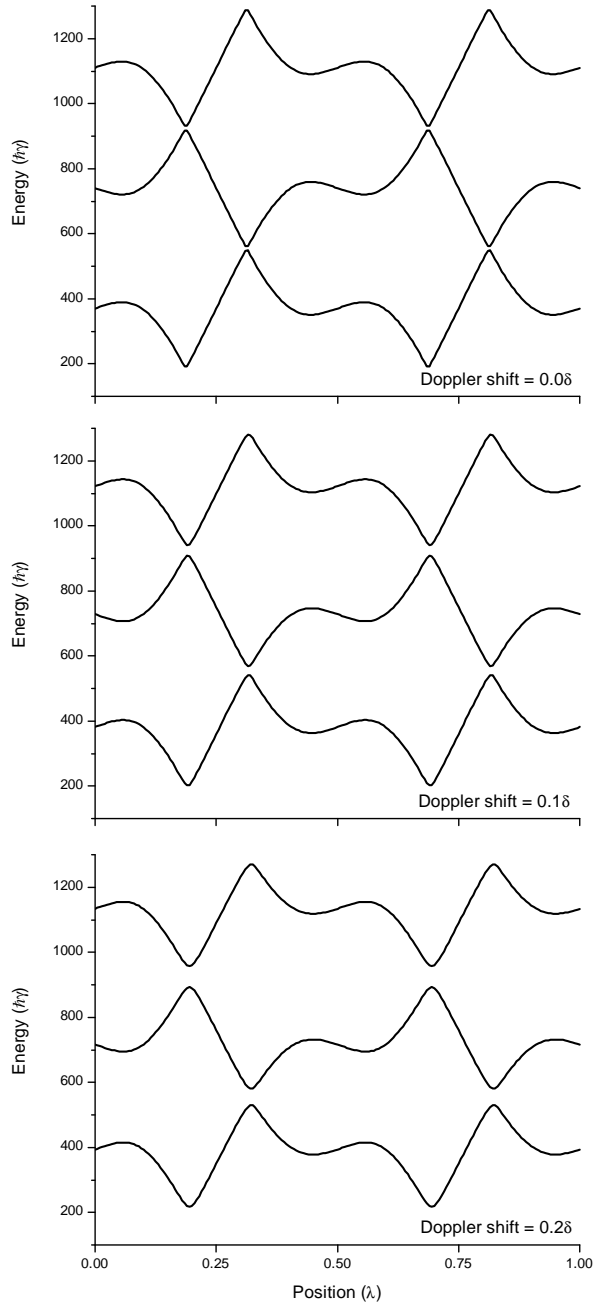


Fig. 3.3: Bichromatic dressed energy levels as a function of spatial position for $\delta = 370\gamma$ and $\chi = \pi/4$ for increasing Doppler shifts top to bottom. Notice the energy gaps at avoided crossings are proportionate to the difference in photon energy between the red and blue detuned Doppler shifted fields.

up to a detuning of 185γ [14, 35, 36, and this work]. However, the experimental results described in Ref. [36] and Section 5.2, along with the estimate presented above, indicate strongly that the approximations made in the original OBE solver are not appropriate for detunings of $\delta \gtrsim 200\gamma$ for He*. An effort is currently underway to rewrite the OBE solver program to eliminate the constant velocity approximation.

Within the DDA approximation, the effects of the frequency shifts can be examined through the asymmetry created in the bichromatic detunings, which were assumed to be $\omega_a \pm \delta$ in Section 2.2. Under a frequency shift of magnitude $\Delta\omega$, the bichromatic detunings become $\omega_a + (\delta - \Delta\omega)$ and $\omega_a - (\delta + \Delta\omega)$. This shifts the symmetrically spaced coupled energy levels shown in Fig. 2.3, making them asymmetric with spacings $\hbar(\delta + \Delta\omega)$ and $\hbar(\delta - \Delta\omega)$.

Modifying Eqs. (2.2.1) through (2.2.3) to include a frequency shift produces the energy levels shown in Fig. 3.3. While it is apparent that the reduced probability of an atom traversing the required crossing increases with frequency shift, there is no time dependence in this model and it is not easy to determine the effect on the BCF of a shift that is appreciable on the scale of one radiative lifetime.

3.2 ac Stark Shift

A second potentially limiting effect is laser-induced mixing with nearby states via ac Stark shifts [9, 57]. The ac Stark effect causes shifts and splittings of atomic levels due to such mixing in the presence of a time-varying electromagnetic field. This was first observed in an intense laser field by Bonch-Bruevich and coworkers [58] (but was well-understood much earlier in rf spectroscopy).

There can be significant ac Stark shifts in the 2^3P_2 level due to laser-induced

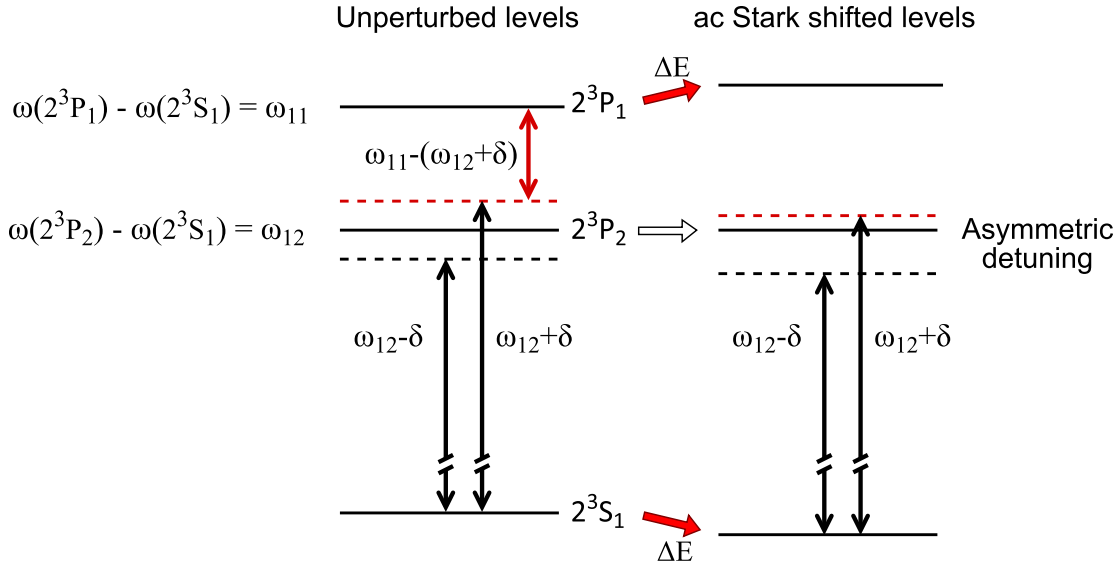


Fig. 3.4: He* levels of interest in these experiments in both unperturbed and ac Stark shifted configurations. In the case of large detunings the upper bichromatic component $\omega_{12} + \delta$ is close enough to the 2^3P_1 level to induce significant coupling with the 2^3S_1 level, with the relevant detuning shown by the short red arrow. The unwanted coupling shifts the 2^3S_1 level down and the 2^3P_1 level up by ΔE , resulting in an asymmetry in the bichromatic detunings relative to the 2^3P_2 level.

coupling with the 2^3P_1 level, as shown in Fig. 3.4. A perturbative treatment of the ac Stark shift can be found in Sobelman's text [59]. The energy shift of a lower state $|g\rangle$ can be written generally as (Ref. [59] Eqn. 7.73)

$$\overline{\Delta E} = \frac{1}{3\hbar(2j+1)} \sum_n \frac{\omega_{ng} |\langle n, j | \vec{d} | g, j' \rangle|^2}{\omega_{ng}^2 - \omega^2} \overline{E^2}. \quad (3.2.1)$$

Here, upper atomic states $|n\rangle$ are separated from state $|g\rangle$ by frequencies ω_{ng} . The laser field has frequency ω and amplitude E .

The matrix elements are calculated from the oscillator strengths using re-

duced matrix elements, which can be written [59, Eq. 9.48] as

$$\langle n, j \parallel \vec{d} \parallel g, j' \rangle = \sqrt{f(n, j; g, j')} \frac{3\hbar e^2(2j+1)}{2m\omega_{ng}}, \quad (3.2.2)$$

where $f(n, j; g, j')$ is the oscillator strength for the $|g, j'\rangle \rightarrow |n, j\rangle$ transition. The matrix elements can then be calculated for He* using $3j$ symbols taking into account the field polarization q as well as the quantum numbers j, m and j', m' for the excited 2^3P and ground 2^3S states (respectively). Using the Wigner-Eckart theorem [59],

$$\langle n, j \parallel \vec{d} \parallel g, j' \rangle = (-1)^{j-m} (n, j \parallel \vec{d} \parallel g, j') \cdot \begin{pmatrix} j & 1 & j' \\ -m' & q & m \end{pmatrix}. \quad (3.2.3)$$

The specific case relevant to these experiments in He* has $m' = 1$ (assuming the atom is initially fully optically pumped into 2^3S_1 , $m' = 1$), $m = (-1, 0, 1)$, and $j = j' = 1$. Because of the optical pumping, the sum over upper states n in Eq. (3.2.1) vanishes. The $2^3S_1 \rightarrow 2^3P_1$ oscillator strength $f(2, 1; 1, 1) = 0.17974$ and the binding energies are $E(2^3S_1) = 159855.9743297 \text{ cm}^{-1}$, $E(2^3P_1) = 169086.8428979 \text{ cm}^{-1}$, and $E(2^3P_2) = 169086.7664725 \text{ cm}^{-1}$, all taken from Ref. [60]. These binding energies are used to calculate the relevant transition frequencies in Eq. (3.2.1): $\omega_{ng} = \omega_{11} = [E(2^3P_1) - E(2^3S_1)]/\hbar$ and $\omega_{21} = [E(2^3P_2) - E(2^3S_1)]/\hbar$. The bichromatic field frequency that contributes most of the shift in Eq. (3.2.1) is $\omega = \omega_{21} + \delta$.

For He* only a small portion of the total laser power contributes to coupling with the 2^3P_1 state due to the chosen optical polarization of the bichromatic fields. The bichromatic field polarizations are nominally either σ^+ and σ^+ or σ^- and

σ^- , enforcing the selection rule $\Delta m = \pm 1$ for σ^\mp , corresponding to $q = \pm 1$ in Eq. (3.2.3). This has two effects. First, the He* atom is quickly optically pumped into the $2^3S_1, m' = \pm 1$ level to cycle the $|m'| = 1 \leftrightarrow |m| = 2$ sublevels, which are the strongest transitions. Second, once the atom is optically pumped, only contamination of the laser by π -polarized light will contribute to coupling to the $j = 1$ upper state. In the ideal case where the laser fields are composed of only σ polarized light, coupling to the 2^3P_1 level would be forbidden, prohibiting any ac Stark shifts.

However, in reality the laser polarization is not perfectly circular, but slightly elliptical, allowing coupling to some extent between the $2^3S_1|m'| = 1 \leftrightarrow 2^3P_1|m| = 1$ sublevels. Measurements made during the polarization tuning described in Section 4.10.2 indicate that typically 4 to 5% of the light is not circularly polarized. In these calculations I will assume a conservative contamination of twice the experimental value, or 10% of the irradiance in the π polarization ($q = 0$) state.

The net result of the ac Stark shift is that the initially symmetric bichromatic detunings $\omega_{21} \pm \delta$ are altered into the asymmetric configuration $\omega_{21} \pm (\delta - \Delta\omega_{ac})$, where $\Delta\omega_{ac} = \overline{\Delta E}/\hbar$ is the frequency change from the ac Stark shift in Eq. (3.2.1). This detuning asymmetry can play a major role at large detunings with strong coupling, as shown in Fig. 3.5. However, because of the small fraction of π -polarized light in the bichromatic beam, the coupling is not strong and the effect is usually minor. The calculated effect of the ac Stark shifts on the BCF in our experiments is shown in Fig. 3.6.

This effect due to the ac Stark shift is relatively small, even for large detunings. In the case of metastable helium, it is clearly not a limiting factor. However, when extending BCF slowing to other atomic species or molecules, the ac Stark

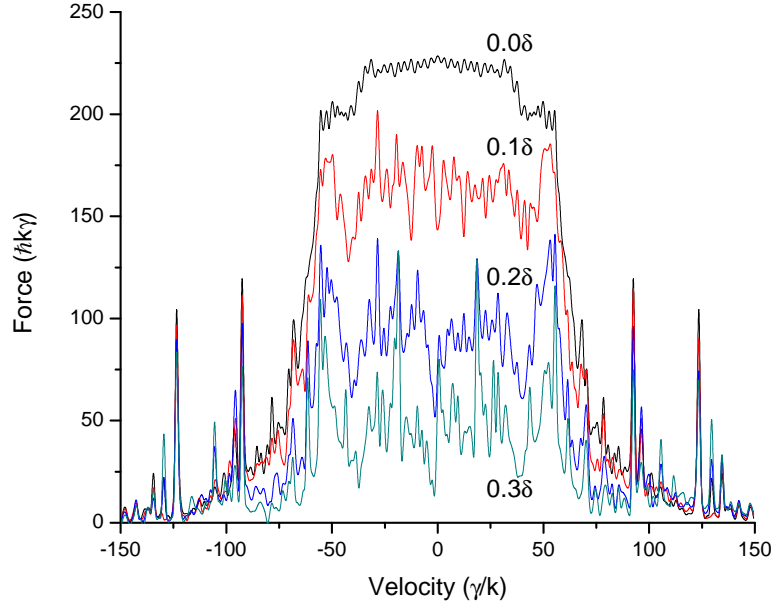


Fig. 3.5: BCF degradation due to the indicated detuning asymmetries for $\delta = 184\gamma$ and $\phi = \pi/2$ from numerical solutions to the OBEs. Note the force magnitude is reduced by more than 50% for an asymmetry of 0.2δ .

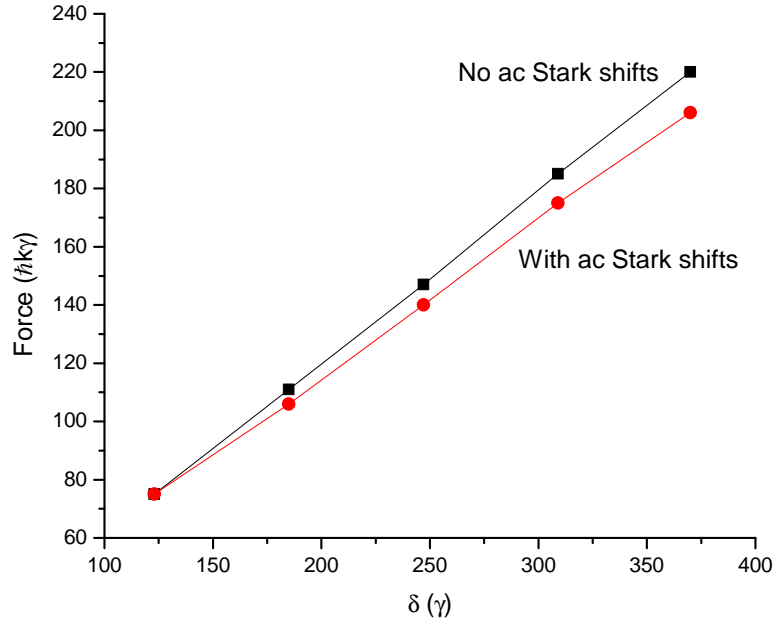


Fig. 3.6: Mean BCF magnitude with and without the detuning asymmetry due to ac Stark shifts. BCF results were numerically calculated from solutions to the OBEs for $\Omega_r = \sqrt{3/2}\delta$, $\phi = \pi/2$, and assuming 10% of the total irradiance in the π -polarized fields relevant for the ac Stark effect.

shift could be a critical consideration.

3.3 Non-Adiabatic Following of Landau-Zener Transitions

One conclusion from the DDA model of the BCF is that in order for the force to exist, the atom must transition diabatically at the level crossings while adiabatically following the energy level between crossings as described in Section 2.2. Failure to do this could cause a breakdown of the BCF. While this effect is inherently included in the OBEs, I think it is instructive to treat it independently. I demonstrate here that an analysis of the Landau-Zener probabilities across a wide range of detunings shows that the transition probabilities at all crossings are independent of δ . The energy levels calculated at $\delta = 185\gamma$ and 370γ are shown in Fig. 3.7 for comparison.

Recalling Eq. (2.2.4), the probability of an atom making a Landau-Zener transition is

$$P_{\text{LZ}} = \exp\left(\frac{-2\pi U^2}{\hbar v \nabla E}\right) \quad (3.3.1)$$

where $2U$ is the energy separation of the avoided crossing, v is the atom velocity, and ∇E is the energy gradient approaching the avoided crossing. Considering the same avoided crossing (same position (λ) in Fig. 3.7) for different detunings, we can analyze the dependence of P_{LZ} to identify any dependence on δ that would lead to a change in the BCF at high detunings. I will follow a similar line of reasoning as that of Yatsenko and Metcalf in Ref. [44] when discussing the velocity range of the force.

The energy separation $2U$ between levels is proportional to δ , so we can write $U = a\hbar\delta$. The constant a , from careful inspection, scales with the choice of the phase χ (from Eq. (2.2.1)), Ω_r , and the position λ of the crossing (see Fig. 3.7),

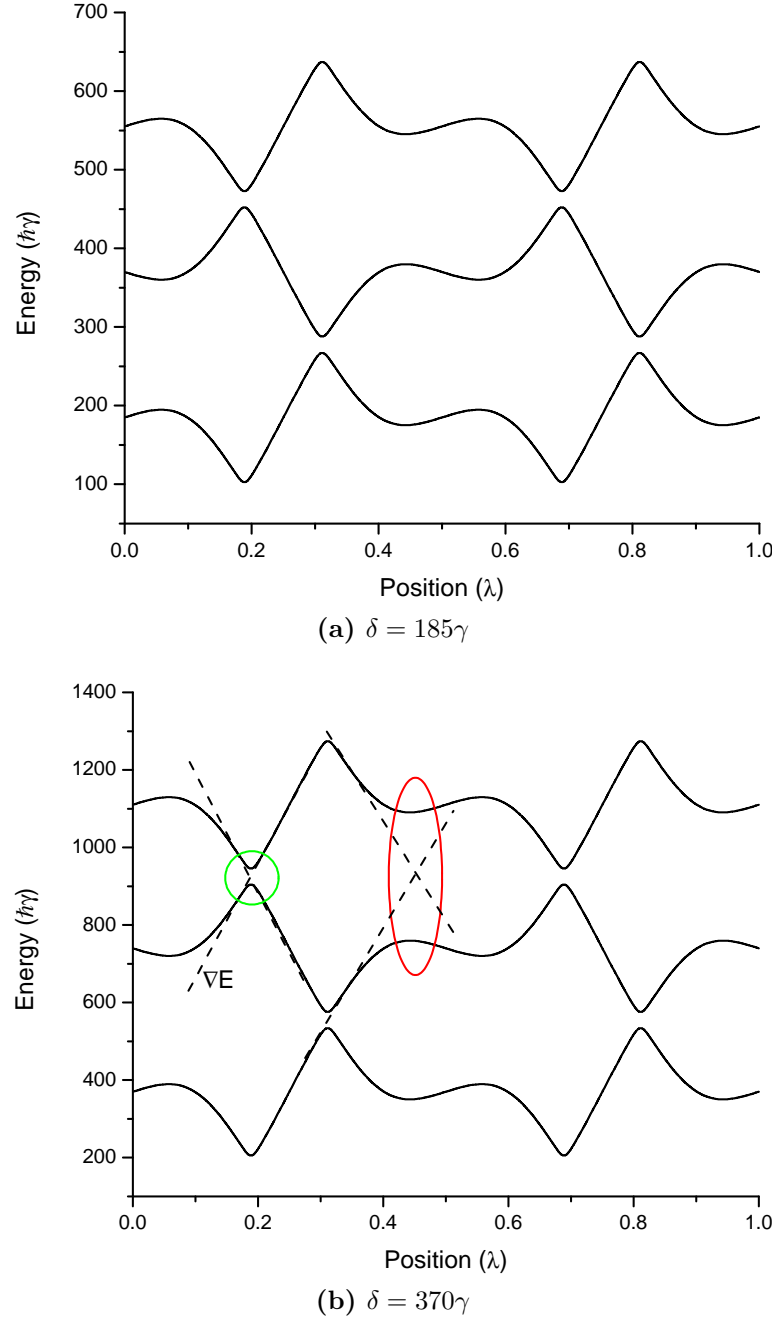


Fig. 3.7: Energy levels for $\Omega_r = 1.1\delta$ and $\chi = \pi/4$ for detunings $\delta = 185\gamma$ in (a) and $\delta = 370\gamma$ in (b) for comparison. Note that the Rabi frequency is below the optimal value and the avoided crossings shown to touch in Fig. 2.4 now have an increased separation for clarity. Dashed lines represent the energy level gradients ∇E . An example of a desired crossing is circled in green, and an undesired (force reversing) crossing is circled in red. Note the uniform scaling of both energy levels and avoided crossings with δ .

but is independent of δ for fixed values of χ and Ω_r .

The energy level gradient ∇E again scales with detuning and can be written $\nabla E = b\hbar\delta/\lambda$ where b is proportional to a , $b = \alpha a$.

Finally, v is the atom velocity which can be written relative to the detuning as $v = \beta\delta/k$ where the constant $|\beta| < 1/4$ such that the atomic velocity falls within the velocity range of the force as described in Sect 2.5.3.

Substituting these approximate expressions into Eq. (3.3.1), the expression reduces to

$$P_{\text{LZ}} \approx \exp\left(\frac{-2\pi ka^2}{b\beta}\right). \quad (3.3.2)$$

Notice that this expression is independent of δ indicating that there is no dependence on the transition probabilities or adiabatic following of energy levels on the detuning at least with the DDA model approximation. This is consistent with numerical solutions of the OBEs, but does not shed any additional light on the experimentally observed upper limit of the BCF.

3.4 Collisional Dephasing

Collisional dephasing is related to the dephasing effect of spontaneous emission, but is caused by collisions of the He^* atoms with other He^* or He atoms while in the interaction region.

This is not a potential contributor to the upper limit of the BCF since the collisional dephasing rates are independent of the laser intensity, depending only on the atomic beam brightness and slower configuration. However, it is a consideration in the design of a slower intended to load a MOT or other atom or molecular trapping system. As such, I will describe an estimated collisional dephasing rate for BCF He^* slowers.

A review of the literature on scattering cross sections and rates for $\text{He}^* - \text{He}^*$ and $\text{He}^* - \text{He}$ reveals calculations and measurements by several authors spanning a half-century [61–64, 64–67]. While the exact rates for the different inelastic collisional processes vary by as much as a factor of 3, it is clear that the two dominant scattering processes, responsible for > 95% of the total scattering rates at moderate velocities, are Penning ionization $\text{He}^* + \text{He}^* \rightarrow \text{He} + \text{He}^+ + e$ and inelastic scattering $\text{He}^* + \text{He} \rightarrow 2\text{He} + h\nu$.

The total scattering cross sections are approximately $Q_{\text{PI}} = 200 \times 10^{-16}\text{cm}^2$ for Penning ionization and $Q_{\text{IS}} = 140 \times 10^{-16}\text{cm}^2$ for inelastic scattering. The total cross sections cited in the surveyed literature vary by a factor of two or three, however. As such, this treatment is intended only to provide an order of magnitude estimation of the effect in the atomic beam.

Because the atomic beam is essentially collimated by the 70 μm aperture, I will treat the atoms as having a velocity in \hat{z} only, and scattering in just one dimension so that they do not change their position in the $x - y$ plane. Also, I assume that the atom flux is uniform across the portion of the beam interacting with the bichromatic lasers.

An interesting observation is that by the time the atoms arrive at the slower after traveling approximately 17 cm from the chopper they have spread longitudinally enough that only atoms within ± 50 m/s are spatially overlapped with one another. This significantly reduces the number of potential collisions, at least for pulsed atomic beams.

I begin by estimating the helium flux per pulse based on a beam solid angle of 1.5×10^{-5} Sr, a measured brightness of $3 \times 10^{13} \frac{\text{atoms}}{\text{Sr}\cdot\text{s}}$, and a chopper “open” time of 20 μs (see Sections 4.2.2 and 4.3). The He^* flux is 9000 atoms/pulse and

the He flux is 1.8×10^8 atoms/pulse. Assuming that the slowest 30% of the atoms fall within the velocity range of the BCF and that velocity groups are spatially bunched as mentioned above, the numbers are reduced to $N_{\text{He}^*} = 2700$ atoms and $N_{\text{He}} = 5.4 \times 10^7$ atoms. Due to the very small number of He^* atoms compared to ground state atoms, and the similarity of the total scattering cross sections, we need only consider the case of He atoms colliding with slowed He^* atoms.

The worst case scenario (and simplest to estimate) is if the He^* atoms are uniformly distributed across the beam cross-section, maximizing the cross-sectional area they occupy. The metastable helium beam has a full-width at half maximum at the slower of about $315 \mu\text{m}$ giving an area of $A_{\text{beam}} = 0.08 \text{ mm}^2$. The probability of an atom making a collision with a He^* atom is then:

$$P = \frac{A_{\text{He}^* \text{ atoms}}}{A_{\text{beam}}} = \frac{N_{\text{He}^*} Q_{\text{PI}}}{A_{\text{beam}}} = 6.75 \times 10^{-8}. \quad (3.4.1)$$

The total scattering per pulse is P times the number of helium atoms in the pulse:

$$N_{\text{scat}} = N_{\text{He}} \times P = 3.6 \text{ collisions/pulse}. \quad (3.4.2)$$

From this result it is clear that a collisional loss of less than 0.2% is not a significant factor in the pulsed BCF slower dynamics.

However, if we move from the immediately relevant case of a pulsed slower to the eventual design of a cw atomic beam slower, the collisional rate increases sharply. Now, because there is a constant flux of helium atoms spanning the full velocity range of the source, we need to account for a significantly larger number of atoms. We approximate the cw beam of slowed atoms as a series of successive pulses traveling at $v = 75 \text{ m/s}$ for some time t_{MOT} to the MOT. Eq. (3.4.2) in the

cw case becomes

$$N_{\text{scat}} = N_{\text{He}} \times P \times t_{\text{MOT}} \quad (3.4.3)$$

and the total scattering is proportional to the time the slowed atoms spend in the same path as the unslowed metastable and ground state helium atoms. This means it is advantageous to separate the two beams of atoms as quickly as possible. Assuming a slowed atom speed of 75 m/s, the scattering amounts to an average of 5% of the slowed atoms for every 5 cm the slow atoms coexist with the unslowed atoms. Fortunately, applying the BCF at a small angle to the atomic beam, as shown in Fig. 4.1, inherently applies a small transverse force to the atoms as they are slowed, separating the slowed atoms from the main atomic beam. Optimization of the crossing angle of the bichromatic beams to the atomic beam needs to be considered in the light of MOT placement and slowed atom number conservation.

3.5 Engineering Limitations

For a fixed-frequency slower, the design goal is to maximize the velocity range of the force $\Delta v \approx \delta/2k$ such that the full range encompasses a sufficient number of atoms in the initial velocity distribution at the high velocity end, while still producing atoms slow enough to be trapped in a MOT. In the case of He* from the atomic beam source described in Section 4.2 deceleration to velocities within the typical 75 m/s capture range of the He* MOT requires very large detunings. For He*, if $\Delta v = 1000$ m/s then $\delta \approx 570\gamma$. The two major practical complications of producing and employing the BCF with detunings this large are the laser intensity required and the very short spatial bichromatic beat note.

3.5.1 Intensity

For a detuning of $\delta \approx 570\gamma$, we can calculate the required laser irradiance to meet the optimum Rabi frequency using Eq. (2.5.3). Recalling that for He* the saturation intensity is $I_s = 0.17 \text{ mW/cm}^2$, each BCF beam requires 320 W/cm^2 . A 1 mm^2 BCF beam waist requires that 3.2 W remain after accounting for all optical losses and high-frequency AOM inefficiencies. In our experimental configuration, shown in Fig. 4.1, there would be two significant issues: first, due to the overall optical efficiency of approximately 25% (mainly due to losses from double-passed AOMs operating at a diffraction efficiency of 50%), we would require a total laser power of at least 25 W. This is significantly more power than the 15 W output of the highest gain laser amplifier currently offered at 1083 nm. Second, with such high laser power there is an increased risk of thermal lensing and damage to coatings and especially the AOMs. If a 12 W laser beam is focused to a gaussian waist with $2\omega_0 = 0.8 \text{ mm}$, as is recommended by AOM manufacturer IntraAction, the peak irradiance in the double-passed AOM will be nearly 100 W/mm^2 . This is twice the optical damage threshold of the TeO₂ AOM acoustic medium [68].

Utilizing a two-stage slower with $\delta' = \delta/2$ reduces the total power requirement by a factor of $2(\delta'/\delta)^2$ to about 12.5 W. This can be further reduced by making the beam waists smaller as necessary.

3.5.2 Phase

A second concern is that as δ increases, the spatial beat note length decreases as $1/\delta$, eventually becoming comparable to the slowing distance. At that point the correct phase relation between the counter-propagating BCF lasers cannot be maintained nor considered constant over the length of the slower. The BCF is

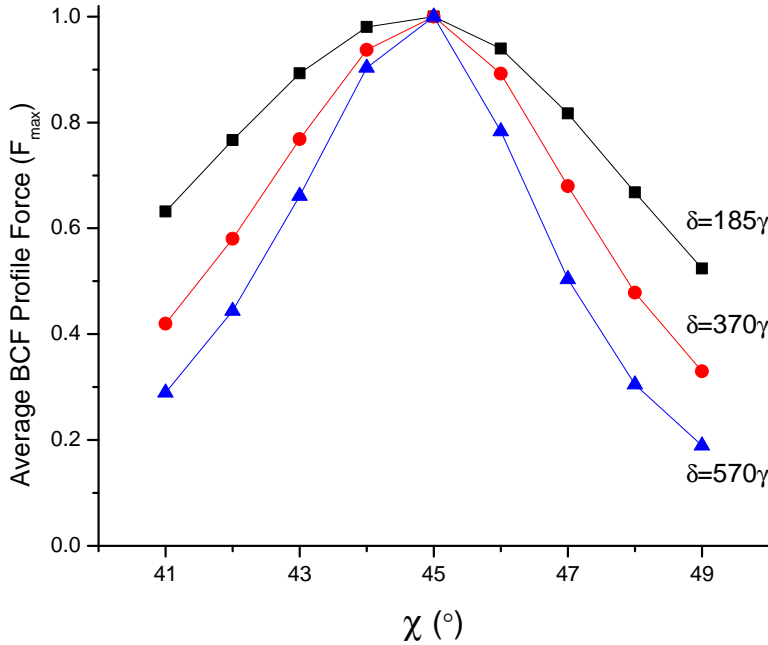


Fig. 3.8: Dependence of the BCF magnitude on phase difference (in $E(z, t)$) from the optimum $\chi = \pi/4$ for detunings of 185γ , 370γ , and 570γ for $\Omega_r = \sqrt{3/2} \delta$. Results are based on numerical solutions to the OBEs as described in Section 2.3. Note the increased sensitivity to phase with increasing detuning.

very sensitive to the relative phase between the slowing beams, and the sensitivity increases with the detuning, as shown in Fig. 3.8. The phase error over one BCF slowing time is velocity dependent, and is compared between detunings in the figure by assuming that the high velocity edge of the force is at 1000 m/s.

At $\delta \approx 570\gamma$ the beat note changes by π in 8 cm, just over twice the 4 cm length of the slowers used in Refs. [35, 36] and this work. In fact, at a detuning of 570γ , the phase changes by over 6° during the BCF characteristic slowing time introduced in Eq. (2.5.4), as shown in Table 3.1. This means that the effective BCF magnitude over one slowing time is reduced by the factors shown in Fig. 3.9 for three values of the detuning.

Achieving the maximum velocity range of $\pm\delta/2k$ in a single-stage slower

δ (γ)	beat note λ (mm)	$\Delta\chi$ over ΔT_{BCF} ($^{\circ}$)	$\pm\Delta\chi$ over 4 cm slower ($^{\circ}$)
185	500	3.5	14.4
370	250	5.6	28.8
570	162	6.4	44.4

Table 3.1: Calculated phase shifts during BCF slowing at high detunings. Slowing has been observed at $\delta = 185\gamma$, BCF slowing was attempted and failed at $\delta = 370\gamma$, and $\delta = 570\gamma$ is necessary if a single stage slower is to achieve velocities in the MOT loading range. Note that the BCF magnitude is reduced by 50% for a phase change of $\pm 5^{\circ}$ from optimum.

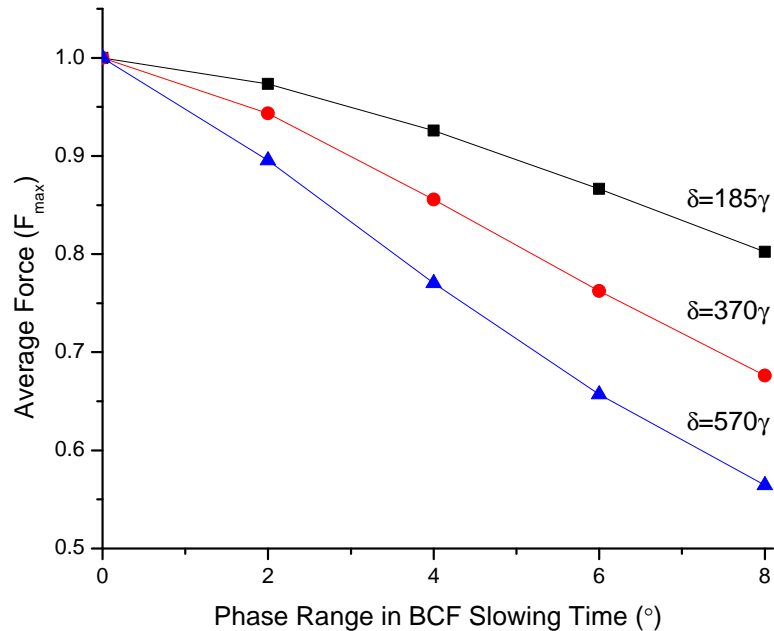


Fig. 3.9: Calculated average BCF magnitude (normalized to optimum conditions) as a function of total phase change over one BCF slowing time, as described in Section 2.5.4. Using information from Table 3.1, the average force experienced by the atoms drops sharply with increasing phase change, and the relative change in force magnitude increases for larger detunings.

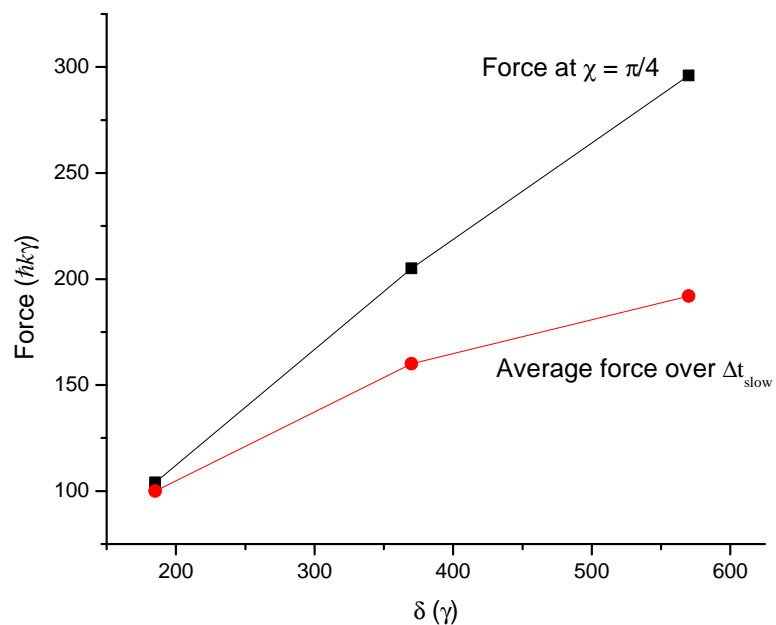


Fig. 3.10: Average force applied to an atom during one BCF slowing time taking into account the phase change, assuming an initial atom velocity of 1000 m/s, compared to the force for fixed $\chi = \pi/4$. Note the leveling off of the force magnitude at high detunings, which sets a limit on the maximum slowing.

with a detuning of $\delta = 570\gamma$ is physically impossible—the atom never experiences a strong enough force for a long enough time to be fully slowed. Analyzing numerically calculated force profiles over a range of intensities and phases, the largest slowing possible for metastable helium is the equivalent of $\delta \approx 380\gamma$, but requiring a Rabi frequency of $\Omega_r \approx \sqrt{3/2} 590\gamma$, as can be seen in part from the trend of the average force in Fig. 3.10. This requires two stages with extremely high irradiance as discussed in Section 3.5.1. Extending the length of the slower above about 2 cm makes almost no difference since the force at either end of the slower is negligible. This makes the realization of a static single stage slower of metastable helium rather unrealistic, and a static multi-stage slower very difficult.

However, even in the highest detuning of $\delta = 570\gamma$ the sign of the force is the same over the entire slowing distance, so based on this consideration alone there should still be evidence of slowing for this detuning or any lower value. These problems cannot fully explain the lack of slowing observed by Partlow and Cashen at $\delta = 368\gamma$ [35, 36], or the evidence of a sign change in the force at $\delta = 278\gamma$ discussed in Chapter 5.

Chapter 4

Large-Detuning BCF: Experiment

4.1 Large Detuning BCF Overview

A block diagram of our experiment to investigate the upper velocity range limit of the bichromatic force in order to develop a useful He* slower is shown in Fig. 4.1. Ideally, a slower could be developed with a single pair of counter-propagating beams producing a BCF profile with a velocity range large enough to slow atoms from the peak of the velocity distribution to MOT capture velocities. However, because of the high irradiances required for such a large velocity range, breaking up the required velocity range into two or more sub-ranges may be more feasible. The two-stage slower uses two consecutive BCF profiles to obtain the same total slowing as a single-stage slower. The first profile is Doppler shifted so that the leading edge is located in an appropriate portion of the slow tail of the atom velocity profile. The second profile has a smaller Doppler shift so that its leading edge just overlaps the trailing edge of the first profile. The atoms will be sequentially slowed by the first, then the second profile, experiencing a total velocity change equal to approximately twice one of the two profiles.

In these experiments, a portion of the laser output is split off and sent to a saturated absorption spectrometer to lock the laser to the $2^3S_1 \rightarrow 2^3P_2$ transition of helium at 1083 nm. The rest of the laser output goes through a double-passed

acousto-optic modulator (AOM) such that the output contains the bichromatic detunings $\omega_a \pm \delta$ and is coupled into a fiber laser amplifier. The amplified output is then split, and double-passed AOMs are used to frequency shift one beam pair by $+kv_c$ and the other by $-kv_c$ for Doppler compensation, as discussed in Section 2.4. The two beam pairs are now respectively the co- and counterpropagating pulse trains required for bichromatic deceleration. The beams are steered over to the metastable helium beam chamber where quarter-wave retarders are used to change the light polarizations to σ^+ (or σ^-) before the beams are overlapped with each other and the atom beam. Each major step in the process will be discussed in more detail in the following sections.

4.2 Metastable Helium Source

The bichromatic force discussed in Chapter 2 is described in terms of a two-level atom: an idealized atom with only two energy levels, ground and excited. Fortunately the metastable 2^3S state of helium (He^*) can provide an effective two-level system. The state is metastable because decay to the ground state via an electric dipole transition is prohibited by both spin and parity selection rules. Because of this, the metastable state of helium has a lifetime of approximately 8000 seconds [9], providing ample time for slowing and time-of-flight measurement, or trapping and cooling. Energy levels relevant to these experiments are shown in Fig. 4.2 and a summary of relevant physical properties is shown in Table 4.1.

The metastable state is 19.92 eV above the ground state, making laser excitation exceedingly difficult, requiring a single photon at 62.5 nm [60]. A much simpler and more efficient means is through electron collisions, the method employed in our metastable helium source.

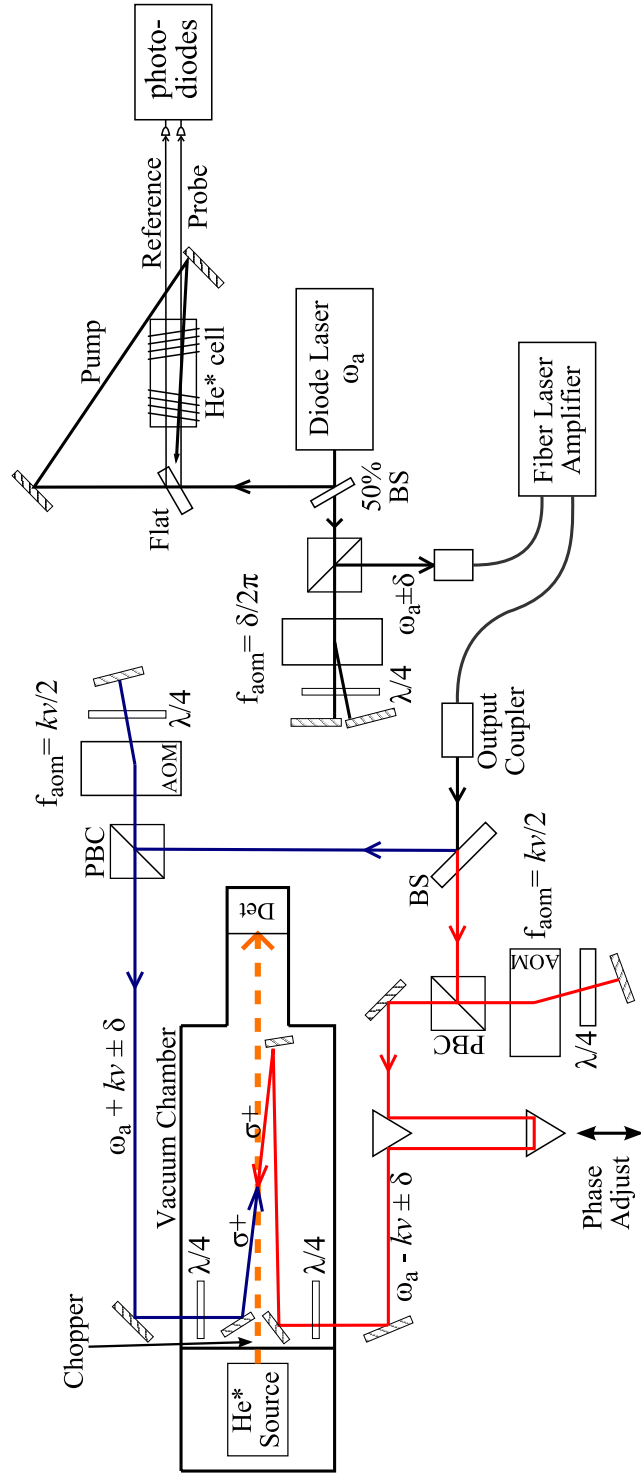


Fig. 4.1: Somewhat simplified experimental layout for the large-detuning BCF decelerator.

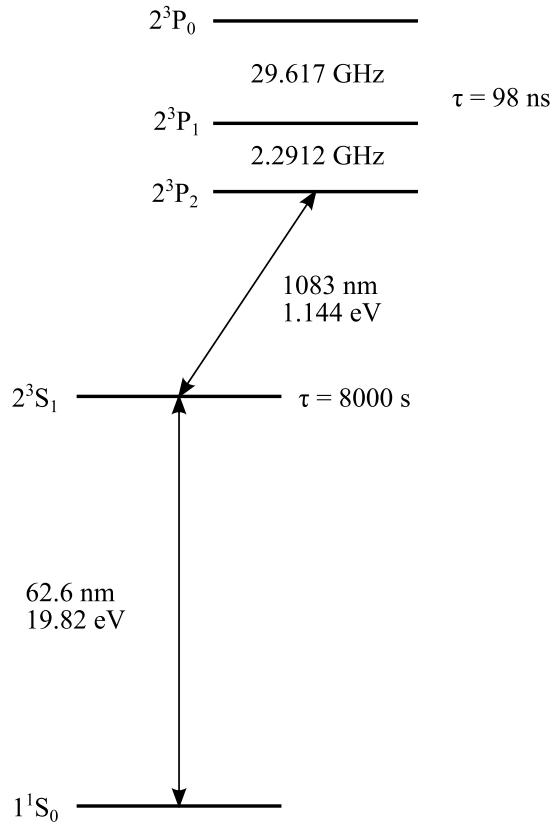


Fig. 4.2: Energy level diagram for helium showing the transitions of interest to these experiments. Note that the level spacings are not drawn to scale.

λ (nm)	$\hbar\omega_a$ (eV)	τ (ns)	$\gamma/2\pi$ (MHz)	I_s (mW/cm ²)	$\omega_r/2\pi$ (kHz)
1083.33	1.114	98.04	1.62	0.17	42.46

Table 4.1: Values for various properties of the $2^3S_1 \rightarrow 2^3P_2$ transition in helium used in these experiments, taken from [9].

4.2.1 Design and Construction

The metastable helium source is a near-copy of the source used by the Metcalf group at Stony Brook University for their own bichromatic force work [35, 36]. It is based on a design by Kawanaka and co-workers [69] as modified by Mastwijk et al. [70]. The source is a reverse pumped DC discharge design, providing a continuous and stable metastable helium beam with a mean velocity of about 1050 m/s.

The source is based around a 1 cm diameter quartz tube housing a tungsten discharge needle as shown in Fig. 4.3. The tube sits inside a stainless steel jacket that is filled with liquid nitrogen to pre-cool the helium atoms, providing a somewhat supersonic metastable helium beam at near 77 K. Cooling reduces the most probable atom velocity from approximately 3000 m/s at room temperature to the measured 1000 – 1100 m/s, depending on operating parameters. Ultra-high purity helium gas flows into the rear of the source through the narrow volume between the cooling jacket and the outside of the quartz tube, where it is cooled as it flows toward the front. At the front of the source, where the exit nozzle and tungsten needle are located, most of the helium is pumped out through the center of the quartz tube. The remaining gas supports a glow discharge between the negatively biased tungsten needle cathode and the grounded exit nozzle anode, where a small fraction of the helium atoms are excited to the metastable state through electron impact [71].

Modifications to the Stony Brook design were made primarily to adapt the source to an existing large vacuum chamber that was available for the experiments. The “beam machine” is a large, open, flexible vacuum platform designed specifically for atomic beam experiments, especially spectroscopy. The chamber

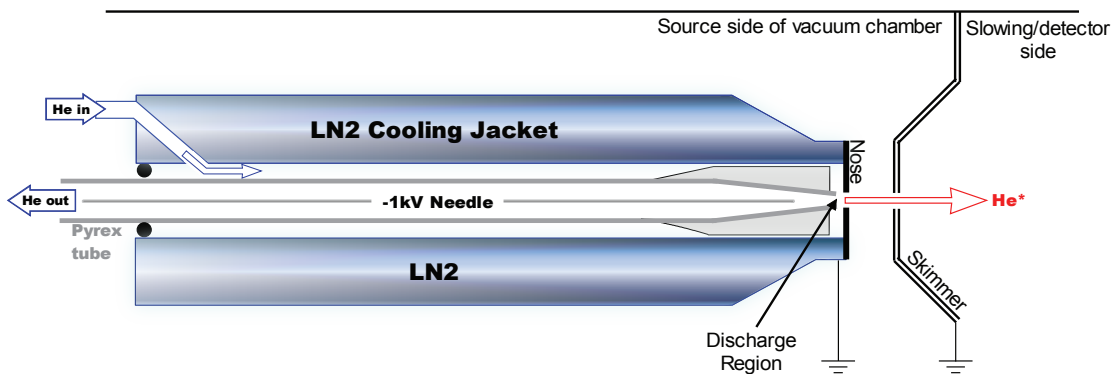


Fig. 4.3: Metastable helium source. Source operation is described in the text



Fig. 4.4: Metastable helium source detail showing nozzle end of Pyrex tube with cathode needle installed. The nominal spacing is 15 mm from the needle tip to the front end of the Pyrex tube. The teflon needle centering spacer is also shown surrounding the polished aluminum needle holder. Notice the Pyrex insulator tube beginning at the rear of the centering spacer that runs the rest of the electrode length to suppress unwanted glow discharges in the rear of the source.

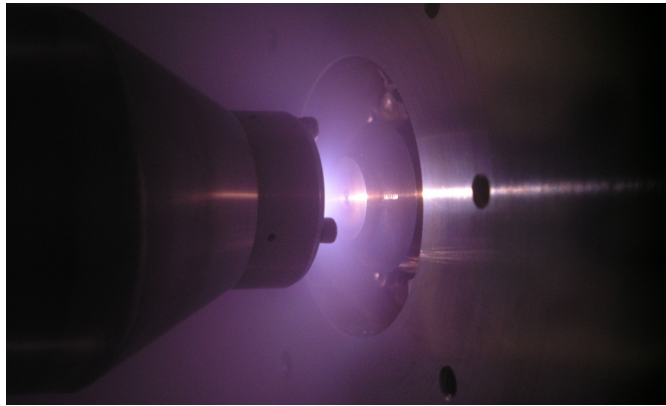


Fig. 4.5: Metastable helium source discharge. Source nozzle at left, skimmer at right. Along with metastable helium atoms and visible light, the source produces a significant amount of ultraviolet light.

itself measures 94 cm by 45 cm by 32 cm and is divided into two differentially pumped sections by a movable partition with provisions for mounting a skimmer or other beam defining aperture, as shown in Fig. 4.6.

The “source” side is pumped by a Varian VHS10 ten inch diffusion pump. This large diffusion pump provides ample throughput to handle the excessive gas loads an atomic beam source generates. This pump is backed by a Welch DuoSeal 1397 mechanical vane pump, which also serves as the roughing pump for both sides. The “detector” side is pumped by a Pfeiffer TPH180H 180 l/s turbomolecular/molecular drag vacuum pump backed by a separate Welch DuoSeal rotary vane pump.

To adapt the source design to fit the beam machine, several external modifications were required, visible in Fig. 4.7. Most significantly, the mating/tilt flange in the original design was replaced with a clamping assembly mounted to a three-axis translation stage, accessed via three rotary vacuum feedthroughs. The integrated LN_2 reservoir was replaced by an external glass dewar and smaller, flexible fill and vent lines. Other modifications provided the ability to route liquid

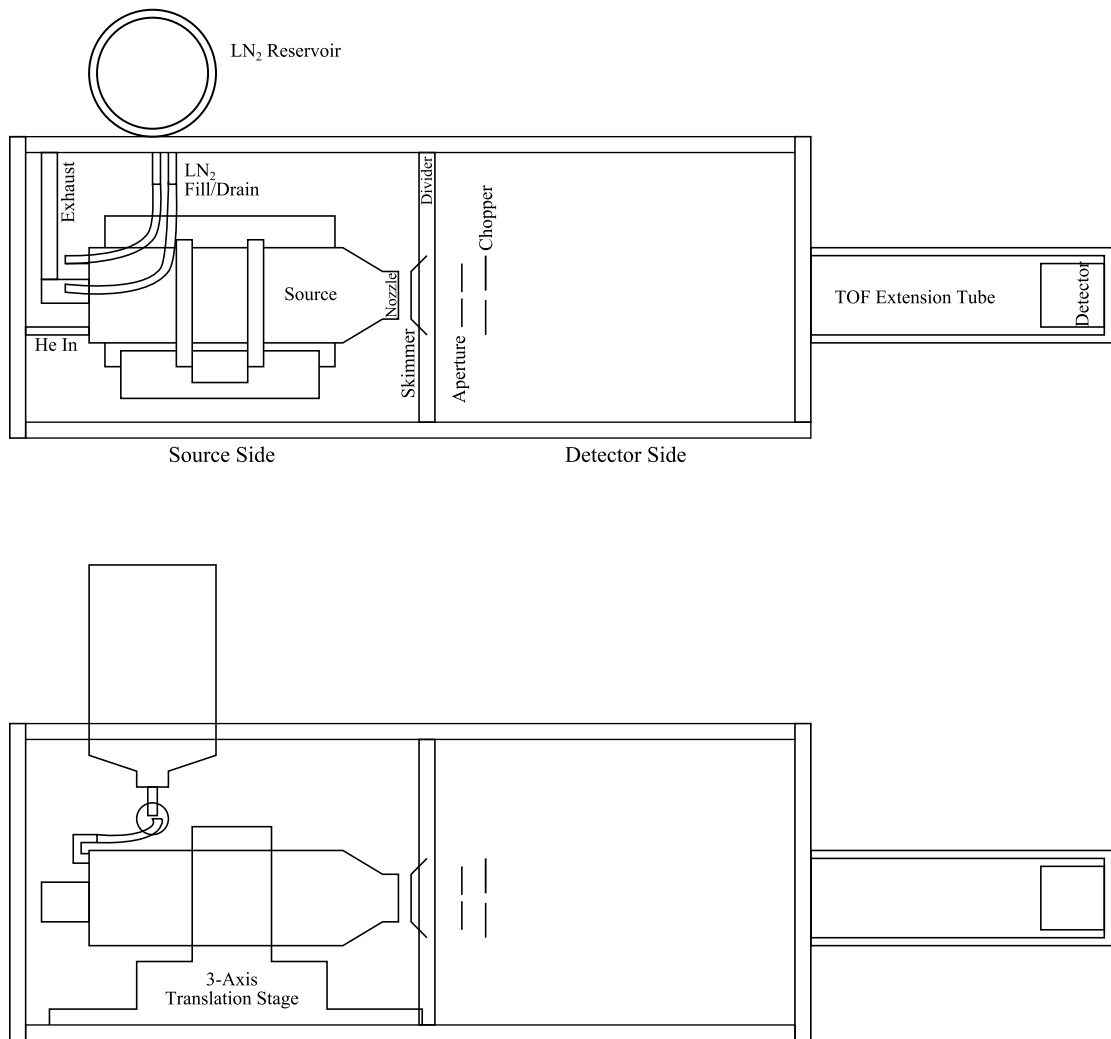


Fig. 4.6: Beam Machine layout top (upper) and side (lower) views showing source location and related connections.

nitrogen fill and drain lines, the helium input line, and exhaust pumping port, all accomplished using stainless steel bellows tubing, permitting the source to be aligned to the skimmer.

One consequence of the redesign of the rear of the source was that unwanted glow discharges would regularly ignite in the exhaust portion of the source surrounding the needle electrode. Our solution was to completely insulate the needle electrode from the needle centering spacer to the rear of the source where the electrode passes through a Teflon insulator bushing. This was done using Pyrex capillary tubes that are just large enough to fit around the tungsten electrode as shown in Fig. 4.4. The capillary tube sits flush against the needle centering spacer at the front, and fits snugly into a recess in the insulating Teflon bushing at the rear of the source.

The helium gas inlet pressure is controlled with a variable leak valve and monitored with an analog absolute pressure gauge. The source exhaust is pumped by a separate Welch DuoSeal 1402 rotary vane mechanical vacuum pump. The source exhaust has a vacuum shut-off valve so that the source and associated vacuum can be maintained when the source is not in use, while the exhaust vacuum pump is off and vented to atmosphere. The exhaust valve is also used to throttle the exhaust vacuum conductance to moderate the source exhaust pressure.

High voltage for the discharge is supplied by a Kepko BHK-2000-0.1M high voltage power supply, operated in constant voltage mode. The power supply is connected to the source discharge needle through a $25\text{ k}\Omega$ ballast resistor and its voltage and current were monitored through a digital ammeter and voltmeter (Digital Panel Meter PM1285).

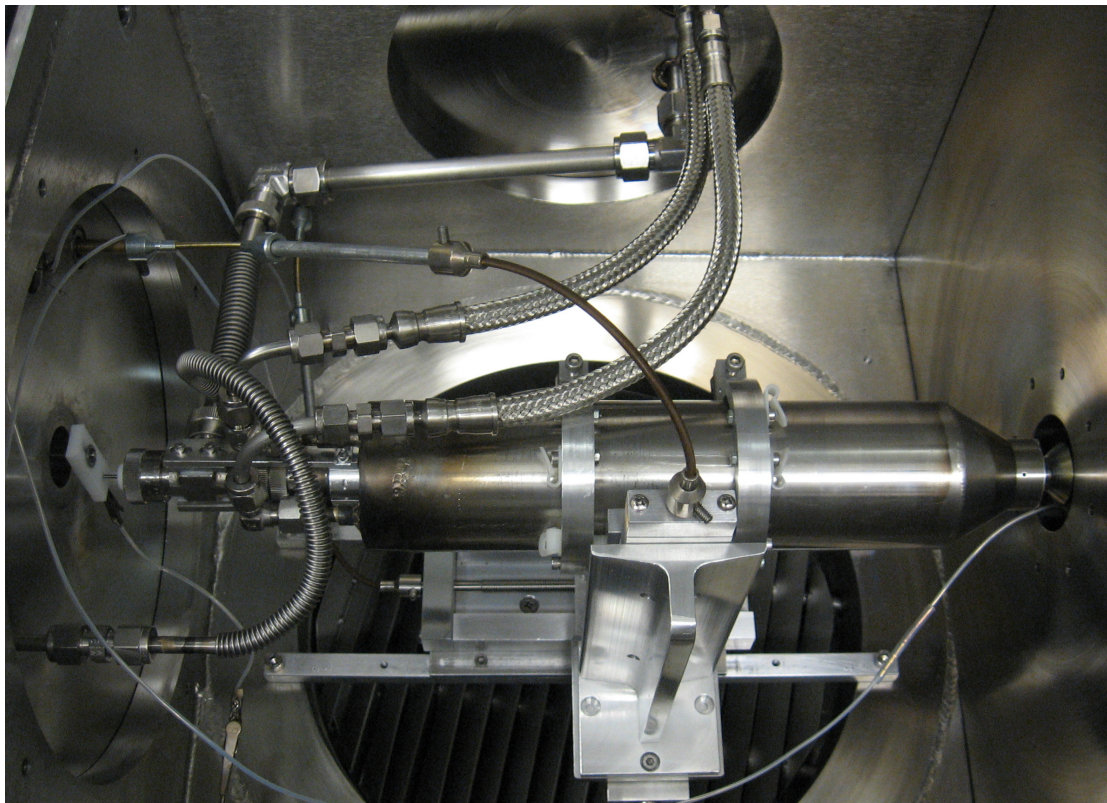


Fig. 4.7: UConn first-generation metastable helium source installed in the vacuum chamber showing source nozzle and skimmer (at right), helium inlet (lower left), liquid nitrogen fill and drain lines (braided stainless steel), and source exhaust bellows. Louvers for the water-cooled oil trap above the diffusion pump are visible below the source.

4.2.2 Operation and Characterization

The discharge can be maintained at currents of between 1 and 10 mA depending on the needle potential, input and exhaust helium pressures. Typical operating parameters for a reasonable balance between brightness and mean velocity include a tungsten needle voltage between -900 and -1100 V, helium inlet pressure between 6 and 6.5 Torr, and source exhaust pressure between 1.8 and 2.0 Torr. These parameters yield a stable discharge current of around 6 mA and a most-probable atom velocity of ~ 1050 m/s. Several factors determine the exact operating parameters required. The most critical seem to be the age of the cathode and any contamination of the inside of the source.

The source has a relatively narrow operating “sweet spot” and is very sensitive to contamination, both of the helium gas and of the source itself. Therefore it is best to maintain a slow flow of dry nitrogen gas through the source whenever the vacuum chamber is vented. Additionally, evacuating the helium supply lines before starting the source, and providing a slow flow of helium while the source is cooling will also help the source stability. Perhaps the most critical aspect of the source construction is the tungsten needle cathode. The cleanliness of the needle and the 20° grinding angle of the tip are critical considerations. The source is not particularly sensitive to the spacing between the tungsten needle and the anode, however a temporary reduction of the spacing can aid in initiating the discharge.

The source brightness is measured by moving a stainless steel plate into the beam path and measuring the current in the beam with a Keithly PicoAmmeter using the method discussed in Refs. [35, 36]. A tungsten grid was located 1 cm in front of the plate held at a potential of 300V. Secondary electrons ejected from metastable helium atoms impacting the stainless steel plate are accelerated toward

the grid, and a positive current is measured with the picoammeter.

By scanning a knife edge across the atom beam at the center of the interaction region with a $100 \mu\text{m}$ beam defining aperture in place, the diameter between the 25% and 75% current levels was measured to be $450 \mu\text{m}$, corresponding to a top-hat radius of 0.472 mm. I calculated the atomic beam half-angle based on this diameter and the distance from the aperture, assuming an effective point source. The result is 3.1 mrad, giving the beam a solid angle of $3.0 \times 10^{-5} \text{ Sr}$.

Taking into account the transparency of the grid and the 80% quantum efficiency of secondary electron emission for He* impinging on stainless steel [72], the source brightness was calculated to be $3 \times 10^{13} \text{ atoms/Sr}\cdot\text{s}$.

Note that in the interim the beam defining aperture has been changed from $100 \mu\text{m}$ diameter to $70 \mu\text{m}$ diameter, reducing the atom beam half angle to 2.2 mrad and the subtended solid angle to $1.5 \times 10^{-5} \text{ Sr}$.

4.3 Time of Flight Velocity Profiling

Metastable helium atoms created by the source pass through the $500 \mu\text{m}$ diameter skimmer aperture from the source side of the vacuum chamber into the detector side. Once on the detector side, the atoms pass through the $70 \mu\text{m}$ diameter collimating aperture. To perform time-of-flight measurements on the metastable helium atoms the cw atom beam must be chopped into pulses. This is done with a mechanical tuning fork chopper (EOPC model CH-10 Optical Modulator). The chopper is designed to operate at a resonant frequency of 160 Hz and is driven by an EOPC Automatic Gain Control Driver board, model AGC-PC. The optical chopper has only one vane with a $500 \mu\text{m}$ wide slit (the other arm is appropriately weighted to maintain the desired resonant frequency). The

slit is further masked to a width of approximately $100 \mu\text{m}$ and is placed in the atom beam path. Because the chopper slit passes across the beam twice per cycle, the atom beam is effectively pulsed at 320 Hz. This was chosen to provide a fast pulse repetition rate to expedite data collection while still avoiding any overlap of the slowest atoms with the next pulse. The AGC-PC also provides a TTL trigger synchronized with the chopper which is used to trigger the data acquisition tasks.

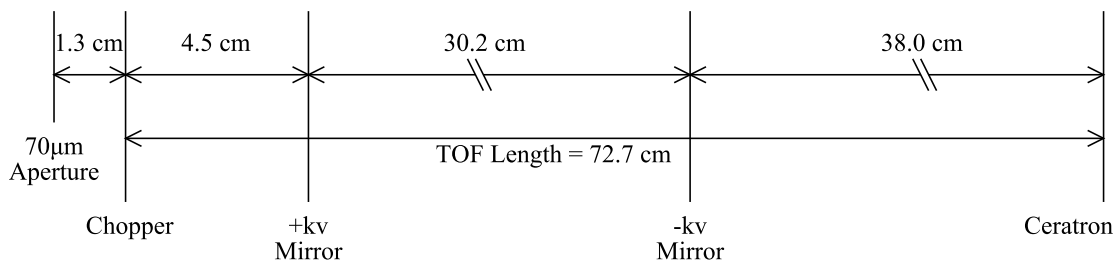


Fig. 4.8: Critical distances in the bichromatic slower time of flight. The $\pm kv$ mirror positions represent the final turning mirrors before the slower beams cross the metastable helium beam, nominally at the center of the mirror separation. The relatively large mirror separation facilitates a small crossing angle between the slowing lasers and the atom beam, providing the longest overlap possible.

A typical TOF spectrum is shown in Fig. 4.9. There are two distinct elements to the spectrum. In time-order, the first narrow, sharp peak is a result of ultraviolet photons emitted from the metastable helium source (see Fig. 4.5). Due to the near-instantaneous arrival at the detector of the photons compared to the atoms, this peak serves as a repeatable measure of the absolute zero of time for the TOF. The second broader peak is the TOF spectrum of the metastable helium atoms. The resolution of the TOF system is calculated to be 68 m/s defined as the separation of the closest two velocity groups that overlap at 50% of their peak height.

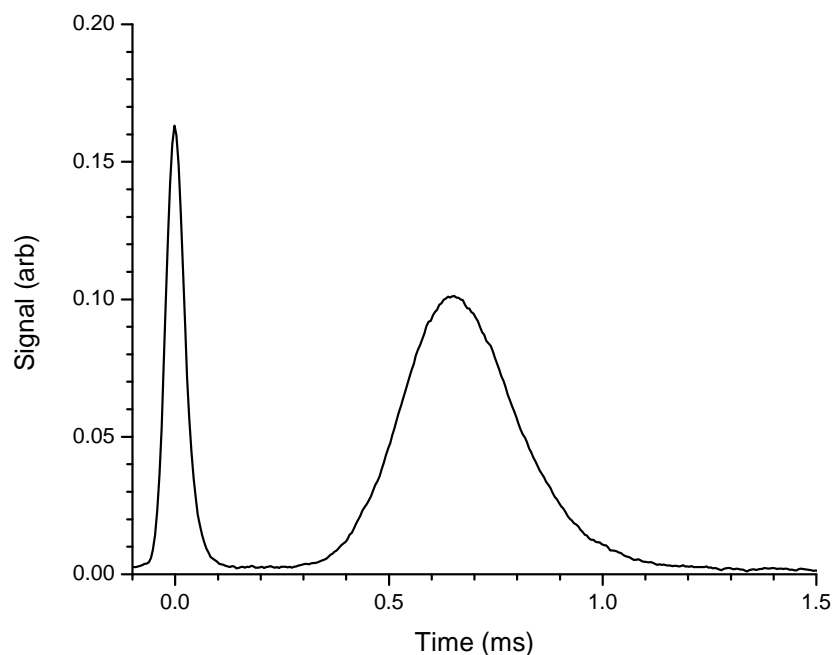


Fig. 4.9: Time of flight spectra for metastable helium. The sharp peak at $t \approx 0.0$ ms is the uv light peak and the broader peak is from the metastable helium atoms. Note that the zero of the timebase has been shifted to coincide with the center of the uv peak.

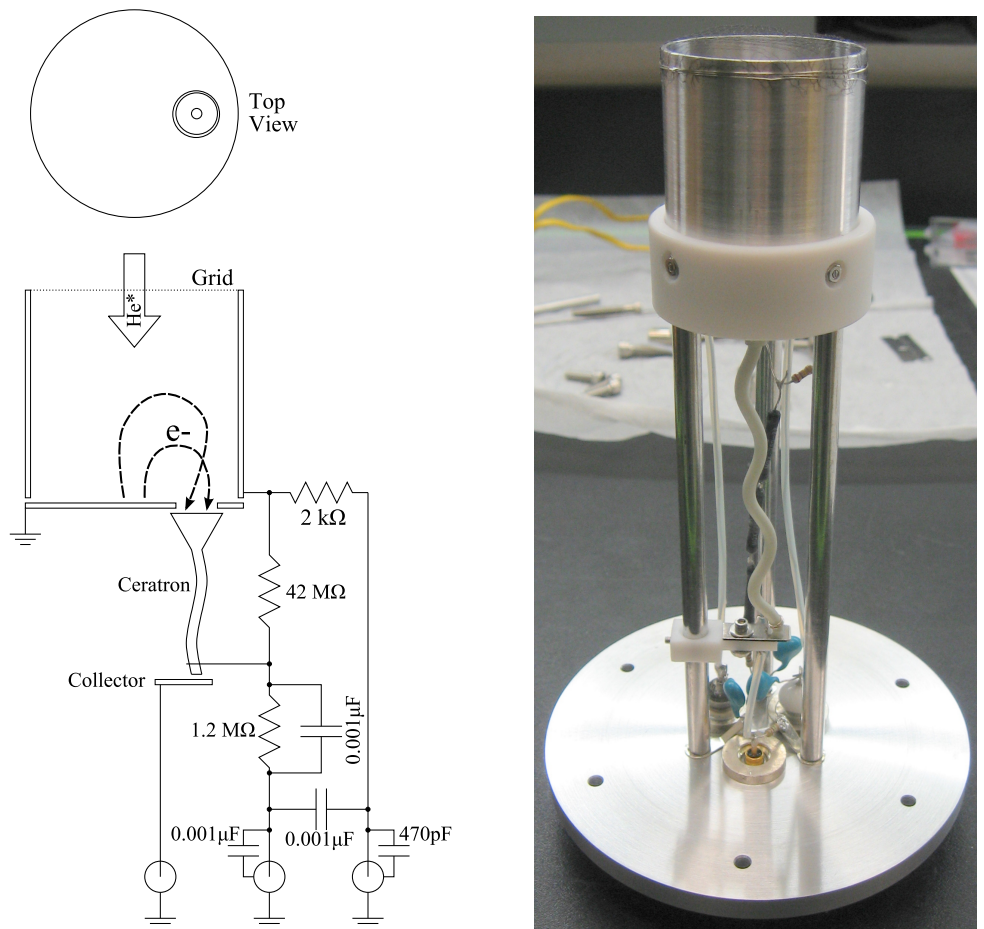
4.4 Metastable Helium Detection

4.4.1 Detector and Ceratron Electron Multiplier

The atoms travel from the chopper to the atom detector at a distance of 72.7 cm as shown in Fig. 4.8. Detection of the metastable helium atoms is accomplished with a stainless steel Faraday cup and MuRata Ceratron-E (Model EMW-1081B) electron multiplier, shown in Figures 4.10a and 4.10b. The design was optimized using Simion v7.0 charged particle simulation software. The impact of a metastable helium atom with the stainless steel plate results in the emission of a secondary electron from the surface with an efficiency of greater than 80% [72]. The negative relative bias of the grid and positive bias of the Ceratron collector horn guide the electrons toward the Ceratron horn. Once inside the Ceratron, the electrons are accelerated from the horn to the exit by the potential gradient and are multiplied at each impact with the Ceratron wall. The detector was operated at -3100 V provided by a Bertran Model 305 power supply.

4.4.2 Transimpedance Amplifier

The Ceratron output current is amplified using a high gain, low noise transimpedance amplifier based on the ADL 8606 chip shown in Fig. 4.11. Great care was taken in the design and construction to eliminate the potential for ground loops and noise, especially oscillations in the second op-amp. The amplifier gain is about 1.1×10^7 V/A for the frequency range of interest (DC to about 50kHz) and the 3 dB point slightly more than 200 KHz based on the measurements shown in Fig. 4.12. Given the typical detector output with the Ceratron-E operating at a -3100 V bias, the amplifier output levels are in the tens of millivolt range.



(a) Top view (upper) and side view with bias electronics (lower). Representative secondary electron paths were originally calculated using a 3D model in Simion v7.0.

(b) Photograph showing detector, mounting flange, and hardware.

Fig. 4.10: Metastable helium detector with modified Faraday cup.

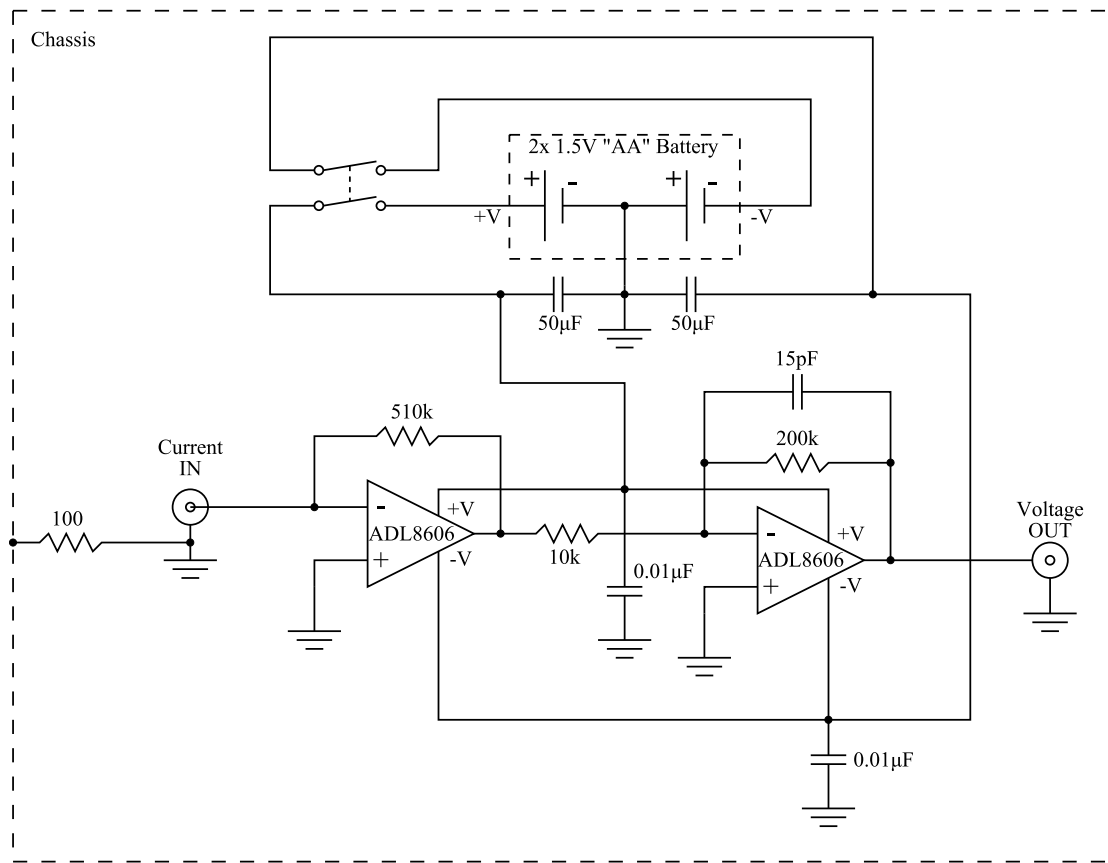


Fig. 4.11: Transimpedance amplifier circuit for the metastable helium TOF signal.

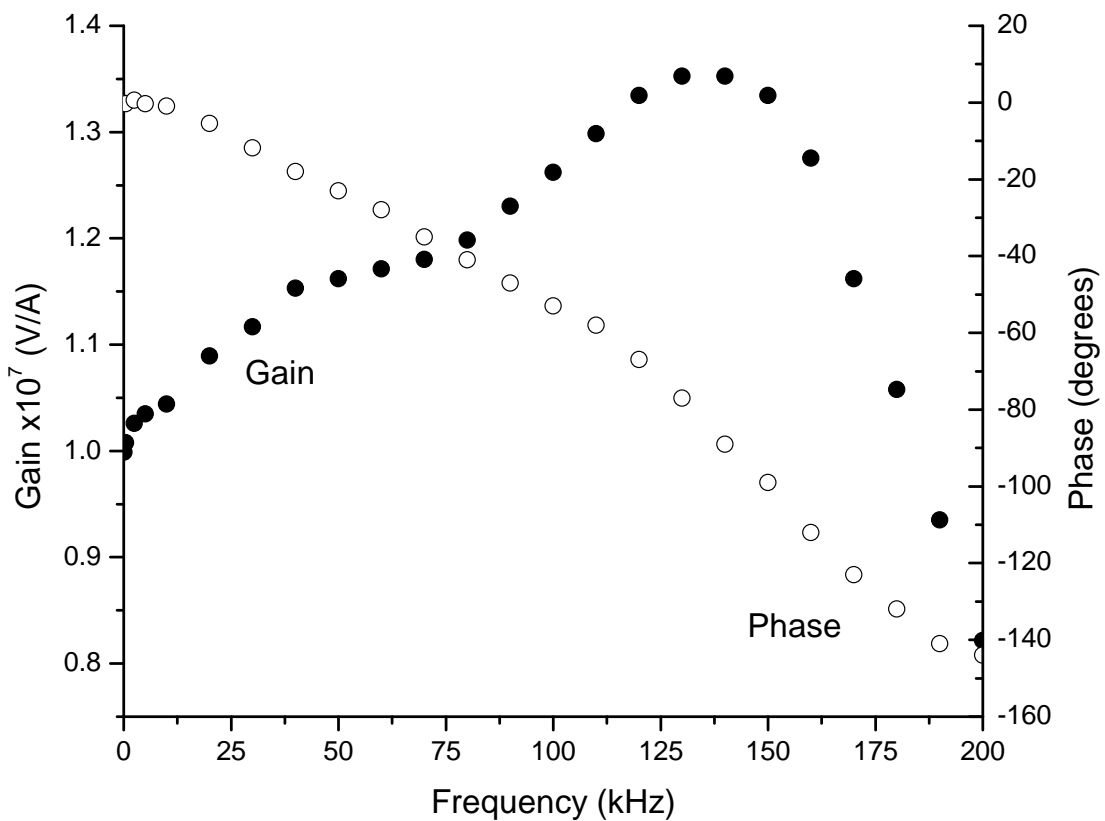


Fig. 4.12: Gain and phase delay measurements for the transimpedance amplifier. All measurements were made using a 22 nA peak-to-peak sine wave input and recorded with a Tektronix TDS 3036 oscilloscope.

4.5 Diode Laser and Frequency Stabilization

4.5.1 Diode Laser

The seed laser used in this experiment is a commercial TuiOptics (now called Toptica) DL100 external cavity diode laser in a Littrow configuration [73]. The laser is fitted with a nominally 1080 nm high power 300 mW laser diode (P/N LD-1080-0300-1) capable of producing up to 150 mW post-cavity, tuned to the $2^3S_1 \rightarrow 2^3P_2$ transition at 1083.3 nm. The laser diode is operated with the standard Toptica electronics package including a DTC100 30 W Temperature Control, a DCC100 500 mA Current Control, and a SC100 Scan Control for the grating piezo element. The laser beam shape and divergence are corrected to provide a suitably round beam using a short focal length cylindrical telescope. The laser beam then passes through an optical isolator (OFR IO-3-1064-HP) to protect the laser diode from unwanted optical feedback and retroreflections.

4.5.2 Saturated Absorption Spectroscopy

A 50% non-polarizing beam splitter is used to pick off half the output power, which is split again and sent both to a scanning fabry-perot cavity to monitor the laser mode, and to a metastable helium saturated absorption spectroscopy (SAS) cell for frequency stabilization. Helium in the SAS cell is excited to the metastable state by an rf discharge as described by Koelemeij and co-workers [74] with modifications inspired by Lu et. al. [75]. The cell consists of a 2.5 cm diameter Pyrex cross to which a pair of quartz windows are fixed, providing optical access for the laser beams. One of the remaining sides of the cross (on the bottom) goes through a 90 degree bend and is attached to a short bellows section then to a UHV vacuum valve. The valve is used to seal off the cell once it is baked and filled

with helium, and the bellows serves to relieve any strain on the glass cell from the mounting or the valve. The top side of the cross is welded to a 1 liter glass sphere which serves as a ballast volume to reduce the concentration of impurities that accumulate during use of the cell, thereby extending the time between refills [75]. The optical access arms are each wrapped with 15 turns of magnet wire that provides the rf coupling into the gas sample. For SAS at 1083 nm, the optimal conditions of the cell are an internal helium partial pressure of 70 to 90 mTorr and an rf drive power of about 200 mW at 50 to 60 MHz, provided by a Hewlett Packard 3200B VHF Oscillator.

The rest of the SAS cell vacuum system consists of a Conveptron gauge and readout unit (Granville Phillips Model 275) to monitor pressure during the refill, and a variable leak valve attached to a small lecture bottle of ultra-high purity helium gas which facilitates refilling the SAS cell to the proper pressure. Pumping is accomplished with a Pfeiffer TCP300 turbomolecular pumping station. Currently, the cell must be refilled about every two weeks.

A schematic of the laser locking feedback loop is shown in Fig. 4.13. An SRS SR530 Lock-In Amplifier is used to supply a 10 kHz sine wave dither to the laser diode frequency via the modulation input on the front panel of the DCC100. The amplitude of the dither is 1 V peak to peak, and is attenuated to about 20 mV pk-pk before being coupled into the DCC100 providing a frequency dither of about 8 MHz. This is enough to provide an adequate error signal but minimizes the total laser frequency oscillation.

The intensities of the probe and reference beams are detected by a pair of InGaAs photodiodes (Edmund Optics P/N NT55-753). The subtraction circuit is closely based on the shot noise limited “noise canceler circuit” described by

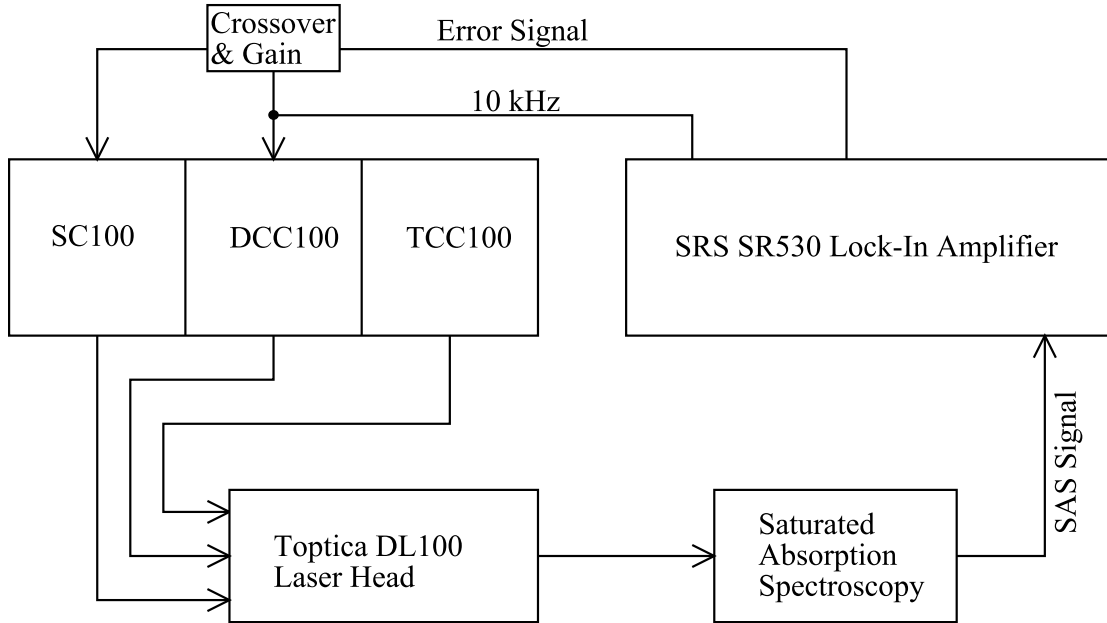


Fig. 4.13: Schematic of diode laser frequency control using saturated absorption spectroscopy. The 10 kHz dither scans the laser across the Doppler-free absorption peak causing a modulation in the SAS output signal. The lock-in amplifier is used to derive an error signal from the SAS modulation, which is used as feedback to the laser control electronics to stabilize the laser frequency.

Hobbs [76] with modifications only to accommodate the feedback loop gain and time constant.

4.6 Bichromatic Frequency Production

The BCF requires bichromatic light—two frequencies superimposed in one laser beam. To achieve this, we use an acousto-optic modulator (AOM) to generate the second optical frequency from our frequency stabilized laser. An AOM consists of a crystal, Tellurium Dioxide (TeO_2) in this case, with a piezoelectric transducer bonded to one end. When the transducer is driven with radio frequency energy (up to 1.5 W for these AOMs), a traveling acoustic wave is generated in the crystal resulting in a periodic modulation of the refractive index. This sound wave acts

like a sinusoidal grating and the laser, if entering at an angle matching both the Bragg condition and the specular reflection condition, will be diffracted efficiently. The first-order diffracted beam is either up- or down-shifted in frequency by the rf drive frequency and exits the AOM at an angle to the zero-order (undiffracted) beam approximately equal to the Bragg angle [68].

To produce the bichromatic light used in this first round of experiments as shown in Fig. 4.1, I used the configuration shown in detail in Fig. 4.14. IntraAction 375 MHz AOMs (P/N ATM-375-1A2) with a frequency tuning range of 280 MHz to 468 MHz were used, covering the bichromatic detunings of interest. At the rf frequencies that were used in these experiments, diffraction efficiencies, defined as the ratio of the first-order diffracted beam power to the total incoming beam power, could reach a safe maximum of about 50% with 1 W rf drive power. Care must be taken to thermally sink the AOMs, and possibly mount them to a water cooled plate if drive powers above 1 W are to be used, to reduce the risk of the transducer debonding or the fine wires connected to the transducer from melting.

The radio frequency was generated by a miniature single-board frequency synthesizer designed by Dr. Eyler based on his work with microcontroller based instrumentation [77]. The frequency synthesizer uses a phase-locked loop chip (ADF4112) to upscale a reference oscillator operating at 10 MHz based on input from the user via a dsPIC30F3013 microcontroller. A complete circuit layout is included in Appendix D and a complete description is available online [78].

One potential problem with this double-pass technique is that each of the two emerging frequency components will have a different distortion due to the acousto-optic diffraction process [79]. This is further complicated by the loss of area in the zero-order beam from diffraction of light into the first order beam, as

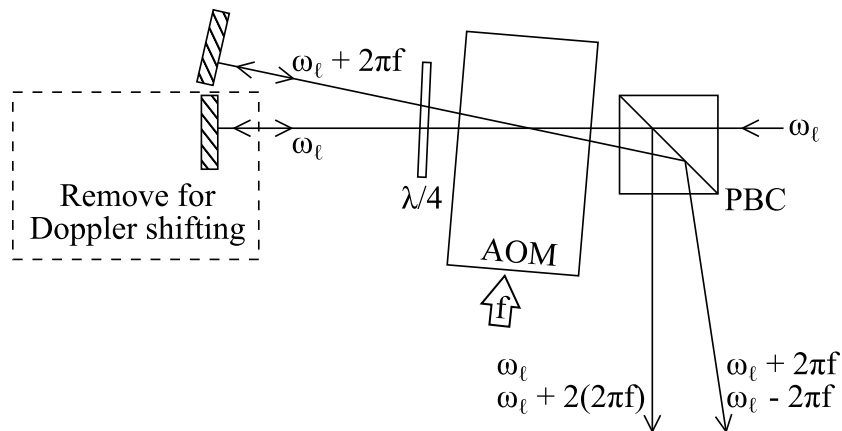


Fig. 4.14: Double-passed AOM used to produce two superimposed frequencies for bichromatic slowing as shown in Fig. 4.1. Linearly polarized laser light on the first pass through the AOM, driven at radio frequency f , produces frequencies ω_ℓ (zero-order) and $\omega_\ell + 2\pi f$ (first-order). The two orders pass through a quarter-wave retarder and are retroreflected back through the AOM, but with linear polarization perpendicular to the incoming light. Each of the first-pass beams are split into zero- and first-order components again, producing four frequencies in two beams: ω_ℓ and $\omega_\ell + 2(2\pi f)$ and $\omega_\ell \pm 2\pi f$. For the bichromatic slowing, the AOM drive frequency was the bichromatic detuning: $f = \delta/2\pi$.

shown in Fig. 4.15. Using the fiber-optic laser amplifier alleviates this problem since the distortions at most will slightly reduce the coupling efficiency into the input optical fiber of each frequency component. The output optical fiber and coupler ensures that the dual-frequency output beam is gaussian. However, without a fiber-coupled output to match the beam spatial modes, it is in general better to tune the AOM slightly away from the optimal Bragg angle. This produces zero and first order beams that have a better matched spatial mode as shown in the uppermost image in Fig. 4.15.

4.7 Optical Amplification

The irradiance of each frequency component increases quadratically with detuning δ in order to satisfy the optimal Rabi frequency, as shown in Eq. (2.5.3). Slowing experiments using a single high power diode laser can only support detunings up to about $\delta = 2\pi \times 100$ MHz. For larger detunings, the laser must be amplified. A Nufern NuAMP (p/n NUA-1064-PB-0010-B0) single frequency, monolithic, polarization maintaining fiber amplifier was used to increase the laser power from tens of milliwatts to power as high as 7 W cw. The amplifier was seeded with the AOM output components $\omega_\ell \pm \delta$ so that each of the two bichromatic frequency components are amplified simultaneously. This amplification provided sufficient optical power for detunings up to $\delta = 2\pi \times 450$ MHz taking into account the losses inherent in our experimental design, primarily in the Doppler shifting of the bichromatic beams discussed in Section 4.8. The output of the fiber amplifier was optically isolated and fiber coupled with an APC/FC connector. A Thorlabs CFC-8X-C collimator was used to collimate the fiber amplifier output.

The amplifier operated with the input heavily saturated so even large dis-

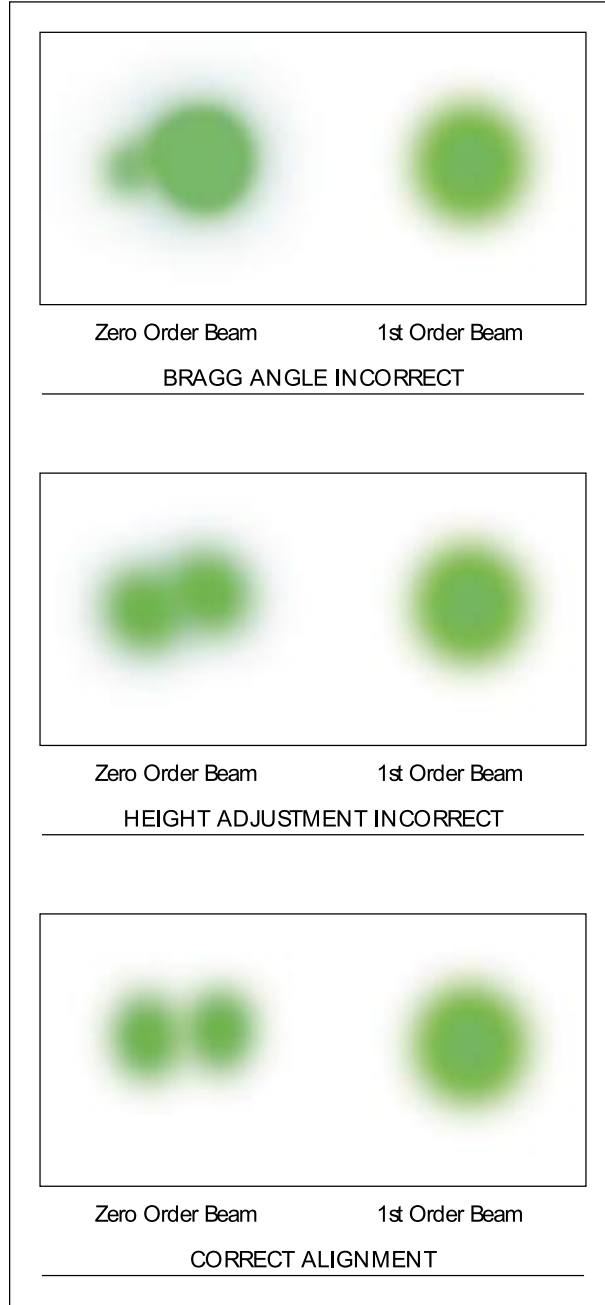


Fig. 4.15: AOM alignment beam patterns showing spatial mode structure of the zero- and first-order beams under different angle tuning conditions. Note that when the AOM is rotated to the Bragg angle, the zero-order beam loses a significant area that is diffracted into the first-order beam. The spatial modes of the two orders are better matched when the AOM is rotated to slightly less than the Bragg angle, as shown in the top image. Images are courtesy of Ref. [80].

crepancies in power between the two frequency components of the seed were balanced at the output. It was verified experimentally that even in the extreme case of a 10:1 ratio in the power between the $\omega_\ell + \delta$ and $\omega_\ell - \delta$ seed components, as long as the weaker component met the minimum seed power requirement for the amplifier of 1 mW, each component constituted exactly half of the output power.

Despite observing all recommendations and warnings, however, the amplifier was very difficult to work with. The first-generation unit we initially received developed severe problems with high internal back reflections, failing to operate reliably above 60% of its rated output. Eventually the unit was upgraded to a second-generation design in March of 2009 and showed marked improvements. However, it exhibited intermittent output dropouts which were resolved by mounting the unit to a cooling plate and recirculating chiller set to 16 C. The unit suffered a catastrophic failure ten months later in January of 2010 after only a few thousand hours of operation. Nufern was generous enough to loan a demonstration unit to us for four weeks to finish the experiment, but that unit failed in a similar manner before the end of the loan period, causing an abrupt end to the experiment.

4.8 Doppler Shifting The Bichromatic Force

As discussed in Section 2.4, the center of the bichromatic force must be shifted to resonance with a select group of moving atoms. This shifting is accomplished using double-passed AOMs, much like the technique used to generate the bichromatic detuning described in Section 4.6. The only difference is that after the first pass through the AOM, only the first-order beam is reflected by removing the first-pass zero-order mirror as shown in Fig. 4.14. This creates two

output beams, each with a single, shifted frequency: $\omega_\ell + 2(2\pi f)$ and $\omega_\ell + 2\pi f$ (or $\omega_\ell - 2(2\pi f)$ and $\omega_\ell - 2\pi f$ if the negative first order is used). In these experiments the $\omega_\ell \mp 2(2\pi f)$ orders are used for the co- and counterpropagating beams respectively. The beams then have a Doppler shift (kv) of twice the AOM rf drive frequency. The same IntraAction ATM-375-1A2 (375MHz center frequency) AOMs are used as for the BCF beam creation, although for this application they are mounted to water cooling plates. The water is cooled to about 16 C using a recirculating chiller.

For these experiments the bichromatic detuning AOM is driven at frequency $f = \delta/2\pi$, the Doppler shifting AOMs are driven at frequency $F = kv/2$, and the laser is tuned to the atomic resonance ($\omega_\ell = \omega_a$). Then the copropagating slowing beam will consist of frequency components $\omega_a + kv \pm \delta$ and the counterpropagating beam will consist of components $\omega_a - kv \pm \delta$, as shown in red and blue (respectively) in Fig. 4.1. In these experiments the Doppler shift AOMs are operated at around 1 W rf at $F = 400$ MHz resulting in a Doppler shift of ± 800 MHz, shifting the center of the force onto resonance with atoms traveling at $v = 2F\lambda = 867$ m/s. This is sufficiently far up the slow end of the atom velocity distribution to provide a reasonable number of atoms to slow while conserving laser power. At higher detunings the AOM diffraction efficiency falls off in inverse proportion to the rf frequency.

4.9 RF Phase Adjustment

As described in Section 2.1 the co- and counterpropagaing slower beams must have the proper phase relation in order to achieve slowing (or acceleration). The optimal condition is that the $+kv$ beam follows the $-kv$ beam by $\pi/2$. Since

there is no way of knowing ahead of time what the phase relation will be at the atomic beam location, a means of adjustment is necessary. This was accomplished with the optical delay line shown in Fig. 4.1. One of the two slower beams (here, the $-kv$ beam) is steered off path by a dielectric mirror. A reflecting corner cube is mounted to a Newport Universal Base (model BUP-2) and aligned to return the laser parallel to the incoming laser path but displaced from it. Another mirror reflects the laser back onto the original path. The Newport base has two steel ball bearings set in to one side that serve as precision alignment points. A precision-ground aluminum rail is aligned to the first leg of the optical delay line to maintain alignment when changing the position of the retro-reflecting prism.

A ruler was taped to the optical table next to the rail so that the position of the base could be repeatably located within 0.5 mm. An additional fine adjustment translator with a total range of 1 cm was also available, but in practice it was not necessary since even at the largest detuning (shortest beat length) $\delta/2\pi = 450$ MHz, a phase shift of 1° corresponds to 1.8 mm. This is within the tolerance range of the bichromatic force measured by [14].

4.10 Interaction Region

4.10.1 Beam Waists

Once the bichromatic slowing beam frequency components have been successfully generated and the optical powers set to the optimal Rabi frequencies, the beams are steered into the beam machine to cross the metastable helium beam. Lenses are used to position the beam waist halfway between the two final steering mirrors (see Fig. 4.1). For these experiments, the beam waist top-hat radii were set to 343 μm for the $+kv$ beam and 390 μm for the $-kv$ beam. The beam waists

were not exactly the same due to limitations caused by lens placement from interfering structures and/or a lack of lens mounting access. The beam waists were measured in the beam machine at the nominal center of the slower by using a knife edge to measure the 25% – 75% diameter. Multiplying by 1.05 converts the measurement to the top-hat radius, assuming a gaussian transverse profile. While this beam waist is substantially smaller than the atom beam at the slower, it is the largest beam waist the available laser amplifier output of 7 W could support while maintaining the optimal Rabi frequency at the largest detuning we studied. The beam waists were kept constant during the range of experiments to facilitate direct comparisons of the decelerator performance at different detunings.

4.10.2 Polarization Control

A quarter-wave retarder plate was inserted into each beam as shown in Fig. 4.1 to produce circular polarization. For the bichromatic force to cycle the strongest transition, $|m_j| = 1 \leftrightarrow |m_j| = 2$, the counterpropagating beams must have polarizations (relative to the atoms) of σ^+ and σ^+ or alternatively, σ^- and σ^- . Both beams enter the beam machine with identical linear polarizations, so the quarter wave retarders must be set accordingly. The retarders are placed as close as possible to the interaction region to minimize unwanted phase changes in the light due to the multilayer dielectric mirror coatings and windows.

The quarter wave retarders are tuned using a 1-inch polarizing beam splitter cube (PBC) mounted in a 1-inch plastic ball bearing assembly. The PBC is then rotated at ≈ 10 Hz using a small dc motor powered by a single size “AA” battery, using a rubber band as a drive belt. The transmitted laser light is measured with a silicon photodiode behind a ground glass plate. The rotational angle of the

$\delta/2\pi$ (MHz)	Irradiance (W/cm ²)	+kv Power (mW)	-kv Power (mW)
200	3.82	32.0	41.4
250	5.97	50.1	64.8
300	8.59	72.2	93.3
450	19.3	162	209

Table 4.2: Calculated optimal irradiances and optical powers for bichromatic detunings used in these experiments. The frequencies missing from this sequence (350 MHz and 400 MHz) could not be investigated due to the unexpected failure of the laser amplifier.

quarter wave retarder is adjusted to minimize the peak to peak variation in the photodiode signal.

4.10.3 Optimal Irradiance

To realize the optimal Rabi frequency $\Omega_r = \sqrt{3/2} \delta$, the optical irradiance of each component of each beam must be adjusted. This can be done by adjusting the laser amplifier to make coarse power adjustments, and then by adjusting the rf drive power in each of the Doppler shifting AOMs for fine tuning. Table 4.2 shows the optimal beam powers for the range of bichromatic detunings used in these experiments. It should be noted that using the top-hat radius measurement for the beam waists in the irradiance calculations yielded very accurate estimates of the optical power requirements.

4.11 Data Acquisition

Data acquisition control and sequencing, velocity distribution calculations, and data file saving are all controlled via a program written in National Instruments LabView. The program runs on a 2.8 GHz Dell OptiPlex GX620 Tower computer with a National Instruments PCI-6036E DAC card and BNC-

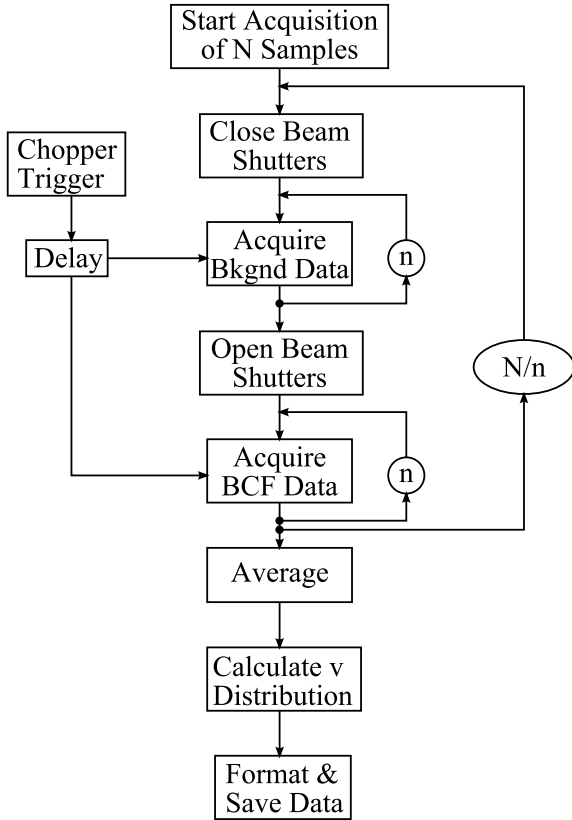


Fig. 4.16: Diagram of data acquisition and processing. For an N sample average, the acquisition is broken into subunits of size n , where n is usually 200. This helps to reduce the effects of slow drifts in the source brightness over long acquisitions, reducing offset errors when comparing the slowed velocity distribution (BCF) to the unslowed (Bkgnd) distribution. Circles represent repetition and averaging by the number indicated inside the circle.

2120 shielded interface box. The primary tasks of the control program are to sequence the beam shutters and acquisition to the chopper trigger, compute the velocity distributions, perform basic slowing analyses, and format and save the data to a file shown diagrammatically in Fig. 4.16. A complete description of the program and its components can be found in Appendix B.

4.11.1 Data Averaging and Analysis

Due to the relatively small signal sizes, several thousand individual TOF spectra are averaged and analyzed for each run of the experiment. From the measured time of flight one can easily calculate the atom transit time t . The velocity is related to the distance traveled d_{TOF} by

$$v = \frac{d_{\text{TOF}}}{t}. \quad (4.11.1)$$

Because a normalized probability distribution for the velocities is needed, the conversion from times to velocities must correctly preserve areas. Therefore, we have to re-normalize each piece of the velocity distribution:

$$\begin{aligned} N(v)dv &= N(t)dt \\ N(v) &= \frac{N(t)dt}{dv}. \end{aligned} \quad (4.11.2)$$

Chapter 5

Large Detuning BCF: Analysis

5.1 Experimental Slowing Results and Analysis

The original experimental goal was to acquire data on BCF slowing of metastable helium using the configuration shown in Fig. 4.1 over a range of detunings limited by the laser amplifier. The range of detunings covered 123 to 278γ to provide a series of data points below and including 185γ as a baseline, extending half way to the largest detuning of the Metcalf group of 368γ . The intent was to acquire sequential slowing data to identify a trend in the change or reduction in the force, with the expectation that it would lead to an understanding of the mechanism of any upper limit. All experiments were executed with the optimum Rabi frequency of $\sqrt{3/2}\delta$, phase of $\pi/2$, and static Doppler detunings ± 800 MHz ($\pm 493 \gamma/k$).

Unfortunately, the fiber laser amplifier ceased functioning before the experiment was complete, as did a second unit on loan from Nufern. The laser amplifier failures brought a premature end to this portion of the experiment, and data was only collected at detunings of 123 , 154 , 185 , and 278γ . The results, shown in Fig. 5.1, have not been enhanced based on the difference between the atomic beam diameter and the bichromatic beam waists, as was done in some other BCF experiments [36, 42]. Only about 40% of the atoms overlap the slower beams, so

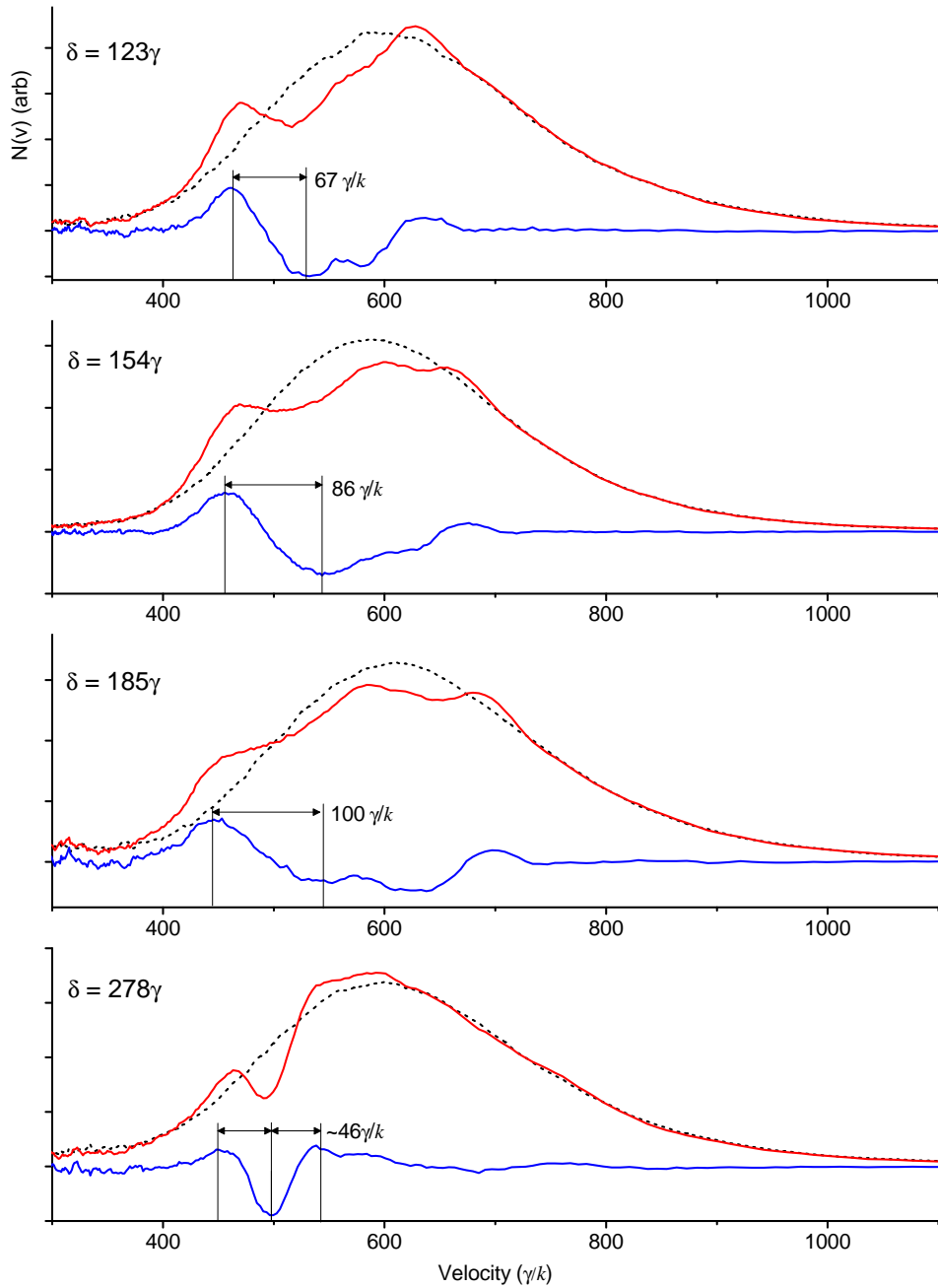


Fig. 5.1: Experimentally observed velocity profiles for BCF slowing, increasing in detuning from top to bottom. The dotted black trace is the unslowed (background) distribution, red is the slowed distribution, and blue is the difference. Notice the anomalous result at $\delta = 278\gamma$, which seems to support the observation of an upper limit for the BCF detuning.

the majority of atoms in any velocity group will not experience any force. Consequently, the depth of the holes in the velocity profiles will necessarily be at most 40% of the population. Only one set of data was acquired in the previously unexplored range between 185γ and 368γ . However, the result is very interesting and does support the observation of an upper limit of the BCF, which will be discussed further in Section 5.2.

The forces responsible for the changes in the velocity profiles shown in Fig. 5.1 were confirmed to be due to the BCF by adjusting the phase and blocking one of the two bichromatic beams, or one component of one of the beams. In each case, when the phase was increased by π to $\phi = 3\pi/2$, the sign of the force changed and the deceleration became an acceleration. This is perhaps the most obvious and identifying signature of the BCF. Also, when the phase was set to $\phi = 0$ or $\phi = \pi$, the force vanished altogether, as expected. If one of the frequency components of one of the bichromatic beams is blocked, the force vanishes as well, but smaller “single-beam” peaks appear, which are discussed in more detail in Section 5.3.

The rest of the bichromatic slowing results are consistent both with our models and previous results by the Metcalf group [36] and are summarized in Table 5.1.

There is no agreed-upon convention for measuring slowing, velocity range, or cooling, so I will use the following definitions for the remainder of this thesis:

“Slowing” is defined as the velocity difference between the peak of the slowed atom distribution and the corresponding minimum of the hole in the slowed velocity distribution, as indicated in Fig. 5.1. This is reasonable because the goal in slowing an atomic beam is to create a group of atoms whose most probable ve-

Table 5.1: Summary of BCF slowing results on metastable helium. Slowing measurements are made from the maximum of the peak to the minimum of the corresponding hole in the velocity distribution. The velocity range is measured using the Metcalf group convention of the FWHM of the combined peak and corresponding hole in the velocity distribution.

Detuning γ	Slowing γ/k	Velocity Range δ/k	Cooling %
123	67	0.55	1.04
154	86	0.56	1.08
185	100	0.54	1.00
278	46 ¹	0.16	N/A

¹ The result for $\delta = 278\gamma$ does not follow the typical BCF slowing velocity change, so the slowing measurement is shown only for comparison.

locity is slower than the most probable velocity of that group without the optical forces.

The velocity range of the BCF can be estimated by measuring the full width between the half-maximum of the slow side of the slowed atom peak and the half-minimum on the fast side of the hole in the original velocity distribution. This is the convention used by the Metcalf group in their BCF slowing experiments [36, 42]. There is some argument that this is equivalent to the full width of the BCF velocity profile. While this may represent an overstatement of the velocity range, I will adopt this convention to facilitate comparisons between the Eyler and Metcalf group results.

“Cooling” is defined here as the ratio of the FWHM of the slow atom peak to the FWHM of the corresponding hole in the unslowed velocity distribution. This ratio then is the factor by which the velocity distribution of atoms affected by the slower is changed. Therefore, a value less than one indicates compression, or cooling, and a value greater than one indicates an expansion, or heating.

Examining the slowing data summarized in Table 5.1, we can see that the BCF slowing experimentally is proportional to δ , and the velocity range of the force is very close to δ/k as predicted by the numerical calculations described in Section 2.3, and in agreement with previous results from the Metcalf group at $\delta = 185\gamma$ [36]. The cooling ratio is also consistent, indicating that the velocity width of the slowed atoms is reduced by about 37% in all three cases. This provides clear evidence of cooling as well as slowing, as discussed in Section 2.5.5.

Because the length of the slower was about 3.7 cm, the atoms experienced 6 to 8 BCF slowing time intervals Δt (see Eq. (2.5.4)) during the interaction region, depending on detuning. This complicates a direct measurement of the BCF magnitude since the atoms will be slowed by the full velocity range even for magnitudes well below the $\hbar k \delta / 2$ optimum. An attempt was made to pulse on the bichromatic slower beams for a time comparable to the bichromatic slowing time of 5.8 μs to quantitatively measure the force magnitude. I used an rf switch to rapidly turn the rf to the Doppler detuning AOMs on and off, controlled by a TTL pulse from a BNC pulse delay generator triggered with the chopper sync pulse. Unfortunately, the results were inconclusive and inconsistent, so the BCF magnitude cannot be addressed quantitatively.

5.2 Evidence of a Possible Upper Limit

Despite the failure of the fiber laser amplifiers and the resulting premature end of this set of experiments, there is some insight that can be gained from the anomalous velocity profile obtained with $\delta = 278\gamma$. The velocity distribution shows both a deceleration and acceleration, but with a velocity range or peak-to-peak range much less than expected based on the trend of the results at smaller

detunings. The length of the slower prohibits a full quantitative understanding of the spatial and temporal scales of the acceleration and deceleration.

The distinct pattern of a centralized hole with peaks on either side indicates forces are present in both directions—accelerating and decelerating. This is also similar to a one-dimensional random walk, in which a “person” walking one step at a time along a line, has a random but equal probability of continuing in the same direction or reversing direction with each step [81]. This is analogous to the sign of the force changing randomly, as would happen if the atom were to make several unwanted transitions at avoided crossings (see Sections 2.2 and 3.3) or experienced some other phenomenon that changed the sign of the force at random.

The center of the hole is at the center of the force profile, which in these experiments is Doppler shifted by 800 MHz, or $493 \gamma/k$. We can rule out any of the individual bichromatic frequency components which all have the wrong Doppler shifts, located $\pm 158 \gamma/k$ from the center of the velocity hole. Therefore, the effect must at least be bichromatic in nature. This was confirmed by blocking one or more of the bichromatic frequency components, which resulted in a complete loss of the bichromatic velocity shifts.

A Monte Carlo simulation was created using a BCF profile with $\delta = 61\gamma$, with each atom experiencing an independently randomly varying force direction (sign), simulating a random strong dephasing with $\Delta\phi = \pi$. The resulting atomic velocity distribution is binned and smoothed to simulate the 66 m/s ($38 \gamma/k$) resolution of our TOF system. The results are shown in Fig. 5.2 and agree quite well with experimental observation. However, due to a lack of additional data between the detunings of 185γ and 278γ , there is no information regarding the transition from the slowing velocity distribution we expect to see and this abnormal distri-

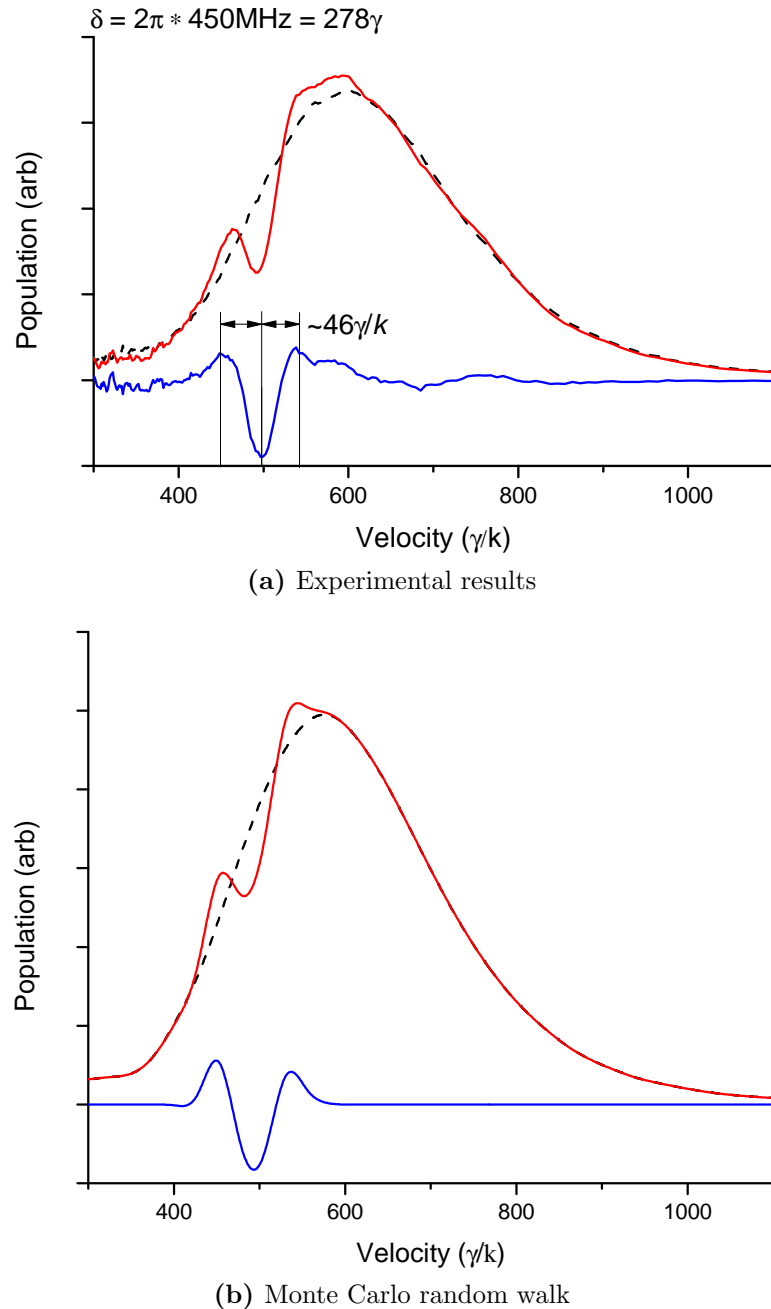


Fig. 5.2: Comparison of experimental results with $\delta = 278\gamma$ and a Monte Carlo random walk model with a BCF profile $61\gamma/k$ wide with simulated random strong dephasing ($\Delta\phi = \pi$). Doppler shifts for the model and experiment are the same.

bution. However, this result may be consistent with the experimentally observed vanishing of the force at 368γ , and is consistent with the onset of an increasing partial dephasing between $\delta = 185$ and 370γ .

5.3 Discussion of Single-Beam Forces

One additional phenomenon apparent in BCF experiments was the presence of a force larger than originally expected when one or more of the bichromatic components is blocked. There are residual effects that can be seen as a small bump in Fig. 5.1 to the right of any velocity distribution hole. At first, this effect seemed far too large to be due to radiative forces, so we investigated it further.

A single component of a 100 MHz detuning BCF beam acting on the metastable helium beam is shown with the green line in Fig. 5.3. Since the force is present in a monochromatic field, the radiative force was the first interaction modeled. A Monte Carlo model was created in Mathematica taking into account the following factors:

1. The gaussian intensity gradient each atom sees as a result of the gaussian profile of the laser and the crossing angle of the laser to the atom beam.
2. The relative diameters of the atomic beam and the laser.
3. The time each atom spends in the laser due to its speed.
4. The peak irradiance of the laser.

The program is based on the Monte Carlo model described in Appendix F, modified to use a calculated radiative force instead of the BCF. A large number of atoms with a statistical distribution of velocities derived from an experimental

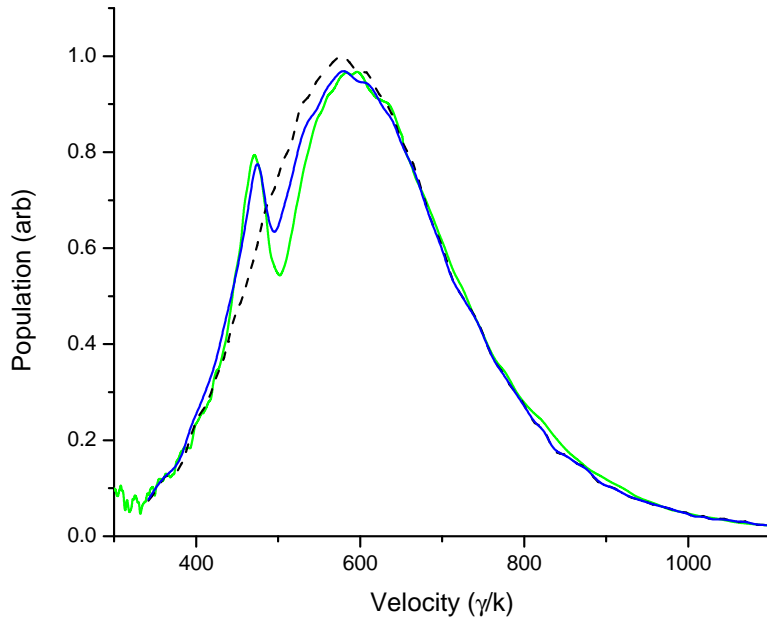


Fig. 5.3: Comparison of the observed “single beam” force (green) to a simulated velocity profile using a monochromatic laser field and the radiative force (blue), with an unperturbed atomic velocity distribution with the dashed black line.

distribution are created. The atoms are randomly assigned a position in the atom beam for the vertical irradiance scaling, then they are stepped through a gaussian laser field profile and the radiative force is calculated at each step for each atom based on the local field irradiance and Doppler detuning. The resulting velocity change is calculated and applied to the atom. The final velocity distribution can then be analyzed and compared to the experimental data.

The radiative force model result is shown in blue in Fig. 5.3. The model uses the same irradiance ($s = 1100$) and ratio of laser to atomic beam diameters as the experimental velocity distribution (shown in green). The resulting changes in the velocity distributions are reasonably close—very close on the low velocity side, but less so on the higher velocity side. While the single beam force appeared at first to be too large to be radiative in nature, the Monte Carlo model shows

that the effect is apparently radiative.

Chapter 6

Chirped BCF: Experiment

6.1 Chirped BCF Experiment Overview

The chirped BCF decelerator accomplishes the same goal of slowing metastable helium atoms using bichromatic forces with a somewhat different approach. In a static slower as described in Chapter 4, a BCF force profile with a constant center and very large velocity range is created to slow atoms from a large initial velocity to the lower velocity edge of the profile. To circumvent the difficulties involved with implementing such a slower as discussed in Chapter 3, we now substitute a BCF with a relatively small velocity range, in which the center of the BCF (Doppler shift) is dynamically adjusted to stay resonant with the He^* atoms while they are slowed. This is done by sweeping (chirping) [21, 22] both laser frequencies to follow the changing Doppler shift. This allows one to use smaller bichromatic detunings $\pm\delta$, substantially reducing laser power requirements and operating with the BCF in a regime in which it is reliable.

The chirped slower uses two diode lasers—one for the copropagating $+kv$ beam and one for the counterpropagating $-kv$ beam, as shown in Fig. 6.1. This allows independent control of the co- and counterpropagating beam ($\pm kv$) Doppler shifts. The lasers are initially locked (without a chirp in progress) at the Doppler shift of a velocity group $v(t_0)$ near the center of the atomic velocity distribution,

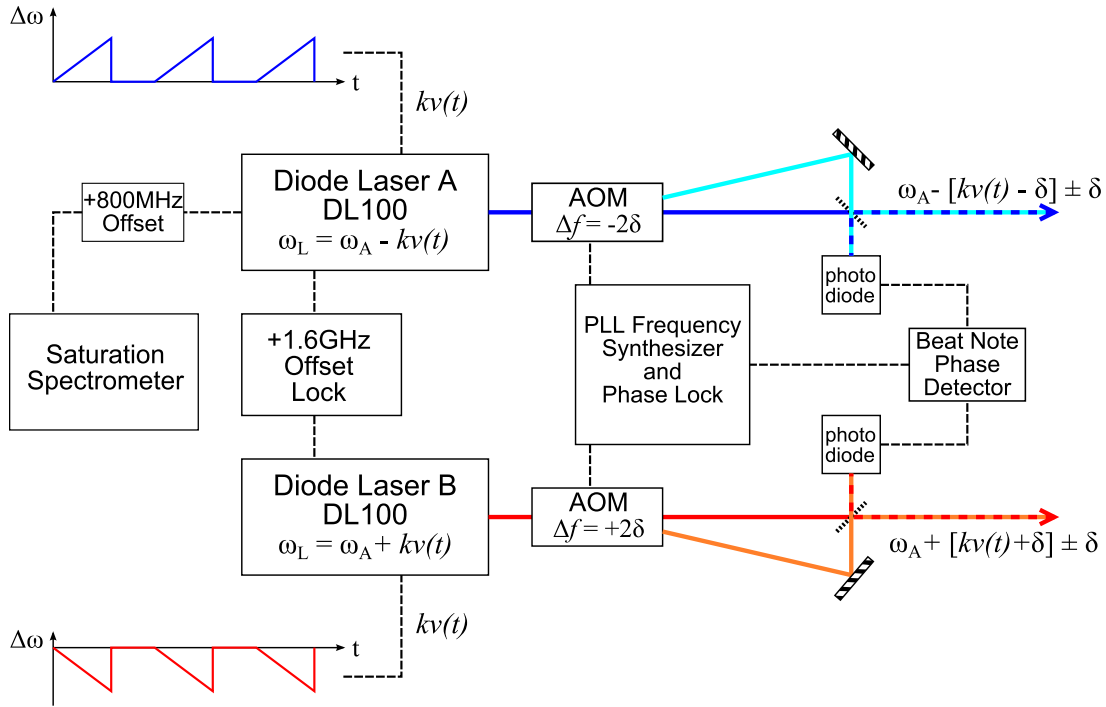


Fig. 6.1: Chirped BCF slower experiment block diagram showing key optical and electronic components.

$\omega_\ell = \omega_a \pm kv(t_0)$, and then chirped in opposite directions to follow the Doppler shift as a function of time. This is accomplished through the use of diode laser current modulation and offset locks, further discussed in Section 6.3. The bichromatic frequencies are generated for each laser separately using a single-passed AOM driven at rf frequency $f = 2(\delta/2\pi)$. For each laser, the zero- and first-order components are recombined using a 50% beam splitter to form the $\pm\delta$ beat notes. The beat note phase (see Eqs. 2.1.3 and 2.2.1) is controlled by locking the rf phase driving the two AOMs, an electronically adjustable alternative to the optical delay line described in Section 4.8.

The chirped BCF slower shares the same metastable helium source and TOF scheme described in Sections 4.2 and 4.3. The TuiOptics diode laser and SAS

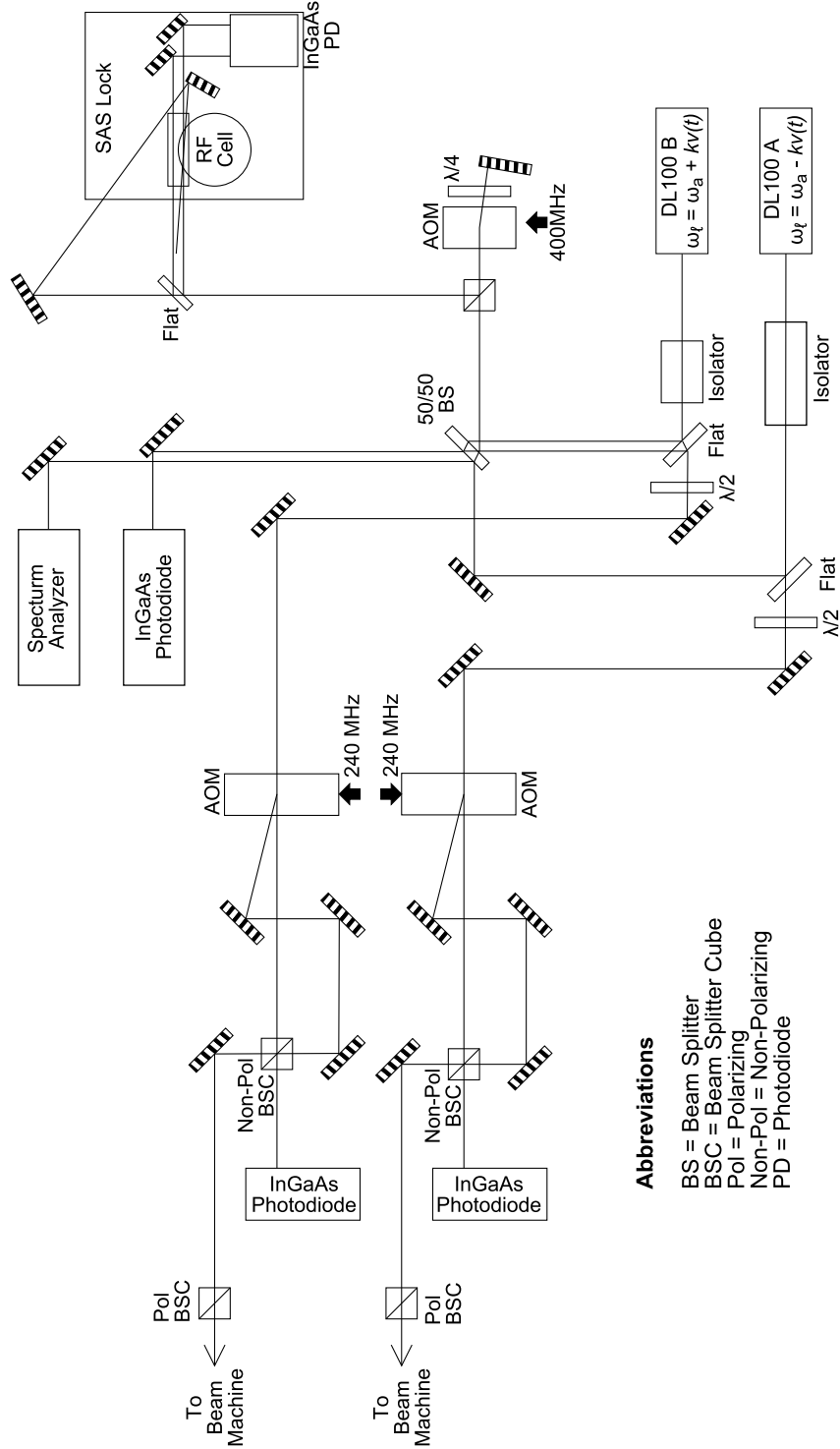


Fig. 6.2: Chirped BCF slower experimental layout showing frequency stabilization and bichromatic frequency generation optics. The He^{*} source and the optics in the beam machine are the same as shown in Fig. 4.1

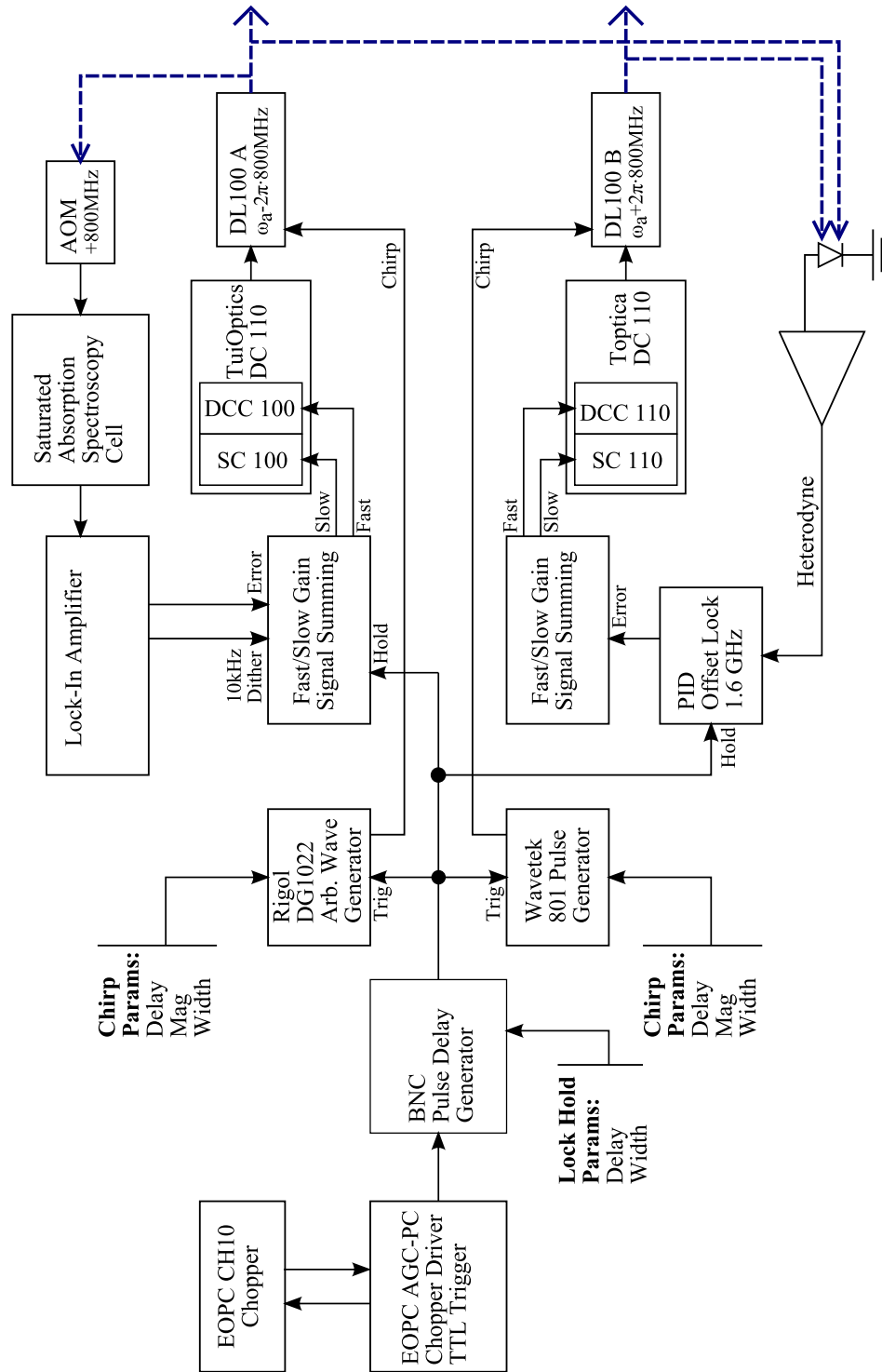


Fig. 6.3: Chirped BCF slower electronic components and connections showing frequency stabilization and chirped signal generation.

frequency stabilization are the same as discussed in Section 4.5. However, there are several significant differences in the manner in which the various frequencies are generated and modulated, as discussed below.

6.2 Biased Photodiodes

All of the photodiodes used for heterodyne detection in the offset lock (Section 6.3.3) and rf phase lock (Section 6.5) are Edmund Optics InGaAs photodiode detectors with a $70 \mu\text{m}$ active area (p/n NT55-753). I installed them in small aluminum boxes with a bias circuit designed to be used at frequencies above 1 GHz as shown in Fig. 6.4.

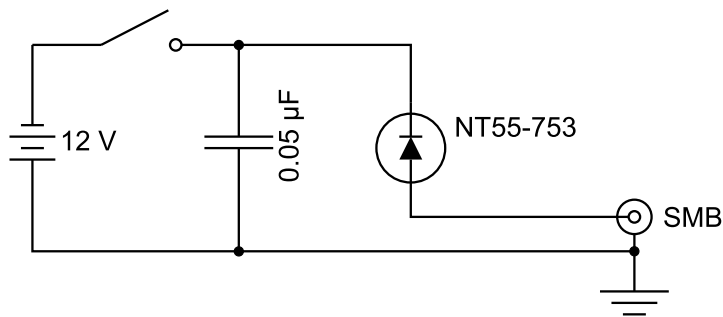


Fig. 6.4: Photodiode bias circuit. The reverse bias voltage, which reduces diode capacitance, can be anywhere from 9 V to 15 V. We typically used one type A23 12 V battery to eliminate the problems associated with external power supplies—power supply voltage fluctuations, noise pickup in power cables, and ground loops.

6.3 Lasers and Shifting the Force

6.3.1 Lasers

In addition to the TuiOptics DL100 described in Section 4.5 a second (and much newer) Toptica DL100 tunable diode laser is used. To assist in referring to the two lasers, the TuiOptics laser will be referred to as “DL100 A”, and the Toptica laser as “DL100 B”. Just as for the TuiOptics laser, a standard commercial electronics package supplies the laser current drive and temperature control. The laser is fitted with a 1080 nm high power 300 mW laser diode (Toptica P/N LD-1080-0300-1) capable of producing up to 150 mW of post-cavity output, which can be tuned from 1066 to 1086 nm. The laser shape and divergence are corrected to provide a suitably round beam using a short focal length cylindrical telescope before passing through a homemade optical isolator to protect the laser diode from unwanted optical feedback and retroreflections.

The optical isolator uses a Faraday crystal and magnet assembly salvaged from a Continuum SI100 diode laser (design wavelength of 1064 nm). A simple bracket was made to mount the assembly with a pair of Thorlabs polarizing beam-splitter cubes to enforce the correct linear polarization entering and exiting the isolator.

In these experiments the TuiOptics DL100 laser was used to supply the counterpropagating $-kv(t)$ beam and the Toptica DL100 to supply the $+kv(t)$ beam.

6.3.2 Laser Frequency Modulation Interface

An important addition to the newer DL100 is the optional DL-Mod field-effect transistor (FET) and bias-T modulation interface. This sits on an accessory

printed circuit board factory installed in the rear of the laser head that includes two modulation inputs:

- An FET circuit that is dc-coupled with an electrical bandwidth (-3 dB) of 20 MHz.
- A Bias-T port that is ac-coupled with an electrical bandwidth of > 300 MHz.

For the chirp rates required (ramps as short as $10\ \mu s$) the FET circuit is appropriate. I tested the Bias-T using chirped modulation and found that the frequency response at our chirp rates was severely attenuated, as expected. The FET current modulation uses an FET in parallel with the laser diode. A positive voltage on the FET gate forward-biases the transistor causing current to flow from the source to drain (at ground), thereby reducing the current available to the laser diode and increasing its frequency.

The older TuiOptics DL100 had no such modulation option, and the bandwidth of the DCC100 modulation input used for laser locking was too low to chirp the laser. Also, since the frequency chirp profiles need to be very closely matched in time, rate, linearity, and magnitude, using the same modulation interface for both lasers should make that task simpler. Because the DL-MOD is proprietary to Toptica, I had to reverse-engineer the DL-MOD circuit and design a similar (but not identical) FET modulation input for their older laser. The reverse-engineered DL-MOD circuit is shown in Appendix C for reference, although I would recommend using the commercial DL-MOD package if possible.

The resulting FET modulation circuit is shown in Fig. 6.5. One additional change I had to make to the TuiOptics DL100 laser head was to modify where the laser diode voltage is measured by the DCC100 current controller. Originally the interface circuit in the laser head where the DCC100 and DTC100 temperature

controller connect was relatively simple and the control electronics monitored the voltage across the laser diode at that point as a failsafe. However, with the addition of the modulation board, which draws several millamps of current when not undergoing a chirp, the voltage drop now included the FET and was prematurely limiting the diode current. A wire was added so that the U-LD sense now (as in the DL-MOD) measures the potential drop at the laser diode. Pictures of the TuiOptics laser head before and after FET circuit installation and the Toptica DL100 laser head for reference are shown in Fig. 6.6.

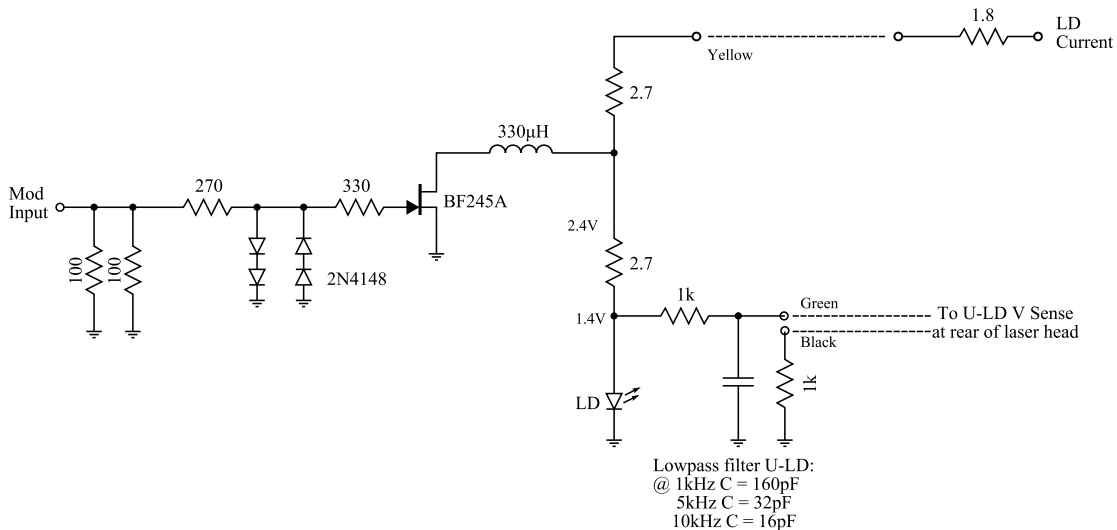


Fig. 6.5: FET current modulation interface circuit for the TuiOptics DL100. The modulation input voltage on the FET gate causes a small amount of current to bypass the laser diode, changing the lasing frequency. The 2N4148 diodes limit the modulation voltage, protecting the laser diode. In addition to this circuit, the laser diode voltage sense (U-LD) had to be re-routed from its original measurement point at the rear of the laser head to sense the voltage drop directly at the diode as shown.

If the chirp modulation potentials are limited to the range of -1 V to 0.5 V, which affords a tuning range greater than 450 MHz, the two circuits have very similar dc response as shown in Fig. 6.7. I was unable to compare the rf responses between the two circuits since the DL-MOD was already installed in the laser head.

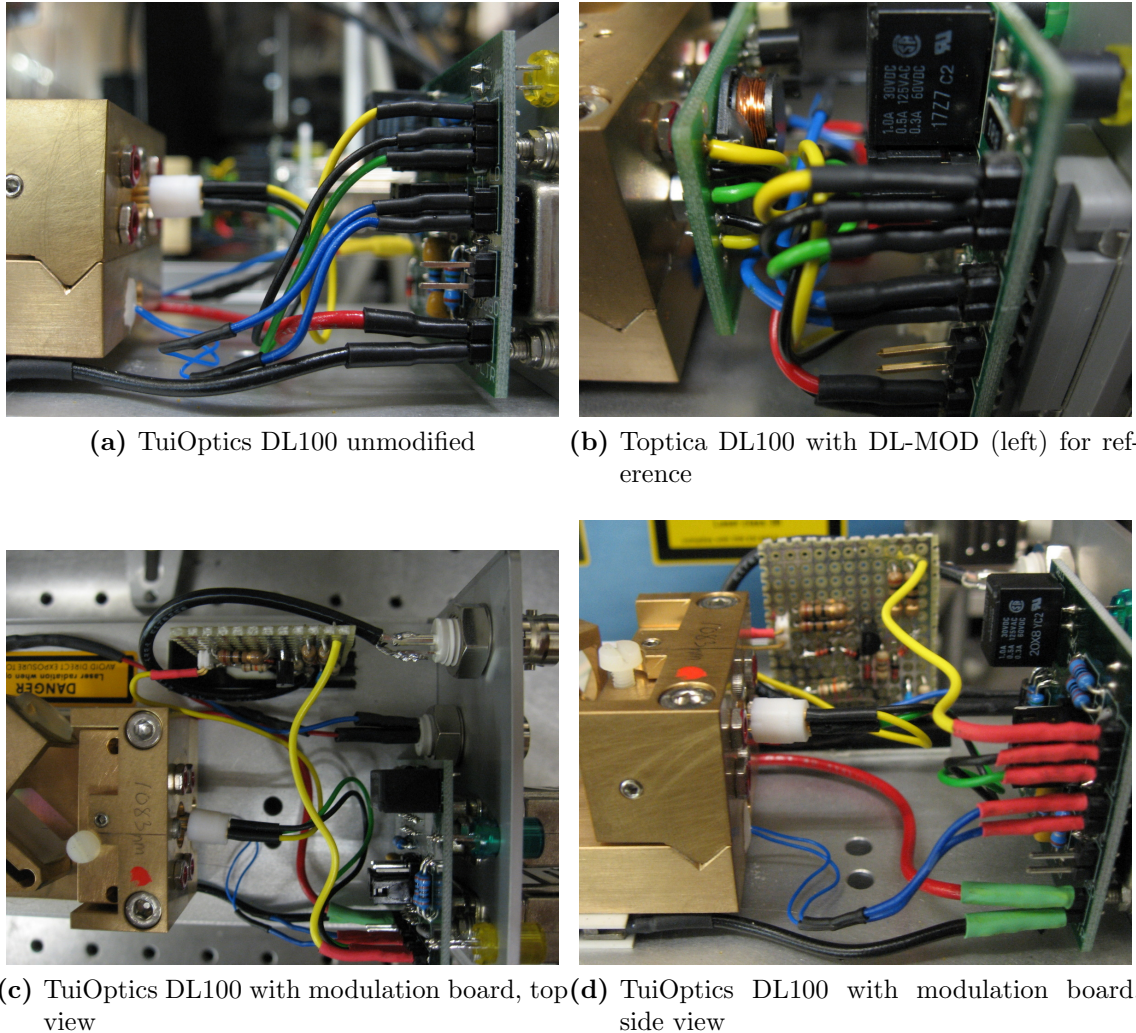


Fig. 6.6: DL100 FET current modulation board installations showing the factory installed PCB and the custom built circuit. In all photos, the laser head connector plane is to the right, and the laser diode mount is the brass block on the left. The lasers are facing to the left.

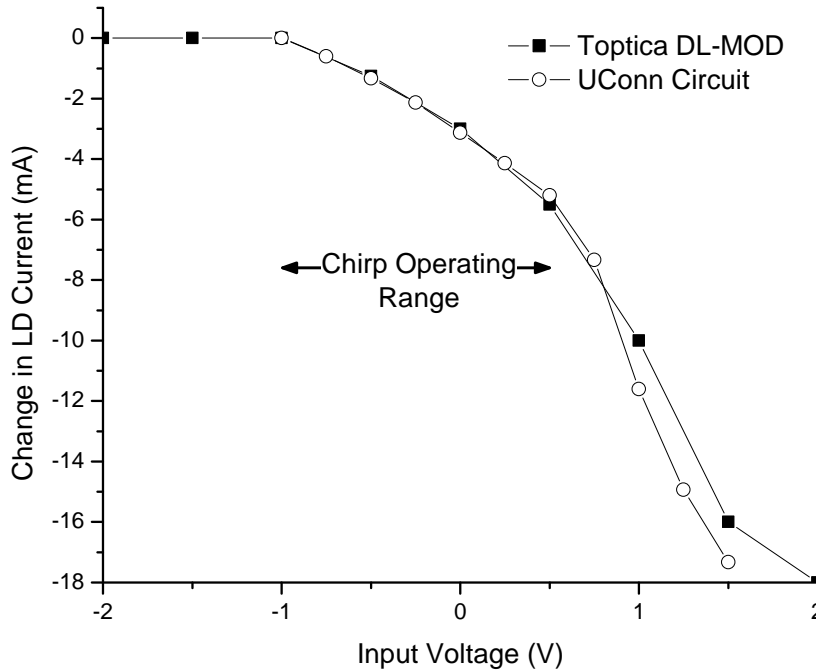


Fig. 6.7: Calibration of the UConn FET current modulation circuit and comparison to the commercial Toptica DL-MOD FET current modulation board. Data for DL-MOD response curve was taken from [82].

Note that the current response is not linear, and neither is the laser frequency exactly proportional to current. This nonlinearity must be compensated for in at least one laser to properly match the frequency chirp profiles, as discussed in Section 6.6.

6.3.3 Frequency Stabilization

For frequency stabilization purposes, the TuiOptics DL100(A) can be considered the “master” laser and is locked to the $2^3S_1 \rightarrow 2^3P_2$ transition via saturated absorption spectroscopy. After the laser exits the optical isolator, it passes through an optical flat oriented at 45° to the beam, as shown in Fig. 6.2. This creates two weak reflections, one from each surface. One reflection is sent to the SAS experiment for laser locking. This is essentially the same as for the large-

detuning experiment described in Section 4.5.2, except that the laser is given a frequency offset before the SAS experiment. With the addition of the second laser, a second identifying subscript will be added to the laser frequency ω_ℓ used previously so that the TuiOptics “DL100 A” has frequency $\omega_{\ell A}$ and the Toptica “DL100 B” has frequency $\omega_{\ell B}$. Using a double-passed AOM driven at rf frequency $F/2\pi = kv(t_0)/2 = 400$ MHz, the positive first-order, double-passed component $\omega_{\ell A} + 2F = \omega_{\ell A} + kv(t_0)$ is sent to the SAS locking apparatus. Due to the AOM-induced frequency shift, the laser frequency when the SAS signal is locked is offset from resonance by the inverse of the AOM frequency shift, here -800 MHz. If the shift is set to $-kv(t_0)$, it provides the static (unchirped) Doppler offset of the counterpropagating laser.

The copropagating beam must have a Doppler-compensating shift equal in magnitude but in the opposite direction from resonance as the counterpropagating laser. This is achieved by locking diode laser B (the Toptica DL100) to laser A with a frequency offset of twice the Doppler shift, so that $\omega_{\ell B} = \omega_{\ell A} + 2kv(t_0)$. The laser frequencies will then be $\omega_{\ell A} = \omega_a - kv(t_0)$ and $\omega_{\ell B} = \omega_a + kv(t_0)$. In these experiments $kv(t_0)$ is set to 800 MHz, so the frequency offset between the two lasers must be 1.6 GHz.

Samples of each laser beam are combined on an optical flat and focused onto a biased InGaAs photodiode to obtain a heterodyne signal at the difference frequency between the two lasers. The heterodyne signal is then ac-coupled into a Mini-Circuits ZKL-2R6 33 dB rf amplifier before being connected to the offset lock circuit. The offset lock is implemented using a phase-lock-loop (PLL) to compare the heterodyne frequency to an internally generated frequency reference (the offset lock frequency). This circuit is a modification of the PLL frequency synthesizer

discussed in Section 6.4, changed so that the heterodyne signal replaces the VCO at the PLL input. An error signal proportional to the frequency difference between the heterodyne and lock frequency is thus generated. This error signal is split into “fast” and “slow” components using high- and low-pass filters (3 dB point at 10 Hz). The slow correction signal is sent to the SC110 backplane input to correct for slow drifts by modulating the high voltage applied to the grating piezo. The fast correction signal is sent to the modulation input on the front panel of the DCC110 to correct faster frequency excursions by modulating the laser diode current.

Immediately prior to starting a frequency sweep, the laser lock error signals are sampled and held constant so the locking circuits do not counteract the frequency chirps. The laser frequencies are then chirped from their initial Doppler offsets toward resonance by applying carefully calibrated voltage ramps to the laser diode drive current modulators. The lock sample-and-hold time is significantly longer than the chirp, which provides additional time for the lasers to settle down after their frequency excursions. The frequency locks are then re-enabled for about 2 ms to re-establish the locks, and the process repeats for the next chopper trigger. The sample-and-hold time is much longer than necessary because the 160 Hz atom pulse repetition rate limits the decelerator repetition rate. In a fully realized design with a cw atomic beam, the chirp would reset and immediately repeat to maximize the number of atoms slowed. Monte Carlo simulations described in Section 7.2 and Appendix F predict that the required chirp repetition rate will be between 10 kHz and 40 kHz, depending on the detuning and BCF optimization.

There is no need for additional Doppler offset frequency shifts as in the

large-detuning BCF experiments, since the offsets are built into the frequency stabilization.

6.4 Bichromatic Frequency Generation

The bichromatic frequency components are generated, as in the large detuning BCF slower, with AOMs. Unlike the large-detuning experiment, however, the AOM is only single-passed, as shown in Fig. 6.2. Frequency shifting in a single AOM pass is feasible because of the reduced magnitude of the bichromatic detuning, $\delta/2\pi = 100 - 120$ MHz. The AOMs now can now be driven at 2δ and still maintain a diffraction efficiency of $\sim 50\%$ at 1 W of rf drive power. The advantage of single-passed AOM frequency shifting is that the frequency components are spatially separated and can be independently corrected for distortions introduced by the AOM [79] using appropriate short focal length cylindrical lens telescopes before the individual components are re-combined on a beam splitter.

6.5 RF Phase

Another major departure from previous experiments on BCF slowing of atoms is the direct electronic control of the rf phase in the bichromatic detuning AOMs. This improvement eliminated the need for an optical delay line which, at bichromatic detunings of 100 to 200 MHz, would be ~ 1 m long. Such large changes in the optical path significantly affect the locations and sizes of the beam waists in the interaction region.

Control of the rf phase is accomplished using two linked PLL frequency synthesizers that share a common 10 MHz clock as shown schematically in Fig. 6.1. One complete frequency synthesizer circuit acts as the “master”. Locked to its ref-

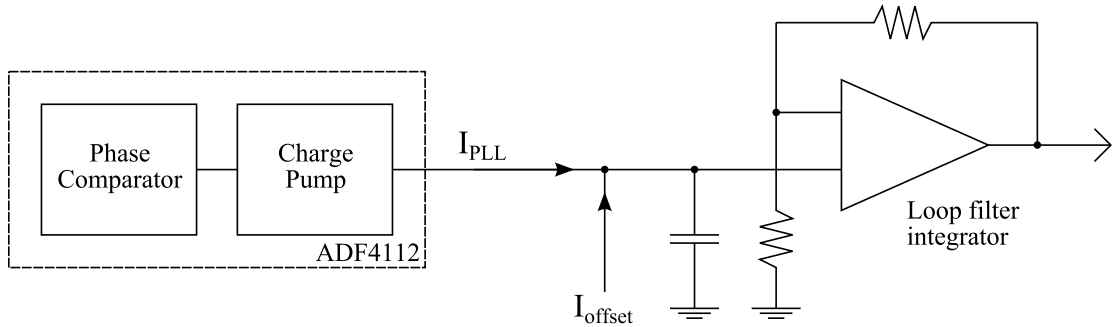


Fig. 6.8: Schematic of the rf phase shifting method used to electronically control the relative rf phase in two AOMs. Reference oscillator frequency f_{ref} is supplied by the master PLL circuit. Additional information can be found in Ref. [78].

erence oscillator clock phase, it can only be adjusted in frequency and amplitude. A second frequency synthesizer, the “slave”, has a 10 MHz reference oscillator provided by the master via a 50Ω coaxial patch cable. The slave frequency synthesizer can be adjusted in relative phase, in addition to frequency and amplitude.

The phase shifting methodology we employed was inspired by that described by Golnabi et. al. [83] and shown schematically in Fig. 6.8. The phase is shifted by changing the tuning input to the VCO by adding an offset current to the integrating charge amplifier after the PLL (ADF4112). This offset shifts the relative phase between the VCO output and the clock input to the phase comparator. Assuming a fixed frequency multiplier for the PLL, the magnitude of the phase shift is proportional to the offset current I_{offset} in Fig. 6.8.

I soon found that simply locking the rf phase is not sufficient to maintain the phase relationship between the two beams. By pressing on the optical table near one of the AOMs or anywhere along the optical path between the lasers and the AOMs, I could shift the relative phase of the beat notes by more than π . This was caused by small shifts in the optical beam paths relative to the short-

wavelength acoustic waves in the AOMs. There were several options for improving the reliability of the rf phase lock (not all are exclusive):

1. Add an active feedback loop that would monitor the relative phase between the two heterodyne signals and provide a correction signal that can be used by the phase offset circuit.
2. Bring the AOMs as close to the lasers as possible and modify the optics to minimize optical path differences between the two lasers. This would entail primarily aligning the lasers to have parallel paths, millimeters apart, sharing the same mirrors when possible.
3. Steer both lasers through the same AOM. While requiring tricky alignments, this would ensure the relative phase is constant save for movements in the AOM itself. The rf phase could be adjusted by making small changes in the rf frequency, since this changes the acoustic wave phase shift between a pair of fixed laser positions in the crystal.
4. Eliminate the electronic rf phase locking and return to using an optical delay line.

In the end I chose the first option after discovering the existence of the Analog Devices AD8302 RF/IF gain and phase detector chip. It requires two inputs from $60 - 0$ dBm in a 50Ω system with frequencies up to 2.7 GHz. The outputs provide accurate measurements of relative amplitude (not used) and of phase over a 0° to 180° range, scaled to 10 mV/degree. The AD8302 chip was soldered to an adapter, then the simple circuit shown in Fig. 6.9 was designed and constructed with a great deal of attention to reducing electrical noise and pickup. The +5 V power was taken from the 5 V supply on the slave frequency

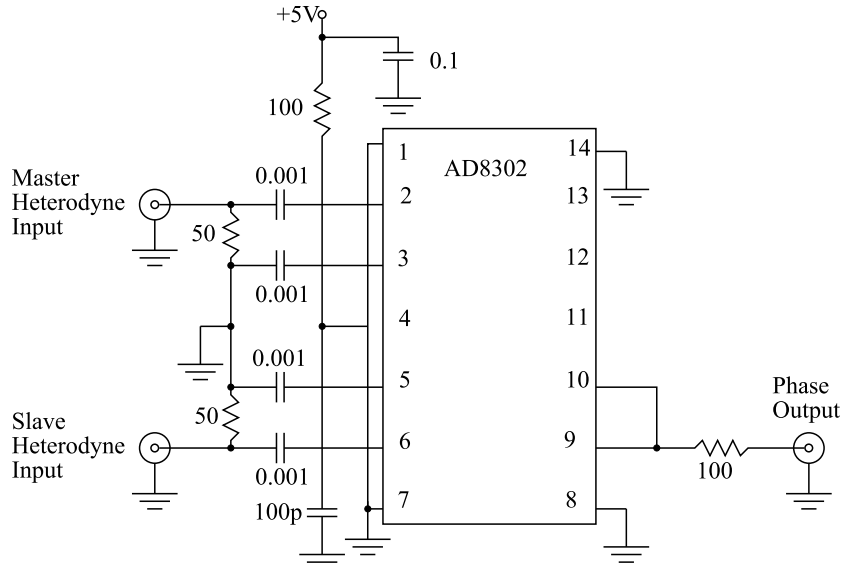


Fig. 6.9: Phase detection circuit used for rf phase lock feedback in the chirped BCF experiment.

synthesizer board to eliminate ground loops, although using a battery to power the circuit might provide lower noise and better performance.

6.6 Frequency Chirping

The laser frequency chirping is achieved by applying a voltage ramp to the gate of the FET current modulation circuit. Both laser heads have a BNC connector on the rear panel for such a purpose. As already described in Section 6.3.2, this is factory installed on the Toptica DL100 (laser B), and homemade on the TuiOptics DL100 (laser A). Referring to Fig. 6.7, we can see that to maximize the current tuning range, the $+kv$ laser (negative frequency chirp), needs to have a dc offset of 0.5 V and a negative chirp voltage. Conversely, the $-kv$ laser (positive frequency chirp) will require a dc offset of -1.0 V and a positive-going voltage ramp. Note that larger chirp ranges are possible than those used in the present experiments.

The $+kv(t)$ voltage ramp is generated by a Wavetek 801 50 MHz analog pulse generator, and $-kv(t)$ ramp is generated by a Rigol DG1022 200 MHz arbitrary waveform generator (AWG). I chose to use the analog pulse generator with the Toptica DL100 laser because it has a more linear response to the voltage ramp. The Rigol DG1022 allows a pulse of arbitrary shape to be programmed, so it can be set to compensate for nonlinearities in the laser frequency response. Both pulse generators are triggered by a Berkley Nucleonics Corp. model 555 pulse delay generator that is itself triggered by the sync pulse from the EOPC chopper drive circuit. The same pulse is also used as the gate signal that freezes the laser locking circuits. The Wavetek output voltage ramp is set to have a nominal delay of 20 μ s from the rising edge of the trigger. The delay of the Rigol pulse ramp is adjusted so the two frequency chirps begin at the same time.

To calibrate the $+kv(t)$ and $-kv(t)$ chirps, a MiniCircuits ZX30-17-5-S directional coupler was inserted between the amplifier and the offset lock electronics. A sample of the heterodyne signal was connected to an Agilent Infinium 54852A 2 GHz oscilloscope borrowed from the Gould laboratory, triggered by the output of the BNC 555. The trigger delay was set to 50 μ s so that the entire frequency ramp could be captured. The heterodyne waveform was saved to a computer and then analyzed using a Mathematica notebook to extract the instantaneous frequency from the heterodyne signal. The analysis technique was an FFT method first proposed by Fee et. al. [84], then further developed by the research groups of Orr and Baldwin [85, 86], and Eyler [87]. I based this particular version on the thesis work by Gangopadhyay [88]. The algorithm is described in detail in Appendix E. The essential steps are to take the forward FFT of the heterodyne, and filter and shift the spectrum to reduce noise and eliminate the dc component

$2kv(t_0)$. Then I take the inverse FFT and extract the phase from the imaginary component

$$x + iy = ze^{i\phi}, \quad (6.6.1)$$

and compute the instantaneous change in phase, which is the time-varying frequency:

$$f(t) = \frac{-1}{2\pi} \frac{d\phi}{dt}. \quad (6.6.2)$$

To calibrate the chirp ranges, I first chirped only the $+kv$ laser (laser B) while keeping laser A locked and unchirped as a frequency reference. I adjusted the voltage ramp rate, width, and magnitude until the desired chirp frequency excursion and width were obtained. Then, laser A was chirped while laser B (unchirped) served as the reference frequency. Now, using the arbitrary waveform generator and comparing the frequency chirp with that of laser B, I could adjust the width, magnitude, and shape of the chirp pulse until the two frequency chirps match as shown in Fig. 6.10. The target accuracy was 1% of the total ramp size, based on numerical calculations described in Section 7.2. The correction required to the A ramp linearity was a convex curvature as can be seen in Fig. 6.11. The amount of correction and the consequent number of additional points required to define the curved ramp increased with increasing magnitude.

Once the chirps were calibrated for a particular magnitude and (temporal) width, the waveform definition and instrumentation state (which includes the trigger and delay information) was stored on the Rigol AWG. The Wavetek analog pulse generator has no such storage feature, so I saved the chirp voltage waveform to the oscilloscope so that it could be recalled later as a reference waveform. Then the various pulse parameters on the Wavetek could be adjusted until the live pulse

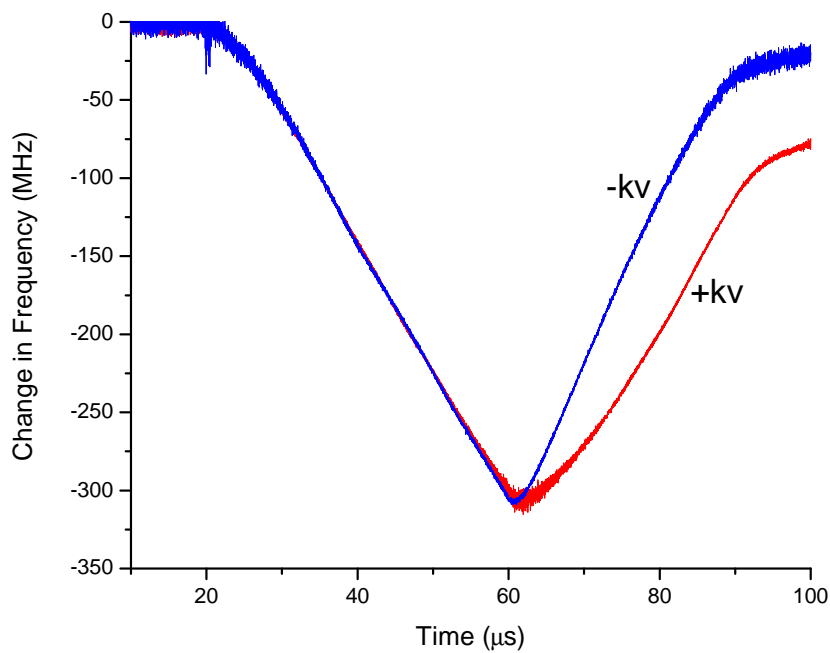
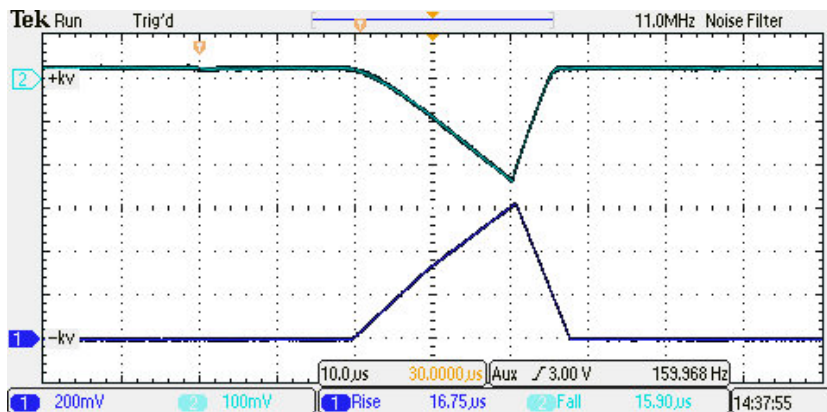
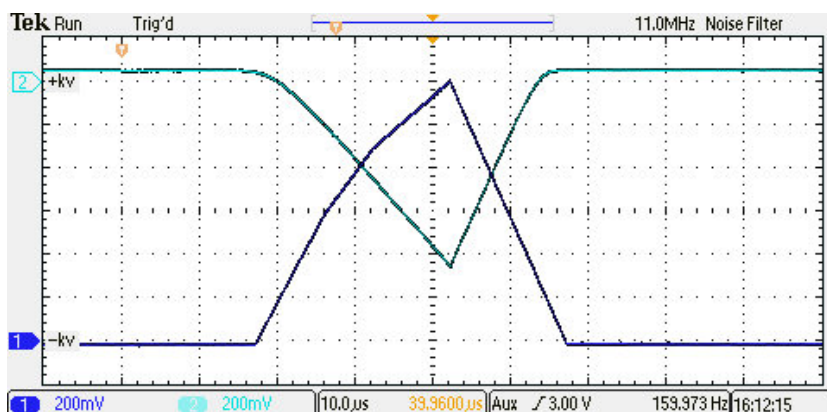


Fig. 6.10: Example of properly calibrated frequency chirps showing good overlap between the laser B ($+kv$, red) and laser A ($-kv$, blue) chirps, done for 300 MHz chirp over approximately 40 μ s. Note that despite the chirp ramps having the same return back to zero, the two diode laser responses are distinctly different. There is no need to correct for this as it does not play a role in slowing the atoms.



(a) Chirp pulse waveforms for a 100 MHz frequency chirp



(b) Chirp pulse waveforms for a 300 MHz frequency chirp

Fig. 6.11: Chirp pulse waveforms for 100 MHz and 300 MHz chirps showing the increasing nonlinearity in the laser A ($-kv$) voltage ramp necessary to compensate for differences in the FET current modulation and laser diode responses.

waveform matched the recalled reference waveform.

Unfortunately, the chirps are sensitive to the diode laser temperature and current tuning, and must be recalibrated if one or both of the lasers requires adjustment.

6.7 Interaction Region

The configuration of the interaction region for the chirped BCF slower was the same as with the large detuning BCF slower except that focusing lenses were placed so that the beam waists had a top-hat radius of $440 \mu\text{m}$ to compensate for the lower optical power of $\leq 40 \text{ mW}$ delivered to the atoms from each bichromatic beam pair. The beams then have a top-hat area 0.606 mm^2 and an optimal irradiance of 5 W/cm^2 at $\delta = 74\gamma = 2\pi \times 120 \text{ MHz}$, requiring 38 mW of optical power in each beam. Otherwise, the experimental configuration is the same as described in Sections 4.10.1 and 4.10.2.

Chapter 7

Chirped BCF: Analysis

7.1 Experimental Results

The first generation of chirped BCF experiments used a bichromatic detuning of 74γ , with the laser irradiances set to achieve $\Omega_r = \sqrt{3/2}\delta$, requiring an irradiance per bichromatic beam of approximately 5 W/cm^2 . The phase was set to $\phi = \pi/2$ in keeping with conditions for the optimum BCF. Frequency offset ramps were calibrated for chirp magnitudes of 100, 200, 300, and 400 MHz, with ramp widths from 10 to 60 μs in steps of 10 μs . The largest frequency chirp of 400 MHz was chosen since that would put the resulting slow atom peak at the lower extreme of our TOF measurement capability. The largest ramp interval of 60 μs is about 10 μs longer than the transit time of a slowed atom through the interaction region.

Velocity distributions for the range of frequency chirps 0 – 300 MHz are shown in Fig. 7.1. Experiments with a frequency chirp of 400 MHz were unsuccessful and did not yield an identifiable group of slowed atoms in the distribution, and are excluded.

To verify that the results were due to the bichromatic force and not some other effect, such as complete loss of the BCF and appearance of single-beam optical forces at frequency shifted positions, data was also taken with the bichromatic

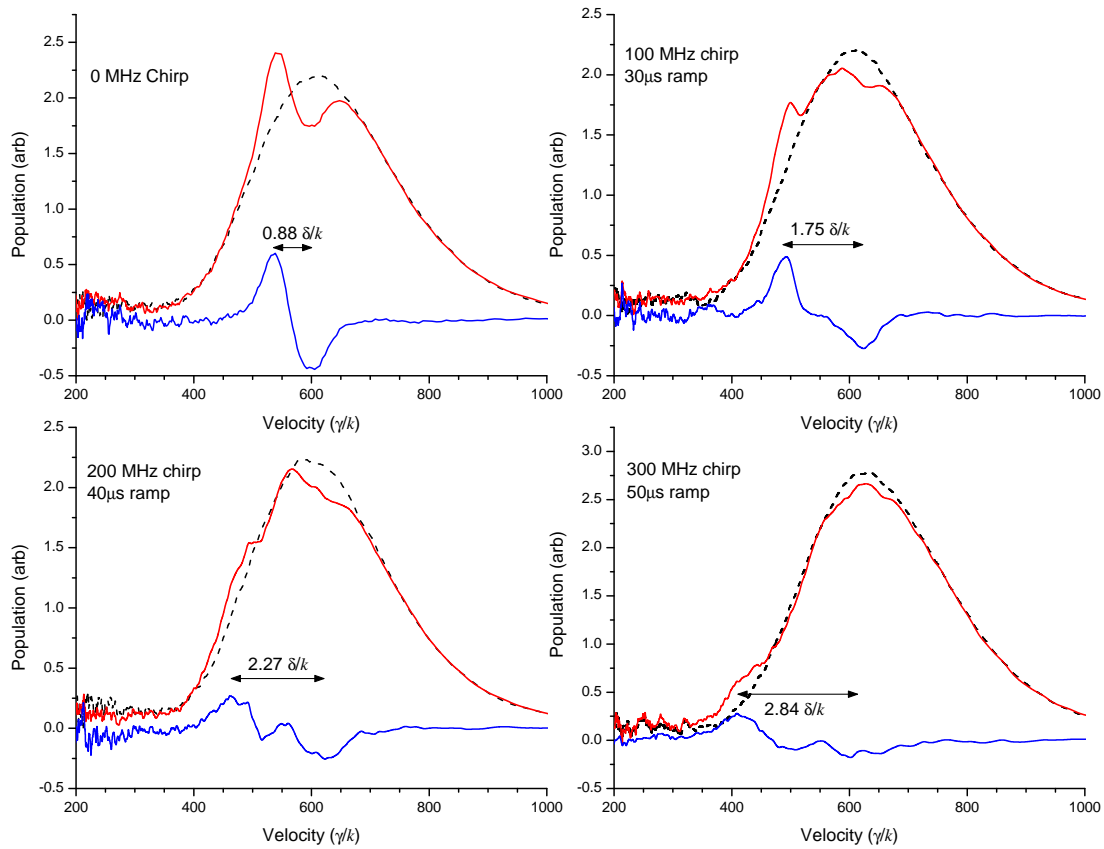


Fig. 7.1: Experimentally observed velocity profiles for $\delta = 74\gamma$, $\Omega_r = \sqrt{3/2}\delta$, and $\phi = \pi/2$ bichromatic force chirped by 0 MHz, 100 MHz in 30 μ s, 200 MHz in 40 μ s, and 300 MHz in 50 μ s.

phase $\phi = 0$ so that the BCF vanished. When chirped in this configuration, there was no repeatable change to the velocity distribution, confirming that the effect was due to the frequency chirping of the BCF.

A second method to verify the BCF is to adjust the bichromatic phase to $\phi = 3\pi/2$ such that the atoms are accelerated. This was done in a static mode to verify the presence of the BCF, but not in a chirped configuration. The inverting of the frequency chirps to create a chirped accelerator would have required extensive physical changes to the optics and re-calibration of new frequency chirp profiles. Because the result in the $\phi = 0$ result confirmed the dependence on the chirped result on the BCF, this was not done.

Additionally, the chirp was applied to one of the bichromatic beams while the other was blocked, resulting in a chirped single beam force, as described in Section 5.3. This was done in part to verify that the BCF is the dominant force component in the chirping. The result of a frequency chirped counterpropagating only bichromatic beam is shown in Fig. 7.2. As can be seen in the difference in velocity distributions of the static and chirped cases, the resulting shift in the single-beam peaks is much less than with the chirped BCF result. The chirped single-beam effect is largest at smaller frequency chirps, and decreases at higher rates. This is consistent with the difference in magnitude between the BCF and radiative forces, which assures that atoms affected only by radiative forces are not decelerated rapidly enough to stay resonant with the more rapidly changing Doppler shifts during a frequency chirp.

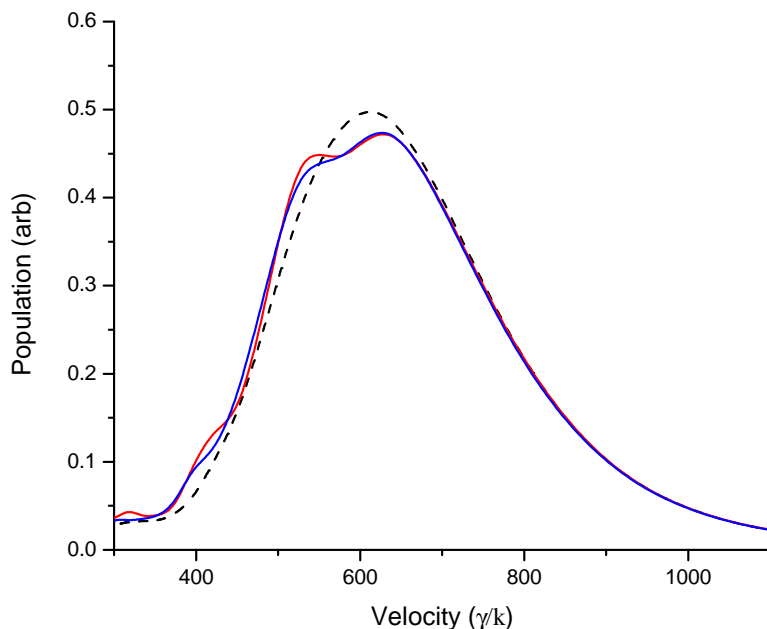


Fig. 7.2: Unchirped velocity distribution using only the counterpropagating bichromatic beam showing radiative force effects of each $\omega_a - kv \pm \delta$ frequency component (blue). The red plot is the same single bichromatic beam with a 40 μs wide 100 MHz chirp. Notice the very small but non-zero change in the locations of the $\pm\delta$ peaks at approximately 400 and 510 γ/k . The effect is much smaller than the corresponding chirp of the BCF data in Fig. 7.1 and vanishes when the matching copropagating frequency component is present.

Chirp MHz	Ramp μs	Slowing γ/k	Velocity Range δ/k
0	0	65	0.88
100	20 – 40	129	1.75
200	40 – 50	168	2.27
300	50	210	2.84
			3.67

Table 7.1: Summary of experimental BCF Chirp results for $\delta = 74\gamma$. All experiments used the optimal BCF parameters $\Omega_r = \sqrt{3/2}\delta$ and $\phi = \pi/2$

7.2 Analysis

The analysis of the chirp results are shown in Table 7.1, with slowing and velocity range measurements as defined in Section 5.1. A detuning of $\delta = 74\gamma$ with a 300 MHz frequency chirp provided a measured slowing of 210 γ/k , more than twice the slowing measured for a static detuning of $\delta = 185\gamma$ as reported in Section 5.1. Scaling the static $\delta = 185\gamma$ detuning to 370γ , to match the slowing result of the chirped slower, and comparing the irradiance requirements shows that the chirped method of BCF slowing results in a reduction in laser irradiance by nearly a factor of 10.

The experimental slowing results are in reasonably good agreement with the results of the Monte Carlo model described in detail in Appendix F, but with a reduced bichromatic force magnitude. The results of these model calculations are shown in Fig. 7.3.

The optimal experimental chirp ramp durations are found to increase with increasing chirp magnitude, consistent with the Monte Carlo models. However, the optimal ramps are in general longer than those predicted by the models. There was also no slowing observed with a 400 MHz chirp, indicating badly sub-optimal BCF conditions. The model predicts this behavior in two scenarios—a smaller BCF magnitude than expected, or periodic, temporary loss of the BCF as would

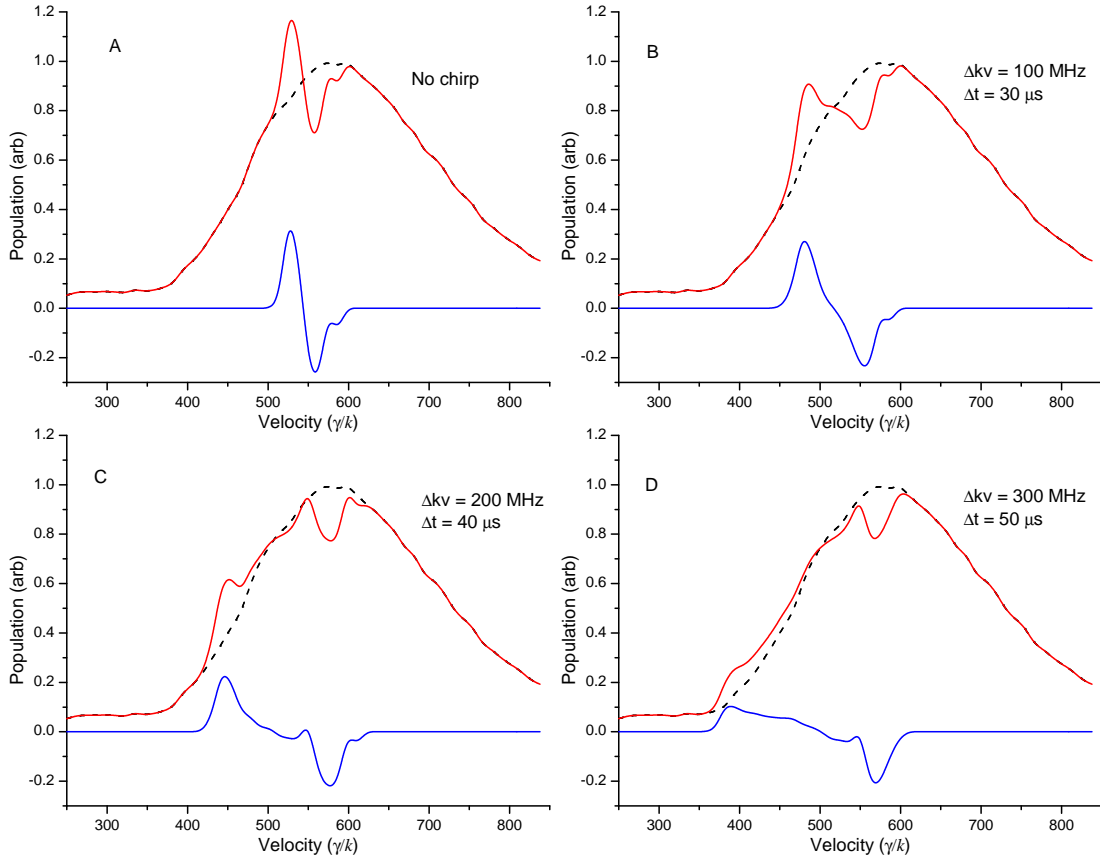


Fig. 7.3: Monte Carlo simulation results of the first generation chirped BCF slower showing unslowed atomic velocities (black, dashed) along with the slowed atomic velocity distribution (in red) and the difference (in blue). The BCF magnitude was reduced by 50% uniformly to obtain the data shown above, otherwise experimentally accurate parameters were used in the simulation. Compare to Fig. 7.1.

be caused by occasional large phase errors. Both of these factors are potentially present in the first generation configuration, as discussed in Section 7.3.

In the model calculation, the optimal ramp durations are about $10 \mu\text{s}$, which as just mentioned is considerably shorter than the experimentally observed optimum ramp durations listed in Table 7.1. Decreasing the magnitude of the BCF in the model results in an increase of the optimum duration, and can easily be made to coincide with experimentally observed values.

One difficulty in using a chopped atomic beam with a single frequency chirp such as the first generation slower used in these experiments is the relatively long atomic beam pulse duration. The chirped force velocity profiles in Fig. 7.3 show the result of this long pulse in which atoms are only slowed from a finite range. By the time the slower half of the atom pulse reaches the deceleration region, the initial pulse width of $40 \mu\text{s}$ has expanded to more than $120 \mu\text{s}$. Atoms on the leading edge and trailing edges of the pulse, especially the slowest atoms which arrive after the chirp ramp has ended, fall outside the chirped BCF profile and are not slowed. This effect is more pronounced with faster frequency ramps and is discussed in greater detail in Section 7.4. In a fully realized design, rapidly repeating chirp sequences could be used to assure that many more atoms experience the fully chirped force, as discussed in Section 7.4.

The most probable velocity of the chirped group of atoms experimentally matches the model prediction within $20 \gamma/k$, despite slowing a relatively small portion of the atoms from the initial velocity distribution.

7.3 First Generation Chirped BCF Hardware Shortcomings

Analysis of the mechanical and electronic stability of various components and subsystems of the first generation experimental configuration has led to the identification of several areas in need of improvement in the second generation slower.

7.3.1 Bichromatic Beat Note Phase Lock

Stability of the phase lock as described in Section 6.5 was measured by adding directional couplers to the beat note monitor photodiodes between the photodiode housing and the input to the phase discriminator circuit (Fig. 6.9). The 2 GHz Agilent oscilloscope used to calibrate the frequency chirps (Section 6.6) was used to display both beat notes, each on a separate input channel. The oscilloscope was triggered on the “master” rf AOM heterodyne signal, and the phase between the master and slave heterodyne beats was measured and the statistical averages taken for 1000 measurements. The standard deviation of the phase measurements was 3.5° with a range of 28° . The phase is most stable when set to the middle of the tuning range near 0.9 V, and gets progressively less stable toward each extreme, with both the standard deviation and range increasing by about 10%.

With a small detuning, this standard deviation is acceptable and will result in only a small loss of force. However, the larger excursions would significantly reduce the force magnitude. The length of these excursions at higher chirp rates is long enough to lose most atoms from inclusion in the BCF velocity profile, prematurely ending the Doppler frequency chirp at a random intermediate frequency.

There are two main sources of the instability, based on my analysis—

electronic noise and mechanical vibrations. The electronic noise is primarily in the phase discriminator circuit and electronic noise pickup in portions of the BNC cables, especially in locations with low signal amplitudes such as between the photodiodes and the AD8032 chip. Noise on the heterodyne beats causes error in the phase measurement and subsequent feedback to the rf amplifier phase lock. Efforts were made to physically and electrically isolate the bichromatic detuning rf components from other rf sources, which improved the stability, but only to the point reported above.

Mechanical and acoustic vibrations can include any physical process causing optical-scale path length changes between the lasers and the AOMs. Several improvements were made to the experimental configuration, included reducing thermal gradients and acoustic isolation of the bichromatic frequency generation optics. Increasing the chiller temperature to 20 C and thermally isolating the cooling lines from the optical table aided in reducing thermally-induced changes to the optical paths. Increasing the time allotted for thermal equilibration also helped. The effects of acoustic coupling to the optics and thermal changes due to the air conditioner cycling were reduced by enclosing the bichromatic frequency generation optics from AOM to beam re-combiner in a box constructed of one-inch thick rigid foam house insulation and acoustic damping foam. Reducing mechanical vibrations coupled into the floor of the lab from mechanical vacuum pumps was accomplished by placing them on one-inch pads of open cell rubber. This also measurably improved the phase lock stability.

7.3.2 Bichromatic Beam Pointing

Another significant issue that was never fully resolved in the first generation slower is the relative motion between the beam machine and the optical table. The beam machine has two small optical breadboard shelves, one on each side, that support focusing and steering optics of the bichromatic beams. Inside the beam machine five mirrors that steer the bichromatic beams to cross the atomic beam are mounted to the bottom plate of the beam machine.

When the beam machine is evacuated, the base plate flexes somewhat, changing the alignment of the five mirrors which are now under vacuum and cannot be adjusted. Very accurate pre-alignment of the lasers minimizes the amount of steering required to re-overlap the co- and counterpropagating bichromatic beams, but their locations relative to the atomic beam also change, requiring that the atomic beam defining aperture be adjustable. In short, there is no way to accurately ensure the positioning and overlap of the beams at the slower once the beam machine is under vacuum.

The second pointing error is a dynamic steering of the two bichromatic beams due to mechanical vibrations of the vacuum pumps coupled into the beam machine stand and the structures that support the two optical shelves. These vibrations cause an independent, periodic steering of each bichromatic beam resulting in a time-dependent variation in the overlap of the bichromatic beams in the interaction region with the atoms. This causes a fluctuation and reduction in the Rabi frequency where the beams overlap, reducing the BCF.

7.3.3 Repeatability of the Chirp Peak Magnitude

The frequency response of the lasers to the sharp change in chirp voltage that occurs at the chirp peak varies somewhat. If the return ramp is made longer, reducing the sharpness of the peak, the response consistency improves considerably, but variations can still be on the order of 10%. This will result in a spread in the Doppler shift at which the deceleration terminates, and a corresponding spread in the slow atom velocity distribution.

7.4 Extension to a Useful He* Slower

The results of the first generation of chirped BCF experiments were in keeping with the Monte Carlo model assuming that the BCF magnitude is somewhat reduced from optimal, although the model cannot account for variations in the chirp itself. The problems are likely due to some of several reasons identified and discussed in Section 7.3, with proposed remedies discussed in Chapter 9.

Even without major changes, simply scaling the 300 MHz chirp at $\delta = 74\gamma$ up to a detuning of approximately 123γ and better matching the bichromatic beam to atomic beam diameters will permit a frequency chirp magnitude of 600 MHz. This chirp, assuming an initial Doppler shift of 800 MHz, is the minimum required to slow a reasonable number of atoms to a final velocity of $\approx 50 \gamma/k$. Reducing the initial Doppler shift would permit a smaller frequency chirp magnitude at the expense of the number of slowed atoms.

The brightness of such a chopped atomic beam slower will be very low due to the atom beam duty cycle of only 1%. To create a slower capable of replacing the Zeeman slower, the chirp configuration must be adapted to use a non-chopped (cw) atomic beam. This requires that the frequency chirp repeats continuously

and as quickly as possible. Using a chirp ramp duration of $10 \mu\text{s}$ with an additional $5 \mu\text{s}$ to reset the laser frequency gives a cycle period of $15 \mu\text{s}$. The laser locks need to occasionally be reset, but it suffices to do this once every few milliseconds. For these estimates, we will assume the laser locks require $500 \mu\text{s}$ to reset, which must occur every 2 ms. This results in a fairly realistic estimate of a 50% duty cycle.

Assuming somewhat pessimistically that 10% of the metastable helium atoms are subject to slowing, combined with information from the model simulations, as shown in Fig. 7.4, we can estimate the brightness for the slower. The 50% duty cycle reduces the estimate of the number of He^* atoms slowed to 5% of the total metastable helium flux. From Section 4.2.2 the total He^* flux is $3 \times 10^{13} \text{ atoms/Sr}\cdot\text{s}$, so the effective slowed atom brightness will be $0.05(3 \times 10^{13} \text{ atoms/Sr}\cdot\text{s}) = 1.5 \times 10^{12} \text{ atoms/Sr}\cdot\text{s}$.

The predicted chirped BCF slower brightness is comparable to typical Zeeman slower brightness values, about $10^{12} \text{ atoms/Sr}\cdot\text{s}$ according to Refs. [24–27, 89]. As is common practice with Zeeman slowers, additional collimation of the atomic beam could increase the brightness by a factor of 2 to 50 depending on the method, if necessary [42, 89, 90]. However, due to the greatly reduced length of the slower, this scheme will not suffer from the transverse heating effects common in long Zeeman slowers.

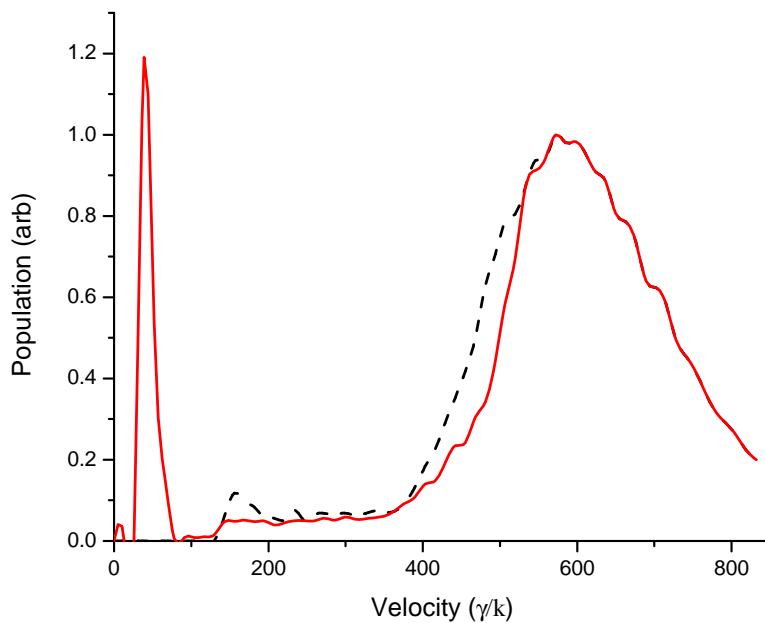


Fig. 7.4: Monte Carlo model for a chirped metastable helium slower using continuously repeating frequency chirps to maximize slowing showing the unslowed velocity distribution (black, dashed line) and the slowed velocity distribution in red. For this simulation $\delta = 123\gamma$, $\Omega_r = \sqrt{3/2}\delta$, $\phi = \pi/2$, and the frequency was chirped 600 MHz in 10 μ s, and the lasers and atom beam were the same diameter. Notice the wide range of initial atomic velocities contributing to the slowed atom peak centered at around $v = 50\gamma/k$. This results in a He* slower with a brightness comparable to a typical Zeeman slower.

Chapter 8

BCF in Multilevel Systems

We recently published a paper describing the potential of BCFs for direct laser slowing of molecules [91]. One major difference between the molecular case and the typical configuration for slowing metastable helium is the presence of several sublevels, all of which are included in the transitions cycled by the bichromatic fields. While there was nothing in any of the models described in Chapter 2 which would preclude several cycling transitions from contributing simultaneously to the BCF, this had never before been tested. We realized that it was possible to verify that this would work in He^* by using linearly polarized light to cycle multiple Zeeman sublevels simultaneously. Modifying the single-stage slower configuration described in Chapter 4 by removing the final quarter-wave retarder from the path of each bichromatic beam allowed us to test such a multilevel configuration and compare the results to the single-level system. The experiment in He^* and its results are summarized in this chapter, as is our proposed scheme to use the BCF to slow molecules. Please see the original work in Ref. [91] for additional details.

8.1 BCF in He* with π -Polarized Light

8.1.1 Theoretical Considerations

The BCF slowing of He* typically used in these experiments and prior work [35, 36] cycles the $2^3S_1 \leftrightarrow 2^3P_2$ transition at 1083 nm. The $(m', m) = (1, 2)$ component is cycled by the use of σ^+ circularly polarized light, where m' denotes the projection quantum number in the 2^3S state and m , the 2^3P state, as indicated by the angled (black) dashed line in Fig. 8.1(b). This arrangement has the advantages of providing the largest possible transition strength as well as behaving like a near-perfect two level atom due to the lack of hyperfine structure. An important consequence of this, discussed in Section 3.2, is that unwanted coupling to the 2^3P_1 state is minimized, significantly reducing ac Stark effects.

If the bichromatic beams are instead linearly polarized (π polarization), then the (-1,-1), (0,0), and (1,1) transitions will be cycled simultaneously, as shown in Fig. 8.1(b). Although the $2^3S_1 \leftrightarrow 2^3P_2$ transition is closed, there is strong off-resonant coupling to the 2^3P_1 level via the (-1,-1) and (1,1) transitions (the (0,0) transition is forbidden by selection rules). In moving to this multilevel scheme in He*, the optical power requirements increase somewhat because the line strengths are weaker. Considering the difference in transition strengths, the largest force should occur when the (-1,-1) and (1,1) transitions are driven slightly below the optimal Rabi frequency $\Omega_r = \sqrt{3/2} \delta$, where in these experiments $\delta = 185\gamma$. This requires an irradiance of $\lesssim 68 \text{ W/cm}^2$, about twice the irradiance required to optimally drive the (1,2) transition with σ^+ -polarized light at the same detuning. We choose to use the full 68 W/cm² irradiance, so the slightly stronger (0,0) transition is consequently driven at a Rabi frequency of $\Omega_r = \sqrt{2} \delta$, too high by about 15%. Based on experimental measurements of the BCF with σ^+ -polarized

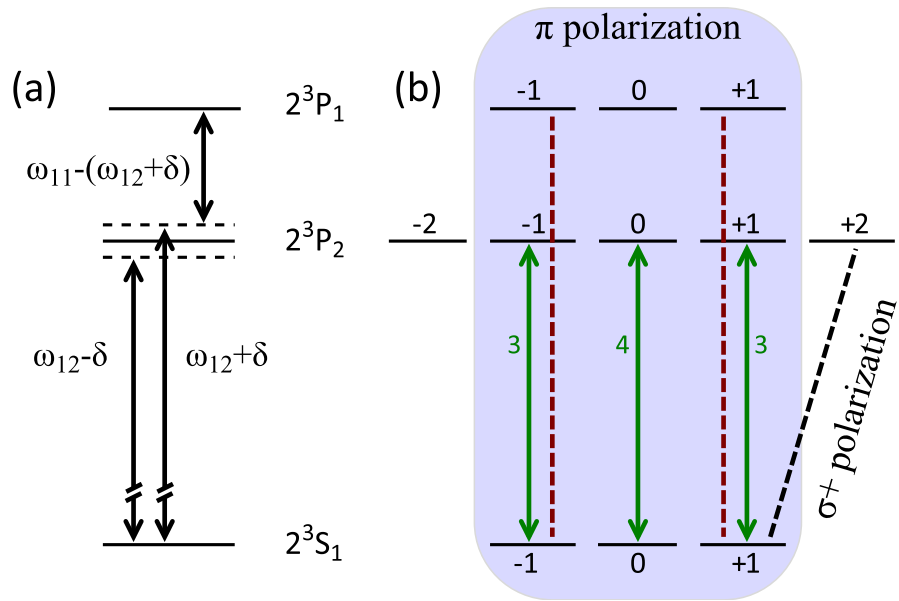


Fig. 8.1: (a) Relevant energy levels in metastable helium, showing the two BCF frequency components and an off-resonant coupling to the 2^3P_1 state, discussed in the text. The distant $J' = 0$ fine-structure level plays no significant role and is not shown. (b) Zeeman sublevels, with vertical solid arrows indicating allowed transitions for π -polarized light, labeled with their relative transition strengths [60]. The vertical dashed lines indicate transitions giving rise to off-resonant excitation and ac Stark shifts, and the angled dashed line indicates the transition excited by σ^+ polarization in the conventional BCF configuration for He^* .

light using a range of irradiances, the predicted reduction in force is only about 5% when the peak irradiance is too high by 15%.

As discussed in Section 3.2, off-resonant coupling to nearby fine-structure levels is a significant consideration. Coupling to the 2^3P_1 level, which lies 2.29 GHz above the target 2^3P_2 state, occurs via the (-1,-1) and (1,1) transitions, indicated in Fig. 8.1 by vertical dashed lines, with the same line strengths as for equivalent components of the $2^3S_1 \leftrightarrow 2^3P_2$ transition. Because the 2^3P_1 state decays radiatively back to the 2^3S_1 state, there is no loss of atoms, but this coupling does cause two other issues:

(1) If the laser power is sufficiently high, the off-resonant transition rate can be significant, but still much slower than the transition rate for the target transition, so it should not interfere with the BCF. However, if the rate is comparable to the spontaneous decay rate γ , then the two coupled sublevels may be significantly populated. The estimated excitation rate for the current experimental parameters is only 0.027γ , too small to have any measurable effect.

(2) There can be significant level-dependent ac Stark shifts for the 2^3S_1 , $m = \pm 1$ levels, which shift the typically symmetric $\pm\delta$ detuning into an asymmetric configuration, as described in Section 3.2. The differences between the σ^+ -polarized light case discussed earlier and the current consideration of π -polarized light is that there are two coupled sublevels and the full laser irradiance contributes to the coupling. The ac Stark shift is calculated following the same procedure described in Section 3.2, except that there are two contributing transitions so the summation in Eq. (3.2.1) is over the participating $m = 1, -1$ levels. The time-averaged shift is $\Delta\omega_{\text{ac}} = -120\gamma$. This is more than 1/3 of the bichromatic detuning which, using Table 8.1, leads to a reduction in the BCF of about 20%.

However, the $m = 0$ sublevel is nearly unaffected since its only interaction is with the distant 2^3P_0 state, which is detuned by 32 GHz.

Taking all these effects into account and averaging over the three m sublevels of the 2^3S_1 state, we estimate that the effective bichromatic force should be $F_{\text{eff}} \approx 0.45F_{\text{BCF}}$, where F_{BCF} is the average bichromatic force for σ^+ polarization. While the reduction in force is significant, the atoms spend approximately 26 μs in the bichromatic beams, about 5.6 times the bichromatic slowing time given by Eq. (2.5.4) for σ^+ light. Thus, even with a 55% reduction in the average force, the atoms should still be slowed through the full velocity range of the BCF.

8.1.2 Experiment and Results

To test the BCF cycling multiple sublevels, the experimental configuration shown in Fig. 4.1 for σ^+ polarization was modified by removing the pair of $\lambda/4$ retarders from the vacuum system. The AOMs were then configured such that the bichromatic detuning is $\delta = 185\gamma$ and the BCF center frequency was shifted to $\pm kv/2\pi = \pm 800$ MHz, corresponding to an atom velocity of $494\gamma/k$. The irradiance was set to 68 W/cm² to drive the three cycling transitions as described above. The other experimental details were the same as those in the σ^+ polarization case described in Chapter 4.

The velocity profiles of He* with BCF slowing using σ^+ and π polarizations are shown in Fig. 8.2. The slowing in both cases is approximately $100\gamma/k \approx \delta/2k$, as expected, and consistent with other results in Section 5.1. Although we cannot accurately measure the force reduction in the π polarization case, we can deduce from the similarity of the slowing profiles in Fig. 8.2 that the reduction is by no more than a factor of 3 – 4. This demonstration confirms that the BCF can be

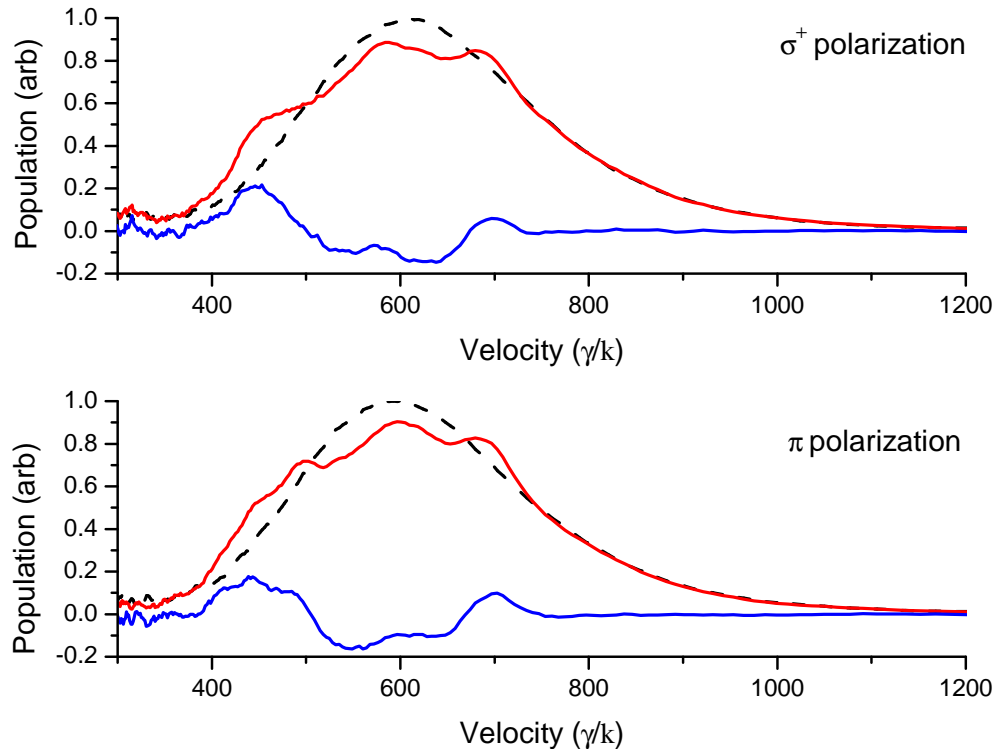


Fig. 8.2: Comparison of bichromatic slowing of metastable helium using σ^+ polarization (top) and π polarization at twice the laser irradiance (bottom). The atom velocity profile without the BCF present is shown in dashed black line, with the BCF in red, and the difference in blue. Effects of the BCF are observed between about 400 and 600 γ/k , but are confined to about 20% of the atoms within the BCF velocity range, because of limited transverse overlap with the tightly focused lasers. The additional shifts in the velocity profile at 600 – 750 γ/k are not bichromatic in nature—they arise from the strongly saturated force from one of the four component beams acting alone, as discussed in Section 5.3.

Table 8.1: Calculated BCF magnitude and measured BCF depletion percentages, as a function of the frequency shift of ω_0 from exact atomic resonance. Shifts are measured as a fraction of the bichromatic detuning δ . Because the interaction length for this measurement was 3–4 times the BCF slowing distance, little effect is expected until the force is reduced by a corresponding factor. The calculated BCF magnitude for a shift of 0.4δ could not be quantified due to the presence of resonance peaks and noise.

Fractional Shift	Force Reduction η	Depletion (%)
0	1.0	35
0.1	0.76	30
0.2	0.45	27
0.3	0.25	29
0.4	N/A	16

used to slow atoms with more than one cycling transition.

In a related experiment, I tested the effects of frequency shifts in the pure two-level configuration (using σ^+ polarization). The basic BCF slowing experiment shown in Fig. 4.1 was modified by removing the laser amplifier, and a smaller bichromatic detuning $\delta = 62\gamma$ was used. AOMs in each bichromatic beam were used to shift the center frequency ω_0 of the bichromatic spectrum. The slowing efficiency was analyzed by measuring the depth of the depletion dip in the velocity profile. The results are summarized in Table 8.1 and show only minor effects until the center frequency shift is 0.4δ . Calculated force profiles (see Fig. 3.5 for an example) with the same fractional shifts were used to estimate the “force reduction factor” η , such that the asymmetrically detuned or shifted force can be written $F'_{\text{BCF}} = \eta F_{\text{BCF}}$. The experimental results are consistent with the calculated forces after taking into account that the slower length is 3 – 4 times the BCF slowing distance. The key result from this experiment is that by providing a sufficient slower length, the BCF works well for shifts of up to 0.3δ , which is an important verification that the BCF will be robust against small molecular frequency

splittings, as discussed in Section 8.2.

8.2 Direct Laser Slowing of Molecules

The application of the BCF to the direct laser slowing of molecules is discussed in depth in Ref. [91], so I will only summarize the key points. The dramatically increased magnitude of the BCF at large bichromatic detunings compared to the radiative force makes it appealing for slowing molecules, where the available interaction time is typically limited by out-of-system radiative decays. As many as several hundred stimulated BCF cycles can occur between successive radiative decays, reducing their impact commensurately. Despite the potential benefit of the BCF as a means to slow molecules, there appears to be just one previous attempt to apply a BCF-like force to molecules [16]. In that experiment, Voitsekhovich and co-workers used counterpropagating mode-locked pulse trains to produce a small transverse deflection in a Na_2 beam. The laser pulses approximated π -pulses and the temporal pulse separation was analogous to the beat note phase ϕ . The total momentum shift given to the molecule was $20\hbar k$, and was limited by unwanted optical pumping into dark states. An alternative to BCF slowing is described more recently by Barker [92] in which he uses a high intensity moving optical lattice to create strong optical forces on benzene.

Slowing molecules with the BCF is much like slowing atoms, as described in Chapter 2, with the significant exception that the transitions are at best near-cycling, so molecules will eventually be lost to out-of-system radiative decay unless additional repump lasers are added. One particularly good candidate for BCF slowing is the $A - X$, $(0 - 0)$ band in MgF, CaF, or SrF, which has a Franck-Condon factor in the range $0.98 - 0.99$ [93–95]. These transitions can undergo

50 – 100 spontaneous decay cycles before a vibrational repump is needed. The loss-limited interaction time for a molecule with spontaneous decay lifetime $1/\gamma$ and Franck-Condon factor \mathfrak{F} can be written

$$T_{\text{loss}} = \frac{1}{\gamma P_e(1 - \mathfrak{F})} \quad (8.2.1)$$

where P_e is the probability that the molecule is in the excited state. For a single-frequency laser at the optimal irradiance $P_e = 0.3$, but the situation is more complicated with the four frequencies in the BCF. Referring to the DDA model of the BCF described in Section 2.2, we see that a molecule following the optimal dressed-atom trajectories will be composed primarily of the ground-state wave function. However, because of averaging over velocity profiles and laser mode profiles we assume that $P_e \approx 1/3$, near the center of the possible range. Assuming the BCF is constant over the velocity range, the change in velocity over the time T_{loss} is

$$\Delta v_{\text{loss}} = \frac{F_{\text{BCF}}}{M} T_{\text{loss}}, \quad (8.2.2)$$

where M is the mass of the molecule. In the two-level case, using Eq. (2.1.8), this simplifies to

$$\Delta v_{\text{loss}}^{\text{TLA}} \simeq \frac{3}{\gamma(1 - \mathfrak{F})} \frac{\hbar k \delta}{\pi M}. \quad (8.2.3)$$

Ignoring internal splittings and degeneracies is not realistic, however, and the fine structure (fs) and hyperfine structure (hfs) as well as the magnetic quantum numbers m_J or m_F must be included in any realistic model. For example, both CaF and SrF have nuclear and electronic spins $I = S = 1/2$, leading to the structure shown in Fig. 8.3. The aspects of particular importance to bichromatic slowing are that the sublevels each have different transition rates that span

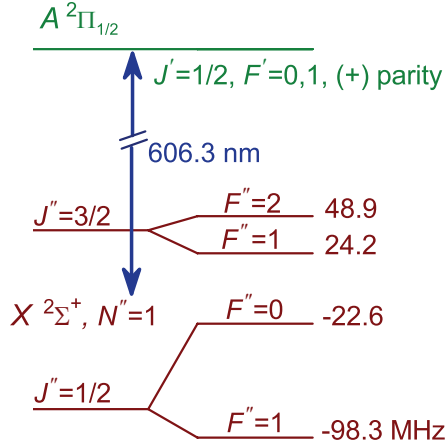


Fig. 8.3: Rotationally closed transition from the $N''=1$ level of the $X\ ^2\Sigma^+, v''=0$ ground state of CaF to $J'=1/2$ in the $A\ ^2\Pi_{1/2}, v'=0$ state. The corresponding transition in SrF was used for laser cooling in Ref. [96]. The ground-state fine structure and hyperfine structure give rise to a total of 12 m'_F and m''_F levels, not shown. In traditional notation [97] this is a combination of the near-degenerate $Q_{12}(0.5)$ and $P_{11}(1.5)$ branches. Figure is reproduced from Ref. [91].

nearly an order of magnitude [95], and some will be detuned from resonance and not driven at the optimal rate. To account for these effects, two adjustments are made. First, the estimate for P_e must be modified to include a weighted degeneracy factor with the same limit as the two-level case,

$$P_e \approx \frac{g_e/2}{g_e/2 + g_a + g_d}. \quad (8.2.4)$$

Here g_e is the degeneracy of the excited state, g_a is the degeneracy of the ground-state levels active in the BCF, and g_d is the degeneracy of “dark” ground state levels that are populated but do not participate in the BCF. The method used for adjusting the excited-state fraction to a slightly non-statistical value has an inherent arbitrariness to it, since for a strongly coupled multilevel system, the actual value is determined by system-dependent coherent cycling. The $g_e/2$ weighting

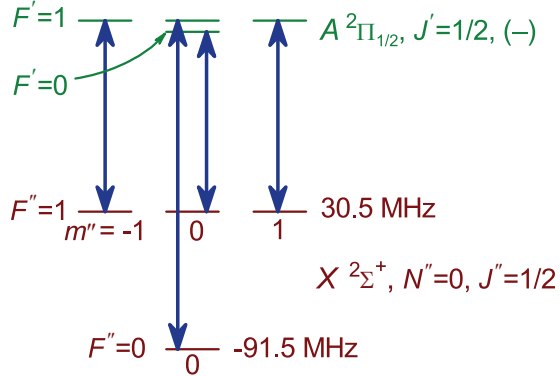


Fig. 8.4: Arrows show the four quasi-cycling transitions between the m''_F and m'_F sublevels of the $Q_{11}(0.5)$ branch in CaF, when illuminated with π -polarized light. All four line strengths are the same. Energies are not drawn to scale. Radiative decay to $N'' = 2$ is allowed, so a rotational repumping laser tuned 62 GHz to the red is required. Figure is reproduced from Ref. [91].

is chosen because it correctly treats the effects of weakly-coupled dark levels on a system with multiple decoupled two-level cycles, such as the scheme shown in Fig. 8.4. The BCF level-averaged cycling rate is reduced if only a small portion of ground-state levels are active, requiring an additional degeneracy factor g_a in the denominator of Eq. (8.2.4).

The second adjustment accounts for additional effects such as variations in line strength and frequency shifts, as well as system-dependent deviations due to interference in multilevel coherent cycling that will further reduce the BCF, by again using a “force reduction factor” η . With both of these adjustments, Eq. (2.1.8) becomes

$$F_{\text{BCF}} = \frac{\hbar k \delta}{\pi} \frac{g_e/2 + g_a}{g_e/2 + g_a + g_d} \eta. \quad (8.2.5)$$

The radiative force will also be reduced, although here the treatment of dark

states and degeneracies is purely statistical:

$$F_{\text{rad}} = \frac{\hbar k \gamma}{2} \frac{g_e}{g_e + g_a + g_d}. \quad (8.2.6)$$

Three experimental schemes have been devised to deal with the impact of degeneracies and inexact Rabi frequencies described above. Any one of these may be preferable depending on the exact system being investigated:

- (1) Add a small magnetic field to circumvent optical pumping into dark states, but otherwise ignore the degeneracies. The BCF is always positive or zero given the proper beat note phase, so as long as the force is applied for several radiative lifetimes, each molecule will spend some time in cycling in sublevels for which the BCF is near optimal. The time averaged force, although reduced significantly, is the same for all molecules. An experiment and accompanying calculations based on solutions to the optical Bloch equations (see Section 2.3) is described in Section 8.1 and shown in Table 8.1. These calculations show that for the case of unequal detunings, the force is reduced under increasing center frequency shifts, but retains about the same velocity range.
- (2) Use alternating pulses of BCF beams with σ^- polarization, and optical pumping cycles with σ^+ polarization. To access all of the fs and hfs levels, superimposed modulator-induced sidebands can also be added, as described in Ref. [93]. The population will mainly cycle between extremal m_F levels, creating an effective two-level system that lasts for a few radiative cycles. By applying the BCF beams during this time, then applying the repump beam for 4-10 radiative cycles, a BCF with values of η in the range of 0.2 to 0.6 might be achievable.
- (3) Avoid the problem by using a rotational branch in which the upper and lower state sublevel structures are similar and there are no dark states, such as

Table 8.2: Representative BCF parameters for CaF, assuming no vibrational repumping, $P_e = 2/19$, $\eta = 0.78$, and a degeneracy factor of $6/19$ in Eq. (8.2.5). With vibrational repumping, T_{loss} would increase to $\approx 350 \mu\text{s}$ and Δv_{loss} would exceed Δv_b , although the forces F_b and F_{rad} would be reduced by nearly a factor of two due to the additional degeneracy of 17 dark states with $v''=1$.

Parameter	Symbol	Value
Bichromatic detuning	$\delta/2\pi$	250 MHz
Deceleration	a	$1.4 \times 10^6 \text{ m/s}^2$
Bichromatic velocity range	Δv_b	150 m/s
Loss time	T_{loss}	$14 \mu\text{s}$
Loss-limited velocity range	Δv_{loss}	19.4 m/s
Optimal irradiance	I_b	60 W/cm ²
Ratio of BCF to rad. force	$F_b : F_{\text{rad}}$	12.4

the $Q_{11}(0.5)$ branch in CaF, shown in Fig. 8.4. These transitions are typically not rotationally closed, but using a rotational repump laser can close the hole. Using π polarized lasers, there are four separate pairs of cycling magnetic sublevels, all with the same line strength, as indicated by the vertical arrows in Fig. 8.4. In this case η depends primarily on frequency shifts, and the degeneracy factors g_a and g_d must be addressed.

Table 8.2 lists representative parameters based on the A -state lifetime and the $Q_{11}(0.5)$ saturation irradiance $I_s = 22.2 \text{ mW/cm}^2$ [95]. If a bichromatic detuning of $\delta/2\pi = 250 \text{ MHz}$ (154γ) is used, Eq. (8.2.2) predicts a velocity range of $\Delta v_b = 150 \text{ m/s}$. Using a buffer-gas cooled source producing CaF with a common-mode velocity of 140 m/s as used in Ref. [98], this range is sufficient to slow the molecules all the way to zero velocity. The excited state probability is calculated using Eq. (8.2.4) with $g_e = 4$, $g_a = 4$, and $g_d = 13$, based on the 13 dark sublevels of the $N'' = 2$ state. The force reduction factor is estimated to be $\eta = 0.78$ based on optimal BCF for the three $F'' = 1$ levels and a very inefficient BCF for the $F'' = 0$ level. In the table, the attainable velocity change is limited to only

19.4 m/s due to vibrational loss to $v'' = 1$. However, the addition of a vibrational repump would remedy this and permit slowing through the full range of the BCF.

An experiment is currently underway to study BCF slowing of CaF, although it will initially utilize $B - X$ transitions rather than $A - X$, due to an even higher Franck-Condon factor accompanied by some practical laser considerations. The even greater promise of the B state was recognized only after Ref. [91], as well as my own role in the project, was complete.

Chapter 9

Next Generation BCF Decelerator for He*

Based on the results of the first generation chirped BCF experiments described in Chapter 7 and the issues with the experimental configuration discussed in detail in Section 7.3, there are several changes that should be made in the design of a second generation system:

1. Increase the bichromatic detuning to $\delta = 123\gamma$ or greater, and increase the beam waists as much as available laser power will allow.
2. Improve the stability of the beat note phase.
3. Redesign the vacuum chamber enclosing the BCF interaction region to improve optical access.
4. Replace the fixed quarter-wave retarders with liquid crystal variable retarders.
5. Reduce vibration and motion of the beam machine.

9.1 Bichromatic Detuning Increase

One proposed experimental reconfiguration addressing these recommendations is shown in Fig. 9.1. The detuning is increased to 123γ in order to ensure the

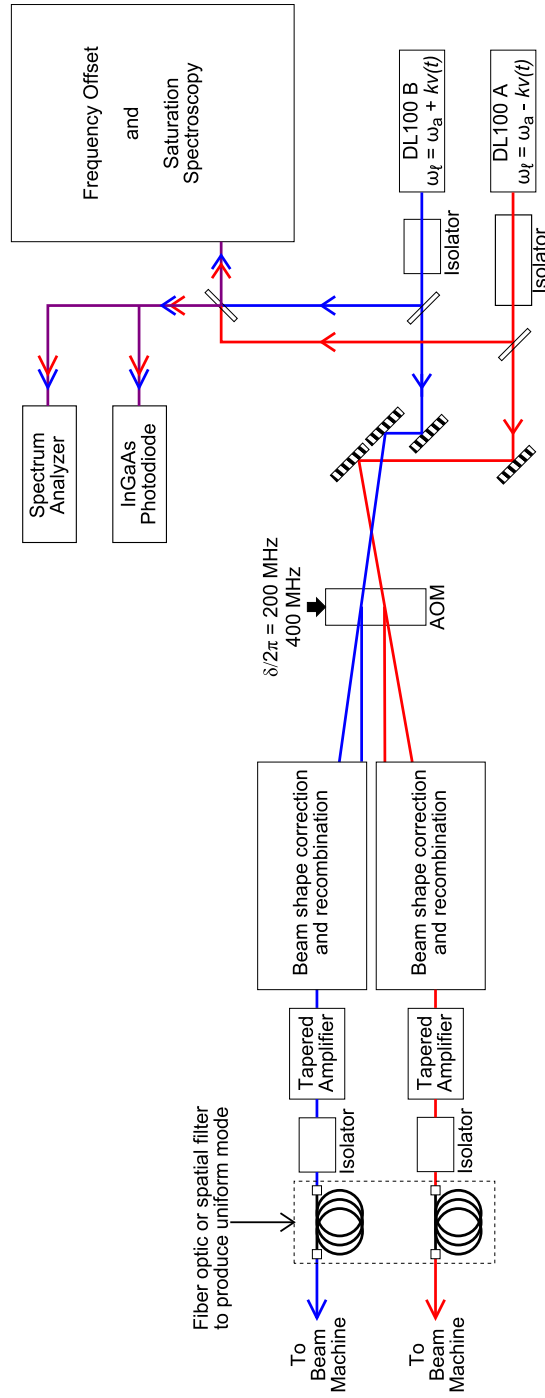


Fig. 9.1: Proposed second generation chirped BCF slower. Major changes include increasing the bichromatic detuning to $\delta = 123\gamma$, inclusion of tapered amplifiers, and the reconfiguration of the bichromatic frequency AOM.

required 600 MHz chirp can be met by scaling up the results at 74γ as discussed in Section 7.4. The first generation experiment with a detuning of 74γ had little overhead left in the diode laser outputs. In order to scale up the bichromatic detuning, the laser power requirement will increase quadratically from approximately 55 mW/mm^2 at 74γ to 153 mW/mm^2 at 123γ . The addition of a pair of tapered amplifier (TA) laser diodes, one to each of the $\pm kv(t)$ beams, will provide sufficient power to meet the increased bichromatic detuning with enough overhead to increase the diameter of the beam waists, increasing the number of slowed atoms.

There are two obvious possible locations for the TAs—before the bichromatic frequency generation, or after, where the bichromatic beams would be amplified, as shown in Fig. 9.1. The DL100 lasers should provide enough power to saturate the TAs at each bichromatic frequency, and placing the amplifiers after the bichromatic frequency generation conserves laser power since the portion lost in the bichromatic beam recombination is from the seed laser power, not the amplified power. This placement has the added benefit that it will eliminate the various optical issues introduced by the AOM discussed in Section 4.6. The TA scrambles the laser modes, eliminating the AOM-induced hole in the zero-order mode, allowing better AOM diffraction efficiencies and mode overlap of the bichromatic frequencies. Additionally, as long as the optical power in each frequency component will saturate the amplifier, the two output frequencies in each bichromatic beam will have the same optical powers. This power equalization has already been observed when using a saturated fiber amplifier. And finally, beam shape corrections after the AOMs need only be sufficient that the zero and first-order frequency components each saturate the TA.

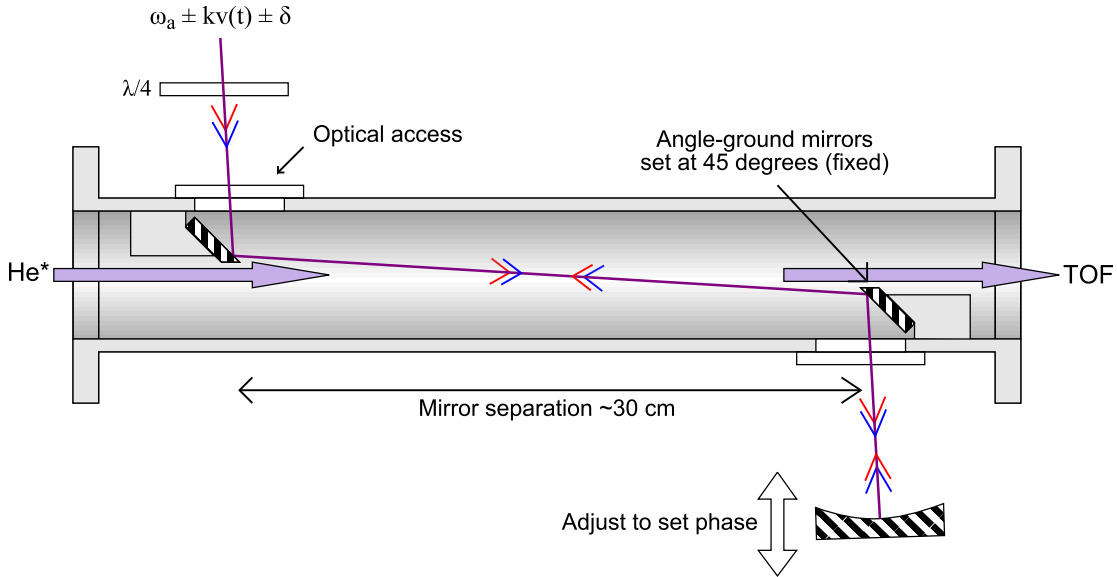


Fig. 9.2: Diagram of the improved interaction tube described in Section 9.3 showing the single TA configuration with both bichromatic beams copropagating through the interaction region. The arrows indicate red or blue detuning, and the leading arrow of the pair indicates the beam detuned to interact with the atomic beam.

A third possibility, which would be a significant departure from the experimental configuration of the first generation slower, is to amplify both bichromatic beams together in the same TA. This results in a single beam containing all four frequencies. The multi-frequency slower beam can be passed copropagating through the atomic beam (e.g., as the $+kv(t)$ beam) and retroreflected to create the counterpropagating (e.g., $-kv(t)$) beam, as shown in Fig. 9.2. The Doppler offsets of each bichromatic pair provide sufficient detuning ($\pm 2kv(t) \pm \delta$) that the improperly Doppler shifted components should not interfere with the slowing. This is somewhat similar to the configuration used for the bichromatic collimation experiments in the Metcalf group, described in Refs. [35, 36]. Here, the beat note phase can be controlled in two ways—using the frequency tuning method discussed in Section 9.2, and by adjusting the position of the retroreflecting mirror. The

round-trip distance from the center of the interaction region to the retroreflecting mirror sets the optical delay between the co- and counterpropagating beat notes, determining the phase. The distance from the center of the interaction region to the retroreflecting mirror can be measured accurately and therefore only a limited amount of adjustability needs to be incorporated. This optical arrangement is also easier to align than the previous ones employing separate bichromatic beams.

Some attention, however, needs to be paid to the potential of large ac Stark shifts due to the retroreflected $+kv(t)$ components, which will be detuned by as little as 400 MHz from the 2^3P_1 level. This could potentially lead to very strong coupling of that state to the 2^3S_1 level, depending on the portion of the bichromatic beam that is contaminated with linear polarization. See the discussion in Section 3.2 for more information.

9.2 Improved Beat Note Phase Stability

The stability of the bichromatic beat note phase can be addressed in several ways, two of which will be discussed here: by improving the first generation scheme, or passing both beams through a single AOM. Improving the first generation scheme would primarily include cleaning up electronic noise in the AD8025 phase error feedback loop and improving the mechanical stability of the optics. The photodiodes should be integrated into the same enclosure as the AD8025 chip, probably battery powered. This should reduce pickup accompanying the low amplitude beat note signals and reduce power supply fluctuations and pickup along the power cable. The AD8025 circuit board and circuit design needs additional rf optimization. Probably the easiest means to implement this is to purchase the development package from Analog Devices that includes the AD8025 installed on

a multilayer board designed for use up to 3 GHz.

The second method is to pass both beams through a single AOM, as shown in Fig. 9.1. In this case, the phase between the two bichromatic beat notes is set by the separation of the two input beams in the AOM crystal, modulo the acoustic wavelength. The phase can be adjusted by making small changes in the AOM rf frequency. The phase stability then depends only on the frequency stability of the rf oscillator, which in this case is better than one part in 10^4 , and on the stability of the optics steering the beams into the AOM.

In both cases, keeping the two beams on closely spaced parallel optical paths until they enter the AOM is critical for reducing thermally induced path length changes on the optical table. Where possible, the beams could even use the same mirrors, and the length of the optical path should be minimized. The stability of the optics mounts, in particular the AOM and beam re-combiner mounts, should be improved. The mounting of the lenses in the cylindrical telescopes could be improved as well.

9.3 Improved Optical Access to Interaction Region

The major drawback of the beam machine is its large volume, which requires several *in vacuo* optical components in order to have a $\approx 1^\circ$ bichromatic beam crossing angle with the atomic beam. Flexing of the beam machine base, to which the optics are fastened, causes misalignment of the optical elements. Inaccessibility of the optical elements complicates re-alignment during an experiment.

At minimum, an optical breadboard should be cut to fit inside the detector side of the beam machine to decouple the optics mounting from the beam machine base. It should be fastened to the beam machine base only at the cor-

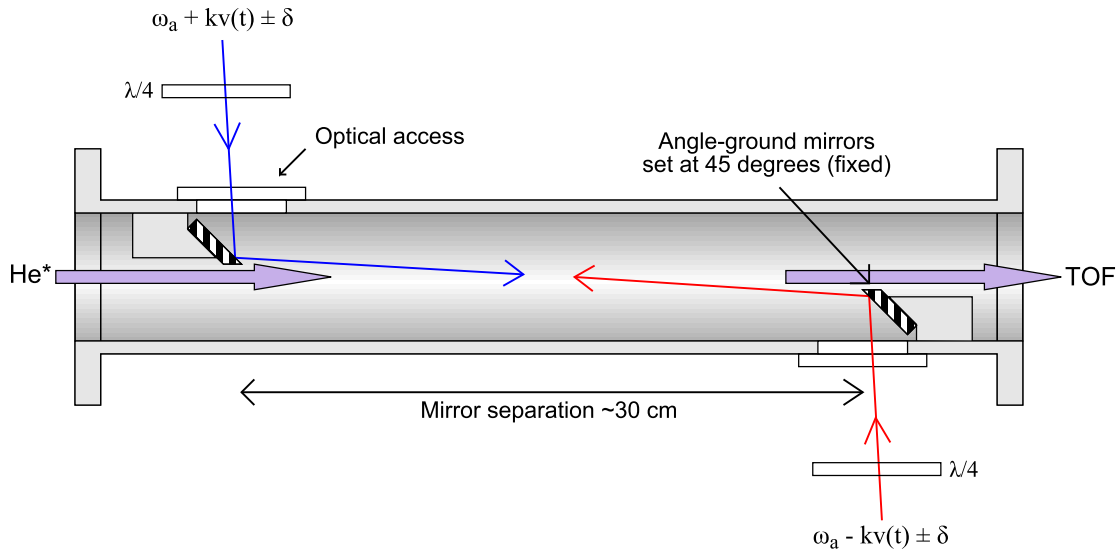


Fig. 9.3: Proposed interaction tube showing basic structure and essential elements. The He^* atomic beam passes through the center of the tube. Internal mirrors, mounted at fixed 45° angles to the central axis at either end, are angle ground to minimize the distance to the atomic beam. External optics steer the bichromatic beams to cross the atomic beam at $\approx 1^\circ$. Electrically adjustable quarter-wave retarders rotate the linearly polarized bichromatic beams to either σ^+ and σ^+ or σ^- and σ^- .

ners where the deflection is minimized, and larger holes could be cut to increase conductance to the turbomolecular pump. This would dramatically reduce the misalignment caused by deflection of the beam machine base under vacuum, but without addressing the lack of optical access to the experiment.

A better approach is to re-configure the beam machine, and design an interaction tube which contains only the final pair of steering mirrors and the helium beam, as shown in Fig. 9.3. The mirrors have an angle-ground edge to minimize the spacing to the atomic beam and are fastened to fixed-angle mounts. The transverse separation of the mirrors will probably need to be on the order of 2 mm based on the first generation slower, but this will need to be optimized once the system is complete. Because the final mirror angles are fixed, alignment

of the bichromatic beams to each other and to the atomic beam will require two mirrors in each beam prior to the interaction region. The optical retarders can also be placed outside the vacuum now, and the voltage variable retarders that were previously purchased can be used.

The atomic beam entrance end of the interaction tube will be fixed to the beam machine which will need to be re-configured as discussed in Section 9.6. The slowed atom beam output end should be mated to the TOF tube via an intermediate coupling chamber with a port for the turbomolecular pump that will provide pumping for the entire slowing and detection volume. This coupling chamber could also double as a MOT loading chamber after the development phase is over and the TOF setup is no longer needed.

9.4 Prescale the Heterodyne Frequency

The heterodyne signal used in the offset lock has a frequency of approximately 1.6 GHz. One complication this presents is that a high frequency oscilloscope such as the 2 GHz oscilloscope referenced in Section 6.6 must be used to calibrate the chirp voltage ramps. Oscilloscopes this fast are expensive, and datasets spanning at least $50 \mu\text{s}$ are very large making them slower to process. However, detuning one diode laser during the chirp calibration to reduce the heterodyne frequency is unreasonable since the laser chirp calibration would be different with the changed operating conditions. A better solution is to divide down the heterodyne frequency using a purpose-built divide-by- n prescaler chip such as the divide-by-4 Hittite Microwave HMC365S8GE. Using such a prescaler would allow the use of a 400 MHz oscilloscope with no loss in chirp calibration accuracy. Additionally, two cascaded prescalers could be used to monitor the

frequency chirps in real time using a relatively inexpensive oscilloscope.

9.5 Liquid Crystal Variable Retarders

Optimization of the polarization of the bichromatic beams may be facilitated by replacing the standard quarter-wave retarders in Figs. 9.2 and 9.3 with liquid crystal variable retarders. The variable retarders can produce an e -ray retardation of 0 to 90° . Phase shifts in the dielectric mirror coatings have been measured to be on the order of $1 - 2^\circ$. Consequently, a retardation a few degrees more or less than 45° should produce a purer circular polarization than that obtained using a zero- or low-order $\lambda/4$ retarder plate. The variable retarders also allow rapid polarization changes for test purposes. However, these retarders have not yet been tested in the specific application of static or chirped BCF slowing of atoms or molecules.

9.6 Reconfiguration of the He* Source and Beam Machine

As mentioned already in Section 9.3, the most expedient reconfiguration of the source to provide a metastable helium beam for the second generation chirped slower is to reverse the direction of the current source in the beam machine, as shown in Fig. 9.4. The flange currently providing access for the high voltage needle spacing (which is not required for the source operation) can be reconfigured to mate to the interaction tube. The skimmer (acting as a differential pumping aperture), chopper, and beam defining apertures will need to be placed inside the beam machine. This is to minimize the diameter of the interaction tube, providing better optical access to the beam. Also, in the third phase when the chirped BCF slower is realized in a cw beam, the chopper will no longer be needed,

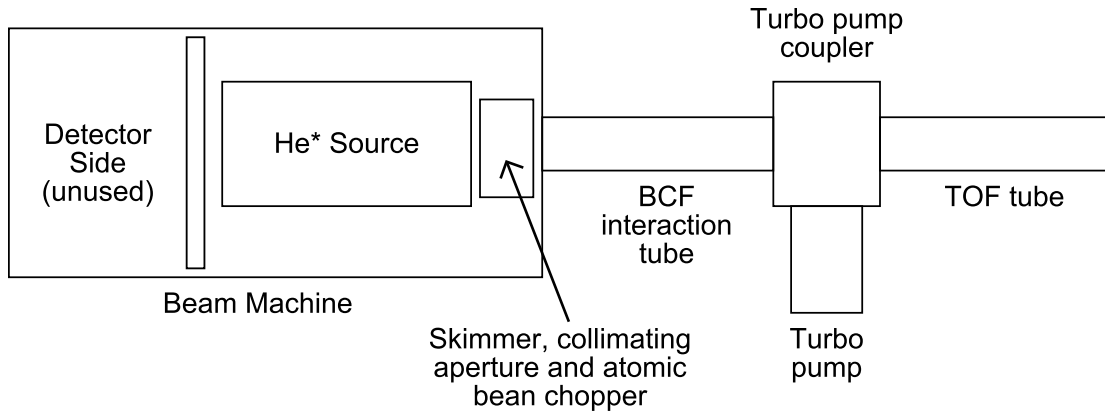


Fig. 9.4: Proposed reconfiguration of the He* source and beam machine to replace the detector side of the beam machine with an interaction tube for improved optical access and reduced *in vacuo* optics. The direction of the He* source is reversed and the interaction tube is coupled to the TOF tube using an intermediate chamber acting as a coupler and attachment point for the turbomolecular pump.

and the source will probably need to be re-designed to mount externally to the final slowing assembly.

Appendix A

Numerical OBE Solver Programs

The original Fortran code [13] was provided courtesy of Hal Metcalf. Several changes to the source code were necessary, the first of which was to change the numerical ODE solver package, which was a commercial package in the Stony Brook version. I changed the source to use a widely used publicly available ODE solver by Shampine and Gordon [99] using Adam's methods, the same as the original commercial package. This resulted in small but noticeable changes in the force profiles compared to those obtained by the Metcalf group [35, 36]. One modification was required to correct an inconsistency in the optical Bloch equations as they were written, indicated by the overbrace

$$\begin{aligned}\dot{u}(z, t) &= -(1/2)u(t) - \Delta v(t) - \text{Im}(\Omega_r)w(t), \\ \dot{v}(z, t) &= \Delta u(t) - (1/2)v(t) + \text{Re}(\Omega_r)w(t), \\ \dot{w}(z, t) &= \text{Im}(\Omega_r)u(t) - \text{Re}(\Omega_r)v(t) - (w(t) + \overbrace{1/2}).\end{aligned}\tag{A.0.1}$$

I made the changes so that the equations match my derivations and Eqs. (2.16)-(2.17) in Ref. [36] and Eqs. (A.1) in Ref. [35].

$$\begin{aligned}\dot{u}(z, t) &= -(1/2)u(t) - \Delta v(t) - \text{Im}(\Omega_r)w(t), \\ \dot{v}(z, t) &= \Delta u(t) - (1/2)v(t) + \text{Re}(\Omega_r)w(t), \\ \dot{w}(z, t) &= \text{Im}(\Omega_r)u(t) - \text{Re}(\Omega_r)v(t) - (w(t) + 1).\end{aligned}\quad (\text{A.0.2})$$

The changes only had very minor effects on the output force profiles. The Fortran program was delivered with no information about the revision history or whether or not it was actually used in that form. The updated Fortran program is listed in Section A.1.

In an effort to identify the source of the differences, I rewrote the OBE numerical solver program in Mathematica, reproduced in Section A.2. Using the highly optimized list processing routines available, I was able to improve the speed enough that this interpreter-based code, while slower than the compiled version, ran quickly enough to make it a viable alternative. The results from the Mathematica program match those from the Fortran code with the updated ODE solver.

A.1 Numerical OBE Solver in Fortran

Below is the slightly modified Fortran code.

```
C Calculate the force in a strong bichromatic standing wave
C light field
C by solving the Optical Bloch Equations in the constant-v-
C approximation.
C
C Original code provided by Hal Metcalf at SUNY Stony Brook
C Modified 10/2006 by Drew Chieda at UConn:
C           1. Added comments and cleaned up code.
```

```

C      2. Modified code to use the freeware ODE solver , not
C      the
C      commercial package that was originally
C      implemented .
C
C
C Definitions and formatting of the input file:
C      wR = Rabi frequency of a single beam
C      dsym = detuning delta
C      d = any asymmetry in the detuning , usually zero
C      xphi = phase difference of counterpropagating
C      waves (degrees)
C      kvmin = min velocity for calc (m/s)
C      kvmax = max velocity for calc (m/s)
C      N = number of steps between kvmin and kvmax to
C      compute
C The input looks like :
C      1
C      43.        39.        0.        45.        -50.        50.        100
C      wR          Dsym         d         xphi       kvmin     kvmax      N

implicit real*8 (a-h,o-z)
dimension F(5000) , u(3) , du(3)
dimension work(100+21*3) , iwork(5)
integer n, ndata
parameter (pi=3.1415926)
external OBE      ! optical bloch equations routine
external ode      ! ODE numerical solver
common wR, dsym, d, phi, dF, xkv, tend

open(unit=11,file='force1.dat') ! Input data file
open(unit=12,file='forcurv.dat') ! Output data file
read(11,12) ncalcs
format(i5)

do 123 ijk=1,ncalcs
read(11,10)wR,dsym,d,xphi,xkvmin,xkvmax,n      ! Read
computation params
10 format(6f10.5,i5)
phi = (pi/180.)*xphi
write(6,11)
write(6,10)wR,dsym,d,phi,xkvmin,xkvmax,n
write(12,11)
write(12,15)wR,dsym,d,phi,xkvmin,xkvmax,n      ! write output
header
11 format (' ',6X,'wR',4X,'dsym',9X,'d',9X,'phi',5X,'xkvmin'
 $\quad \&4X,'xkvmax',3X,'n')$ 

```

```

15  format(6 f8.3 , i5)

      vrangle=xkvmax-xkvmmin
      ndata=0
C      loop on velocities
      do 1 xkv = xkvmmin+vrangle/(2.*n) , xkvmax , vrangle/n
           ndata=ndata+1
      !
C      Initialize computational parameters for force and OBE:
      dF = 0.
      u(1) = 0.0
      u(2) = 0.0
      u(3) = -.5
C      Define Relative (rtol) and Absolute (atol) errors:
C      rtol = 1.E-5
      ! 1E-7
      => rel.dev.<<1%
          rtol = 1.E-6
          atol = 1.E-5
C      tstart = -8.
      ! t=-10
      => rel.dev.<1E-7
          tstart = -1.
          dt = 1./(max(dabs(dsym) , dabs(xkv))*10.)      ! /100. =>
              rel.dev.<1E-4
          tend = 2*pi/dabs(xkv)*idint(1.+200*dabs(xkv)/dsym)
              ! /400. =>
                  rel.
                      dev.<1%
FF=0.
icount=0
iflag=1
ntime=idint((tend-tstart)/dt)      ! number of time
steps

C      loop on time
      do 2 it=1,ntime
          tstop=tstart+dt
          call ode (OBE,3,u,tstart,tstop,rtol,atol,iflag,
                  work,iwork)
C      ode changes tstart to be tstop which amounts to
      tstart+dt
C      write(12,9993)icount,(u(jj),jj=1,3),dF
      if (tstop.lt.0.0)go to 2
      icount=icount+1
      dF= -4*wR*(dcos(phi/2)*dcos(dsym*tstop)*dsin(xkv*
                  tstop)*
      &           u(1)-dsin(phi/2)*dsin(dsym*tstop)*dcos(xkv*
                  tstop)*u(2))
                  FF=FF+dF
2      continue

```

```
9993  format(i7,4f15.2)
      F(ndata)=FF/icount
C      write(6,9998) xkv, F(ndata), xkvmax
      write(12,9999) xkv, F(ndata)
1    continue
123  continue
9998 format(3F15.6,' xkv, F, and xkvmax')
9999 format(2F15.6)
      stop
      end
```

A.2 Numerical OBE Solver in Mathematica

The Mathematica notebook is reproduced below:

```

(*
Drew Chieda
12/03/2010
Version 1.3
Notebook to calculate the force in a strong bichromatic
standing wave light field by numerically solving the optical
Bloch equations in the constant v approximation

Version history
1.3 First fully functioning version with output plotting and
file save
*)
(* Define functions for the calculation *)
a[t_]:= -4\[CapitalOmega] Sin[\[Phi]/2] Sin[BCF[[vcnt,1]]*t] Sin[d
*t];
b[t_]:= 4\[CapitalOmega] Cos[\[Phi]/2] Cos[BCF[[vcnt,1]]*t] Cos[d*
t];
(* Select and read input file *)
{FileNameSetter[Dynamic[infile]] Dynamic[infile]}
instr=OpenRead[infile];
indir=DirectoryName[infile];
SetDirectory[indir];
nacalcs=Read[instr,Number]; (* read number of batch calcs to
make *)
dircount=1;
While[DirectoryQ["BCF_"<>DateString[{ "MonthShort", "-", "DayShort
"}]<>"_"]<>ToString[dircount]], dircount++];
outdir=CreateDirectory["BCF_"<>DateString[{ "MonthShort", "-", ","
DayShort }]<>"_"]<>ToString[dircount]];
SetDirectory[outdir];
xkvstepsD=1;
ntimeD=1;
(* Batch calculations *)
ProgressIndicator[Dynamic[cprog], {1, nacalcs}]
(* Velocity steps *)
ProgressIndicator[Dynamic[vprog], {1, Dynamic[xkvstepsD]}]
(* Time steps *)
ProgressIndicator[Dynamic[tprog], {1, Dynamic[ntimeD]}]
(* Loop over number of calculations ncalc *)
Timing[
Do[
cprog=calc;

```

```

(* Read computational parameters from input file *)
\[CapitalOmega]=Read[instr,Number]; (* Rabi frequency in terms
of \[Delta] *)
d=Read[instr,Number]; (* symmetric bichromatic detuning in
terms of \[Delta] *)
dasym=Read[instr,Number]; (* asymmetry in the bichromatic
detuning *)
xphi=Read[instr,Number]; (* phase difference of the
counterpropagating waves in degrees *)
xk vmin=Read[instr,Number]; (* minimum velocity for calc in m/s
*)
xk vmax=Read[instr,Number]; (* maximum velocity for calc in m/s
*)
xkvsteps=Read[instr,Number]; (* number of velocity steps
between kvmin and kvmax *)
xkvstepsD=xkvsteps;
(* prepare data for calculations *)
\[Phi] = xphi/180*\[Pi]; (* phase diffrence in radians *)
vrangle = xk vmax-xk vmin;
BCF=Table[{i,0},{i,xk vmin+(vrangle/(2xkvsteps)),xk vmax,vrangle/
xkvsteps}]; (* BCF Data from calculation *)
(* Open the output file and write computational information in
header *)
outstr=OpenWrite["BCFout"]<>ToString[calc]<>.dat];
Write[outstr,"Calculation Number "<>ToString[calc]<>" of "<>
ToString[nalcs]];
Write[outstr,"Parameters"];
Write[outstr,"Rabi frequency = "<>ToString[\[CapitalOmega]]]
<>" delta"];
Write[outstr,"Detuning = "<>ToString[d]<>" delta"];
Write[outstr,"Asymmetry = "<>ToString[dasym]<>" delta"];
Write[outstr,"Phase difference = "<>ToString[xphi]<>" deg"]
];
Write[outstr,"Min kv = "<>ToString[xk vmin]<>" m/s"];
Write[outstr,"Max kv = "<>ToString[xk vmax]<>" m/s"];
Write[outstr,"Velcsty steps = "<>ToString[xkvsteps]];
(* Add other output file opening and header information here *)
(* Header complete *)
(* Loop over velocities *)
Do[
vprog=vcnt;
(* Initialize computational parameters for force and ODE *)
dF=0;
(* Define/reset computational rolerances *)
rtol=5; (* relative tolerance *)
atol = 5; (* absolute tolerance *)

```

```

tstart=-1;
(* Cumbersome way to automatically adjust loop end time, as in
original Fortran code *)
dt=1/(Max[Abs[d],Abs[BCF[[vcnt,1]]]]*10)*10;
tend=2\[\Pi]/Abs[BCF[[vcnt,1]]]*(1+200*Abs[BCF[[vcnt,1]]]/d);
FF=0;
icount=0;
iflag=1;
utemp=0;
vtemp=0;
wtemp=-0.5;
ntime=IntegerPart[(tend-tstart)/dt]; (* number of time steps *)
ntimeD=ntime;
(* Loop over time steps *)
Do[
tprog=tcnt;
tstop=tstart+dt; (* assign new tstop *)
s=NDSolve[{u'[t]==-u[t]-dasym v[t]+a[t] w[t],v'[t]==dasym u[t]
]-v[t]+b[t] w[t],w'[t]==-a[t] u[t]-b[t] v[t]-(w[t]+1),u[
tstart]==utemp,v[tstart]==vtemp,w[tstart]==wtemp},{u,v,w},{t,
tstart,tstop},AccuracyGoal->rtol,PrecisionGoal->atol];
If[tstop>0,
icount++;
dF=-4\[CapitalOmega] (\Cos[\Phi]/2)\Cos[d*tstop]\Sin[BCF[[vcnt
,1]]*tstop] u[tstop]-\Sin[\Phi/2]\Sin[d*tstop]\Cos[BCF[[vcnt
,1]]*tstop] v[tstop])/s[[1]];
FF=FF+dF;
]; (* end if - if solver reaches real times... *)
utemp=u[tstop]/.s[[1]]; (* save output parameters for next
input cycle *)
vtemp=v[tstop]/.s[[1]];
wtemp=w[tstop]/.s[[1]];
tstart=tstop;
,{tcnt,1,ntime}]; (* Do loop over time *)
BCF[[vcnt,2]]=FF/icount;
(* Write data to file here *)
(* Write[outstr,{xkv[[v]],F[[v]]}]; *)
,{vcnt,1,xkvsteps}]; (* Do loop over velocitites *)
Export[outstr,BCF,"TSV"]; (* Save output force vs. velocity
data to file *)
Close[outstr];
,{calc,1,ncalcs}]; (* Do loop over ncalcs *)
Close[instr];
SetDirectory[indir];
] (* end timing call *)

```

```
ListPlot[BCF, AxesLabel->{"velocity  $(\sqrt{[Gamma]}/k)$ ", "Force  $(\sqrt{HBar} k \sqrt{[Gamma]})$ "}, PlotLabel->outdir<>"\BCFout" <> ToString[cprog]<> ".dat", Joined->True]
```

Appendix B

Data Acquisition Programs

The function and operation of the LabView experiment control and data acquisition program is detailed in Section 4.11. These are the LabView programs for reference, including both the user interface and the program block.

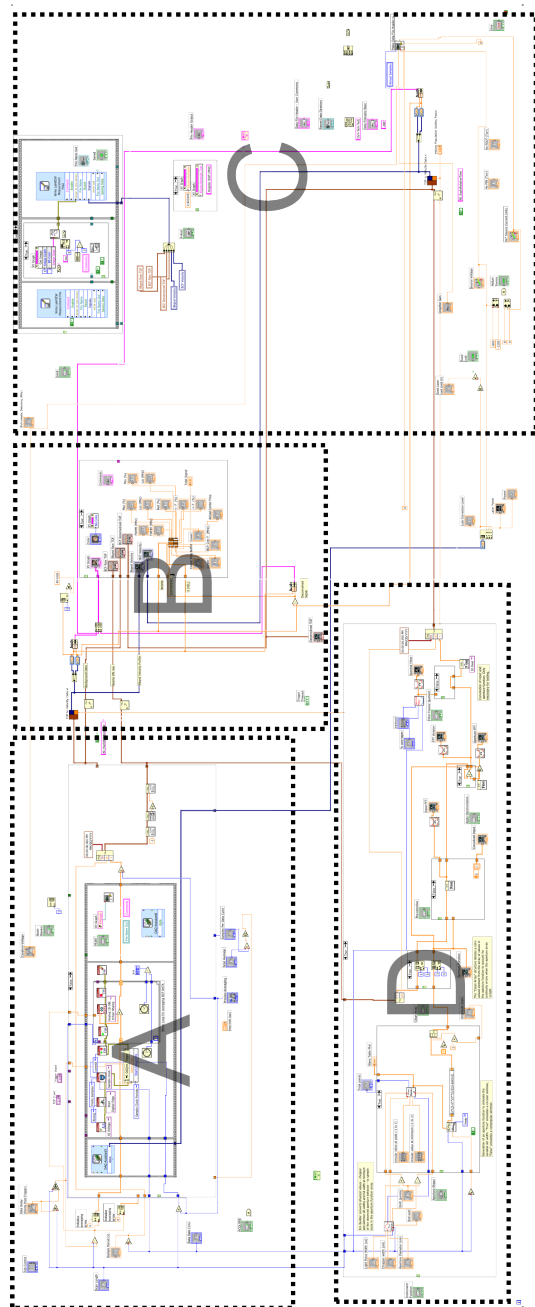


Fig. B.1: Data acquisition and experiment control program written in National Instruments LabView®. Main program sections are outlined and described in more detail in following pages. Sections are: (A) data acquisition, (B) TOF data to velocity distribution and analysis, (C) data file formatting and saving, and (D) TOF instrument function deconvolution (not fully implemented).

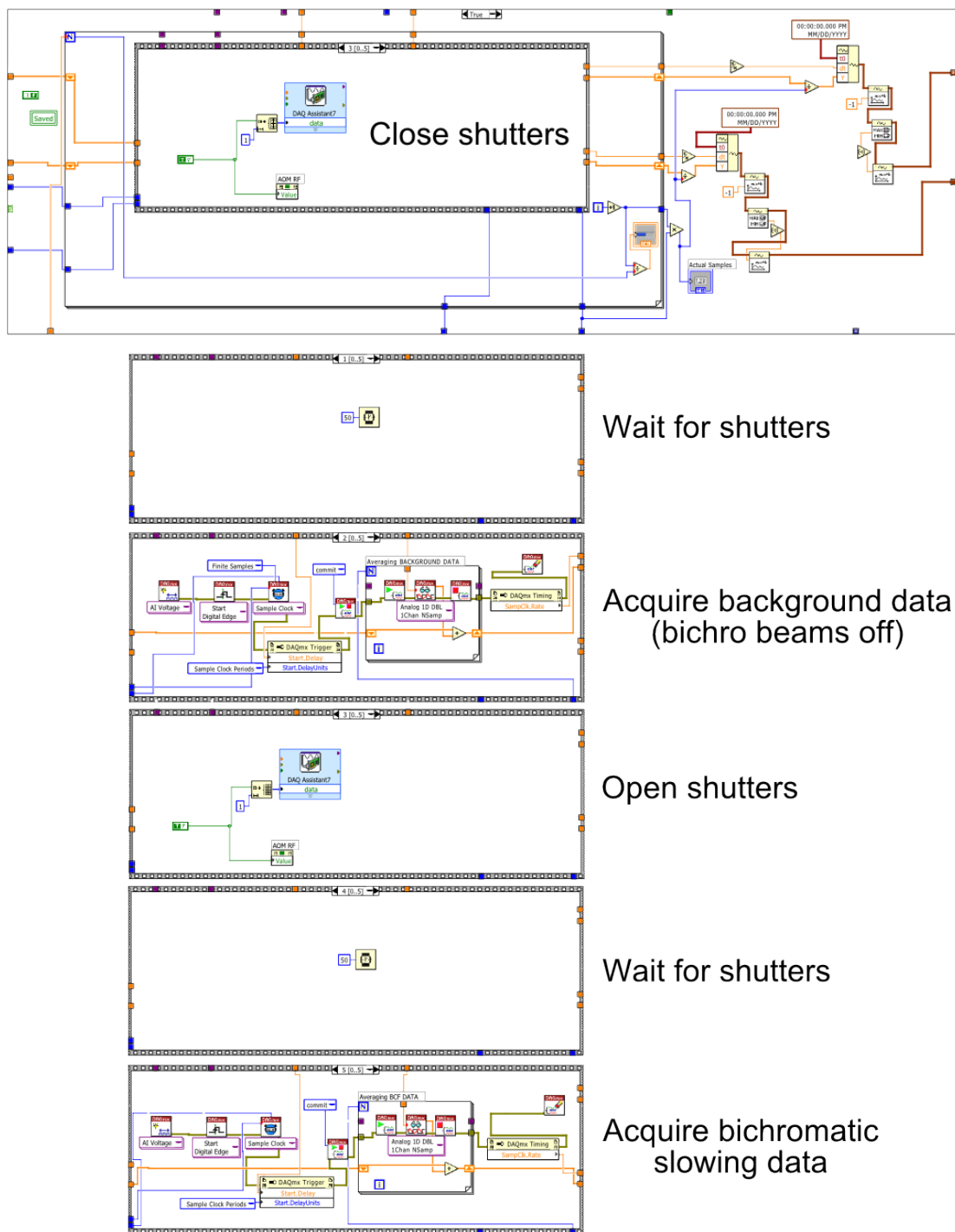


Fig. B.2: (A) LabView code section for the data acquisition subroutine showing expanded acquisition loop.

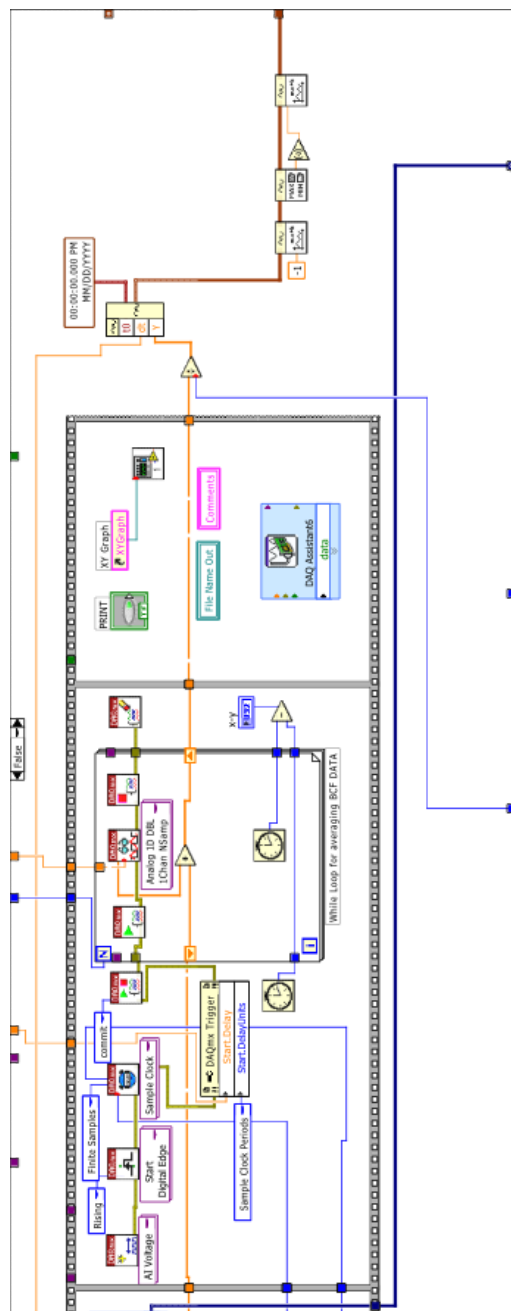


Fig. B.3: (A) LabView data monitor control, in use when not actively acquiring a data run. Continuously displays the TOF data (only) with user selectable averaging.

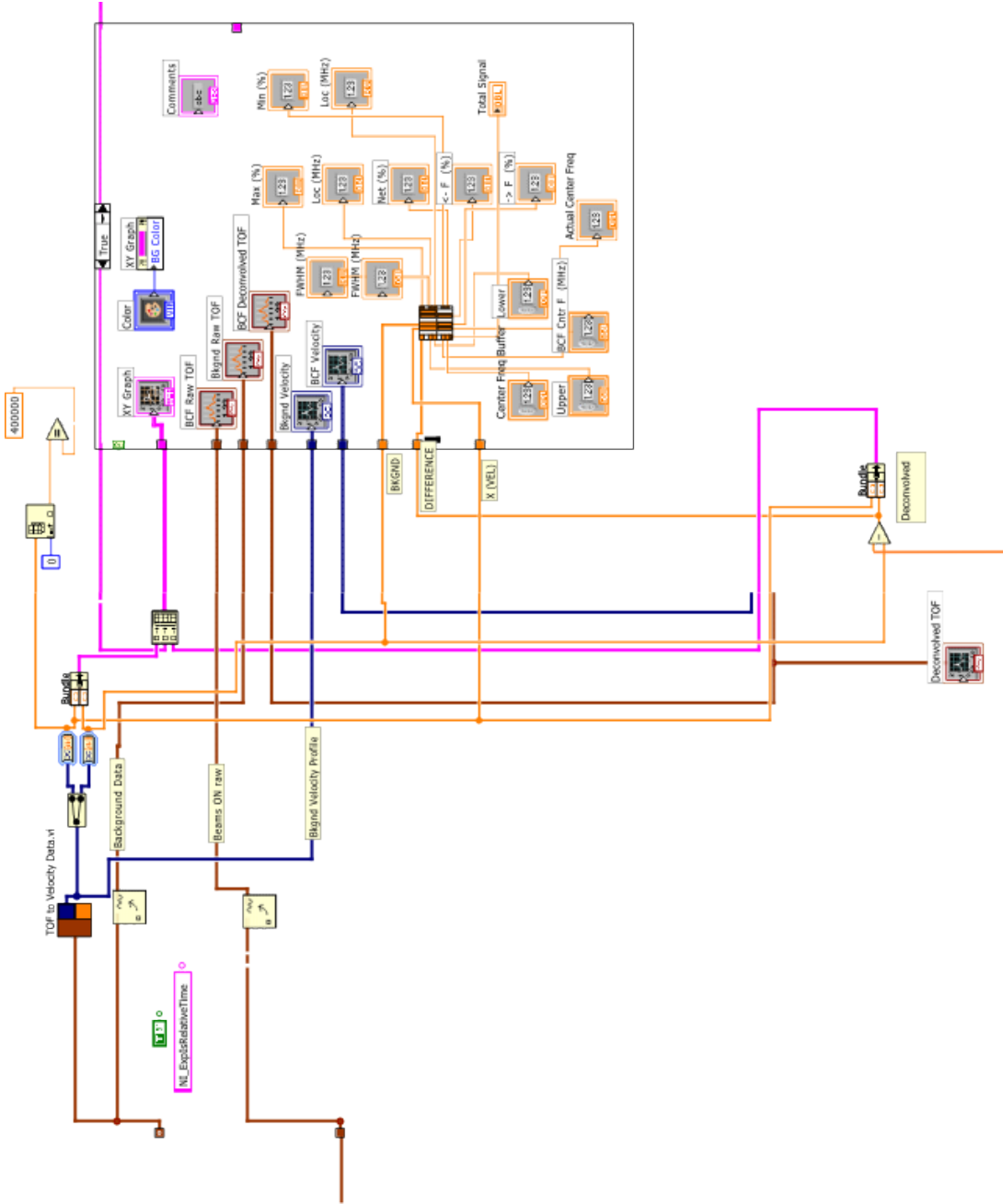


Fig. B.4: (B) LabView code section to convert TOF data to a velocity distribution using the VI shown in Fig. B.7. Analysis of the change in velocity distribution due to the presence of the BCF is calculated using the VI shown in Fig. B.8.

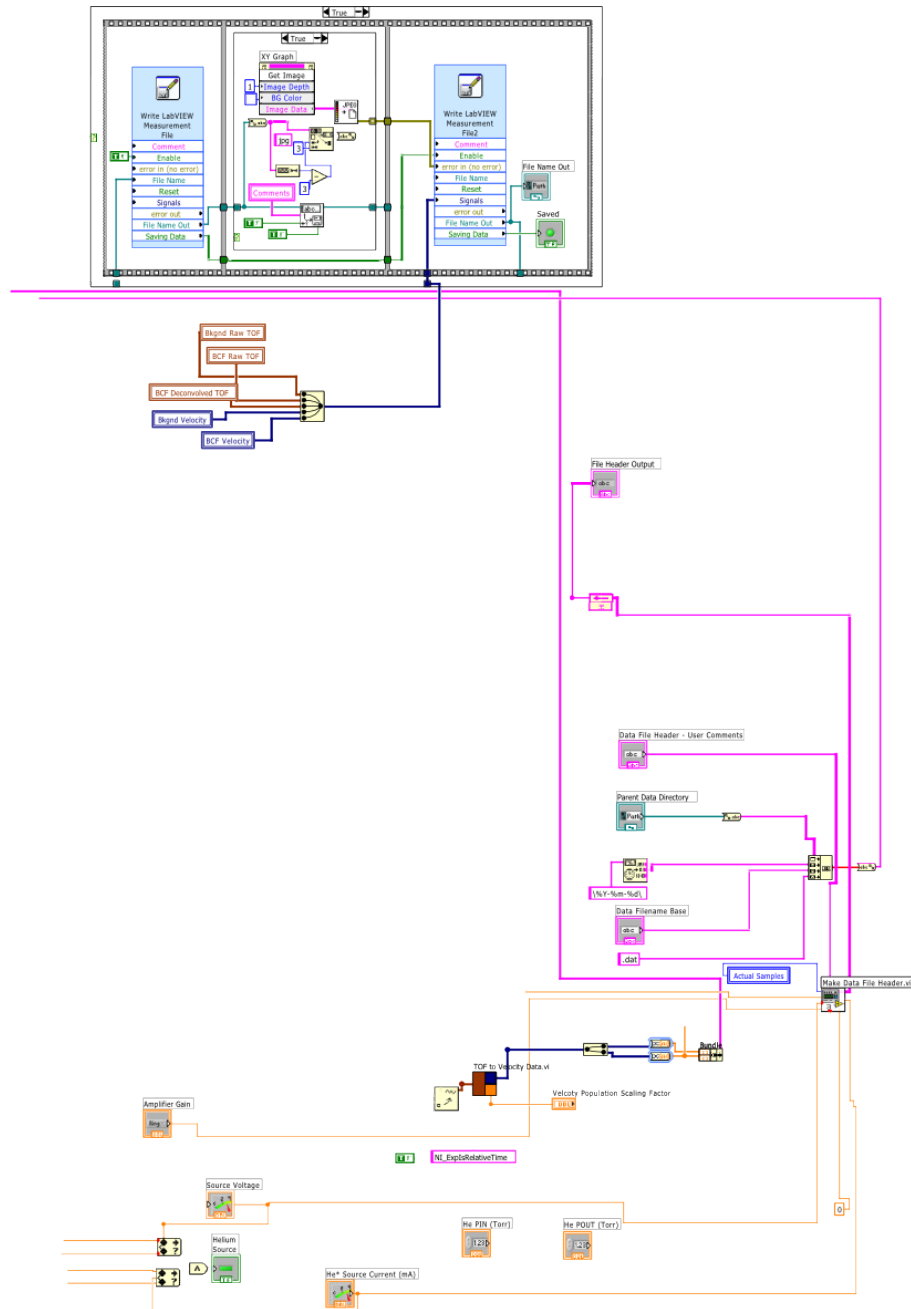


Fig. B.5: (C) LabView code section to save the data to a text file. There are three primary functions—compile the header text, assemble the data into a structure that the LabView Save Datafile can use, and write the data to disk. Note some wires unrelated to the tasks described have been removed for clarity.

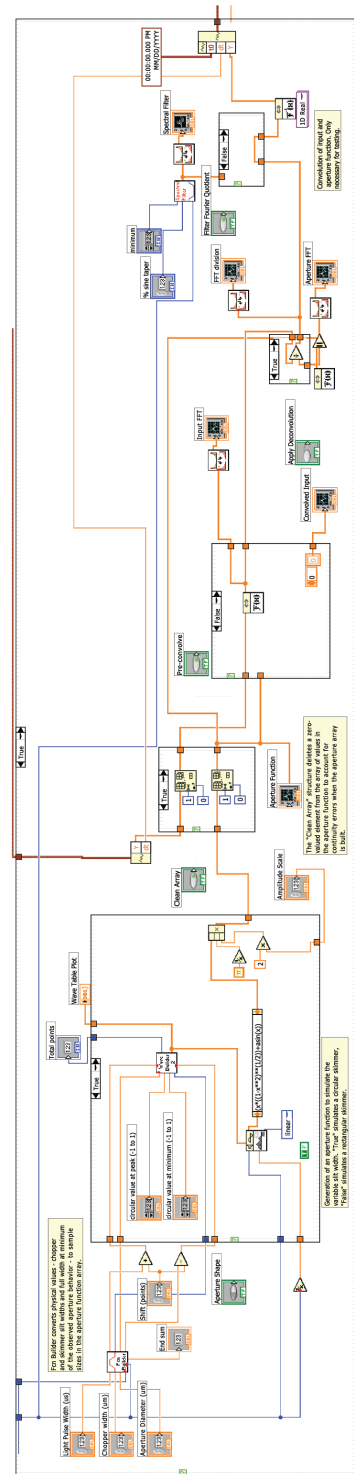


Fig. B.6: (D) Instrument function routine. Partially functioning, not implemented. For reference only.

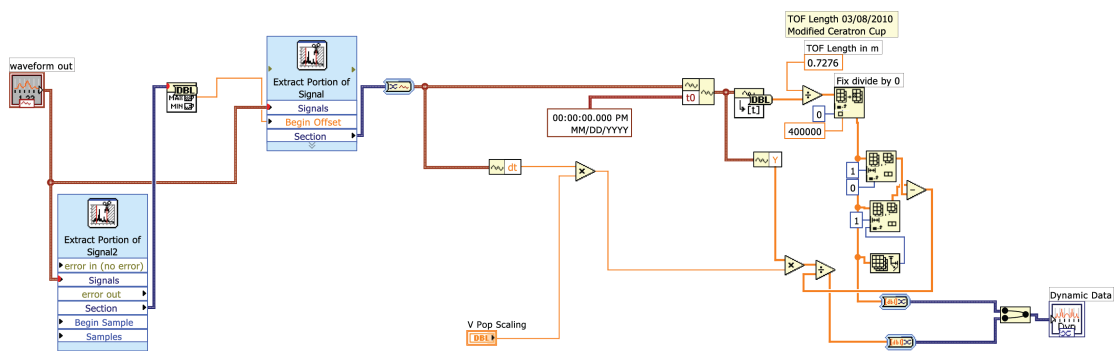


Fig. B.7: LabView SubVI to calculate the velocity distribution from the raw time of flight data.

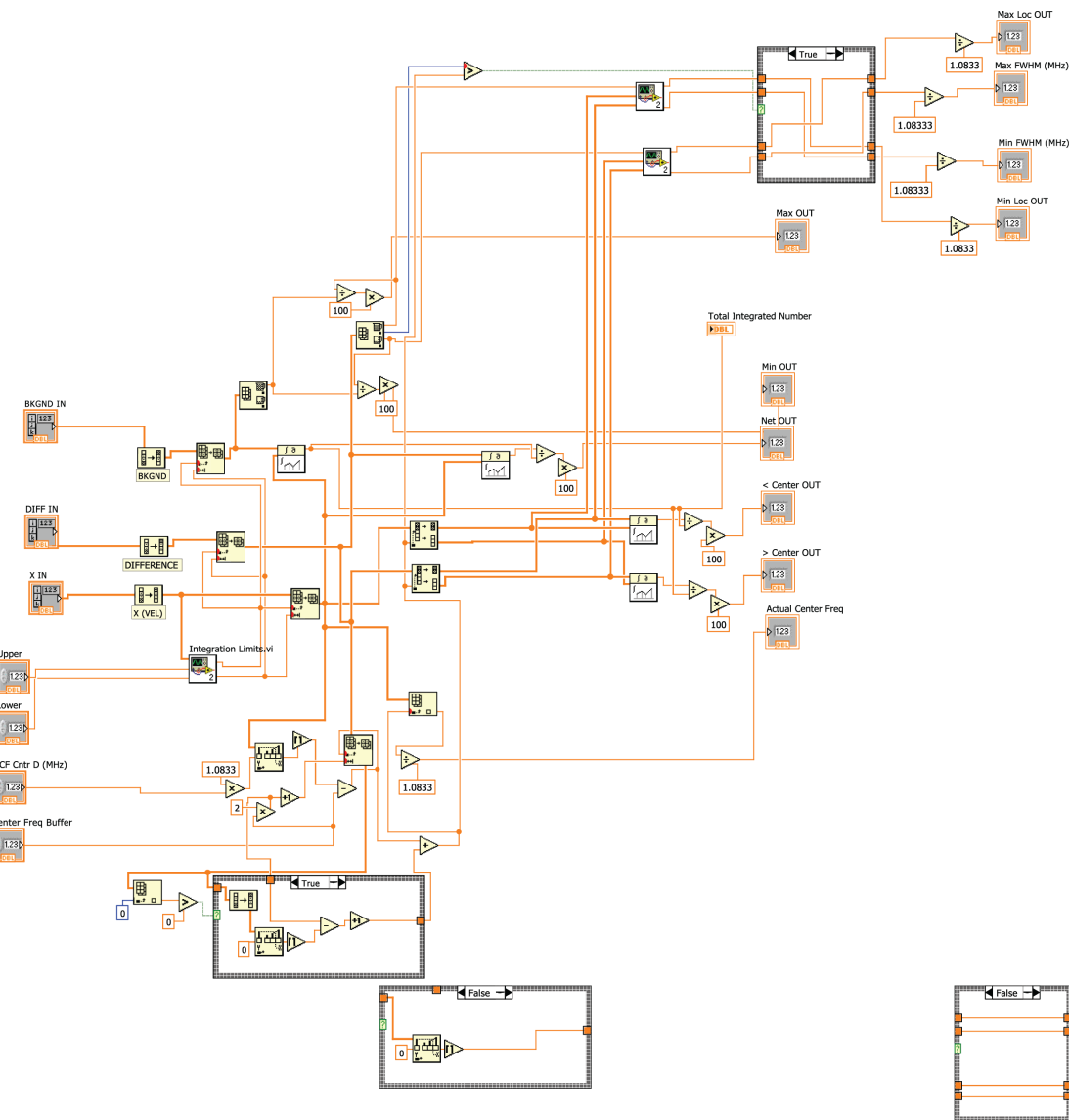


Fig. B.8: LabView SubVI to perform quantitative analysis on the slowed atom peak and hole to assess optimization of BCF parameters. The VI calculates the location, normalized height and area, and FWHM of the peak and “hole” in the velocity distribution, as well as an estimate of the amount of velocity slowing and the change in the total atom number.

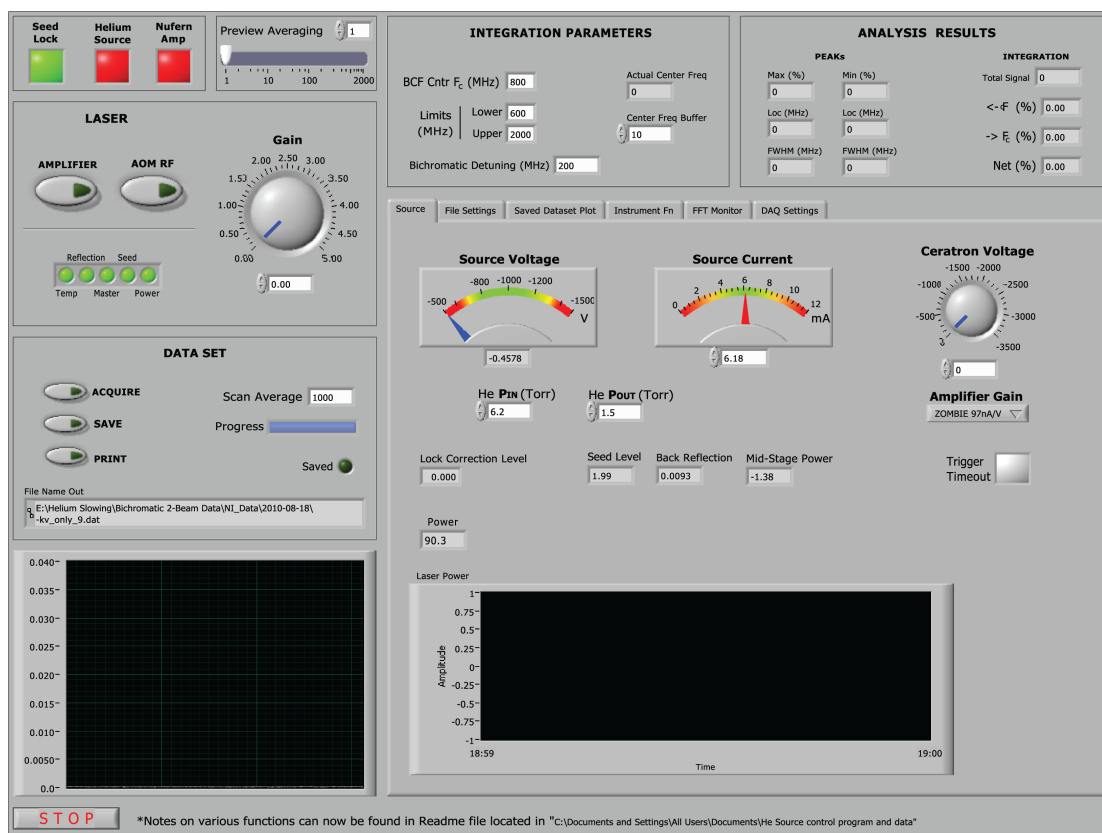


Fig. B.9: User interface showing main experiment control tab.

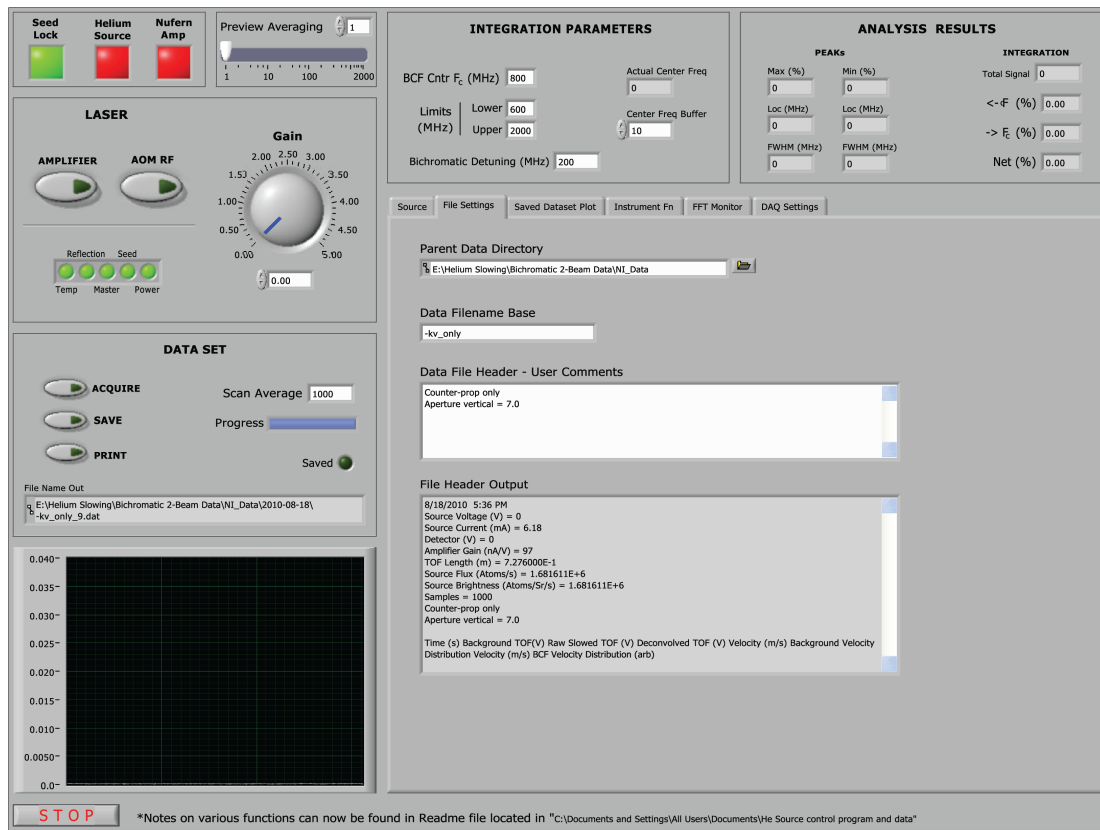


Fig. B.10: User interface showing data file save options tab, including automatic and manual file header information.

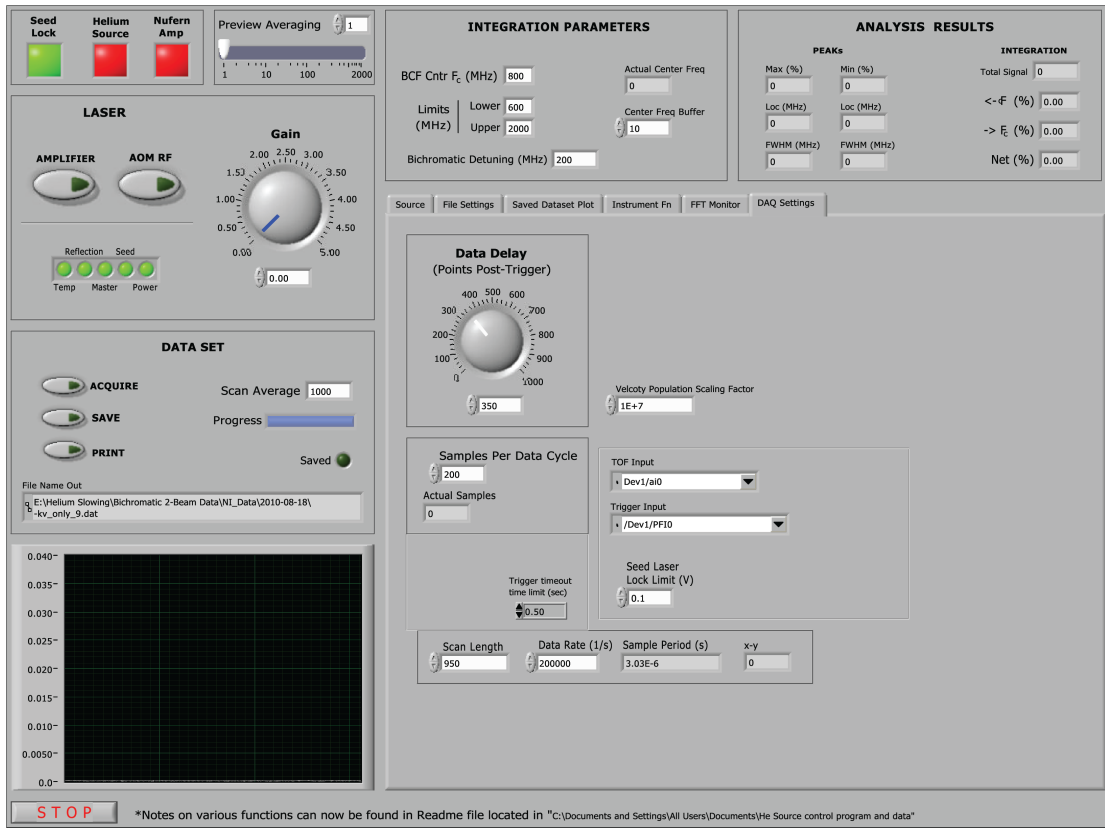


Fig. B.11: User interface showing data acquisition parameter setup tab. The other tabs not specifically discussed are for the display of information for debugging purposes and the TOF instrument function, which is not implemented.

Appendix C

Toptica DL-MOD FET Current Modulation Circuit

Fig. C.1 shows the Toptica DL-MOD circuit as I was able to reverse-engineer it. It is not necessarily complete as there may have been additional changes to the temperature and current control interface circuitry, but without an unmodified DL100 to compare it to, I could not be sure. The Zener diodes only act as voltage limiters on the input, so they can be replaced with pairs of signal diodes such as the 1N4148 to achieve the same effect. There is also a small unmarked inductor whose presumably small inductance I was unable to ascertain without removing the board from the laser head, risking damage to the laser diode.

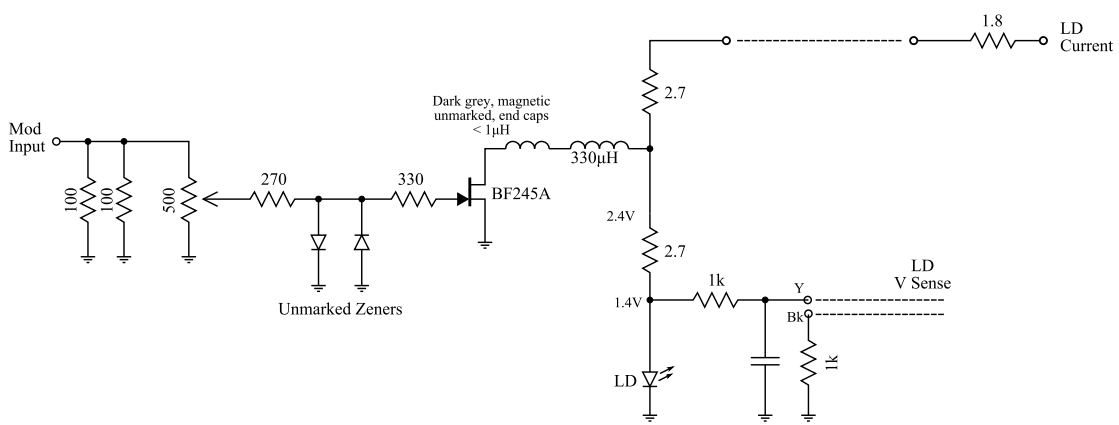
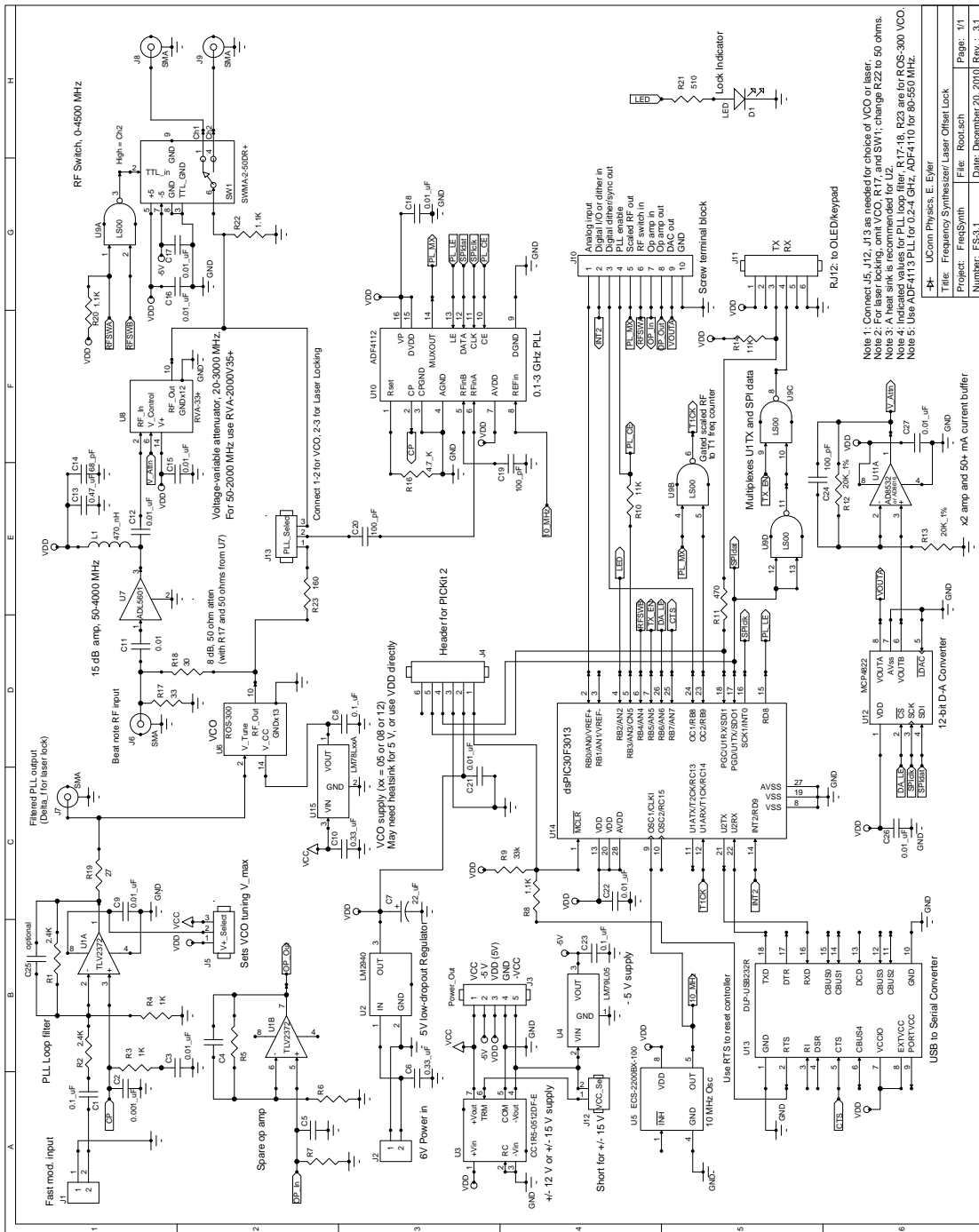


Fig. C.1: Toptica DL-MOD FET current modulation circuit. A positive voltage on the FET gate causes a portion of the laser diode current to be shorted to ground around the laser diode. Two unidentifiable components were the Zener diodes and the small inductor. Note that there appear to be additional changes to the main current and temperature interface PCB in the laser head with the DL-MOD.

Appendix D

Microcontroller-based Frequency Synthesizer



Appendix E

FFT-Based Heterodyne Chirp Analysis Program

This is the Mathematica notebook listing for the FFT-based heterodyne frequency analysis. It is based on the method of Gangopadhyay [88], adapted and optimized for chirps at the rate present in these experiments. The program actually operates relatively quickly given the size of the dataset, thanks to highly optimized list routines available in Mathematica.

FFT - Based Heterodyne Chirp Analysis Essential steps :

- Time - domain bandpass filter if data is noisy (not implemented here).
- Forward FFT
- Spectral filtering of the beat frequencies. Blackman and Tukey windows are currently implemented, modify as necessary.
- Spectral shift of the heterodyne (carrier) frequency to 0.
- Inverse FFT
- Extraction of phase ϕ from $x + iy = ze^{i\phi}$ with phase wrapping corrections.
- Computation of the instantaneous frequency $f(t) = \vec{k} \cdot \vec{v}(t) = (-1/2\pi)d\phi/dt$.

Notes : File open and read is designed specifically for the comma-separated-value (csv) data files stored from the Agilent 2 GHz oscilloscope in the Gould Lab.

The header read code must be changed and the sample period entered by hand if other file formats are used.

FFT – Based Heterodyne Chirp Analysis
Essential steps :
 Time – domain bandpass filter if data is noisy (not implemented here).
Forward FFT
 Spectral filtering of the beat frequencies. Blackman and Tukey windows are currently implemented, modify as necessary.
 Spectral shift of the heterodyne (carrier) frequency to 0.
Inverse FFT
 Extraction of phase Φ from $x+iy=zE^i\Phi$ with phase wrapping corrections.
 Computation of the instantaneous frequency $=-1/(2\Phi)$ ($d\Phi/dt$).
Notes :
File open and read is designed specifically for the csv data files stored from the Agilent 2 GHz o-scope in Gould Lab. Header read must be changed and sample period entered by hand if other file formats are used.
Author : Drew Chieda
Date : 9/15/2011
Version : 2.0
(Open the file , read the header information and data *)*
 directory="D:\\My Documents\\Research\\Chirped Slower\\Chirp Heterodyne\\200MHz_50us\\";
(directory="F:\\";*)*
 file = "-kv_200_50_c3";
 snum=OpenRead[directory <> file <> ".csv"];
 header=ReadList[snum, String, 21];
 indata=Import[snum, "CSV"];
 Close[snum];
(factor by which to subsample data , if any *)*
 subsamp=4;
(time data *)*
 t=Total[Partition[indata[[All, 1]], subsamp], {2}]/subsample;
(heterodyne signal *)*
 sig=Total[Partition[indata[[All, 2]], subsamp], {2}]/subsample;
Remove[indata];
(From the sample period in the header information , calculate the sampling frequency *)*
 samp=StringSplit[StringSplit[header[[8]]][[2]], "E"];
 samper=subsample*ToExpression[samp[[1]]]*10^ToExpression[samp[[2]]];
 samfreq=1/samper;

```

(* Take the forward FFT, only keeping the positive frequency
components *)
fftdata=Fourier[sig,FourierParameters -> {1,1}][[1;;Round[Length[
sig]/2,2]]];
(* Calculate the corresponding frequency table *)
freq=Table[i*samfreq/2,{i,0,1,1/(Length[fftdata]-1)}];
Remove[sig];
(* ListLinePlot[Partition[Riffle[freq,Abs[fftdata]^2],2],
PlotRange->{All,{0,5000}}] *)
(* Parameters and definition for a Blackman filter, not used
because the Tukey window is a better fit to the chirp
spectrum
\[Delta]f=0.5*10^9; (* half width *)
fc=1.4*10^9; (* center frequency *)
blackman[f_]=Piecewise[{{(1-((f-fc)/\[Delta]f)^2)^2,fc-\[Delta]
f<f<fc+\[Delta]f}},0];
filtfft=fftdata*Map[blackman,freq]; (* filtered fft data *) *)
Define parameters for the Tukey frequency filter, define the
filter function, and apply it to the FFT data via a mask.
The most suitable window function (i.e., Blackman vs Tukey
etc.) will depend on the spectral shape of the chirp. YMMV
alpha=.25*10^9; (* window width in Hz *)
fc=1.5*10^9; (* window center frequency in Hz *)
tukey[f_]=Piecewise[{{1/2 (1+Cos[(2\[Pi])/alpha (f-fc-alpha/2)
]),fc-alpha<=f<fc-alpha/2},{1,fc-alpha/2<=f<fc+alpha/2},{1/2
(1+Cos[(2\[Pi])/alpha (f-fc+alpha/2)]),fc+alpha/2<f<fc+
alpha}},0];
Plot the calculated window over the chirp spectrum. Verify
that the window encompasses the entire chirp, adjust
parameters as necessary. /@ maps the function onto every
element of the list - much faster than element-by-element
sequential. If window and chirp spectrum don't overlap
properly, adjust alpha and fc above.
(* ListLinePlot[{Abs[fftdata]^2,500*tukey/@freq},PlotRange
->{{1.2*10^5,1.7*10^5},{0,5000}},AxesLabel->{"Freq (kHz)","
Amplitude (arb)"},PlotLabel->"Verify Overlap of Chirp and
Filter Window"]
Beep[] *)
Create a filter mask and apply to the data ...
filfft=fftdata*tukey/@freq;
Now, shift the frequencies so that the carrier at 1.4 GHz is
removed. Ordering finds the location of the max (assuming
it's the carrier), then shift the spectrum so that it's at
the far right, the reverse it. The far right of the
spectrum had to be manually set to zero due to wrap-around.
fft2=RotateRight[filfft,Length[filfft]-160000];

```

```

(* fft2=RotateRight[filfft ,Length[filfft]-Ordering[Abs[filfft
]^2,-1]]; *)
fft2[[1;;200]]=0.0;
(* ListLinePlot[Partition[Riffle[freq,Abs[fft2]^2],2],PlotRange
->All]*)
Remove[filfft,fftdata,freq];
OK, now we need to apply the inverse transform, calculate the
phase, then the instantaneous frequency
phasewrap[p_]=Piecewise[{{p+2\[Pi],p<=-\[Pi]},{p-2\[Pi],p>=\[Pi]
}},p];
phase=Arg[InverseFourier[fft2,FourierParameters->{1,1}]];
instfreq=-1/(2\[Pi]) phasewrap /@ Differences[phase]/(2*sampler)
;
dataout=Partition[Riffle[Take[t,{1,-4,2}]*10^6,instfreq
*10^-6],2];
Remove[fft2,t];
avgdata=MovingAverage[dataout,11];
(* ListPlot[avgdata,PlotRange->{All,{ -300,0}},AxesLabel->{"Time
(\[Mu]s)", "Frequency (MHz)"},PlotLabel->"Instantaneous
Frequency"] *)
Export[directory<>file<>"FFT_FINAL.csv",dataout[[1;;-1;;20]]];
Remove[dataout];
(* minpos=Position[avgdata[[All,2]],Min[avgdata[[All,2]]][[Round
[Length[avgdata]/4,2];;-1]]][[1]];
minfreq=avgdata[[ minpos,2]];
a=0.1*minfreq;
b=0.9*minfreq;
relevent=Position[avgdata,Nearest[avgdata[[All
,1]],15]][[1]][[1,1]];
start=Position[avgdata,Nearest[avgdata[[relevent;;minpos
[[1]],2]],a]][[1]][[1,1]];
end=Position[avgdata,Nearest[avgdata[[relevent;;minpos
[[1]],2]],b]][[1]][[1,1]];
lm=LinearModelFit[avgdata[[start;;end]],x,x];
delay=x/.Solve[lm[x]==0,x][[1]];
dataplot=GraphicsColumn[{Item[Show[ListPlot[avgdata[[relevent
;;-1;;20]],Plot[lm[x],{x,20,50},PlotStyle->{Red}],PlotRange
->{{10,100},{All,0}},GridLines->Automatic,AxesLabel->{
"Time (\[Mu]s)", "Frequency (MHz)"},PlotLabel->"Linear Fit to
Chirp "<>file],Alignment->Bottom],Item[
TableForm[{{"file:",file}, {"delay",delay,"\[Mu]s"}, {"width",
avgdata[[minpos,1]][[1]]-delay,"\[Mu]s"}, {"magnitude",
minfreq[[1]],"MHz"}}],Alignment->Top]}];
Export[directory<>file<>"FFT_FINAL.jpg",dataplot]; *)
Quit[];

```

Appendix F

Chirped BCF Monte Carlo Simulation

The Monte Carlo simulation of the chirped BCF was written in Mathematica and is listed in full below. The program tracks the time each atom takes to travel from the chopper to the detector, including any changes in velocity due to interaction with the bichromatic beams via the BCF. It begins by loading a population of 100,000 atoms with random velocities assigned using a probability distribution function derived from experimental TOF data. The BCF profile is computed before-hand over several velocities and irradiances to form a three-dimensional BCF surface as shown in Fig. F.1.

The model proceeds by assigning each atom in the distribution an initial time ($-40\mu\text{s} \leq t_0 \leq 0$), simulating the finite atomic pulse duration, and a randomly assigned irradiance scaling factor to account for the vertical Gaussian profile of the slowing beams. Each atom's position is calculated during the transit from chopper to interaction region with the bichromatic beams. During the time an atom is in the interaction region, the force on the atom is calculated based on the local irradiance (taking into account both the atom's vertical position in the beam and the transit through the extended Gaussian profile of the slower laser) and atom velocity using the BCF surface of Fig. F.1. The calculation is repeated in small time steps, much smaller than the characteristic slowing time of $5.8\ \mu\text{s}$.

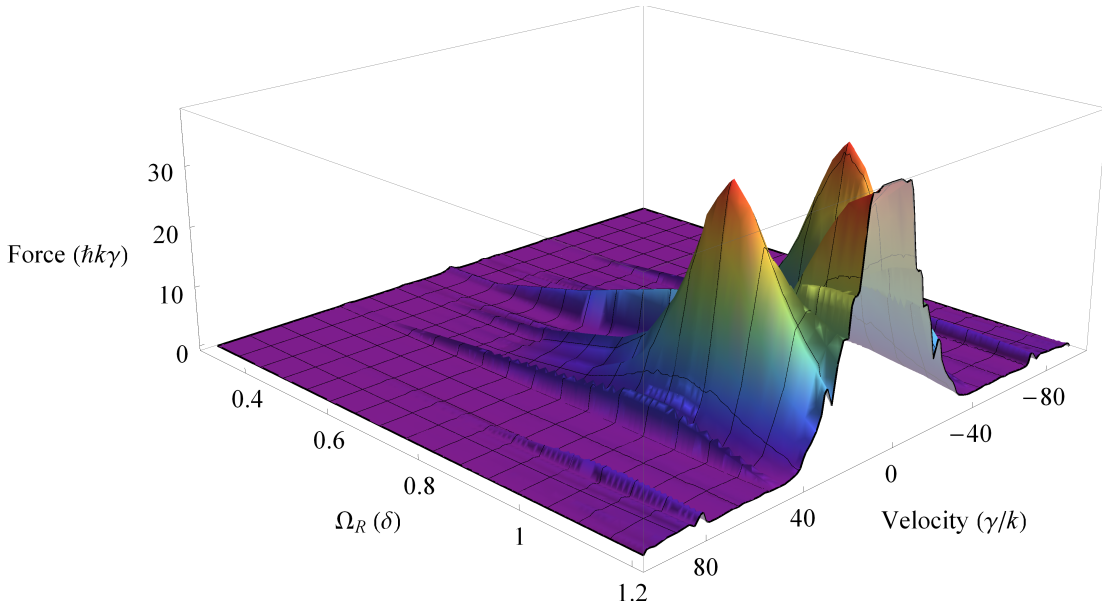


Fig. F.1: 3D BCF surface calculated for $-100\gamma/k < v < +100\gamma/k$ and $\Omega_r \leq \sqrt{3/2} \delta$, for $\delta/2\pi = 100$ MHz.

for metastable helium. At each step the atom velocity is adjusted based on the force calculation. The calculation proceeds over all the atoms until they all leave the interaction region. The time each atom takes to travel from the slower exit to the detector position is calculated and added to the total, providing a time of flight for each atom. From the TOF information, the average atom velocity is calculated using the same algorithm described in Section 4.3 and a final velocity probability distribution is calculated.

The Monte Carlo model takes into account the varying bichromatic field irradiance, temporal width of the atomic pulse, and the BCF dependence on irradiance and atomic velocity. The model does not account for variations in the relative phase of the bichromatic beat notes over the length of the slower—even at a detuning of 123γ the effect should be small. The model also does not take into account any difference in the frequency chirp between the two lasers; however, nonlinear frequency chirps can be analyzed with only minor modification to the

code. The Mathematica program is listed below:

```
(*  
Monte Carlo Simulation of the chirped slower scheme.  
Last Update: 10/23/2011  
Drew Chieda
```

V10: 10/23/11 Added option to calculate the TOF we'd see in experiment assuming the atom velocity is constant. Much slower since I can no longer delete atoms that are out of the slower region since the atom position in the table cannot change.

V9: 10/05/11 Modify atom initial time to simulate finite width of chopper/aperture window.

V8: dump atoms from list as soon as they exit the slower to speed things up.

V7: Full Monte Carlo factoring in: atom velocity, z-position, r-position (laser irradiance), and actual BCF interpolated function of (v , irr).

First, open a sample data set from lab, create an empirical function for the velocity distribution, and define N atoms with velocities that match the experimental distribution. For each atom create another list that contains the z position of the atom in the same place in the velocity list. For starters, just calculate the BCF as a top hat function with the proper magnitude and width for a detuning of $\Delta = 2\pi \times 100\text{MHz}$, which is what we plan to use, at least at first. Probably use 25% of the atoms to make it realistic.

This version is one step more complex as it adds the time progression of the atoms through the slower instead of just assuming one bichro slowing time. Still uses the top-hat function for the BCF so it's a simple model.

NEW: Open the pre-smoothed background data (smoothed in Origin using Savitz-Golay 30pt. and exported as ascii)

V3 : changes made to monte carlo to include transit time of atoms to the slower. To make it simpler we can start the pulse as those at 1000 m/s are at the start of the slower, and the atoms start all at $t=0$ at the chopper. Make a

```

second list the corresponds to the z-location of the atom...
*)
(* Create a velocity distribution using a background data set
   as a model *)
snum=OpenRead["D:\My Documents\Research\Sample Data\Smoothed
    Background.dat"];
indata=Import[snum,"Table"];
Close[snum];
data=Drop[indata,1];
Clear[indata];
(*
Parse out the columns of interest. Note the processed velocity
distributions are shorter than the TOF, which makes the
Transpose function puke, so we need to drop them. If there
is an error here, increase the number of rows dopped.
scaling of 1/81.8748 is from the integral of the
interpolating function to normalize the area.
*)
velocity=Transpose[data][[1]];
bkgnd=Transpose[data][[2]];
bkgnd=bkgnd/Max[bkgnd];
(* expdata=Flatten[Transpose[Take[Transpose[Drop[data
    , -100]],{8,8}]]];
diff=(expdata-bkgnd)/Max[bkgnd];
*)
(* Re-organize and normalize the lists to make it suitable
   for plotting *)
plotbkgnd=Partition[Riffle[velocity,bkgnd],2];
(* plotdata=Partition[Riffle[velocity,expdata/Max[bkgnd]],2];
plotdiff=Partition[Riffle[velocity,diff],2];
ListLinePlot[{plotbkgnd,plotdata,diff},DataRange->Automatic,
    PlotRange->{{600,2000},{-0.1,1}}]
*)
(* OK, Interpolate a probability distribution from the
   background data... *)
ibkgnd=Interpolation[plotbkgnd];
norm=Integrate[ibkgnd[x],{x,Min[velocity],Max[velocity]}];
Clear[ibkgnd];
ibkgnd=Interpolation[Partition[Riffle[velocity,bkgnd/norm],2]];
Integrate[ibkgnd[x],{x,Min[velocity],Max[velocity]}]
(* OK, finally, create the distribution of atoms from the
   probability function ... Takes a while, really should split
   it into to parts and send one to each parallel kernel.
   Later. Use ParallelMap! *)
totalatoms=200000; (* number of atoms to keep *)
i=0;

```

```

problimit=FindMaxValue[ibkgnd[x],{x,900}];
vdist={}; (* atom array initialization*)
ProgressIndicator[Dynamic[i],{0,totalatoms}]
While[i<totalatoms,
atomvel=RandomReal[{300,2000}]; If[RandomReal[problimit]<=ibkgnd
[atomvel],vdist=Append[vdist,atomvel]; i++];
];
(* drop the original data point *)
(* Save the distribution if you want ... *)
Save["D:/My Documents/Research/Sample Data/V_Dist_Smoothed_100k
.dat",vdist];
(* OR, read a saved distribution to save time ... *)
vdist=Flatten[ReadList["D:/My Documents/Research/Sample Data/
V_Dist_Smoothed_100k.dat"]];
ListLinePlot[Partition[Riffle[Range[300,2000,15],BinCounts[
vdist,{300,2000,15}]],2]]
(*
OK, Open the 3D force profile interpolation function. We get a
function in terms of the atom velocity (centered at 0) and
the laser irradiance as a % of peak (assuming peak is
Subscript[\[CapitalOmega], Rabi]=1.2\[Delta]). N.B.:
velocity is in terms of \[Gamma]/k
*)
snum=OpenRead["D:\My Documents\Research\Chirped Slower\
Calculations\\100MHz 3D BCF Function.dat"];
BCF=Read[snum];
Close[snum];
Plot3D[BCF[v,i],{v,-99,99},{i,0,1.2},PlotRange->All,PlotPoints
->20,AxesLabel->{"Velocity (\[Gamma]/k)",Subscript[\[CapitalOmega],
Rabi] (*1.2\[Delta]),"BCF (\[HBar]k\[Gamma])"
}]
(*
Now, for starters define the simplest BCF profile - a top-hat
function with sloping sides, width = \[Delta]/(2k) and F=\[
HBar/k\[Delta]\/\[Pi]
To that, we need to add several time steps to allow the atoms
to progress through the slower. Assume t=0 is when the
first atoms enter the slower, and assume that the atoms all
arrive at the same time (i.e., assume that the atom pulse is
thin compared to the slower length). The time step must be
small compared to the bichromatic characteristic slowing
time : Subscript[t, step] \[LessLess] Subscript[\[Tau], BCF]
]=5.8\[Mu]s.
*)
(** Physical Constants ****)
m=6.6464*10^-27; (* mass of He atom in kg *)

```

```

\[HBar]=1.05457148*10^-34; (* \[HBar] *)
\[Lambda]=1083.3*10^-9; (* laser wavelength in m *)
\[Tau] = 98.17*10^-9; (* upper state lifetime in sec *)
k=2\[Pi]/\[Lambda]; (* wave vector *)
\[Gamma]=1/\[Tau]; (* He 2S->2P transition rate *)

(* ***** Experimental Variables *****)

(* Frequencies and chirp *)

\[Delta]=2\[Pi]*200*10^6; (* bichromatic detuning in Hz*)
startfreq=800*10^6; (* initial unchirped center freq in Hz *)
dchirp = 600*10^6; (* chirp magnitude in Hz *)
tchirp=10*10^-6; (* length of chirp in s *)
thold = 10*10^-6; (* time to hold chirped frequency at end of
chirp in s *)
chirpdelay = 240.0*10^-6 ;(* time from t=0 (aperture open) to
chirp start *)
direction=-1; (* -1 for deceleration, +1 for acceleration *)
nsteps=20; (* number of steps over each critical slowing period
5.8\[Mu]s to step *)
vcenter=startfreq*\[Lambda]; (* convert a doppler frequency
shift to an atom velocity in m/s*)
fscale=2; (* factor to reduce BCF magnitude by 0.0 <= forcefact
<= 1.0 *)
vscale=2; (* scale the 100 MHz force width up. Make sure to
scale \[Delta], too. This is a patch moving from 100MHz to
120MHz. Probably want to build a new force profile for the
second generation slower. *)
(* Chopper and aperture parameters *)

dap=70*10^-6; (* aperture diameter in m *)
wch=100*10^-6; (* chopper slit width in m*)
vch=2.5; (* chopper speed in m/s *)
rap=dap/2; (* aperture radius in m *)
angle[t3_]=2 ArcCos[(rap-vch*t3*10^-6)/rap];
area[t2_]=rap^2/2 (angle[t2]-Sin[angle[t2]])/(\[Pi] rap^2);
sweep[t1_]=Piecewise[{{area[t1],0<=t1*1*10^-6<dap/vch},{1,dap/
vch<=t1*1*10^-6<wch/vch},{1-area[t1-40],wch/vch<=t1
*1*10^-6<(dap+wch)/vch}}]/40;
(* Slower and beam parameters *)

Rl=.43; (* Top Hat radius of slower beam in mm *)
Ra=.5; (* Top Hat radius of atom beam in mm *)
beamangle = 1.4Degree ;(* laser beam crossing angle *)

```

```

w0=Sqrt[2] Rl; (* Corresponding Subscript[\[Omega], 0]
   measurement for the slower beams *)
gausswidth = (2w0/1000/Tan[beamangle])^2; (* longitudinal w0 *)
Lslow=Rl/1000/Tan[beamangle]; (* slower length in m*)
Lpre=0.18-Lslow/2 ;(* dist from chopper to start of slower in m
   *)
Lpost=0.74-(Lpre+Lslow); (* dist from slower exit to detector
   in m *)
tpre=Lpre/(vcenter+\[Delta]/k); (* time the first of the
   fastest atoms that will be slowed enter the slower. Start
   here to speed things up *)
tstep=5.8*10^-6/nsteps; (* time step in seconds as divisions of
   the characteristic slowing time *)
chirpstep=dchirp/tchirp*tstep ;(* chirp freq change per time
   step *)
(* chirpstep=0; (* no chirp *) *)
vstep=chirpstep*\[Lambda]; (* velocity center change (chirp) in
   m/s per time step *)
deltav[vel_,pos_,ir_]=If[-99.5<=vel*1.756<=99.5 \[And] Lpre<=pos
   ,vel+direction*tstep*fscale*BCF[vel*1.756,ir]*\[HBar] k \[
   Gamma]/m,vel]; (* velocity change due to BCF. Note the BCF
   function needs v in \[Gamma]/k *)
(* Initialize parameters for monte carlo simulation *)

end=IntegerPart[Length[vdist]*Rl^2/Ra^2]; (* beam size
   mismatching *)
modvdist=Take[vdist,end]; (* define modified velocity
   distribution in m/s *)
initvdist=modvdist; (* initial velocities *)
(* Set up the time corrections for the chopper sweep if it hasn
   't already been done *)
If[Length[tdist]<end,
i=0;
tdist={};
problimit=1/40;
ProgressIndicator[Dynamic[i],{0,end}]
While[i<end,
timestart=RandomReal[{0,68}]; If[RandomReal[problimit]<=sweep[
   timestart],tdist=Append[tdist,timestart]; i++];
];
];
modposition=modvdist*(tpre-tdist*10^-6); (* randomly adjust
   time for the chopper window *)
(* modposition=modvdist*tpre;*) (* No velocity scatter - \
   Infinity] shutter speed *)
(* set all atoms to their position at the monte carlo start in

```

```

m *)
(* Set up irradiances for BCF calcualtions such that the peak
height of gaussian = 1.0 which equates to Subscript[\[
CapitalOmega], rabi]=1.2\[Delta] *)
outvdist={}; (* final velocity output storage array *)
modinitvdist={}; (* re-ordered array of initial velocities so
that atom initial velocity matches the outout velocity
position in outvdist *)
irr=Map[PDF[NormalDistribution[0,w0]] ,RandomReal[{-Sqrt[2] Ra,
Sqrt[2] Ra},end]]/Max[PDF[NormalDistribution[0,w0],0]]*1.19;
(* irradiances *)
tfly=tper; (* initialize time variable *)
zstart=Min[modposition];
vchirp=vcenter; (* chirped velocity center *)
z=zstart; (* initialize the position "counter" *)
chirpend=chirpdelay+tchirp; (* end time of chirp *)
holdend = chirpend + thold ;(* end time of hold *)
(* ProgressIndicator[Dynamic[z],{zstart,Lpre+Lslow}] *)(* watch
the position of the slowest atom... *)
n=0;
chirpstore={};
While[z<=Lpre+Lslow ,
loc={};
Do[If[modposition[[j]]>Lpre+Lslow ,loc=Append[loc,j]],{j,1,
Length[modposition]}];
outvdist=Flatten[Append[outvdist,modvdist[[loc]]]]; (* move
atoms that are outside the slower *)
modinitvdist=Flatten[Append[modinitvdist,initvdist[[loc]]]]; (*
move corresponding initial velocities *)
modvdist=Delete[modvdist,Partition[loc,1]]; modposition=Delete[
modposition,Partition[loc,1]]; initvdist=Delete[initvdist,
Partition[loc,1]]; irr=Delete[irr,Partition[loc,1]];
modvdist=vscale*MapThread[deltav,{(modvdist-vchirp)/vscale,
modposition,irr*E^((-2 (modposition-(0.18))^2)/gausswidth)
}]+vchirp;
modposition=modposition+modvdist*tstep;
vchirp=Piecewise[{{vchirp-vstep, chirpdelay<=tfly<chirpend},{vchirp,
chirpend<=tfly<holdend}},vcenter];
If[Mod[n,nsteps]==0, chirpstore=Append[chirpstore,vchirp]];
tfly=tfly+tstep;
n=n+1;
z=Min[modposition];
];
(* Bin the distributions and set up plotting vectors *)
bin=13;
binstart=0;

```

```

binend = 850;
binvel=Range[ binstart ,binend ,bin ];
modeldatabin=BinCounts[ Flatten[ Append[ outvdist ,Drop[ vdist ,end
+1]]]/1.755,{ binstart ,binend ,bin }];
modelbkgndbin=BinCounts[ vdist /1.755,{ binstart ,binend ,bin }];
norm=Max[ modelbkgndbin ];
modeldatabin=modeldatabin/norm;
modelbkgndbin=modelbkgndbin/norm;
plotbkgndmc=Partition[ Riffle [ binvel ,modelbkgndbin ] ,2];
plotchirpmc=Partition[ Riffle [ binvel ,modeldatabin ] ,2];
plotdiffmc=Partition[ Riffle [ binvel ,modeldatabin-modelbkgndbin
] ,2];
What we should see in the experiment where the TOF includes
both pre - and post - slower velocities
expvel=(Lpre+Lslow/2)/(Lpre+Lslow+Lpost)*modinitvdist+(Lslow/2+
Lpost)/(Lpre+Lslow+Lpost)*outvdist;(* assume the
deceleration was constant *)
expdatabin=BinCounts[ Flatten[ Append[ expvel ,Drop[ vdist ,end
+1]]]/1.755,{ binstart ,binend ,bin }]/norm;
plotchirpexp=Partition[ Riffle [ binvel ,expdatabin ] ,2];
plotdiffexp=Partition[ Riffle [ binvel ,expdatabin-modelbkgndbin
] ,2];
graphout1=ListLinePlot [ { plotchirpmc ,plotbkgndmc ,plotdiffmc } ,
InterpolationOrder->2,ImageSize->Large ,PlotRange->All ,
AxesLabel-> {" Velocity ( \[Gamma]/k ) " , " Population ( arb ) " } ,
PlotLabel-> " Actual Velocity Profile
F = "<>ToString[N[ fscale]]<>" BCF, "<>ToString[Round[N[ dchirp
*10^-6]]]<>" MHz chirp in "<>ToString[Round[N[ tchirp
*10^6]]]<>" \[Mu] s
"<> ToString[Round[N[ chirpdelay*10^6]]]<>" \[Mu] s delay, "<>
ToString[Round[N[ thold*10^6]]]<>" \[Mu] s hold ."
graphout2=ListLinePlot [ { plotchirpexp ,plotbkgndmc ,plotdiffexp } ,
InterpolationOrder->2,PlotRange->All ,ImageSize->Large ,
AxesLabel-> {" Velocity ( \[Gamma]/k ) " , " Population ( arb ) " } ,
PlotLabel-> " Simulated TOF Output
F = "<>ToString[N[ fscale]]<>" BCF, "<>ToString[Round[N[ dchirp
*10^-6]]]<>" MHz chirp in "<>ToString[Round[N[ tchirp
*10^6]]]<>" \[Mu] s
"<> ToString[Round[N[ chirpdelay*10^6]]]<>" \[Mu] s delay, "<>
ToString[Round[N[ thold*10^6]]]<>" \[Mu] s hold ."
(*
Make and save data output files for import into Orgin or other
graphics program
*)
Export[ "D:/My Documents/Research/Chirped Slower/Monte Carlo

```

```
Output/300MHz_50_210B.dat", Partition[Drop[Riffle[Flatten[N[plotbkgndmc]], Flatten[N[plotchirpexp]]], {2, -1, 4}], 3]];
Export["D:/My Documents/Research/Chirped Slower/Monte Carlo
Output/"<>ToString[N[fscale]]<>"F_"<>ToString[Round[N[dchirp
*10^-6]]]<>"_MHz_"<>ToString[Round[N[tchirp*10^6]]]<>" us_"<>
ToString[Round[N[chirpdelay*10^6]]]<>"_delay_"<>ToString[
Round[N[thold*10^6]]]<>"_hold.jpg", graphout2]
Plot[E^((-2 (z-(0.18))^2)/gausswidth),{z, Lpre,(Lpre+Lslow)}]
```

References

- [1] D. Wineland and H. Dehmelt, Bull. Am. Phys. Soc. **20**, 637 (1975).
- [2] D. Wineland and W. Itano, Phys. Rev. A **20**, 1521 (1979).
- [3] T. Hänsch and A. Schawlow, Opt. Comm. **13**, 68 (1975).
- [4] P. Meystre and S. Stenholm, J. Opt. Soc. Am. B **2**, 1705 (1985).
- [5] S. Chu and C. Wieman, J. Opt. Soc. Am. B **6**, 2020 (1989).
- [6] W. D. Phillips and H. Metcalf, Phys. Rev. Lett. **48**, 596 (1982).
- [7] J. V. Prodan, W. D. Phillips, and H. Metcalf, Phys. Rev. Lett. **49**, 1149 (1982).
- [8] E. L. Raab, M. Prentiss, A. Cable, S. Chu, and D. E. Pritchard, Phys. Rev. Lett. **59**, 2631 (1987).
- [9] H. J. Metcalf and P. van der Straten, *Laser Cooling and Trapping*, Springer-Verlag, 1999.
- [10] C. S. Adams and E. Riis, Prog. Quantum Electron. **21**, 1 (1997).
- [11] D. Suter, *The Physics of Laser-Atom Interactions*, Cambridge Studies in Modern Optics, Cambridge University Press, Cambridge, 1997.
- [12] A. P. Kazantsev and I. V. Krasnov, JETP Lett. **46**, 420 (1987).
- [13] R. Grimm, Y. B. Ovchinnikov, A. I. Sidorov, and V. S. Letokhov, Phys. Rev. Lett. **65**, 1415 (1990).
- [14] J. Söding, R. Grimm, Y. B. Ovchinnikov, P. Bouyer, and C. Salomon, Phys. Rev. Lett. **78**, 1420 (1997).
- [15] V. S. Voitsekhovich, M. V. Danileiko, A. M. Negriiko, V. I. Romanenko, and L. P. Yatsenko, JEPT Lett. **49**, 161 (1989).
- [16] V. S. Voitsekhovich, M. V. Danileiko, A. M. Negriiko, V. I. Romanenko, and L. P. Yatsenko, JEPT Lett. **59**, 408 (1994).

- [17] M. R. Williams, F. Chi, M. T. Cashen, and H. Metcalf, Phys. Rev. A **60**, R1763 (1999).
- [18] M. R. Williams, F. Chi, M. T. Cashen, and H. Metcalf, Phys. Rev. A **61**, 023408 (2000).
- [19] M. T. Cashen and H. Metcalf, Phys. Rev. A **63**, 025406 (2001).
- [20] M. Cashen and H. Metcalf, J. Opt. Soc. Am. B **20**, 915 (2003).
- [21] R. N. Watts and C. E. Wieman, Opt. Lett. **11**, 291 (1986).
- [22] B. Sheehy, S.-Q. Shang, R. Watts, S. Hatamian, and H. Metcalf, J. Opt. Soc. Am. B **6**, 2165 (1989).
- [23] R. Schumann, C. Schubert, U. Eichmann, R. Jung, and G. von Oppen, Phys. Rev. A **59**, 2120 (1999).
- [24] W. Rooijackers, W. Hogervorst, and W. Vassen, Optics Comm. **135**, 149 (1997).
- [25] P. J. J. Tol, N. Herschbach, E. A. Hessels, W. Hogervorst, and W. Vassen, Phys. Rev. A **60**, R761 (1999).
- [26] A. S. Tychkov, J. C. J. Koelemeij, T. Jeltes, W. Hogervorst, and W. Vassen, Phys. Rev. A **69**, 055401 (2004).
- [27] J. C. J. Koelemeij, R. J. W. Stas, W. Hogervorst, and W. Vassen, Phys. Rev. A **67**, 053406 (2003).
- [28] P. J. Ungar, D. S. Weiss, E. Riis, and S. Chu, J. Opt. Soc. Am. B **6**, 2058 (1989).
- [29] J. Dalibard and C. Cohen-Tannoudji, J. Opt. Soc. Am. B **6**, 2023 (1989).
- [30] C. N. Cohen-Tannoudji and W. D. Phillips, Physics Today **43**, 33 (1990).
- [31] J. Dalibard and C. Cohen-Tannoudji, J. Opt. Soc. Am. B **2**, 1707 (1985).
- [32] E. Kyrölä and S. Stenholm, Optics Communications **22**, 123 (1977).
- [33] J. Javanainen, Phys. Rev. Lett. **64**, 519 (1990).
- [34] A. Aspect, W. Barletta, and R. Bonifacio, editors, *Laser Cooling and Trapping with Rectified Optical Dipole Forces*, Amsterdam, 1996, Società Italiana di Fisica, IOS Press.

- [35] M. T. Cashen, *Optical Forces on Atoms in Polychromatic Light Fields*, PhD thesis, State University of New York at Stony Brook, 2002.
- [36] M. J. Partlow, *Bichromatic Collimation to Make and Intense Helium Beam*, PhD thesis, State University of New York at Stony Brook, 2004.
- [37] V. S. Voitsekhovich, M. V. Danileiko, V. I. Negrilko, V. I. Romanenko, and L. P. Yatsenko, Sov. Phys. JETP **72**, 219 (1991).
- [38] R. Gupta, C. Xie, S. Padua, H. Batelaan, and H. Metcalf, Phys. Rev. Lett. **71**, 3087 (1993).
- [39] F. Bloch, Z. Phys. A-Hadron Nucl. **52**, 555 (1929).
- [40] R. P. Feynman, F. L. Vernon, Jr., and R. W. Hellwarth, J. Appl. Phys. **28**, 49 (1957).
- [41] L. Allen and J. H. Eberly, *Optical Resonance and Two-Level Atoms*, Dover books on physics and chemistry, Dover, 1987.
- [42] M. Partlow, X. Miao, J. Bochmann, M. Cashen, and H. Metcalf, Phys. Rev. Lett. **93**, 213004 (2004).
- [43] R. Grimm, J. Söding, and Y. B. Ovchinnikov, Opt. Lett. **19**, 658 (1994).
- [44] L. Yatsenko and H. Metcalf, Phys. Rev. A **70**, 063402 (2004).
- [45] C. Cohen-Tannoudji, J. Dupont-Roc, and G. Grynberg, *Atom-Photon Interactions*, Wiley & Sons, New York, 1992.
- [46] C. Zener, Proc. R. Soc. A **137**, 696 (1932).
- [47] J. R. Rubbmark, M. M. Kash, M. G. Littman, and D. Kleppner, Phys. Rev. A **23**, 3107 (1981).
- [48] L. D. Landau and L. M. Lifshitz, *Quantum Mechanics (Non-relativistic Theory)*, Elsiver Science Ltd., third edition, 1977.
- [49] J. H. Shirley, Phys. Rev. **138**, B979 (1965).
- [50] S. Guérin and H. R. Jauslin, *Control of Quantum Dynamics by Laser Pulses: Adiabatic Floquet Theory*, pages 147–267, Advances in Chemical Physics, John Wiley & Sons, Inc., 2003.
- [51] S. Guérin, F. Monti, J.-M. Dupont, and H. R. Jauslin, J. Phys. A **30**, 7193 (1997).

- [52] J. M. Supplee, Am. J. Phys. **68**, 180 (2000).
- [53] R. W. Boyd, *Nonlinear Optics*, Academic Press, 2008.
- [54] H. J. Metcalf and P. van der Straten, J. Opt. Soc. Am. B **20**, 887 (2003).
- [55] M. Cashen, O. Rivoire, V. Romanenko, L. Yatsenko, and H. Metcalf, Phys. Rev. A **64**, 063411 (2001).
- [56] H. Metcalf, Phys. Rev. A **77**, 061401 (2008).
- [57] N. B. Delone and V. P. Krainov, Phys. Usp. **42**, 669 (1999).
- [58] A. M. Bonch-Bruevich, N. N. Kostin, V. A. Khodovoi, and V. V. Khromov, Sov. Phys. JETP **29**, 82 (1969).
- [59] I. I. Sobelman, *Atomic Spectra and Radiative Transitions*, Springer-Verlag, second edition, 1996.
- [60] Y. Ralchenko, A. Kramida, J. Reader, and NIST ASD Team, NIST Atomic Spectra Database, Online, 2011.
- [61] O. von Roos, The Journal of Chemical Physics **30**, 729 (1959).
- [62] E. W. Rothe, R. H. Neynaber, and S. M. Trujillo, J. Chem. Phys. **42**, 3310 (1965).
- [63] B. Zygelman, Phys. Rev. A **43**, 575 (1991).
- [64] R. J. W. Stas, J. M. McNamara, W. Hogervorst, and W. Vassen, Phys. Rev. A **73**, 032713 (2006).
- [65] R. H. Neynaber, G. D. Magnuson, and S. Y. Tang, The Journal of Chemical Physics **68**, 5112 (1978).
- [66] E. H. S. Burhop, Proceedings of the Physical Society. Section A **67**, 276 (1954).
- [67] H. J. Kolker and H. H. Michels, The Journal of Chemical Physics **50**, 1762 (1969).
- [68] IntraAction Corp., *Model ATM-Series Acousto-Optic Modulator Instruction Manual*, 1992.
- [69] J. Kawanaka, M. Hagiuda, K. Shimizu, F. Shimizu, and H. Takuma, Appl. Phys. B **56**, 21 (1993).

- [70] H. C. Mastwijk, M. van Rijnbach, J. W. Thomsen, P. van der Straten, and A. Niehaus, Eur. Phys. J. D **4**, 131 (1998).
- [71] G. R. Woestenenk, J. W. Thomsen, M. van Rijnbach, P. van der Straten, and A. Niehaus, Rev. Sci. Instrum. **72**, 3842 (2001).
- [72] C. Kurtsiefer and J. Mlynek, Appl. Phys. B **64**, 85 (1996).
- [73] T. W. Hänsch, Appl. Opt. **11**, 895 (1972).
- [74] J. C. J. Koelemeij, W. Hogervorst, and W. Vassen, Rev. Sci. Instrum. **76**, 033104 (2005).
- [75] W. Lu et al., Rev. Sci. Instrum. **67**, 3003 (1996).
- [76] P. C. D. Hobbs, Opt. Photon. News **2**, 17 (1991).
- [77] E. E. Eyler, Rev. Sci. Instrum. **82**, 013105 (2011).
- [78] E. E. Eyler, Microcontroller designs for atomic, molecular, and optical physics laboratories, Online, 2011.
- [79] V. M. Kotov and G. N. Shkerdin, J. Commun. Technol. El. **39**, 45 (1994).
- [80] Crystal Technology, Inc., *Acousto-Optic Application Note– Modulator Model 3000 Series*, DO-16-A 01/06 edition, 2006.
- [81] K. Pearson, Nature **72**, 318 (1905).
- [82] Toptica Photonics AG, *DL100 Grating Stabilized Diode Laser Head Manual*, M-008 version 01 edition, 2006.
- [83] H. Golnabi and A. Ashrafi, Rev. Sci. Instrum. **67**, 2017 (1996).
- [84] M. S. Fee, K. Danzmann, and S. Chu, Phys. Rev. A **45**, 4911 (1992).
- [85] R. T. White, Y. He, B. J. Orr, M. Kono, and K. G. H. Baldwin, J. Opt. Soc. Am. B **21**, 1577 (2004).
- [86] R. T. White, Y. He, B. J. Orr, M. Kono, and K. G. H. Baldwin, J. Opt. Soc. Am. B **24**, 2601 (2007).
- [87] N. Melikechi, S. Gangopadhyay, and E. E. Eyler, J. Opt. Soc. Am. B **11**, 2402 (1994).
- [88] S. Gangopadhyay, *Optical phase distortions in nanosecond laser pulses and their effects on high resolution spectroscopy*, PhD thesis, University of Delaware, 1995.

- [89] P. A. Molenaar, P. van der Straten, H. G. M. Heideman, and H. Metcalf, Phys. Rev. A **55**, 605 (1997).
- [90] M. A. Joffe, W. Ketterle, A. Martin, and D. E. Pritchard, J. Opt. Soc. Am. B **10**, 2257 (1993).
- [91] M. A. Chieda and E. E. Eyler, Phys. Rev. A **84**, 063401 (2011).
- [92] P. F. Barker, AIP Conference Proceedings **1333**, 31 (2011).
- [93] E. S. Shuman, J. F. B. D. R. Glen, and D. DeMille, Phys. Rev. Lett. **103**, 223001 (2009).
- [94] M. Pelegrini, C. S. Vivacqua, O. Roberto-Neto, F. R. Ornellas, and F. B. C. Machado, Brazilian Journal of Physics **35**, 950 (2005).
- [95] T. E. Wall et al., Phys. Rev. A **78**, 062509 (2008).
- [96] E. S. Shuman, J. F. Barry, and D. DeMille, Nature (London) **467**, 820 (2010).
- [97] R. W. Field, D. O. Harris, and T. Tanaka, Journal of Molecular Spectroscopy **57**, 107 (1975).
- [98] K. Maussang, D. Egorov, J. S. Helton, S. V. Nguyen, and J. M. Doyle, Phys. Rev. Lett. **94**, 123002 (2005).
- [99] L. Shampine and M. Gordon, *Computer Solution of Ordinary Differential Equations: The Initial Value Problem*, Freeman Press, 1975.